

ISTANBUL TECHNICAL UNIVERSITY ★ GRADUATE SCHOOL OF SCIENCE
ENGINEERING AND TECHNOLOGY

**EFFECT OF SURFACE ROUGHNESS ON THE TURBULENT BOUNDARY
LAYER DUE TO MARINE COATINGS**

Ph.D. THESIS

Burcu ÜNAL

Department of Naval Architecture and Marine Engineering

Naval Architecture and Marine Engineering Programme

SEPTEMBER 2012

ISTANBUL TECHNICAL UNIVERSITY ★ GRADUATE SCHOOL OF SCIENCE
ENGINEERING AND TECHNOLOGY

**EFFECT OF SURFACE ROUGHNESS ON THE TURBULENT BOUNDARY
LAYER DUE TO MARINE COATINGS**

Ph.D. THESIS

Burcu ÜNAL
(508042004)

Department of Naval Architecture and Marine Engineering

Naval Architecture and Marine Engineering Programme

Thesis Advisor: Prof. Dr. Muhittin SÖYLEMEZ

SEPTEMBER 2012

İSTANBUL TEKNİK ÜNİVERSİTESİ ★ FEN BİLİMLERİ ENSTİTÜSÜ

**GEMİ BOYALARINA AİT YÜZEY PÜRÜZLÜLÜĞÜNÜN TÜRBÜLANSLI
SINIR TABAKAYA ETKİSİ**

DOKTORA TEZİ

**Burcu ÜNAL
(508042004)**

Gemi İnşaatı ve Gemi Makinaları Mühendisliği Bölümü

Gemi İnşaatı ve Gemi Makinaları Mühendisliği Programı

Tez Danışmanı: Prof. Dr. Muhittin SÖYLEMEZ

EYLÜL 2012

Burcu Ünal, a **Ph.D.** student of ITU **Graduate School of Science Engineering and Technology** student ID 508042004, successfully defended the **thesis/dissertation** entitled “**EFFECT OF SURFACE ROUGHNESS ON THE TURBULENT BOUNDARY LAYER DUE TO MARINE COATINGS**”, which she prepared after fulfilling the requirements specified in the associated legislations, before the jury whose signatures are below.

Thesis Advisor: **Prof. Dr. Muhittin SÖYLEMEZ**

İstanbul Technical University

Jury Members: **Prof. Dr. Emin KORKUT**

İstanbul Technical University

Doç. Dr. Okşan ÇETİNER YILDIRIM

İstanbul Technical University

Prof. Dr. Mehmet ATLAR

Newcastle University

Prof. Dr. Ercan KÖSE

Karadeniz Technical University

Prof. Dr. Deniz ÜNSALAN

Piri Reis University

Date of Submission :16 August 2012

Date of Defense : 28 September 2012

FOREWORD

It is not easy to find the correct words to express my feelings while writing these lines. One thing is certain that completing this research work was a major milestone on the road to fulfil one of my lifetime professional and personal goals. I am therefore most grateful to God for providing me with such a lifetime opportunity and strength to achieve it.

In addition, there have been number of people for whom I would like to thank wholeheartedly since this work would not have been possible without their sterling support. Amongst them first and foremost, I would like to gratefully acknowledge my advisor, Prof.Dr. Muhittin Söylemez for all his support and guidance. I am so grateful to him for accepting me to be his research assistant years ago, although he barely knew me by then. I would like to pay my highest gratitude to late Prof.Dr. Yücel Odabaşı who led me to study on this topic and therefore I hope that this work is worthy for his great memory. This study is dedicated to the great memories of Prof.Dr. Yücel Odabaşı and Prof.Dr. Muhittin Söylemez.

I would like to express my profound gratitude to Prof.Dr. Mehmet Atlar of Newcastle University, who gave me the chance to feel myself as a part of the Emerson Cavitation Tunnel group in the School of Marine Science and Technology, who encouraged me throughout the study and supported this thesis in countless aspects. This included kindly inviting me to Newcastle University for study visits and access to the experiments conducted in the FP6 AMBIO Project as well as numerous other tests supported by International Paints Ltd of AKZO-NOBEL.

My appreciation also goes to the members of my advisory committee, Prof.Dr. Emin Korkut and Doç.Dr. Okşan Çetiner Yıldırım, for their invaluable suggestions throughout the study.

I gratefully acknowledge Istanbul Technical University (ITU) and Naval Architecture and Engineering Faculty of ITU for supporting my visits to Newcastle University.

My special thanks are to Mr. Georgios Politis who put great effort in helping in the experiments and succeeded in cheering us even when everything broke down, and even in his hardest times.

I also would like to thank to Prof. Michael P. Schultz for his invaluable advice specifically about the LDV and turbulence spectra measurements and to Dr. Holger Nobach for his kind support about Nambis and his suggestions for my code.

I would like to express my gratitude to my parents who taught me the power of knowledge, gave me the courage to stand on my own feet, and supported me with their endless love throughout my life.

I also would like to thank my parents in law, for their prayers, for always being full of love to me and accepting me as their daughter from the time we met.

Finally, Oral, my loving husband, you are my best friend, my precious lover and my joy of life. Your love and support mean the world and happiness to me. I am so grateful to know you, to share our lives together, and to see the world from the same window together. Thank you very much for always being there.

September 2012

Burcu ÜNAL

TABLE OF CONTENTS

	<u>Page</u>
FOREWORD	vii
TABLE OF CONTENTS	ix
ABBREVIATIONS	xiii
LIST OF TABLES	xv
LIST OF FIGURES	xvii
SYMBOL LIST	xxi
SUMMARY	xxiii
ÖZET	xxvii
1. INTRODUCTION	1
1.1 Introduction	1
1.2 Literature Review on Rough Wall Turbulent Boundary Layers	2
1.3 Motivation of Thesis	11
1.4 Aim and Objectives of Thesis	11
1.5 Layout of Thesis	13
1.6 Summary	15
2. TURBULENT BOUNDARY LAYER	17
2.1 Introduction	17
2.2 Turbulent Flow	17
2.3 Turbulent Boundary Layer	18
2.4 The Reynolds-Averaged Navier-Stokes Equations and 2-Dimensional Turbulent Boundary Layer Equations	20
2.5 Overall Structure of a Turbulent Boundary Layer and Scaling Laws	21
2.6 The Effect of Wall Roughness on the Turbulent Boundary Layer	25
2.7 The Methods for the Determination of the Skin Friction Drag	28
2.8 Summary	34
3. TURBULENCE SPECTRUM	37
3.1 Introduction	37
3.2 One-Dimensional and Three-Dimensional Spatial Spectrum	37
3.3 Time Spectrum	41
3.4 Calculation of Turbulence Spectra from Laser Doppler Velocimetry Data	43
3.5 Refined Sample and Hold Method for Power Spectral Density Estimation from LDV Data	45
3.5.1 Pre-filtering	46
3.5.2 Block splitting	47
3.5.3 ACF estimation	47
3.5.4 ACF to PSD transform	49
3.5.5 Block Averaging	49
3.6 Transfer Functions	49
3.7 Summary	51
4. SURFACE ROUGHNESS MEASUREMENT AND ANALYSIS	53

4.1 Introduction	53
4.2 Definition of Surface Roughness	53
4.3 Surface Roughness Measurement Devices.....	54
4.4 Analysis of Surface Roughness and Roughness Parameters	57
4.5 Autocorrelation and Power Spectral Density Functions for Surface Roughness	61
4.6 Summary.....	63
5. TURBULENT BOUNDARY LAYER MEASUREMENTS ON FLAT PLATES WITH ZERO-PRESSURE GRADIENT	65
5.1 Introduction	65
5.2 Emerson Cavitation Tunnel	66
5.3 Experimental Set-up.....	67
5.4 LDV System	71
5.5 Surface Roughness Characterization of the Test Plates	74
5.6 Inflow Measurements.....	93
5.7 Uncertainty	96
5.8 Data Analysis Methods and Method Description	99
5.9 Results	100
5.10 Conclusions.....	121
6. ZERO-PRESSURE GRADIENT FLAT PLATE TURBULENT BOUNDARY LAYER MEASUREMENTS FOR TURBULENCE SPECTRUM CALCULATION	125
6.1 Introduction	125
6.2 Experimental Set-Up.....	126
6.3 Preliminary Measurements	132
6.3.1 Inflow measurements	132
6.3.2 Acceleration parameter measurements.....	138
6.4 Roughness Characterization of the Test Plates.....	139
6.5 Data Collection and Analysis	149
6.6 Uncertainty	151
6.7 Results	154
6.7.1 Boundary layer parameters.....	155
6.7.2 Mean velocity profiles in outer and inner scaling.....	156
6.7.3 Local frictional drag coefficients and roughness functions.....	159
6.7.4 Reynolds Stresses.....	166
6.7.5 Higher-order statistics	170
6.7.6 Autocorrelation and spatial correlation functions	178
6.7.7 Turbulence spectra	184
6.7.8 Transfer functions	202
6.8 Conclusions	209
7. CONCLUSIONS AND RECOMMENDATIONS FOR FUTURE WORK..	217
7.1 Introduction	217
7.2 Main Conclusions	219
7.2.1 Roughness characterization	219
7.2.2 Skin friction drag characteristics	219
7.2.3 Correlation of roughness and skin friction drag	220
7.2.4 Outer layer similarity	220
7.2.5 Turbulence spectra	221
7.2.6 Transfer functions	222
7.3 Recommendations for Future Work.....	223

REFERENCES	227
CURRICULUM VITAE.....	247

ABBREVIATIONS

ACF	: Autocorrelation Function
AHR	: Average Hull Roughness
BMT	: British Marine Technology
BMT-HRA	: BMT Hull Roughness Analyser
DNS	: Direct Numerical Simulation
ECT	: Emerson Cavitation Tunnel
FFT	: Fast Fourier Transform
FR	: Foul (ing) - Release
IMO	: International Maritime Organization
ISO	: International Organization for Standardization
LDV	: Laser Doppler Velocimetry
N-S	: Navier-Stokes Equations
PDF	: Probability Density Function
PSD	: Power Spectral Density Function
RANS	: Reynolds Averaged Navier Stokes Equations
SPC	: Self Polishing Copolymer
TBT	: Trybutilin-Tin

LIST OF TABLES

	<u>Page</u>
Table 5.1 : Rt_{50} parameter of the test specimens, from BMT-HRA	76
Table 5.2 : Roughness parameters of the flat plate samples at various cut-off lengths.	85
Table 5.3 : Characteristics of the freestream.	94
Table 5.4 : Estimator variances	96
Table 5.5 : Variation of the boundary layer parameters for reference surfaces.	101
Table 5.6 : Variation of the boundary layer parameters for nanostructured surfaces.....	102
Table 5.7 : Variation of the inner variables for the reference surfaces.	105
Table 5.8 : Variation of the inner variables for nanostructured surfaces.	106
Table 6.1 : The mean velocities and average turbulence intensities accross the test section (Data from Politis, 2010).	134
Table 6.2 : Acceleration parameters.	139
Table 6.3 : The roughness parameters at various cut-off lengths.	143
Table 6.4 : Variation of the boundary layer parameters.....	156
Table 6.5 : The friction velocities and local skin friction drag coefficients.....	161
Table 6.6 : The roughness functions and roughness Reynolds numbers.	163
Table 6.7 : The parameters of the fourth order Fourier function for the transfer functions along with the goodness of fit.	207

LIST OF FIGURES

	<u>Page</u>
Figure 3.1 : Processing steps of ACF and PSD estimation from LDV data.	46
Figure 4.1 : Types of surface deviations (from Whitehouse, 2011).	54
Figure 4.2 : The geometries of stylus and stylus geometry effect on roughness measurement.	55
Figure 4.3 : The BMT hull roughness analyser.	56
Figure 4.4 : The Omniscan Uniscan OSP100A laser profilometer.	57
Figure 4.5 : The lengths used in surface characterization (from Whitehouse, 2002).	58
Figure 4.6 : The surface profile, waviness and roughness (from Whitehouse, 2011).	59
Figure 4.7 : Levelling of the raw surface profile (from Politis et al., 2011).	59
Figure 4.8 : Calculation of the autocorrelation function (from Whitehouse, 2011).	62
Figure 5.1 : Schematic of the Emerson Cavitation Tunnel.	66
Figure 5.2 : Testing bed plate sketch showing the measurement positions and dimensions of the test plate in mm.	68
Figure 5.3 : Test plate before being adjusted into the tunnel with FR specimen (red coloured) fitted on it.	68
Figure 5.4 : The test plate mounted in the tunnel test section, photograph taken just after the changing of the test specimen (pink coloured).	68
Figure 5.5 : The test specimens	70
Figure 5.6 : Test specimens drying after coating application.	71
Figure 5.7 : ECT test section and 2D LDV set-up during the tests of FCP1 coated surface.	72
Figure 5.8 : The components of the 2D LDV system.	72
Figure 5.9 : The beam separator (located at the front right) and the laser light source.	73
Figure 5.10 : 60 mm probe with the beam expander and 500 mm focus length lens.	73
Figure 5.11 : The seeding material.	74
Figure 5.12 : BMT Hull Roughness Analyser.	75
Figure 5.13 : The locations of the three data-collection lines on the actual test specimens (from Ünal et al., 2010 report).	75
Figure 5.14 : Uniscan OSP100 laser profilometer.	77
Figure 5.15 : Roughness topographies of the tested reference surfaces.	77
Figure 5.16 : Roughness topographies of the tested surfaces coated with nanostructured antifouling.	79
Figure 5.17 : An example to noise reduction results.	79
Figure 5.18 : Sample raw profiles (blue) and waviness (red on blue) and roughness profiles (red) for the same profile for various cut-off lengths.	81

Figure 5.19 : Roughness histograms of the reference sample test plates (cut-off=2.5 mm).....	82
Figure 5.20 : Sample roughness histograms of the sample test plates coated with nanostructured antifouling (cut-off=2.5 mm).	84
Figure 5.21 : Autocorrelation functions of the tested surfaces, cut-off 2.5 mm.	86
Figure 5.22 : Autocorrelation functions of the tested surfaces, cut-off 5 mm.	87
Figure 5.23 : Autocorrelation functions of the tested surfaces, cut-off 8 mm.	88
Figure 5.24 : The effect of cut-off length on the autocorrelation functions.	89
Figure 5.25 : Comparison of PSD at a cut-off length of 2.5 mm.	90
Figure 5.26 : Comparison of PSD at a cut-off length of 5 mm.	91
Figure 5.27 : Comparison of PSD at a cut-off length of 8 mm.	92
Figure 5.28 : Cut-off length effect on PSD.....	93
Figure 5.29 : Streamwise and transverse mean velocities for freestream velocity of 2 m/s at IN1 and IN2 sections	95
Figure 5.30 : Streamwise and transverse turbulent intensities for freestream velocity of 2 m/s at IN1 and IN2 sections.....	95
Figure 5.31 : Uncertainties (%) in the mean streamwise and transverse (right) velocities	97
Figure 5.32 : Uncertainties (%) in root-mean-square streamwise and transverse (right) velocities.....	97
Figure 5.33 : Uncertainty (%) in mean streamwise and transverse velocities calculated with repetitive measurements for the FR coated surface... ..	98
Figure 5.34 : Uncertainty (%) in root-mean-square streamwise and transverse velocities and shear stresses calculated with repetitive measurements for the FR coated surface.	99
Figure 5.35 : Streamwise velocity in outer variables at POS2, 3m/s.	103
Figure 5.36 : Streamwise velocity in outer variables for all test cases.....	104
Figure 5.37 : Least-squares curves and measured velocity profiles for FCP1_POS3_3 with HM (Uncertainty in UUe : $\pm 0.6\%$).....	107
Figure 5.38 : Least-squares curves and measured velocity profiles for FCP1_POS3_3 with MCCM (Uncertainty in UUe : $\pm 0.6\%$).....	107
Figure 5.39 : Comparison of local frictional drag for STEEL.....	107
Figure 5.40 : Streamwise velocity in inner variables at various test positions and inflow velocities.	110
Figure 5.41 : Streamwise velocity in velocity defect form.	111
Figure 5.42 : Shape parameter and local skin friction drag correlation.	111
Figure 5.43 : Local frictional drag coefficient of the tested surfaces.....	112
Figure 5.44 : Variation of the roughness function values for reference (top) and nanostructured surfaces.	113
Figure 5.45 : Correlation of the roughness functions and the roughness Reynolds number.	114
Figure 5.46 : Streamwise normal Reynolds stresses in inner (top) and outer scales.	117
Figure 5.47 : Transverse normal Reynolds stresses in inner (top), outer (middle) and George and Castillo (1997) scaling.....	119
Figure 5.48 : Reynolds shear stresses in inner scales.....	120
Figure 6.1 : Schematic of the test bed.	128
Figure 6.2 : Photographs of the test bed; tail section at the right hand side.	128
Figure 6.3 : The steel plates were #120 sanded before the anti-fouling application.	129

Figure 6.4 : The application of anticorrosive with roller.	129
Figure 6.5 : The test specimens.	130
Figure 6.6 : A general view of the tunnel test section and LDV during the measurements.	131
Figure 6.7 : LDV probe with 5° tilt and 45° rotation.	131
Figure 6.8 : The equipment used for adding seeding to the tunnel water and the seeding material.	132
Figure 6.9 : Inflow measurement planes (from Politis, 2010).	133
Figure 6.10 : The streamwise (plots located at the top) and transverse velocity distributions across the tunnel test section for the first 3 planes at 4 m/s inflow velocity (from Politis, 2010).	135
Figure 6.11 : Variation of nondimensional streamwise (left) and transverse velocities.	136
Figure 6.12 : Variation of streamwise (left) and transverse turbulence intensities. .	138
Figure 6.13 : The OSP100 profilometer with the modified legs of the traverse mechanism.	140
Figure 6.14 : Autocorrelation functions calculated for various cut-off lengths.	144
Figure 6.15 : Autocorrelation functions calculated for various cut-off lengths, closer look.	145
Figure 6.16 : Power spectral density functions calculated for cut-off length of 2.5 mm.	146
Figure 6.17 : Power spectral density functions calculated for cut-off length of 5 mm.	146
Figure 6.18 : Power spectral density functions calculated for cut-off length of 8 mm.	147
Figure 6.19 : Power spectral density functions calculated for cut-off length of 50 mm.	147
Figure 6.20 : Power spectral density functions observed in semi-log scale.	148
Figure 6.21 : Variation of uncertainty in streamwise (left) and transverse velocities throughout the boundary layer.	152
Figure 6.22 : Variation of uncertainty in the Reynolds stresses.	153
Figure 6.23 : Uncertainty percentages for the streamwise (left) and transverse triple correlations.	154
Figure 6.24 : Uncertainty percentages for the streamwise (left) and transverse velocities.	154
Figure 6.25 : Mean velocity profiles for the entire test cases, in outer scaling.	157
Figure 6.26 : Streamwise velocity profiles in inner scaling.	158
Figure 6.27 : Velocity profiles in defect form, in Rotta scaling (top) and conventional outer scaling (bottom).	159
Figure 6.28 : Local skin friction drag coefficient of the tested surfaces.	162
Figure 6.29 : Variation of the roughness functions for the test cases.	165
Figure 6.30 : Correlation of the roughness function and the roughness Reynolds number including the new relations.	165
Figure 6.31 : Streamwise Reynolds normal stresses in inner scaling.	167
Figure 6.32 : Wall-normal Reynolds stresses in inner (top) and outer scaling.	169
Figure 6.33 : Reynolds shear stresses in inner (top) and outer scaling.	170
Figure 6.34 : Streamwise (top) and transverse fluctuating velocity components triple correlations.	172
Figure 6.35 : The normalized streamwise (top) and wall-normal turbulent transport of Reynolds stresses in outer scaling.	174

Figure 6.36 : Skewness distributions for the streamwise (top) and transverse velocity fluctuations.....	176
Figure 6.37 : Variation of flatness factors for the streamwise (top) and transverse velocity fluctuations.....	177
Figure 6.38 : The variation of autocorrelation function through the boundary layer.....	179
Figure 6.39 : Compararison of the autocorrelation functions for various surfaces.	181
Figure 6.40 : Variation of the integral time scales.	182
Figure 6.41 : The variation of spatial correlation coefficient.	184
Figure 6.42 : Comparison of the used algorithms in MATLAB code and benchmark test, average sampling rate of the data set is 1470 Hz. ..	188
Figure 6.43 : Comparison of the used algorithms in MATLAB code and benchmark test, average sampling rate of the data set is 300 Hz.	188
Figure 6.44 : Comparison of the S&H algorithms in MATLAB code with and without CFT and benchmark test, average sampling rate of the data set is 1250 Hz.	189
Figure 6.45 : The dimensional streamwise turbulence spectra variation on the surfaces, at five different locations in the boundary layer.	191
Figure 6.46 : Streamwise turbulence spectra at various positions for all tested surfaces in inner scaling.	192
Figure 6.47 : Streamwise turbulence spectra at various positions for all tested surfaces in outer scaling.	193
Figure 6.48 : Comparative plots of the streamwise turbulence spectra for the tested surfaces at various positions in inner scaling.	195
Figure 6.49 : Comparative plots of the streamwise turbulence spectra for the tested surfaces at various positions in outer scaling.	197
Figure 6.50 : The dimensional wall-normal turbulence spectra variation on the surfaces, at five different locations in the boundary layer.	198
Figure 6.51 : Wall-normal turbulence spectra at various positions for the smooth surface in inner scaling.	199
Figure 6.52 : Comparative plots of the wall-normal turbulence spectra for the tested surfaces at various positions in inner scaling.	201
Figure 6.53 : The effect of cut-off lengths used in the roughness analysis on the transfer function, SPC surface.	203
Figure 6.54 : The transfer functions between the roughness and streamwise turbulence spectra, F_{uu}	204
Figure 6.55 : The transfer functions between the roughness and wall-normal turbulence spectra, F_{vv}	205
Figure 6.56 : The agreement of the proposed functions for F_{uu}	206
Figure 6.57 : The agreement of the proposed functions for F_{vv}	208

SYMBOL LIST

B	: Logarithmic law constant for smooth walls
c_f	: Local friction drag coefficient
C_f	: Friction drag coefficient
De	: Number of peaks per unit roughness profile
$E(k)$: Three dimensional turbulence spectra
G	: Body forces
H	: Shape factor
k	: Roughness height, wave number
K	: Acceleration parameter
k_s^+	: Roughness Reynolds number
k_s	: Equivalent sand roughness
k_1	: Streamwise wave number
Ku	: Kurtosis of the probability density function of roughness height distribution
ℓ	: Eddy size
L_c	: Cut-off length
l_v	: Viscous length scale
m_n	: n^{th} moment of the power spectral density function
\dot{n}	: Average data sampling rate
P	: Pressure, Reynolds-averaged pressure
R	: Autocorrelation function
r	: Correlation coefficient
$R_{ij}(\vec{r})$: Spatial correlation tensor
Ra	: Arithmetic mean of the departures of the surface profile from the mean line
Re_L	: Length based Reynolds number
Re_θ	: Momentum thickness Reynolds number
Re_{δ_1}	: Displacement thickness Reynolds number
Rt	: Largest peak to valley height
Rq	: Root-mean-square value of the roughness heights
S	: Mean flow strain rate
S	: Mean spacing between local peaks
Sm	: Mean spacing between profile peaks
Sk	: Skewness of the probability density function of the roughness height distribution
t	: Time
T	: Integral time scale
TI_x	: Turbulence intensity in the streamwise direction
TI_y	: Turbulence intensity in the transverse direction
u'	: Random velocity component, streamwise turbulent velocity component

U	: Flow velocity, mean streamwise velocity
U^+	: Mean streamwise velocity non-dimensionalized with the friction velocity
U_e^+	: Mean freestream velocity non-dimensionalized with the friction velocity
U_e	: Mean freestream velocity
\bar{U}	: Average flow velocity
u_τ	: Friction velocity
V	: Mean transverse velocity
v'	: Transverse turbulent velocity component
W	: Wake function
w_i	: Weighting factor
y	: Wall-normal distance
y^+	: Wall-normal distance non-dimensionalised with the viscous length scale
α	: Bandwidth parameter
δ	: Boundary layer thickness
δ_1	: Displacement thickness
δ^+	: Reynolds number based on boundary layer thickness
ΔU^+	: Roughness function
ε	: Error in the origin of a rough wall, turbulence dissipation rate
$\phi_{ij}(\vec{k})$: Turbulence spectra tensor
$\Psi_{ij}(\omega)$: Turbulence time spectra tensor
ρ	: Fluid density
κ	: von-Karman constant
μ	: Dynamic viscosity
μ_i	: Local mean value of the velocity data
η	: Kolmogorov micro scale
θ	: Momentum thickness
Π	: Wake strength
τ	: Time or space lag
τ_w	: Wall shear stress
τ_{ij}	: Viscous stress tensor
$\tau_{0.5}$: Correlation length
τ_{ij}'	: Reynolds stress tensor
τ_i	: Transit times of the fluid particles through the probe volume
ν	: Kinematic viscosity
v	: Kolmogorov velocity scale
ω	: Frequency

EFFECT OF SURFACE ROUGHNESS ON THE TURBULENT BOUNDARY LAYER DUE TO MARINE COATINGS

SUMMARY

Most of the engineering wall-bounded turbulent flows develop under the influence of surface roughness and therefore the turbulent boundary layer over rough surfaces has been a widely studied research topic. The examples can be given for rough wall flows in a wide range such as pipes, channels, atmospheric boundary layers, ocean beds, geophysical flows, and flow over vehicles, e.g. ship hulls. Although the research on rough wall turbulent boundary layer has gone a long way since the first surface roughness effect studies there still exists unresolved major problems such as the unsatisfying correlation of roughness and friction drag for irregular engineering surfaces such as marine antifoulings, and the discrepancies about the validity of wall similarity. Moreover, there is a lack of data on turbulent boundary layer flow over irregularly rough real engineering surfaces and the research in the literature accumulate on geometrically defined regular and mostly two-dimensional roughness types.

On the other hand, the marine antifouling coatings with copper and co-biocides are also under environmental scrutiny and totally environment friendly non-toxic coatings are favoured. As a consequence, the Foul-Release (FR) antifouling coatings, which are the most competitive alternatives to the biocidal ones, gradually supersede the Self-Polishing-Copolymers (SPC). Moreover, the energy efficiency regulations of IMO for ships will enter into force beginning from 2013, which include performance based standards for ships in order to reduce the greenhouse gas emissions. Therefore, the frictional drag characteristics of the antifouling coatings in the newly applied and clean conditions gain even more importance along with their antifouling properties. Accordingly, there is a continually growing commercial interest and hence support for research and development activities for new coating systems with particular interest to their hydrodynamic characteristics.

With the provided motivation by the underlined unclear areas on rough wall turbulent boundary layer flow in the literature and arised awareness about the hydrodynamic characteristics of the marine antifouling coatings in clean condition, this study aims to make a contribution to the advancement and further understanding of the state-of-the-art rough-wall turbulent boundary layer flows developed over marine antifouling coatings.

Two separate experimental campaigns were conducted consisting of zero-pressure-gradient turbulent boundary layer experiments over surfaces coated with marine antifoulings together with smooth and rough references by using two-dimensional Laser Doppler Velocimetry (LDV). The experiments were conducted in the Emerson Cavitation Tunnel of Newcastle University by using flat plate test models. Different types of marine antifoulings were included in the tests including some novel

nanostructured ones. A total of thirteen different surfaces were tested during the experiments. The first experimental campaign was carried out with four novel nanostructured antifouling coated surfaces along with three reference ones. One of the reference surfaces was coated with a state-of-the-art commercially in use foul-release (FR) coating scheme whilst the other two consisted of a smooth steel and a fully-rough sand grit. Six different surfaces were included in the second experimental campaign, which consist of one smooth reference, a sand grit surface and four surfaces coated with antifouling coatings including Self-Polishing Co-polymer (SPC) and Foul(ing) Release (FR) types, applied either by spraying or rollering. The mean velocity, boundary layer parameters, local skin friction drag, roughness functions, Reynolds normal and shear stresses, third and fourth order turbulence statistics, autocorrelation and spatial correlation functions, turbulence spectra and transfer functions were calculated and discussed for the tested surfaces. In complementing the boundary layer tests, roughness measurements of the test surfaces were carried out by using a laser profilometer. Detailed roughness analyses were also performed for the entire test surfaces which include several roughness parameters, autocorrelation and power spectral density functions at various cut-off lengths. To the best of the Author's knowledge, the relation between the transitionally rough surface roughness and the turbulence properties was for the first time investigated in the present study in the spectral domain and transfer functions were for the first time proposed for setting a relation between the roughness and turbulence spectra. It is thought that this study forms a fundamental step in investigating the roughness effects on the turbulent boundary layer by modelling its effect via transfer functions which constitute an alternative to the classical modelling of roughness effects as well as eliminating the deficiencies in the present models.

As a result of the roughness measurements and analysis it was observed that the entire tested antifouling, which appeared to present low skin friction drag properties, had an important contribution from the long wave-lengths. The difference in the application (i.e. spray or roller) of the foul-release anti-fouling coating significantly changed the spectral behaviour of the surface.

Two of the nanostructured amphiphilic coatings with fluorinated copolymer showed about 2% drag reduction at the higher edge of the tested Reynold number range. The general trend in the frictional characteristics of these two superior coatings over the tested Reynolds number range were found to be relatively different than the other surfaces tested with decreasing roughness functions as the Reynolds number increases. The spray-applied foul-release type antifouling coated test specimens displayed about 4.0-4.5% lower skin friction drag compared to the other spray-applied antifouling coatings. When applied with rollering, the same foul-release type antifouling displayed 5.2% higher frictional drag compared to the other spray-applied antifouling coated specimens.

No correlation was observed between the roughness function variations of the present data and the well-known Colebrook-White law. The present results showed that the marine antifouling coatings produce rather lower roughness function values in the investigated Reynolds number range compared to the Colebrook-White law and there is a great need to develop new correlations, whose validity includes (old or new generation) marine antifouling. Two new relations were proposed for the correlation of the roughness properties and roughness functions within the covered Reynolds number range. However; further work is needed in order to ensure the validity of the proposed relations at the higher Reynold number range. On the other

hand, the roughness parameter measured with the conventional BMT hull roughness analyser, Rt_{50} , appeared not to show any correlation with the frictional drag properties for most of the tested antifouling coated surfaces.

Outer layer similarity, which is one of the most contentious subjects in rough wall research, was observed in the velocity defect profiles, integral time scales and the Reynolds stress components along with the higher order moments for the entire tested coated surfaces. The fully rough reference sand grit surface showed discrepancies in both sets of the experiments, obliterating the validity of outer layer similarity in the Reynolds stresses and higher order moments. However; this behaviour of the fully rough reference was attributed to the step change effect due to the relatively limited distance from the beginning of the sand grit.

The streamwise turbulence spectra of the tested surfaces in inner and outer scaling generally showed similar behaviour with the classical classification and the inverse (-1) and -5/3 power law ranges were observed in a similar manner. In the inner scaling, at wavenumbers below the inertial subrange, fully rough sand grit test specimen spectra consistently showed variation from the others between 68% and 27% decreasing away from the wall which implied non-universal inactive motions. Outer layer similarity was observed for the smooth and coated cases streamwise spectra but not for the fully rough surface.

The wall-normal turbulence spectra appeared to show more powerful indications of the roughness effect. The collapse of the wall-normal spectra in the inactive region in inner scaling was only achieved in some parts of the log-law region, namely the inertial sublayer where a constant stress region exists. Noticeable differences were observed in the mesolayer at inactive region of the wall-normal spectra for the coated and fully rough surfaces with a maximum increment of 77% for the surface with the highest δ/k and a minimum 55% for the fully rough reference compared to smooth. The differences in the wall-normal spectra values at this region increased as δ/k increased.

To the best of the author's knowledge, the relation between the transitionally rough surface roughness and the turbulence properties was for the first time investigated in the present study in the spectral domain along with the transfer function calculations between the roughness spectra and turbulence spectra. The calculated transfer functions formed three distinct groups for the spray-applied antifouling, roller-applied foul-release antifouling and sand roughness. The streamwise and wall-normal transfer functions of each surface collapsed at the points in the constant stress region which is related with the almost constant energy levels and energy distribution along the wavenumbers through the inertial sublayer. Fourth order Fourier functions were proposed to define the calculated transfer functions with high goodness of fit values. The transfer functions can be a solution in estimating the effect of roughness since turbulence spectra consist of valuable information about the flow physics. For example, the kinetic energy, the dissipation rate, and several length scales can be directly calculated from the turbulence spectra which all can constitute boundary conditions as an input for numerical simulation.

GEMİ BOYALARINA AİT YÜZEY PÜRÜZLÜLÜĞÜNÜN TÜRBÜLANSLI SINIR TABAKAYA ETKİSİ

ÖZET

Yüzey pürüzlülüğünün türbülanslı sınır tabaka üzerindeki etkilerinin incelenmesi birçok mühendislik problemi açısından büyük önem teşkil etmektedir. Zira, örneğin boru içi akışlar, atmosfer sınır tabakası, okyanus yatakları ile uçaklar ve gemiler gibi araçların duvar cidarındaki türbülanslı sınır tabaka akışları çoğunlukla pürüzlülük etkisi altında gelişirler. Dolayısıyla pürüzlü duvar üzerindeki sınır tabaka akışları literatürde üzerinde epeyce çalışılan bir konu olmuştur. Buna karşın, çalışmaların çoğu geometrik olarak tanımlanabilen ve hatta çoğunlukla iki boyutlu yapay pürüzlülük tipleri üzerinde yoğunlaşmıştır. Özellikle, düzenli yapıda olmayan pürüzlülüğe sahip gerçek mühendislik yüzeyleri üzerindeki çalışmalar son derece kısıtlıdır. Oysa ki; gemi dip boyaları ile kaplanmış yüzeyler üzerindeki türbülanslı sınır tabaka akışları ile ilgili yapılan son derece sınırlı sayıdaki nispeten yeni bazı çalışmalarda, bu tür kompleks yüzeyler üzerindeki akışın klasik pürüzlülük ve sürtünme direnci ilişkisine uymadığını göstermiştir. Ayrıca, düzenli pürüzlülük yapısındaki yüzeyler üzerinde gelişen türbülanslı sınır tabakaların incelendiği birçok çalışmada, pürüzlülük etkisinin sınır tabakanın dış katmanlarına dek sürdüğü ve dolayısıyla duvar benzerlik hipotezinin geçerliliğini yitirdiği gözlenmiştir. Söz konusu hipotezin geçersizliği, sayısal modelleme açısından tüm klasik yaklaşımları geçersiz kılmakta ve her bir farklı pürüzlülükteki yüzeyin sürtünme direncine ve akışa olan etkisinin saptanabilmesi için özel deneyler ya da Navier-Stokes denklemlerinin bütünüyle çözüldüğü sayısal hesaplar (DNS) yapılması gerekliliğini işaret etmektedir. Dolayısıyla, günümüzde hala bu tür akışlarla ilgili çözülmesi gereken önemli tartışmalı noktalar bulunduğu açıktır.

Öte yandan, su ve deniz suyu ile temas halinde çalışan yapıların ya da araçların cidarlarını zamanla tortu, yosun ya da çeşitli deniz kabukluları gibi canlılar kaplamaktadır. Bu tür gelişimler, yüzeyin pürüzlülüğünü ve dolayısıyla sürtünme direncini ciddi miktarda arttırmakta, türbülanslı sınır tabaka akışını başkalaştırmaktadır. Bahsi geçen biyolojik yapıların gemilerin su altındaki yüzeylerini kaplaması, sert kabuklu deniz kabuklularının da varlığında, gemi direncini %90'a kadar arttırdığı ve dolayısıyla yakıt tüketiminde de önemli kayıplara neden olduğu bilinmektedir. Böylesi istenmeyen durumları önlemek ve bu tür canlıların gemi su altı yüzeyine yapışmasını engellemek amacıyla gemi dip boyaları yıllardır kullanılmaktadır. Eski tip gemi dip boyaları zehir salgılayarak böylesi canlıları öldürme yoluyla etkili olduklarından bu tür boyaların kullanımı günümüzde tamamen yasaklanmıştır. Eski tip gemi dip boyalarının yerini, günümüzde daha az zehirli genellikle bakır içerikli koruyucu boyalar ile yeni nesil silikon bazlı tamamen çevreci ve toksik olmayan, kirlenme salıcı (foul-release) prensibiyle çalışan dip

boyaları almıştır. Literatürde bazı çalışmalarda kirlenme salıcı tamamen çevreci boyaların aynı zamanda daha düşük sürtünme direnci özellikleri sergiledikleri tespit edilmiştir. Öte yandan, Uluslararası Denizcilik Organizasyonu'nun (IMO) 2013 itibarıyla uygulanmaya başlayacak olan enerji verimliliği regülasyonları gemilerin performansları ile ilgili standartlar içermektedir. Tüm bunlar, yeni nesil gemi dip boyalarının hidrodinamik performansları ve karakteristikleri üzerine olan ilgiyi arttırmıştır. Bu tür boyalarla kaplı yüzeyler, düşük pürüzlülük yüksekliklerine sahiptirler ve tamamen irregüler kompleks yüzeyler olmalarının yanı sıra üzerlerinde gelişen türbülanslı sınır tabakaların geçiş pürüzlülük rejiminde olması beklenmektedir. Literatürde bu tür akışlarla ilgili çalışmaların eksikliği, ihtiyaç duyulan pürüzlülük-akış etkileşiminin daha iyi anlaşılabilmesi için böylesi karmaşık yüzeyler üzerinde ve geçiş rejiminde yeni çalışmaların yapılmasını gerektirmektedir.

Bu tez çalışması, yukarıda bahsi geçen literatürdeki eksikliklerin verdiği motivasyon ile, farklı tiplerdeki gemi dip boyaları üzerinde gelişen türbülanslı sınır tabaka akışları ile ilgili bilgilerin geliştirilmesini ve böylesi akışların özelliklerinin daha iyi anlaşılmasını sağlamayı amaçlamaktadır. Bu amaç kapsamında, böylesi yüzeylerde gelişen türbülanslı sınır tabakalar içerisinde özel deneyler yapılarak yeni verilerin toplanması ve bu veriler ile ortalama akış özellikleri, sürtünme direnci-pürüzlülük korelasyonları ile Reynolds gerilmeleri, yüksek mertebeden türbülans istatistikleri, otokorelasyon ve uzaysal korelasyon fonksiyonları ve türbülans spektrumları gibi önemli türbülans parametrelerinin incelenmesi hedeflenmiştir. Bunların yanı sıra, literatürde ilk kez, pürüzlülük ile türbülans ilişkisi spektral analiz kullanılarak, pürüzlülük spektrumlarından türbülans spektrumlarına geçişi sağlayacak transfer fonksiyonlarının hesabıyla sağlanmaya çalışılmıştır.

Belirlenen amaç kapsamında, iki farklı deneysel çalışma yürütülmüştür. Her iki deneysel çalışmada da düz levha üzerinde gelişen ve basınç gradyanı etkisinde olmayan türbülanslı sınır tabaka içerisinde iki boyutlu lazer dopler hız ölçücü (Laser Doppler Velocimetry - LDV) kullanılarak hız ölçümleri yapılmıştır. İngiltere Newcastle Üniversitesi bünyesindeki Emerson Kavite Tüneli'nde yürütülen deneylerde çeşitli gemi dip boyaları ile kaplanmış yüzeyler ile tamamen pürüzsüz ve yüksek pürüzlülüğe sahip referans yüzeyler test edilmiştir. Test edilen gemi dip boyalarının bir kısmını ticari olarak kullanılan yeni nesil kirlenme önleyiciler oluşturmaktadır. Diğer bir kısmı ise tamamen yeni üretilmiş nano yapıli kirlenme önleyici boyalardır. Tamamen pürüzsüz olan çelik ve akrilik iki yüzey ve pürüzlülüğü yüksek seviyede olan kırk numara zımpara kağıdı yüzey ile birlikte toplam onüç farklı yüzey üzerinde sınır tabaka ölçümleri yapılmıştır.

Gerçekleştirilen birinci deneysel çalışma yeni üretilmiş dört farklı nano yapıli kirlenme önleyici ile üç referans yüzey için türbülanslı sınır tabaka ölçümlerini kapsamaktadır. Referans yüzey olarak kirlenme salıcı tipteki ticari olarak günümüzde gemi ve yatlarda kullanılan bir dip boyası püskürtme uygulaması ile hazırlanarak test edilmiştir. Buna ek olarak, 120 numara zımpara kağıdı ile tamamen pürüzsüzleştirilen bir çelik yüzey ve 40 numara zımpara kağıdının çelik test levhasına yapıştırılmasıyla hazırlanmış yüksek pürüzlüklü yüzey referans olarak test edilmişlerdir. Ölçümlerin gerçekleştirildiği gelen akım hızlarında yüksek pürüzlüklü yüzey üzerindeki akış tamamen pürüzlü akış rejiminde iken gemi dip boyaları ile hazırlanmış olan yüzeylerin üzerindeki sınır tabaka akışı, geçiş akış rejiminde yer almıştır. İkinci deneysel çalışmada, bir pürüzsüz, bir yüksek pürüzlüklü ve ticari olarak kullanımda olan farklı tipteki gemi dip boyaları ile hazırlanmış dört yüzey olmak üzere, toplam altı yüzey test edilmiştir. Kullanılan

gemi dip boyaları arasında, kullanım süresince kendini cilalama özelliğine sahip olan bakır içerikli tip (Self-Polishing Copolymer) ile kirlenme salıcı tip boyalar bulunmaktadır. Kirlenme salıcı hem püskürtme hem de rulo yöntemi ile, diğerleri ise yalnızca püskürtme yöntemi kullanılarak yüzeylere uygulanmışlardır. Deney hız-zaman verileri özel olarak hazırlanan çeşitli MATLAB programları kullanılarak analiz edilmiştir. Deney grupları için, ortalama hız profilleri, sınır tabaka parametreleri, lokal yüzey sürtünme direnci, pürüzlülük fonksiyonları, Reynolds normal ve kayma gerilmeleri, üçüncü ve dördüncü derece türbülans istatistikleri, otokorelasyon ve uzaysal korelasyon fonksiyonları, türbülans spektrumları ve transfer fonksiyonları hesaplanarak sunulmuş ve yüzey pürüzlülüğünün söz konusu değişkenler üzerine etkileri incelenmiş ve sonuçlar literatür ile karşılaştırmalar yapılarak irdelenmiştir.

Sınır tabaka deneylerini tamamlayıcı olarak, test edilen tüm yüzeylerin pürüzlülükleri iki boyutlu olarak lazer profilometre ile ölçülmüştür. Birinci deney grubu test yüzeyleri ayrıca konvansiyonel (mekanik) BMT ortalama tekne pürüzlülüğü ölçer ile de ölçülmüştür. Hazırlanan ayrı bir MATLAB programı kullanılarak elde edilen pürüzlülük verilerinin detaylı analizi yapılmış, çok çeşitli pürüzlülük parametreleri, otokorelasyon fonksiyonları ve pürüzlülük spektrumları dört farklı analiz boyları kullanılarak hesaplanmıştır ve ilgili deney bilgilerini içeren bölümlerde sunularak irdelenmiştir.

Pürüzlülük ölçüm ve analizlerinin sonucunda, test edilmiş olan düşük sürtünme direnci özellikleri sergilemiş olan tüm gemi dip boyalarında (nano yapıya ya da değil) uzun dalga boylarındaki pürüzlülüğünden kaynaklanan ciddi katkılar gözlenmiştir. Kirlenme salıcı tipteki gemi dip boyalarındaki püskürtme ya da rulo gibi uygulama farklılıkları yüzeyin spektral davranışını ciddi biçimde değiştirmiştir. Konvansiyonel BMT yüzey pürüzlülüğü ölçüm cihazı ile elde edilmiş olan pürüzlülük parametresi Rt_{50} ile, test edilmiş olan gemi dip boyalarının büyük bir çoğunluğu için, sürtünme direnci özellikleri arasında herhangi bir korelasyon gözlemlenmemiştir.

Pürüzsüz referans çelik yüzeye kıyasla, en fazla sadece %6.6 civarında daha yüksek bölgesel sürtünme direnci katsayısı sergileyen nano yapıya boyaların sürtünme direnci özelliklerinin çok başarılı olduğu ortaya çıkmıştır. Özellikle, florlu kopolimer içeren iki nano yapıya amfifil boya kaplı yüzeylerden elde edilen direnç kazancı çok belirgin olarak nitelenmektedir. Söz konusu iki yüzey test edilen yerdeğiştirme kalınlığına bağlı Reynolds sayısı aralığının üst değerlerinde %2 oranında direnç düşüşü sergilemişlerdir. İkinci deney grubunda, püskürtmeyle uygulanmış kirlenme salıcı tipteki gemi dip boyalı yüzey bölgesel sürtünme direnci katsayısında yalnızca %5 oranında yükseliş göstermişken, diğer püskürtme ile uygulanan gemi dip boyaları aynı değer için en fazla %9.5'e varan artış göstermişlerdir. Öte yandan, aynı kirlenme salıcı gemi dip boyası rulo ile uygulandığında bölgesel yüzey sürtünme direncindeki artış %14.7'ye varmıştır. Tamamıyla pürüzlü zımpara kağıdı yüzey, her iki deney grubunda da diğer test edilmiş yüzeylerden ciddi oranda fazla yüzey sürtünme direnci sergilemiştir.

Test edilen yüzeylerin pürüzlülük fonksiyonu değişimlerinin çok iyi tanınan Colebrook-White kanunu ile korelasyonu olmadığı gözlenmiştir. Mevcut sonuçlar, ayrıca, gemi dip boyalarının incelenmiş olan Reynolds sayısı aralığında Colebrook-White kanununa kıyasla oldukça düşük pürüzlülük fonksiyonu değerleri oluşturduğunu göstermiştir. Bu nedenle geçerliliği eski ve yeni nesil tüm gemi dip boyalarını da içeren yeni korelasyonlar geliştirilmesi gerekliliği ortaya çıkmaktadır.

Kapsanan Reynolds sayısı aralığında pürüzlülük özellikleri ve pürüzlülük fonksiyonu arasında iki yeni korelasyon önerilmiştir. Ancak önerilen korelasyonların daha yüksek bir Reynolds sayısı aralığında geçerli olduğunun kesinleştirilebilmesi için müteakip çalışmalara ihtiyaç duyulmaktadır.

Hız bozulması profillerinin logaritmik tabaka ve dış tabaka içerisinde ilk deney grubu için Rotta ölçeklemesi kullanıldığında ve ikinci deney grubu için Rotta ölçeklemesine ek olarak geleneksel ölçekleme kullanıldığında birbiri ile örtüştüğü görülmüştür. Dahası, pürüzsüz, boyalı ve tamamen pürüzlü yüzeyler için iz kuvveti değerlerinde belirgin farklılıklar gözlenmemiş ve böylelikle Townsen'in Reynolds sayısı benzerliği desteklenmektedir.

Pürüzlü duvar araştırmasında en çok tartışılan konulardan biri olan dış tabaka benzerliği, test edilen tüm boyalı yüzeyler için yüksek derecedeki momentler ile birlikte Reynolds gerilmelerinin akış yönünde, normal yönde ve kayma bileşenlerinde gözlenmiştir. Tamamen pürüzlü referans yüzey zımpara kağıdı her iki deney setinde de bazı uyuşmazlıklar sergilemiştir ve böylece Reynolds gerilmelerinde dış tabaka benzerliğinin varlığını zedelemektedir. Ancak, tamamiyle pürüzlü referans yüzeyin bu davranışı zımpara kağıdının başlangıcından itibaren göreceli olarak sınırlı bir mesafe katedilmesinden kaynaklanan yüzeydeki ani değişim etkisiyle ilişkilendirilebilir.

Test yüzeylerinin integral zaman ölçeği üzerinde etkili oldukları görülmüştür. İç tabakada, hesaplanmış olan integral zaman ölçekleri tamamen pürüzlü referans yüzeyinde, pürüzsüz referansa kıyasla 2 ila 2.5 kat daha kısa olarak bulunmuştur. Rulo ile uygulanmış olan kirlenme salıcı yüzeyde ise logaritmik bölgede 1.6 kat daha düşük integral zaman ölçeği değerine işaret etmiştir.

Boyalı yüzeylerin uzaysal korelasyon fonksiyonları pürüzsüz yüzeye kıyasla, mezotabakada $\Delta x/\delta$ 'in orta değerlerinde daha yüksek değerler sergilemiş iken tamamen pürüzlü referans yüzeyde ciddi oranda azalmıştır. Rulo ile uygulanmış kirlenme salıcı yüzeyin uzaysal korelasyon fonksiyonu boyalı ve pürüzsüz yüzeylerinkine kıyasla logaritmik bölgede ciddi farklılık göstermektedir; ki bu farklılık da integral zaman ölçeğine yansımaktadır. Öte yandan, iç ve logaritmik tabakalarda, tamamen pürüzlü yüzeyin uzaysal korelasyon fonksiyonunda tutarlı olarak belirgin bir farklılık gözlenmiştir. Dış tabakada ise, bu farklılık kaybolmaktadır. Bu ise düzenli girdap paketlerinin oluşması ve sürdürülmesine bağlı duvar cidarı U şekilli girdapların (hairpin) yenilenme mekanizmasının değişmesi ile ilintilendirilebilir.

Test edilen yüzeylerin akış yönündeki türbülans spektrumları iç ve dış ölçekleme ile incelendiğinde, klasik sınıflandırma ile benzer davranış gösterdikleri ve -1 ve -5/3 kuvvet kanunları bölgelerinin gözlendiği söylenebilir. İç ölçeklendirmeye göre, atalet alt bölgesinin altındaki dalga sayılarında, tamamen pürüzlü zımpara kağıdı yüzeyinin spektrumları diğerlerinden %68 ila %27 civarında duvardan uzaklaştıkça azalan yapıda olmak üzere farklılıklar göstermiştir. Bu davranış evrensel olmayan pasif hareketlere işaret etmektedir. Boyalı yüzeyler ile pürüzsüz yüzeylerin pasif aralıkta spektrumları arasındaki fark iç tabakada en fazla %18, dış tabakada ise %5 civarında seyretmektedir. Öte yandan, tamamen pürüzlü yüzey için aktif ve küçük ölçekli girdapsı (eddy) aralıklarında örtüşme ya da en azından benzerlik gözlenmiştir. Pürüzsüz ve boyalı vakaların akış yönündeki spektrumlarında dış katman benzerliği gözlenirken tamamen pürüzlü yüzeyde bu uyum bulunmamıştır. Dış ölçekleme kullanıldığında, mezotabaka içerisinde, farklı pürüzlülük özelliklerine sahip

yüzeyler, atalet alt aralığında δ/k oranlarına bağlı bir sıralanış göstermişlerdir. Tamamen pürüzlü ve boyalı yüzeyler için daha uzun bir atalet alt aralığı gözlenmiştir.

Duvara normal yöndeki türbülanslı akış bileşeni için hesaplanan türbülans spektrumlarının pürüzlülük etkisinin izlerini daha fazla taşıdıkları gözlenmiştir. Söz konusu türbülans spektrumları iç ölçekleme ile incelendiğinde, spektrumun pasif bölgesindeki örtüşmenin yalnızca sınır tabakanın sabit gerilme bölgesinde yapılan ölçümler için gözlendiği söylenebilir. Bu spektrumlarda, $-5/3$ kanunu bölgesi duvara yaklaştıkça daha düşük dalga sayılarına doğru kaydığı gibi, beklendiği üzere -1 kanunu bölgesi bulunmamıştır. Mezotabakada ise, hem tamamen pürüzlü hem de boyalı yüzeylerin duvara normal yöndeki spektrumlarının pasif bölgesinde önemli farklılıklar gözlenmiştir. Bu farklılık en yüksek δ/k oranına sahip yüzey için – pürüzsüz yüzeyinkine oranla- %77 iken, en düşük δ/k oranındaki tamamen pürüzlü yüzey için %55 civarındadır. Anlaşıldığı üzere, δ/k oranı arttıkça spektrumun bu bölgede gösterdiği yükseliş artmaktadır.

Yazarın bilgisine göre, yüzey pürüzlülüğü spektrumu ile türbülans spektrumları arasında transfer fonksiyonlarının hesaplanması literatürde ilk kez gerçekleştirilmiştir. Hesaplanan transfer fonksiyonlarının, günümüzde yüzey pürüzlülüğü etkisinin modellenmesi konusunda literatürde kullanılan klasik yaklaşımların mevcut açıklarını kapatarak önemli bir alternatif yöntem oluşturacağı düşünülmektedir. Hesaplanan transfer fonksiyonları farklı tipteki yüzeyler için farklı gruplar oluştururken benzer spektral karakter sergileyen yüzeylere ait transfer fonksiyonları aynı grupta yer almıştır. Örneğin; püskürtme ile uygulanmış gemi dip boyları için hesaplanan transfer fonksiyonları kendi içlerinde örtüşürken, rulo ile uygulanmış olan yüzeylere ait transfer fonksiyonları ve zımpara kağıdı pürüzlülüğü için hesaplanmış olan tamamen farklı ayrı gruplar oluşturmuşlardır. Öte yandan, her yüzey için, sınır tabakanın sabit gerilme bölgesinde hesaplanan, serbest akım yönündeki ve duvara dik yöndeki akış bileşenleri ile ilişkili transfer fonksiyonlarının da birbirleriyle çakıştıkları gözlenmiştir. Söz konusu gözleme, sınır tabakanın atalet alt bölgesinde enerji seviyelerinin neredeyse sabit olmasının neden olduğu düşünülmektedir. Elde edilen farklı grup transfer fonksiyonlarının temsili için dördüncü dereceden Fourier fonksiyonları önerilmiştir. Önerilen transfer fonksiyonları kullanılarak, incelenen yüzey tipleri için, yalnızca yüzey pürüzlülük spektrumlarının ölçülmesi ile türbülans spektrumlarının tahmin edilmesi ve buna bağlı olarak sayısal simülasyonlarda sınır şartı olarak kullanılabilen kinetik enerji, enerji disipasyon oranı ve boy ölçekleri gibi bir çok akış parametresinin hesaplanabilmesi mümkündür.

1. INTRODUCTION

1.1 Introduction

The prevention of settlement and growth of biofouling on the underwater sections (e.g. ship hull, propeller, etc.) of marine vehicles and structures are of vital importance since such formations increase the surface roughness and lead to drastic increases in friction drag (along with the excessive fuel consumption) due to alteration in the boundary layer flow. Accordingly, antifouling coatings are used in order to control the problem of biofouling formation in aquatic environments. Since the banning of Trybutilin-Tin (TBT) based toxic antifouling coatings by the International Maritime Organization (IMO) in 2008, relatively less toxic but still biocidal new generation Self-Polishing-Copolymer (SPC) coatings are widely used. However, these coatings with copper and co-biocides are also under further environmental scrutiny and totally environment friendly non-toxic coatings are favoured. As a consequence, the Foul-Release (FR) antifouling coatings, which are the most competitive alternatives to the biocidal ones, gradually supersede the SPCs. On the other hand, the energy efficiency regulations of IMO for ships will enter into force beginning from 2013, which include performance based standards for ships in order to reduce the greenhouse gas emissions. Accordingly, the frictional drag characteristics of the antifouling coatings in the newly applied and clean conditions gain even more importance along with their antifouling properties. Based on the above facts, there is a continually growing commercial interest and hence support for research and development activities for new coating systems with particular interest to their hydrodynamic characteristics.

On the other hand, although the rough wall turbulent boundary layer flow is a widely studied research topic in the fluid mechanics field, the surfaces coated with marine antifouling are irregularly rough real engineering surfaces over which the boundary layer flow develops in the transitionally rough regime and there exists a large gap in the investigation of such flows.

Consequently, a detailed literature review is given in the following section in order to present the position of the rough wall turbulent boundary layer research today along with the deficiencies in theory with a specific emphasis on the transitionally rough flow occurring on irregularly rough surfaces. The motivation for the thesis along with the aim and objectives of the study are explained respectively, following the literature review. The chapter finishes with the presentation of the thesis layout and chapter summary.

1.2 Literature Review on Rough Wall Turbulent Boundary Layers

Most of the engineering wall-bounded turbulent flows develop under the influence of surface roughness and therefore the turbulent boundary layer over rough surfaces has been a widely studied research topic. The examples can be given for rough wall flows in a wide range such as pipes, channels, atmospheric boundary layers, ocean beds, geophysical flows, and flow over vehicles, e.g. ship hulls. The most recent and comprehensive reviews on rough wall turbulent boundary layer are those of Jimenez (2004) and Raupach et al. (1991) whilst Gad-el-Hak and Bushman (2011) gives a review of turbulent boundary layers with particular emphasis to the cornerstones and fault lines of the classical theories.

Rough wall research dates back to the early works of Hagen (1854) and Darcy (1857) who studied the pressure loss in water pipes. The uniformly roughened pipe flow experiments of Nikuradse (1933) with graded and closed packed sand revealed that the logarithmic mean velocity distribution over smooth walls were also valid for flows over rough walls with the same value of the von Karman constant. Nikuradse (1933)'s work also experimentally defined the increase in skin friction drag due to the change in the sand grain size. Colebrook and White (1937) also studied the flow in rough pipes; however the work of Colebrook (1939) with particular attention to the transitional range of rough wall flow defined the famous Colebrook-White law for the correlation of roughness function and roughness Reynolds number which is also assumed to be valid for engineering surfaces. The discrepancy between the Colebrook-White law and Nikuradse's data at the transitional range led to the definition of the equivalent or effective sand roughness value by Schlichting (1979). The widely known Moody diagram (Moody, 1944) also relates the pressure drop pipes due to relative surface roughness and Reynolds number which is developed

from the results of Colebrook (1939). These studies brought the definitions of hydraulically smooth, transitionally rough and fully rough flow regimes into practice which are directly associated with the roughness height in definition. The onset of transitionally and fully rough regimes have long been accepted at roughness height based Reynolds number values of 2.25 (Ioselevich and Pilipenko, 1974) to 5 (Schlichting, 1979) and 70 respectively which were deduced from the measurements of Nikuradse (1933). It is interesting to note that, these limit values between the flow regimes were not much questioned for more than five decades until Ligrani and Moffat (1986) showed that the limits of the flow regimes may noticeably vary depending on the geometry of the roughness. Bandhopadhyay (1987) also worked on defining the limits of the transitional roughness by experiments over two and three-dimensional roughness types with different spacings between roughness elements. However, Bradshaw (2000) was the first to identify the critical roughness Reynolds number for the onset of transitional regime effect as erroneous, mainly depending on the superpipe data of Barenblatt and Chorin (1998). Bradshaw (2000) also proposed that the effect of small roughness vary as a power of roughness Reynolds number and gradually becomes negligible as the roughness Reynolds number decreases. In addition, Allan et al. (2005) and Langelandsvik et al. (2008) constitute as examples for further questioning the validity of Colebrook roughness function for wide range of engineering roughness which show that the pressure drop in the transitionally rough regime respectively for honed and commercial steel pipes are much less than the ones predicted with the Moody diagram. Shockling et al. (2006) also reports contradicting behaviour of friction factor with the Moddy chart in honed pipes in transitional regime. On the other hand, recent studies of Candries and Atlar (2005) and Ünal et al. (2012) noted lower values of roughness functions compared to the Colebrook-White law in the range very close to being hydraulically smooth along with significant disagreement with this law at the moderate transitional range for surfaces coated with marine antifouling.

Another problem in defining the correlation between roughness and logarithmic-law shift is the selection of the roughness height. For regular or geometrically defined roughness types such as sand grains, rods or spheres the definition is quite certain; however for irregularly rough engineering surfaces a wide variety of roughness height and texture parameters can be defined at several measurement and analysis

lengths of roughness profiles which carries the problem to a more complicated area. Flack and Schultz (2010) give a review of roughness function correlations together with a relation by using the skewness and root-mean-square roughness height values mainly for regular roughness types in the fully rough regime. Bettermann (1965), Dvorak (1969), Dirling (1973), Sigal and Danberg (1990), and Rij et al. (2002) are the major studies that give relations for regular surface types whilst Rij et al. (2002) and Waigh and Kind (1998) propose correlations for three-dimensional irregular roughness types. However; such correlations are not practical since rather complex numerical calculations in order to determine the needed density and shape parameters for irregularly rough surfaces are required. On the other hand, there is a remarkable amount of correlation studies on ship hull roughness. For example, Musker (1981) and Dey (1989) use moments of the surface profile and power spectral density function of the surface respectively and Medhurst (1989) defines a hydrodynamic roughness number with a Colebrook-type roughness function for replicas of ship hull surfaces, painted ship surfaces and surfaces coated with abrasive paints. More recently, Candries et al. (2003) and Candries and Atlar (2005) propose that a combined roughness parameter of average roughness height and mean absolute slope collapses a range of antifouling surfaces. Schultz (2004) uses a solution valid for his data of painted surfaces by using the 0.17 times of the average roughness height value measured at 50 mm cut-off length for correlation with a Colebrook-type roughness function. However, the lack of satisfactory collapse in the transitional regime for a range of irregular surface types with the mentioned several proposed parameters underlines the need of new correlations and therefore the research on the relation of surface topography and friction drag continues (e.g. Bons, 2002; Flack and Schultz, 2010) although Grigson (1992) brought forward the idea that reliable skin friction drag estimations can never be expected to be made with only the surface roughness statistics.

Most of the research on rough wall turbulent boundary layer flow is accumulated on the roughness effects of regular or geometrically defined two or three-dimensional surface roughness types such as arrays of bars, spheres or rods, woven meshes, sand paper, sand grain and cones, etc. (e.g. Perry et al., 1969; Krogstad and Antonia, 1999; Djenidi et al., 1999; Akinlade et al., 2004; Schultz and Flack, 2005; Pailhas et al., 2008; Schultz and Flack 2009, Volino et al. 2009, Brzek et al. 2010).

Nevertheless, the studies on the irregularly rough walls also grow in number with the recent works of e.g. Schultz (1998, 2000 and 2004), Candries and Atlar (2005), Wu and Christensen (2010), Mejia-Alvarez and Christensen (2010), Bons (2010). It may be highlighted that an important amount of irregular rough wall research is carried out by researchers in hydrodynamics field dealing with either the surfaces coated with marine antifoulings or surfaces subject to biofouling. As an example to this ongoing research; Schultz (1998 and 2000) investigated the turbulent boundary layer velocity structure of surfaces covered with marine biofilms and filamentous algae, respectively. Leer-Andersen and Larsson (2003) work on a method of measuring the full-scale skin friction drag of fouled ship surfaces. Towing tank experiments by using flat plates were also conducted by Schultz (2004) in order to compare the frictional drag of several ship hull coatings in the un-fouled, fouled, and cleaned conditions. Candries and Atlar (2005) systematically compared the drag, boundary layer and roughness characteristics of surfaces coated with new generation antifouling paint systems in the newly applied condition involving commercially competitive Self-Polishing Co-polymer (SPC) and Foul-release (FR) coatings. Schultz (2007) studied the effect of coating roughness and biofouling on ship resistance. This may be related to the raised awareness on the drag penalties due to fouled ship hulls (Townsin 2003, Schultz et al. 2011) supported with the advances in the antifouling paint technologies which indicate noteworthy differences in the skin friction drags of newly applied antifoulings (Candries and Atlar, 2005; Ünal et al., 2012). Banning of the toxic tributyltin (TBT) by the International Maritime Organization (IMO) for newly built ships in year 2003 and a worldwide ban for all ships in 2008, has also been a major factor in increasing the research and development in this area to search for efficient alternative fouling control mechanisms. Although the roughness effect of paint types have been ignored for a long time due to the much higher drag penalties encountered with the fouled surface conditions, with the coincidental discovery of the lower skin friction drag characteristics of non-toxic foul-release type antifoulings alternative to toxic SPCs, research became focused on the anticipation of drag reduction as well as the antifouling properties. A review on antifouling coatings is given by Finnie and Williams (2010).

The levels of surface roughness may change significantly according to the conditions of the surface itself or the environment being exposed, such as the mechanical damage, quality and type of the paint application, corrosion, coating build-up, paint failures or slime and heavy fouling formation in marine applications. Townsin et al. (1981) reported that mechanical damage ratio vary depending upon the ship type between 3.6% and 7.3% of the total hull surface. On the other hand, paint failure ratio is generally much lower and covers about 2% of the hull surface regardless of the ship type whilst corrosion is found to be a rather minor roughness source. The paint application quality and the care for the application procedure needed for the coating schemes may be more important than the paint type itself (Grigson, 1992). A review on the effect of coating roughness was given by Lackenby (1962) which included the early studies. Musker (1981), Granville (1987), Medhurst (1989) and Grigson (1992) focused on the effects of surface roughness changes on the friction drag performance of SPC (TBT) systems whilst Candries (2001) and Candries and Atlar (2005) included the detailed comparison of the hydrodynamic performance of the new generation SPCs (with copper) and their best competitor foul-release antifoulings. Schultz (2004) tested several ship hull coatings in newly applied, fouled and cleaned conditions. The impact of fouling lead to noticeable increase in hull drag in case of slime and the drag increase may reach up to 86% in heavy calcareous fouling (Schultz, 2007). Schultz and Swain (1999), Schultz (2000), Leer-Andersen and Larsson (2003) may be given as example to studies that investigated the effect of different types of fouling on drag whilst Lewthwaite et al. (1985) and Haslbeck and Bohlander (1992) are examples of full-scale ship tests for fouling effect. Schultz (2007) recently presented a method for the estimation of coating and fouling effect on full-scale ship frictional drag and powering. The effect of surface roughness for the earlier mentioned different levels of roughness are included in an allowance factor, which is effective on the smooth wall friction and wave-making resistance, in the determination of full-scale ship overall drags (ITTC, 1978). The allowance factor is a function of the mean hull roughness which is the average of the maximum peak to height roughness values measured with 50 mm cut-off length at several locations over the hull. Bryne (1980) noted the mean hull roughness of newly build ships as 129 μm whilst a typical value of 150 μm was recommended in ITTC (1978). This allowance factor was adopted from the one given in Bowden and Davison (1974). However; the allowance factor is ill-defined due to the included residual components

other than roughness effect (e.g. the model scale effect) and found to be of doubtful accuracy in ITTC (2005). Townsin et al. (1981) also proposed a formula for the prediction of drag increase due to roughness; however this formula is also based on the mean hull roughness along with the Reynolds number and mean hull roughness parameter was shown to not necessarily correlate with the frictional drag increase (Candries, 2001; Atlar et. al, 2012).

The effect of surface roughness is thought to be limited to the roughness sublayer, which is within a few roughness heights from the boundary, except the indirect role of roughness on the outer scales. Therefore outer layer similarity is expected in rough walls along with the smooth ones according to the wall-similarity hypothesis which is an extension of Townsend's (1961, 1976) Reynolds number similarity for turbulent flows. The existence of outer layer similarity has been one of the debate topics in rough wall research since the invalidity of wall-similarity hypothesis pose a significant challenge in modelling of wall-bounded turbulence. Raupach et al. (1991) conclude that similarity exists in the outer region of the rough wall boundary layer depending upon the mass of literature reviewed in their study. However; shortly after that, the questioning of the wall-similarity began with the study of Krogstad et al. (1992) who report that the roughness effects extent well into the outer layer. Since then, Krogstad and Antonia (1994 and 1999), Tachie et al. (2000), Djenidi et al. (2008) and Leonardi et al. (2003) observed significant differences in the turbulent stresses in the outer region of the boundary layer for types of two-dimensional roughness. Brzek et al. (2007) studied the rough wall effects with sand grain roughness including a wide range of Reynold numbers and rough wall flow regimes and reported that differences in the roughness geometry result in variation of Reynolds stresses. On the other hand, the findings of Flack et al. (2005), Kunkel and Marusic (2006), Schultz and Flack (2003 and 2007), Flack et al. (2007), Wu and Christensen (2007) and Brzek et al. (2008) provide support to the existence of outer similarity. Jimenez (2004) attribute the conflicting views on outer layer similarity to the largely varying values of relative roughness height (k/δ) compared to the boundary layer thickness and conclude that outer layer similarity exists if the relative roughness height is small enough; $k/\delta < 1/50$. Flack et al. (2005) supports the conclusion of Jimenez (2004) whilst they state that a criteria based on equivalent sand roughness is observed to better represent this limit. On the other hand, Bakken

et al. (2005) report that the roughness effects are confined to the inner region in internal flows and explain the reason of confusing results due to the difference in the outer boundary condition of internal and external flows. Connelly et al. (2006) report experiments results on flat plates with a wide range of relative roughness height ($1/16 \leq k/\delta \leq 1/110$) which expand the validity of outer layer similarity for mean flow variables. Castro (2007) and Flack et al. (2007) also suggest outer layer similarity at even higher values of relative roughness height. Moreover, Volino et al. (2007) and Flores and Jimenez (2006) experimentally and numerically studied wall roughness effects and found similarity in turbulence structure. The common property of the studies that report outer layer similarity is being confined to the effects of three-dimensional k-type roughness. Most studies (e.g. Keirsbulck et al., 2002; Djenidi et al, 2008; Lee and Sung, 2007; Volino et al., 2009) that focus on the two-dimensional roughness effects report differences in the outer layer that contradicts with the wall-similarity.

The structure of the smooth wall boundary layers is well-known. According to Theodorson (1952) and Townsend (1976), the boundary layer consists of hairpin vortices extending from the wall. Head and Bandhopadhyay (1981) report groups of hairpins with characteristic inclination angles. Adrian et al. (2000) point out the existence of hairpin packets consisting of multiple layers of hairpin vortices. Perry and Chong (1982) provided support to the attached eddies rising from the wall whilst Perry and Marusic (1995) extended the model by proposing detached eddies which are formed by the separated hairpins. Kim et al. (1971) describe bursts near the wall that account for the turbulence production. Na et al. (2001) put forward the superbursts of fluid ejecting from the near-wall whilst Ganapathisubramani et al. (2003) report that superburst can occur in the hairpin packets. Jimenez (1999) gives a review of flow physics for turbulent boundary layers whilst Hunt and Carlotti (2001) present analytical investigation of near wall turbulence statistics. On the other hand, most of the rough wall research accumulates on the single-point statistics; however there also exist some studies that focus on the structural behaviour of rough wall turbulent boundary layers by measurements at multiple spatial locations. Grass (1971) defined ejections of fluid rising from the gaps between the roughness elements that are responsible for the momentum transport. Nakagawa and Hanratty (2001) present spatial correlations of the streamwise and transverse fluctuating

velocity components over a wavy wall. Volino et al. (2007 and 2009) considers the structure of smooth and rough wall boundary layers with a focus to the spatial correlations and swirl length based on experimental investigations. Direct numerical simulations also gain a considerable role in the structural investigation of turbulent boundary layers with the developing super computing capabilities. Krogstad et al. (2005), Orlandi et al. (2006), Flores and Jimenez (2006), Leonardi et al. (2007), Lee and Sung (2007), Burattini et al. (2008) and Heirpin et al. (2010) can be given as recent examples to studies that investigate the turbulent boundary layer structure over rough and smooth walls with direct numerical simulation.

The studies that concentrate on the effect of surface roughness on turbulence spectra are also rather limited as the spatial studies on rough wall turbulent boundary layers. Perry and Abell (1977) give a comparison of the premultiplied streamwise spectra on smooth and rough walls which report agreement above the logarithmic layer. Perry et al. (1986) define universal scaling laws for one-dimensional turbulence spectra whilst Perry et al. (1987) and Perry and Li (1990) present comprehensive spectra measurements for smooth and rough walls that validate the former work. However; in these studies the focus is on the validation of the scaling arguments rather than comparing the rough and smooth wall spectra. Ligrani and Moffat (1986) carry out measurements on uniform spheres roughness and investigate the fully rough and smooth wall turbulence spectra which validate the outer scaling of Perry et al. (1987) and present similar spectral shape for the fully rough wall to that of the smooth. They conclude that the similarity in the spectra for the middle and large wavenumber range in outer scaling is due to the active motions and universal wall structure in inner boundary layer regions whilst variations in the low wavenumbers correspond to non-universal inactive motions. They also propose that for transitionally rough walls, the active motion parts of the spectra is expected to collapse, but do not show evidence. Krogstad and Antonia (1999) experimentally investigate rod and woven mesh roughness types and compare the associated premultiplied spectra along with several turbulent quantities. They report noticeable differences especially in the wall-normal and co-spectra with almost entirely different character for the rod and mesh roughness types; even in the outer layer. Poggi et al. (2003) study the small-scale structure of turbulence in an open channel flow and compare the streamwise spectra of the rough and smooth wall in the buffer and overlap region. They report that a

precise scaling range almost disappears in rough wall spectra in the buffer region associated with the energy directly injected into the flow by the roughness elements. They also note an increment of energy in the rough wall spectra and report the spectrum of rough wall more close to isotropic conditions than the smooth one in the buffer region with lower intermittency and anisotropy at fine scales. Volino et al. (2007) conducted PIV and LDV measurements to investigate the two-point correlations, swirl motions and spectra of mesh roughness in the fully rough regime compared to a smooth wall. They report streamwise, wall-normal and cross spectra at two locations; one in the overlap region and the other in the outer layer. They conclude that a 20% higher energy content exist in the rough wall streamwise pre-multiplied spectra at low wavenumbers compared to smooth one in the overlap region that vanishes in the outer layer, whilst no difference was observed for the wall-normal and cross spectra in overlap or outer regions.

There are valuable studies on the Reynolds stress anisotropy and intermittency properties of rough wall boundary layer flows such as Shafi and Antonia (1997); Antonia and Shafi (1999), Antonia and Krogstad (2001), Smalley et al. (2002) and Poggi et al. (2003) all pointing out the reduction of anisotropy on rough walls whilst Antonia and Krogstad (2001) also note a different behaviour of roughness types (mesh and rods) in small scale structures and report that 3-dimensional mesh roughness conforms more closely with isotropy.

As summarised in the previous paragraphs, research on rough wall turbulent boundary layer has gone a long way since the first surface roughness effect studies. However, there still exist unresolved major problems. One of these problems is the unsatisfactory correlation between the roughness parameters and the increase in frictional drag observed in the recent studies of irregular engineering surfaces. Actually, it is a relatively new problem since irregularly rough engineering surfaces have long been ignored in the rough wall turbulent boundary layer research and the mass of the studies concentrate on geometrically defined or regular roughness types in the fully rough regime. The information on the higher order turbulence statistics is also very limited on irregular transitionally rough surfaces. The second major problem is the disperse data that impair the validity of wall-similarity. Although this problem is recently attributed to the behaviour of relatively sparse two-dimensional roughness there also exist disparities in the three-dimensional regular roughness data.

Therefore, the overall findings on the lack of outer layer similarity bring forward the impossibility of universal numerical modelling for rough walls. The combination of the lack of correlation and wall-similarity imply that separate experimental or numerical-experimental (DNS) work may be needed for the evaluation of the effect of different types of wall roughness except for the sandgrain and some other regular roughness types. Accordingly, there is a need to define universal links between the roughness and turbulence characteristics. Transfer functions may constitute such a link by considering the wide spectral information both for roughness and turbulence.

1.3 Motivation of Thesis

The necessity of further work on some main fields in the rough wall research was emphasized as a summary of the literature review, in the previous section. As a consequence, there are four main motivations in materializing this study:

- Rough wall turbulent boundary layer flows, especially with irregular roughness, are rather complex to understand and there is a lack of investigations in this field;
- The above is further complicated with the lack of reliable experimental data using modern tools and dedicated testing facilities;
- Marine antifouling coatings and their performance are extremely important (topical and complex) practical engineering applications of the rough-wall turbulent boundary layer phenomenon requiring further research;
- The lack of wall-similarity in some rough wall boundary layer flows along with the lack of skin friction drag correlation for marine antifouling coated surfaces imply that there is a need to define new universal links between the roughness and turbulence characteristics.

1.4 Aim and Objectives of Thesis

Under the light of the underlined deficiencies and lack of data in the literature for the transitionally rough irregular surfaces and in particular marine antifouling, this study aims to make a contribution to the advancement and further understanding of

the state-of-the-art rough-wall turbulent boundary layer flows developed over marine antifouling coatings.

In order to materialise the overall aim the specific objectives of the thesis are set as follows:

- To conduct a state-of-the art literature review of the rough wall-turbulence boundary layer flow with a specific emphasis on the marine antifouling coatings;
- To collect dedicated and reliable (two-dimensional) experimental data for the evaluation of mean velocity and turbulence quantities on surfaces coated with marine antifouling coatings along with hydraulically smooth and rough reference surfaces;
- To collect surface roughness data and conduct analysis for roughness characterization of typical marine antifouling coatings including new generation representatives;
- To investigate the existence and validity of Colebrook-White law for the new generation marine antifouling coatings;
- To observe the validity of outer layer similarity in the mean flow and turbulence quantities of the turbulent boundary layers developed over the marine antifouling coatings;
- To investigate the effect of roughness on the higher order turbulence statistics as well as the streamwise and wall-normal turbulence spectra of the tested surfaces;
- To derive transfer functions between the roughness spectra and turbulence spectra.

An extended literature review is carried out and summarized in Section 1.1 for the accomplishment of the first objective. In order to achieve the other above objectives, two sets of zero-pressure gradient turbulent boundary layer experiments were performed over flat plate test beds for various surfaces coated with marine antifouling along with the smooth and fully rough reference surfaces. Data were collected with the aid of a two-dimensional Laser Doppler Velocimetry (LDV) in both sets of the boundary layer experiments. Roughness measurements of the entire

tested surfaces were carried out by using a laser profilometer. BMT hull roughness analyser was also employed in the mean hull roughness value measurements of the tested surfaces in the first set of experiments. The first set of experiments included novel nanostructured antifoulings as well as commercially-in-use foul-release type ones. The mean velocity, boundary layer parameters, local skin friction drag, roughness functions and Reynolds stresses were evaluated for the first set of data which fulfill the first four objectives. The second set of boundary layer experiments were performed for a variety of commercially-in-use marine antifoulings including the self-polishing-copolymer (SPC) with copper and spray and roller application of foul-release (FR) type. Smooth and fully rough reference surfaces were also used as references. The mean velocity, boundary layer parameters, local skin friction drag, roughness functions, Reynolds stresses, third and fourth order turbulence statistics, autocorrelation and spatial correlation functions, turbulence spectra and transfer functions were calculated for the tested surfaces. The second set of data serves for the accomplishment of the entire given objectives. Detailed roughness analyses were carried out for both sets of surfaces which include calculation of several roughness parameters, autocorrelation and power spectral density functions at various cut-off lengths.

1.5 Layout of Thesis

The thesis starts with Chapter 1 which presents a literature review of rough wall turbulent boundary layer studies (Section 1.2) as well as the motivations (in Section 1.3) and the aim and objectives of the thesis (Section 1.4).

Chapter 2 gives an insight to the turbulent boundary layer concept by summarizing the general structure and scaling properties along with the effect of surface roughness on these characteristics. A review of the skin friction drag calculation methods is also included in this chapter.

An extended review is given about the turbulence spectra and its calculation from Laser Doppler Velocimetry (LDV) data in Chapter 3 along with the definition of transfer functions.

Chapter 4 aims to generate basic understanding of the surface roughness concept along with the characterization, measurement and analysis of the irregularly rough surfaces.

Chapter 5 presents the experimental details, analysis procedure and results of the first set of zero-pressure-gradient flat plate turbulent boundary layer experiments. The experiments covered carefully conducted turbulent boundary layer tests with two-dimensional LDV as well as roughness measurements of the tested surfaces. The experimental research was carried out with four novel nanostructured antifouling coated surfaces along with three reference ones. One of the reference surfaces was coated with a state-of-the-art commercially in use foul-release (FR) coating scheme whilst the other two consisted of a smooth steel and a fully-rough sand grit. Detailed roughness characterization of the surfaces is given along with the mean velocity, boundary layer parameters, local skin friction drag, roughness functions and Reynolds stresses.

The second set of zero-pressure gradient turbulent boundary layer experiments was carried out by using two-dimensional Laser Doppler Velocimetry (LDV) with the main purpose of collecting data that is suitable for turbulence spectra calculation. Six different surfaces were included in the tests, which consist of one smooth reference, one sand grit surface and four surfaces coated with anti-fouling coatings including Self-Polishing Co-polymer (SPC) and Foul(ing) Release (FR) types either by spraying or rollering. Presented in Chapter 6 are the experimental details, analysis procedure and results of the mentioned flat plate boundary layer experiments and the related roughness measurements. The mean velocity, boundary layer parameters, local skin friction drag and roughness functions are presented. The results also focus on the turbulence properties such as the Reynolds stresses, higher order moments of turbulent velocity components and time scales in the results as well as the autocorrelation and spatial correlation functions, turbulence spectra and transfer functions between roughness and turbulence spectrum.

Finally, Chapter 7 includes the main conclusions and recommendations for future work.

1.6 Summary

This chapter builds up an introduction to the thesis with the presentation of an extensive literature review on rough wall turbulent boundary layer research with an emphasis on the transitionally rough flow over irregular rough surfaces and marine antifouling. As a result of the literature review, the imperfections and unclear areas in theory and practice were determined which formed a basis for the major motivations of the thesis. The basic aim and the main objectives in materializing this aim were also developed and explained in this chapter as well as the layout of the thesis.

2. TURBULENT BOUNDARY LAYER

2.1 Introduction

The main objective of this chapter is to give an insight into the turbulent boundary layer concept by giving information about the general structure and scaling properties of it along with the effect of surface roughness on these characteristics. A review of the skin friction drag calculation methods is also included in this chapter since the skin friction drag is one of the major consequence of rough wall boundary layer flow and an important indicator of the effect of surface roughness. The chapter can be said to be generally composed of a review of the relevant literature.

Within the above framework Section 2.2 is a basic introduction to the turbulent flow whilst Section 2.3 gives an introduction to the boundary layer concept and defines important boundary layer parameters. In Section 2.4 the boundary layer equations are presented. Extended information about the turbulent boundary layer structure and scaling laws can be found in Section 2.5 whilst the wall roughness effect is reviewed in Section 2.6. Finally, the measurement and calculation techniques of skin friction drag are summarized in Section 2.7 together with an overall summary of the chapter in Section 2.8.

2.2 Turbulent Flow

Most of the flows encountered in the nature and thus in engineering problems are turbulent and laminar flow is an exception which may develop in slow speed, around bodies with small dimensions and high viscosities. The solar flares, motion of the clouds, water currents in the oceans, smoke from a chimney and flow around vehicles (e.g. ships, submarines, and airplanes) are mostly turbulent. The common features of turbulent flows were categorized by Tennekes and Lumley (1972), Bradshaw (1971) and Gad-el-Hak and Buschmann (2011). It is possible to make a definition of the turbulent flow as an unsteady 3-dimensional rotational continuum flow that occurs at large Reynolds numbers and essentially includes a random (or

irregular) motion consisting of a wide range of wavelengths and being diffusive and dissipative.

According to the Reynolds decomposition (Townsend, 1976), the velocity field of a turbulent motion can be defined as:

$$U = \bar{U} + u' \quad (2.1)$$

where \bar{U} is the average velocity component of the flow and u' is the velocity component associated with the random motion.

The boundary layer flow along a smooth wall becomes turbulent when the length based Reynolds number is sufficiently large. The simplest case of a turbulent boundary layer occurs over a flat plate with zero angle of attack which is referred as zero-pressure-gradient turbulent boundary layer. The transition from laminar to turbulent in a smooth wall zero-pressure-gradient boundary layer takes place at a Reynolds number of about 3.2×10^5 (Schlichting, 1979).

2.3 Turbulent Boundary Layer

In a flow near a solid surface, the frictional forces between the wall and the fluid due to the viscosity retards the motion of the fluid and the flow velocity gradually decreases closer to the wall and approaches to zero on the wall. The effect of the wall friction is limited to a rather thin region near the wall and the friction force loses its effect gradually while departing from the wall. The flow regains its momentum due to the interaction with the energetic outer flow and the streamwise velocity reaches to an almost equal value to that of the outer flow. This thin region until the streamwise velocity reaches to the 99% of the outer flow velocity is called the *boundary layer* and the thickness of this region is referred as the *boundary layer thickness* (δ). The concept of the boundary layer was defined by Prandtl in 1904 (White, 1974) who was the first to discover the effects of friction within the fluid were only significant in a thin layer near the wall. Two other relevant length scales are also used to define the properties of a boundary layer, namely the displacement thickness (δ_j) and the momentum thickness (θ). The displacement thickness is the distance by which the wall would have to be displaced outwards in a hypothetical frictionless flow so that the mass flux would be maintained as in the actual flow whilst momentum thickness

is associated with the momentum loss due to the skin friction drag. The definitions of these parameters are given in Equation 2.2 and 2.3, respectively.

$$\delta_1 = \int_0^{\infty} \left[1 - \frac{U}{U_e} \right] dy \quad (2.2)$$

$$\theta = \int_0^{\infty} \frac{U}{U_e} \left[1 - \frac{U}{U_e} \right] dy \quad (2.3)$$

The boundary layer consists of several sublayers which are classified according to the changing characteristics of the flow within the boundary layer. In Figure 2.1, these sublayers are presented for a smooth wall. In the proximity of the wall, the viscous sublayer (or linear subrange) which extends up to $y^+ \approx 5-10$ is dominated by the viscous stresses. For a zero-pressure gradient boundary layer, the total shear stress in the viscous sublayer is equal to the wall shear stress (basically the frictional force on the wall). A combination of the viscous stress and Reynolds stress (due to the turbulent fluctuations) compose the buffer layer ($10 < y^+ < 50$). The part of the boundary layer for $y^+ > 50$ or $y/\delta > 0.1-0.2$ is called the outer layer. The velocity defect law is valid in this region. On the other hand, the overlap region, is the part that the inner and outer layers overlap and is comprised of the mesolayer $30 < y^+ < 300$ and the inertial sublayer between $300 < y^+ < 0.1\delta^+$. The linear (or viscous) sublayer, buffer layer, mesolayer and inertial sublayer form the inner layer which is only the 10% to 20% of the total boundary layer thickness. The expected non-dimensional velocity profile in semi-logarithmic and normal scale is given in Figure 2.1 for a smooth wall boundary layer. A downwards shift in the log-law region is expected for a rough wall boundary layer in such a plot of the velocity profile.

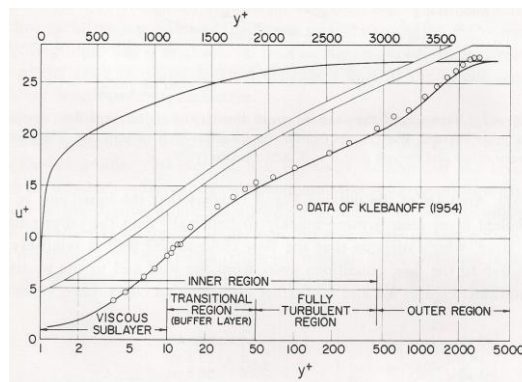


Figure 2.1 : The sublayers of a typical boundary layer (from Cebeci and Smith, 1974).

2.4 The Reynolds-Averaged Navier-Stokes Equations and 2-Dimensional Turbulent Boundary Layer Equations

The Navier-Stokes (N-S) equations, which imply the second law of Newton to a Newtonian viscous fluid, account for all kinds of turbulent motion in their most complex form and are capable of adequately describing the dynamics of fluid flow together with the equation of conservation of mass (continuity equation). The continuity and N-S equations can be written as below in tensor notation for an incompressible fluid.

$$\frac{\partial U_i}{\partial X_i} = 0 \quad (2.4)$$

$$\rho \frac{DU_i}{Dt} = \rho G_i - \frac{\partial P}{\partial X_i} + \mu \frac{\partial^2 U_i}{\partial X_j \partial X_j} \quad (2.5)$$

In order to decrease the complexity of these equations in the pursuit of a numerical solution and reducing the number of the nonlinear terms, Navier-Stokes equations are re-written by using the Reynolds decomposition along with the continuity equation and the ensemble-averages of the resulting four instantaneous equations are taken. The resulting equations are called the Reynolds-Averaged-Navier-Stokes (RANS) equations. If the averaging bar in for e.g. \bar{U} is omitted for simplicity and the averaged components of flow are all written without the bar with capital letters, the RANS equation can be written as:

$$\frac{\partial U_i}{\partial X_i} = 0 \quad (2.6)$$

$$\rho \frac{DU_i}{Dt} = \rho G_i - \frac{\partial P}{\partial X_i} + \frac{\partial \tau_{ij}}{\partial X_j} + \frac{\partial \tau_{ij}'}{\partial X_j} \quad (2.7)$$

with $\tau_{ij} = \mu \left(\frac{\partial u_i}{\partial x_j} + \frac{\partial u_j}{\partial x_i} \right)$ and $\tau_{ij}' = -\rho \overline{u_i' u_j'}$ where τ_{ij}' is called the Reynolds stresses and needs to be modelled with a turbulence model.

By re-writing the equations for 2-dimensional steady flow and using the thin shear layer approximation, the general boundary layer equations are derived as:

$$\frac{\partial U}{\partial x} + \frac{\partial V}{\partial y} = 0 \quad (2.8)$$

$$U \frac{\partial U}{\partial x} + V \frac{\partial U}{\partial y} = -\frac{1}{\rho} \frac{\partial P}{\partial x} + \nu \frac{\partial^2 U}{\partial y^2} - \frac{\partial \overline{u'v'}}{\partial y} - \frac{\partial \overline{u'^2}}{\partial x} \quad (2.9)$$

$$\frac{1}{\rho} \frac{\partial P}{\partial y} = -\frac{\partial \overline{v'^2}}{\partial y} \quad (2.10)$$

If Equation (2.10) is integrated over y, and the derivative of the result is taken over x and substituted into Equation (2.9), the two-dimensional momentum equation is derived:

$$U \frac{\partial U}{\partial x} + V \frac{\partial U}{\partial y} = -\frac{1}{\rho} \frac{\partial P}{\partial x} + \frac{1}{\rho} \frac{\partial}{\partial y} \left[\mu \frac{\partial U}{\partial y} - \rho \overline{u'v'} \right] + \frac{\partial}{\partial x} \left[\overline{v'^2} - \overline{u'^2} \right] \quad (2.11)$$

The left hand side of Equation (2.11) accounts for the momentum transport by the mean flow. The first term on the right hand side manifests itself the effect of the pressure gradient on momentum whilst the second term represent the viscous and turbulent diffusion of momentum and the third term represents the normal Reynolds stresses.

2.5 Overall Structure of a Turbulent Boundary Layer and Scaling Laws

For the wall-bounded shear flows, the most certain constraint is the viscosity of the fluid which enforces the no-slip condition. Accordingly the viscosity dominated characteristic length, which is on the order of the ratio of kinematic viscosity to the level of turbulent velocity fluctuations, becomes crucial (Tennekes and Lumley, 1972). However, at large Reynolds numbers this length scale is much smaller than the boundary layer thickness, implying that two different characteristic lengths possess simultaneously throughout the boundary layer. Accordingly, it is possible to say that two groups of scales are effective on different parts of the boundary layer depending upon the wall normal distance (Jimenez, 2004).

The dominant factor near the wall is the viscosity and two relevant scaling parameters is the friction velocity (u_τ) and the viscous length scale (l_v). Friction

velocity is directly related with the wall shear stress and defined as: $u_\tau = \sqrt{(\tau_w/\rho)}$, where τ_w is the tangential wall shear stress and ρ is the density of the fluid. Whilst l_ν is the ratio of the kinematic viscosity to friction velocity. Viscosity and the related velocity and length scales are dominant up to $y^+ \approx 5-10$. The most active part of the flow is the buffer layer which hosts a nonlinear self-sustaining cycle that is responsible for the generation of most of the turbulent energy in moderate Reynolds number flows (Jimenez and Moin, 1991). This layer encapsulates long streamwise streaks with low and high streamwise velocity and shorter quasi-streamwise vortices (Robinson, 1991). The boundary layer thickness, δ , becomes the relevant length scale at wall-normal distances that are in the order of δ . The Reynolds number based on the boundary layer thickness ($\delta^+ = \delta u_\tau/\nu$) defines the separation between the inner and outer length scales. For large values of δ^+ , an overlap region exists between the inner and outer regions. In this overlap region, the wall normal distance (y) is too small compared to the boundary layer thickness for δ to be the characteristic scale. Moreover, the normalized wall distance $y^+ = yu_\tau/\nu$ is too large for the viscosity to be the dominant scale. Thus, the only available scale is the wall distance, y , in this part of the boundary layer where the mean streamwise velocity has a logarithmic distribution (Townsend, 1976). Accordingly this region is also called as the logarithmic layer. The logarithmic law (log-law) defines the mean streamwise velocity profile as below:

$$U^+ = \frac{1}{\kappa} \ln y^+ + B \quad (2.12)$$

where U^+ is the streamwise velocity non-dimensionalized by friction velocity, u_τ , y^+ is the normalized wall distance such that $y^+ = yu_\tau/\nu$. κ is the von-Karman constant and B is also a constant value which is determined by the no-slip condition at the wall and depends on the properties of the viscous and buffer layers (Jimenez, 2004). Although there is a slightly varying range of the universal constants κ and B in the literature (e.g. Dixit and Ramesh, 2009; McKeon et al., 2004), according to Stanford conventions they are equal to 0.41 and 5.0, respectively.

Although, logarithmic law is mostly preferred as a model for the streamwise mean velocity profile by the researchers, there are also alternative models which fall under the power laws. The power laws generally fit to the velocity profile in a slightly

different y^+ range (Panton, 2000; Buschmann and Meniert, 1999). In its most general form, a power law can be written as:

$$U^+ = c(y^+)^{\beta} \quad (2.13)$$

where c and β are experimentally defined constants that depend on the Reynolds number. The value of β decreases as the velocity profile gets fuller.

Barenblatt (1993) gives a power law in the form of Equation (2.13) and defines c and β constants depending upon the assumption of an overlap region whose characteristics depend on the Reynolds number:

$$\beta = \frac{b_1}{\ln Re} + \frac{b_2}{(\ln Re)^2} + \dots \quad (2.14)$$

$$c = c_1 \ln Re + c_2 + \frac{c_3}{\ln Re} + \dots \quad (2.15)$$

The constants in Equations (2.14) and (2.15) are given as $b_1=1.5$, $c_1= 1/\sqrt{3}$, and $c_2=2.5$ based on the pipe flow data of Barenblatt and Prostokishin (1993). Zagarola et al. (1997) gives the same constants as $b_1=1.085$, $b_2=6.535$, $c_1= 0.7053$, and $c_2=0.3055$ by using the Princeton Super pipe data. Porporato and Sordo (2001) also defined new coefficients for the formulations of Barenblatt (1993) to include the effect of roughness for sand grain.

It should be noted here that, the Reynolds number is based on the pipe diameter in these formulations.

George and Castillo (1997) who observed a Reynolds number dependence in the overlap region also derived a power law in the same form with Equation (2.13) as well as one defined in outer variables:

$$\frac{U}{U_e} = c_0(y/\delta)^{\beta} \quad (2.16)$$

However, their formulations are explicitly dependent on the Reynolds number, δ^+ via the coefficients β , c and c_0 . Kotey et al. (2003) and Seo (2003) modified the power law model of George and Castillo (1997) and incorporated the surface roughness effects by defining new constants.

The discussion on the sufficiency and acceptability of log-law and/or a power law for the overlap region still continues between the researchers. As an example, Barenblatt et al. (2000) recommends a better description is possible for the data of Österlund et al. (2000) with the power law whilst Österlund et al. (2000) suggest that their data supports the log-law. On the other hand, Zagarola et al. (1997) and Panton (2000) agree that the log-law and power law apply to different regions of the boundary layer whilst Bushmann and Gad-el-Hak (2003) prove that a region exists in the overlap region where both the log-law and power law are valid.

A composite velocity profile is valid above $y^+ > 50$, in which the log-law is combined with a wake term to account for the outer layer dynamics as below:

$$U^+ = \frac{1}{\kappa} \ln y^+ + B + \frac{2\Pi}{\kappa} W\left(\frac{y}{\delta}\right) \quad (2.17)$$

where $W\left(\frac{y}{\delta}\right)$ is the wake function and generally negligible for $y/\delta < 0.15$ which is the typical upper limit of the overlap region. Generally, the wake function is defined so that it takes the value of 1 when $y = \delta$. Accordingly $2\Pi/\kappa$ indicate the contribution of the outer layer structures to the mean velocity profile (Jimenez, 2004). The wake parameter Π value is given as 0.55 by Hama (1954) for zero-pressure-gradient smooth walls in low inflow turbulence condition. The pressure gradient and inflow turbulence level have strong effects on this parameter. The value of Π decreases as turbulence intensity increases whilst an adverse pressure gradient causes an increase in its value (Brzek et al., 2009).

In the outer region, the difference between the freestream velocity (U_e) and the local mean velocity (U) is determined by the boundary layer thickness and the friction velocity such that at a distance of y from the wall (von Karman, 1930 from Schultz and Flack, 2007):

$$U_e - U = f(y, \delta, u_\tau) \quad (2.18)$$

This relation is non-dimensionally expressed as:

$$U_e^+ - U^+ = f\left(\frac{y}{\delta}\right) \quad (2.19)$$

which is referred as the velocity defect law which implies a complete similarity in the outer region. Two more velocity scales, other than the friction velocity, were proposed to be effective in the outer region. George and Castillo (1997) suggested that the outer velocity scale is proportional to the freestream velocity. On the other hand, Zagarola and Smits (1998) recommended the use of an outer velocity scale proportional to the mass flux deficit in the boundary layer: $U_e \delta_1 / \delta$ which is successfully used by Castillo and Walker (2002) and Seo (2003).

2.6 The Effect of Wall Roughness on the Turbulent Boundary Layer

Surface roughness alters the structure of the near wall flow at various degrees depending upon the roughness Reynolds number k^+ which is the ratio of the roughness height (k) to the viscous length scale (l_v). If k is in the order of a few wall units the roughness elements interfere with the buffer layer viscous cycle whilst this cycle is completely destroyed for $k^+ > 50-100$. Roughness may also modify the whole boundary layer if the roughness height is comparable to the boundary layer thickness.

The flows over rough walls are defined by three flow regimes in the literature. In Figure 2.2 these flow regimes, which are directly related with the amount of the protrusion of the roughness elements into the near wall flow, are presented with a sketch. If the roughness elements are small enough, compared to the viscous length scale, then the flow is said to be hydraulically smooth. This regime governs until $k^+ \approx 5$ according to the closed-packed uniform sand grain roughness measurements of Nikuradse (1933). On the other hand, this threshold boundary for the critical roughness Reynolds number for hydraulically smooth regime was reported as 2.5 by Schultz and Flack (2007) and suggested as low as 1.4 according to Langelandsvik et al. (2008).

When the roughness elements begin to extend to the outside of the viscous sublayer they start to induce form drag as a contribution to the wall shear stress, while decreasing the viscous stress contribution. This regime continues up to a certain value of k^+ , often given as 70 (Schlichting, 1979). However, Ligrani and Moffat (1986) showed that the limits of the transitionally rough regime can vary significantly with roughness geometry. They presented that the lower and upper limits of the transitionally rough regime change between $3 > k^+ > 15$ and $55 > k^+ > 90$ respectively for uniform spheres and sand roughness. Flack and Schultz (2010) also

pointed out that the boundaries of this flow regime may vary depending on the roughness type.

The fully rough regime, which is assumed for $k^+ > 70$ by Nikuradse, is dominated by the development of eddies shedding from the large roughness elements hence effecting the overlap layer and turbulent energy production. Form drag becomes dominant and viscous effects entirely lose their influence in this flow regime. This regime is also independent of the Reynolds number.

The effect of roughness is conventionally expected with an increase in the log-law constant B and thus a downwards shift in the mean streamwise velocity profile with the resulting increase in the local friction drag coefficient. Nikuradse (1933) was the one to discover that logarithmic law is also valid for rough boundary flows with the same value of the von-Karman constant along with an increase in B . His definition for the rough wall average streamwise velocity profile was

$$U^+ = \frac{1}{\kappa} \ln \left(\frac{y}{k_s} \right) + 8.5 + \frac{\Pi}{\kappa} W \left(\frac{y}{\delta} \right) \quad (2.20)$$

where k_s is the grain size of the sand. This equation is also the basis for calculating the equivalent or effective sand roughness for various experimental data.

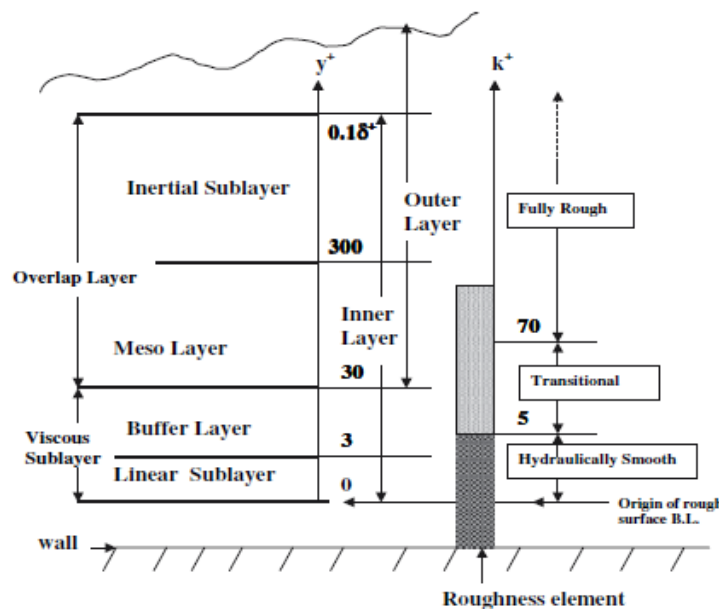


Figure 2.2 : Sublayers of the boundary layer and roughness regimes (from Cal et al., 2009).

Equation (2.20) is expressed in a more general form as below:

$$U^+ = \frac{1}{\kappa} \ln y^+ + B + \frac{2\Pi}{\kappa} W\left(\frac{y}{\delta}\right) - \Delta U^+ \quad (2.21)$$

where ΔU^+ is the roughness function which is defined as the average shift in the mean streamwise velocity profile. Jimenez (2004) discusses the concepts of hydraulically smooth and fully rough regimes using the logarithmic equations of mean velocity profiles for smooth and rough walls. Equation (2.21) can be written for smooth and rough cases respectively, at a given location of y in the boundary layer where mean velocity is U , as:

$$U_s^+ + \frac{1}{\kappa} \ln U_s^+ = \frac{1}{\kappa} \ln\left(\frac{Uy}{\nu}\right) + B_s = C_s \quad (2.22)$$

$$U_r^+ + \frac{1}{\kappa} \ln U_r^+ = \frac{1}{\kappa} \ln\left(\frac{Uy}{\nu k_s^+}\right) + B_r = C_r \quad (2.23)$$

where B_s and B_r are 5.1 and 8.5 respectively and s and r indices refer to smooth and rough values except k_s^+ , since this definition is the universally used symbol for roughness Reynolds number based on equivalent sand roughness. Higher values of $U^+ = U/u_\tau$ imply lower skin friction values and lower skin friction is expected for the smooth wall boundary layer. The difference in smooth and rough wall boundary layer skin friction drag is controlled by the difference between the Equations (2.22) and (2.23) as they are both in the same form:

$$C_s - C_r = \frac{1}{\kappa} \ln\left(\frac{Uy}{\nu}\right) - \frac{1}{\kappa} \ln\left(\frac{Uy}{\nu k_s^+}\right) - 3.4 \quad (2.24)$$

Consequently,

$$\Delta U^+ = \frac{1}{\kappa} \ln k_s^+ - 3.4 \quad (2.25)$$

For $k_s^+ \leq \sim 4$, it is expected that the roughness function would be negative; meaning the skin friction of the rough wall would be lower than the one of the smooth wall. However, in practice this is usually not the case. Jimenez (2004) points out that roughness elements are generally more efficient generators of skin friction than

smooth walls, presumably due to their capacity of higher turbulent dissipation generation than the relatively delicate viscous cycle.

For $C_s \gg C_r$, the viscous drag is negligible compared to the form drag of the roughness protrusions and for this limit the ratio of the friction velocity of the rough wall to that of the smooth one is inversely proportional to C_s/C_r . Consequently, for the rough wall to have a skin friction of larger than twice of the smooth one it is needed that $C_r < \sim C_s/\sqrt{2}$. Since C_s is typically about 20-30 in the overlap region, it is implied that $C_s - C_r \geq \sim 7.5$ and $k_s^+ > \sim 80$ which is also the general condition of being in the fully rough regime.

Two different roughness types are defined regarding the flow characteristics: k-type and d-type roughness. Perry et al. (1969) was the first to study that the distinction between k- and d- type roughness was made. Raupach et al. (1991), Jimenez (2004) and Leonardi et al. (2007) have broad information about the behaviour of the flow around the two roughness types. For a k-type surface ΔU^+ is a function of the roughness height whereas it scales with an outer length scale (e.g. boundary layer thickness or pipe diameter). Perry et al. (1969) explains the behaviour difference in the flow over k-type and d-type rough surfaces as: whilst eddies with a length scale in the order of roughness height are being shed to the flow over k-type roughness elements, stable vortices are formed between the closely packed grooves of the d-type roughness protrusions and there exists no eddy shedding. However, the findings of Djenidi et al. (1999) and Leonardi et al. (2004) showed that the above explanation is not entirely correct and ejection of vortices also takes place for d-type surfaces although they are less intense. Leonardi et al. (2007) recently proposed that the scaling of the ΔU^+ with the outer length scale is also questionable and the most important difference between d-type and k-type roughness is related to the relative magnitudes of the pressure and frictional drag and the frictional drag should be much larger than the pressure drag component with the d-type surfaces.

2.7 The Methods for the Determination of the Skin Friction Drag

The accurate determination of the skin friction drag for the smooth and rough surfaces is an important issue, not only due to its value in engineering point of view but also due to its influence on the interpretation of most of the boundary layer flow

characteristics scaling with the friction velocity which is directly associated with the skin friction drag.

The skin friction drag can be determined by direct force measurements for a floating element (e.g. Karlsson, 1978; Johansson, 1985) or by towing tank experiments with flat plates (e.g. Schultz and Myers, 2003; Schultz, 2004). Schultz and Myers (2003) give an overall uncertainty as $\pm 2\%$ in the measured C_f . Another method is using an oil film interferometer which relies on the change of thickness of a thin oil film when subject to shear (Österlund, 1999). The rate at which oil thins on a surface is a function of the shear stress magnitude. Whilst Naughton and Sheplak (2000) discuss the several variations of the oil film interferometers, Mehta et al. (2000) state that it is possible to achieve accuracy in C_f better than $\pm 5\%$ by using this method. The skin friction drag is also experimentally measured with rotating disk (e.g. Loeb et al., 1984; Holm et al., 2004) or rotating drum (e.g. Candries et al., 2003; Weinell et al., 2003) methods.

A classical method, especially used in the determination of the skin friction drag coefficient for smooth surfaces is the viscous sublayer slope method which is based on the calculation of the wall shear stress by the velocity gradient on the wall (e.g. Tachie, 2000). It is assumed that the turbulent shear stresses are negligible here and the only dominant component of shear stress is the viscous one. So that:

$$\frac{\tau_w}{\rho} = \nu \left. \frac{\partial U}{\partial y} \right|_{y=0} \quad (2.26)$$

The application of this method is rather straightforward; however there exist essential difficulties in collecting data in the near vicinity of the wall. Since the viscous sublayer is very thin, it is a hard work to resolve this part of the boundary layer even with LDV equipment. Moreover, for the flow over fully rough surfaces the viscous sublayer may be fully destroyed. Consequently, the method has a restricted area of application in practice.

The skin friction drag can be calculated by using the integral momentum equation (e.g. Brzek et al., 2008). The challenge of this method is the need of the measurement of the velocity profile at several streamwise locations. The integrated two-dimensional boundary layer momentum equation is:

$$\begin{aligned} \frac{\tau_w}{\rho} = & \nu \frac{\partial U}{\partial y} - \overline{u'v'} - \int_0^y \frac{\partial U^2}{\partial x} dy' + U \int_0^y \frac{\partial U}{\partial x} dy' - \int_0^y \frac{\partial \overline{u^2}}{\partial x} dy' \\ & + \int_0^y \frac{\partial \overline{v^2}}{\partial x} dy' + U_e \frac{\partial U_e}{\partial x} y \end{aligned} \quad (2.27)$$

The mean transverse velocity (V) is calculated by using the continuity equation and written in terms of U in the above equation. The first term on the right hand side represents the viscous shear stress and is negligible in the fully rough regime. Second term is the turbulent shear stress and is dominant throughout a significant fraction of the boundary layer. The third and fourth terms represent the mean momentum flux. The fifth and sixth terms are the gradients of the turbulent normal stresses. The last term is the pressure gradient that balances with the mean convection term in the outer flow. After the calculation of the wall shear stress from Equation (2.26), the skin friction coefficient and friction velocity can be calculated as:

$$C_f = \frac{\tau_w}{\frac{1}{2}\rho U_e^2} = \frac{2u_\tau^2}{U_e^2} \quad (2.28)$$

According Brzek et al. (2008) this method provides an uncertainty of $\pm 3\%$ in C_f .

Another important method is the Reynolds stress method which relies on the assumption that the total shear stress is only composed of the Reynolds shear stresses in the constant stress region (Schultz, 2000; Candries, 2001). This is a more practical method since the local skin friction coefficient can be calculated at each measured streamwise position. Accordingly, in the constant stress region;

$$-\overline{u'v'} = \frac{\tau_w}{\rho} = u_\tau^2 = \frac{c_f U_e^2}{2} \quad (2.29)$$

Flack et al. (2007) consider the contribution of the viscous shear stress along with the Reynolds shear stresses in the plateau region located in the inner layer and call their method as the total stress method. This technique is a very similar approach to that of the Reynolds stress method:

$$\frac{\tau_w}{\rho} = \nu \frac{\partial U}{\partial y} - \overline{u'v'} \quad (2.30)$$

Schultz and Flack (2009) give an uncertainty in the friction velocity as $\pm 6\%$ with this method. It should be born in mind that the uncertainty levels given here for the methods as an example may substantially change (decrease or increase) depending upon the experimental set-up, the measurement device used for velocity data collection and the sample size.

The latter three methods are usually referred as indirect methods along with the profile matching techniques for the calculation of the skin friction drag. In profile matching methods, the logarithmic part of the mean streamwise velocity profile, in some methods together with the wake region, is defined by one or more equations. The solution is achieved by an iterative procedure by calculating the unknowns in the equations such as the friction velocity, the wake strength and virtual origin until the best fit to the experimental data is acquired.

A classical profile matching technique for calculating the friction velocity is the use of the (Standard) Clauser Chart Method (SCCM) (Clauser, 1956). The overlap region of the outer part and inner region of smooth surface zero-pressure-gradient boundary layers is believed to obey the logarithmic law-of-the-wall which is given in Equation (2.12). The method is simply based on an iterative least-squares optimization procedure for the only unknown u_τ in Equation (2.12), such that the logarithmic region of the measured mean velocity profile fits on the curve of the law-of-the-wall. SCCM was used for the smooth reference surfaces in this thesis.

According to Hama (1954) (or e.g. Bandyopadhyay, 1987), whether the surface is smooth or rough, the velocity of the logarithmic and outer part of the boundary layer may be described as:

$$U_e^+ - U^+ = - \left(5.6 \log \left(\frac{y u_\tau}{\delta_1 U_e} \right) + 0.6 \right) \quad (2.31)$$

and

$$U_e^+ - U^+ = 9.6 \left(1 - \frac{y}{0.30 \delta_1 U_e / U_\tau} \right)^2 \quad (2.32)$$

Equation (2.31) is valid throughout the overlap region where $y^+ \geq 32.5$ and $y u_\tau / \delta_1 U_e \leq 0.045$. Equation (2.32), on the other hand, is valid for the outer region of the boundary layer where $0.15 \leq y / \delta \leq 1$. Equations (2.31) and (2.32) connect

smoothly at $y/\delta = 0.15$. Many studies in the literature (e.g. Furuya and Fujita 1967, Perry et al. 1987, Tani 1987) supported this approach of a universal velocity defect profile for both smooth and rough surfaces. The method requires the determination of two parameters, the friction velocity (u_τ) and the error in origin (ε). The latter causes the mean velocity profile to depart from the logarithmic law for the rough cases. This means that the wall distance y should be replaced by $(y + \varepsilon)$ in the equations. These two unknown parameters may be obtained with a least-squares-based optimization procedure in a similar manner to that of the SCCM. This method is called the Hama Method (HM) (Bandyopadhyay, 1987). In the present study, HM was applied to the measured data of the rough surfaces.

On the other hand, a good number of studies, such as Krogstad et al. (1992) and Tachie (2000) observed an increase in the wake strength parameter for the rough cases and reported varying values of Π (e.g. Tani, 1988). Perry and Li (1990) suggested a method which was insensitive to the differences in Π . According to this method, when Π was taken to be equal to 0.55, the logarithmic profile of the boundary layer may be described as:

$$\frac{U}{U_e} = 1 + \frac{1}{\kappa} \frac{u_\tau}{U_e} \ln\left(\frac{y}{\delta_1}\right) + \frac{1}{\kappa} \frac{u_\tau}{U_e} \ln\left(\frac{u_\tau}{U_e}\right) + 0.493 \frac{u_\tau}{U_e} \quad (2.33)$$

ε and u_τ need to be determined with a similar procedure to that of the previous methods. Perry and Li (1990) reported that a $\pm 10\%$ variation in the value of Π will cause only a $\pm 3\%$ variation in the values of u_τ/U_e . This method is usually called as the Modified Clauser method (MCCM) and was used for coated and rough cases in the present study.

As an alternative to the above profile matching methods, Krogstad et al. (1992) and Finley et al. (1996) proposed the use of the velocity defect law with a formulation that allows the optimization of the wake strength together with the friction velocity and error in origin. Accordingly, by ignoring the viscous sublayer or roughness sublayer in the rough case, the velocity distribution across the inner and outer regions may be given as below;

$$U^+ = \frac{1}{\kappa} \ln y^+ + B - \Delta U^+ + \frac{2\Pi}{\kappa} W(\eta) \quad (2.34)$$

where $y^+ = (y + \varepsilon)U_\tau/\nu$ is the non-dimensionalized wall coordinate in inner scales, $\eta = (y + \varepsilon)/\delta$ is the non-dimensionalized wall coordinate in outer scales and ε is the virtual origin (or error in origin due to roughness). ΔU^+ is the roughness function which is equal to zero for smooth surfaces whilst it can change depending upon the surface and inflow properties. Π represents the strength of the wake function, $W(\eta)$, which defines the effect of the outer flow to the outer part of the boundary layer. Depending upon Equation 2.34, it can be said that the description of the mean velocity profile for a rough wall requires four parameters to be determined: ε , U_τ , Π , and ΔU^+ . Rewriting Equation 2.34 in velocity-defect form (i.e. writing the difference between the non-dimensionalized outer flow velocity and velocity in the boundary layer), simplifies the problem by reducing the unknowns to three:

$$U_e^+ - U^+ = \frac{2\Pi}{\kappa} [W(1) - W(\eta)] - \frac{1}{\kappa} \ln(\eta) \quad (2.35)$$

The expression given by Granville (1987) for the determination of the wake function which is given in Equation 2.36 allows making an optimization for Π :

$$W(\eta) = \frac{1}{2\Pi} [(1 + 6\Pi) - (1 + 4\Pi)\eta]\eta^2 \quad (2.36)$$

Accordingly, for the determination of ε , U_τ , and Π a least squares optimization method was applied in order to fit Equations (2.35) and (2.36) to the mean velocity profiles which requires an iterative process. This method was also used for the determination of the friction velocity in Chapter 6.

The local skin friction coefficients (c_f) are calculated for all of the surfaces depending on the friction velocities calculated by the above method. The calculation of c_f is carried out by using the below formula:

$$c_f = 2 \left(\frac{U_\tau}{U_e} \right)^2 \quad (2.37)$$

The roughness function is directly associated with the shift in the non-dimensional velocity profile compared to the smooth wall. This shift is also analytically equal to the difference given by Equation (2.38), provided that this difference is calculated at the same Reynolds numbers based on the displacement thickness (Re_{δ_1}) according to Granville (1987). Thus the roughness function (ΔU^+) is calculated as:

$$\Delta U^+ = \left(\frac{2}{c_f}\right)_{smooth}^{1/2} - \left(\frac{2}{c_f}\right)_{rough}^{1/2} \quad (2.38)$$

On the other hand, Barenblatt (1993) and George and Castillo (1997) gives skin friction coefficient relations based on their power law formulations given in Section 2.4. The skin friction drag relation of Barenblatt (1993) is:

$$c_f = 2 \left(\frac{1}{e^{1.5}} \left(\frac{e^{3/2\beta}}{c} \right)^{1/(1+\beta)} \right)^2 \quad (2.39)$$

whereas the formula of George and Castillo (1997) is given as:

$$c_f = 2 \left(\left(\frac{c_0}{c} \right)^{1/(1+\beta)} \left(\frac{U_e \delta}{\nu} \right)^{-\beta/(1+\beta)} \right)^2 \quad (2.40)$$

Djenidi et al. (1997) and Tachie et al. (2001) found the use of the power law in determining the skin friction reliable and stated that the results obtained from power laws were comparable to the ones from other reliable techniques.

2.8 Summary

A conceptual overview of the turbulent boundary layers was given in this chapter to provide basis for the research conducted in this thesis. According to the literature, it can be said that the overall structure of the smooth wall turbulent boundary layers are well-defined and well-documented although the use of the logarithmic or power law is still being discussed. On the other hand, there are more conflicting views for the rough wall boundary flow such as the mechanism of the interaction throughout the boundary layer, the existence of the outer layer similarity and the skin friction drag calculation methods. The limits of the rough wall flow regimes and the concept of being hydraulically smooth are also still under review. The skin friction drag calculation from the rough wall boundary layer velocity data requires the calculation of at least one or two additional parameters, the virtual origin and the wake strength. Although there are several widely used velocity profile fitting methods that can be used in rough wall turbulent boundary layers, they should be handled with care in the calculation of skin friction drag for irregularly rough surfaces since the methods are

generally proved their reliability on regularly rough walls such as sand roughness, meshes or rods, etc. Accordingly, the use of more than one method along with a Reynolds stress method can be recommended for skin friction drag calculation from velocity data.

3. TURBULENCE SPECTRUM

3.1 Introduction

The velocity components in a turbulent flow field keep randomly changing, in other words fluctuating, both in time scale and in three-dimensional space. Accordingly, the velocity components can be experimentally measured as a random function of time or space coordinates. If the measured random function is stationary and homogeneous (Bendat and Piersol, 1986) then it is possible to calculate an autocorrelation function and a related spectrum for this function. The main objective of this chapter is to give an extended review on the turbulence spectra and its calculation from Laser Doppler Velocimetry (LDV) data.

A basic insight is given to both spatial and time spectra in Sections 3.2 and 3.3 whilst the turbulence spectra calculation methods are reviewed in Section 3.4. The refined sample and hold reconstruction technique, which is used for the calculation of the turbulence spectra in this thesis, is given in detail in Section 3.5. Presented in Section 3.6 is the concept of transfer functions which will be used in defining a relationship between the roughness spectra and turbulence spectra in Chapter 6.

3.2 One-Dimensional and Three-Dimensional Spatial Spectrum

A one-dimensional turbulence spectrum may be calculated depending upon the measurement of the velocity components in one direction (e.g. the freestream direction) or a three-dimensional turbulence spectrum can be calculated by measurement of the velocity components in three spatial directions via a three-dimensional Fourier transform. In both cases the transform parameter will be the wave number. The experimental data gathering for spatial spectra calculation is a rather hard work since the data is needed to be collected with small spatial lags and at several points in order to resolve the spatial length scales of the flow field.

The spatial correlation tensor can be given as in the below equation:

$$R_{ij}(\vec{r}) = \overline{u_i(\vec{x}, t) u_j(\vec{x} + \vec{r}, t)} \quad (3.1)$$

The spectrum tensor, which is the Fourier transform of the correlation tensor, is:

$$\begin{aligned} \phi_{ij}(\vec{k}) &= \frac{1}{(2\pi)^3} \iiint \exp(-i\vec{k} \cdot \vec{r}) R_{ij}(\vec{r}) d\vec{r} \\ R_{ij}(\vec{r}) &= \iiint \exp(i\vec{k} \cdot \vec{r}) \phi_{ij}(\vec{k}) d\vec{k} \end{aligned} \quad (3.2)$$

The sum of the diagonal components of ϕ_{ij} , $\phi_{ii} = \phi_{11} + \phi_{22} + \phi_{33}$, has a special meaning since it is the kinetic energy at a given wave number.

The directional information within $\phi_{ii}(\vec{k})$ can be eliminated by integration about a spherical shell with a radius of k :

$$E(k) = \frac{1}{2} \oint \phi_{ii}(\vec{k}) ds \quad (3.3)$$

In Equation 3.3, ds is the infinitely small surface element on the shell and the $\frac{1}{2}$ constant is used in order to be able to associate the $E(k)$ three-dimensional spectra to the kinetic energy per unit mass so that;

$$\int_0^{\infty} E(k) dk = \frac{1}{2} \overline{u_i u_i} \quad (3.4)$$

The most widely used one-dimensional spatial turbulence spectrum are $F_{11}(k_1)$ and $F_{22}(k_1)$ which can be calculated by the one-dimensional Fourier transform of $R_{11}(r, 0, 0)$ and $R_{22}(r, 0, 0)$ correlations, respectively:

$$\begin{aligned} R_{11}(r, 0, 0) &= \int_{-\infty}^{\infty} \exp(ik_1 r) F_{11}(k_1) dk_1 \\ R_{22}(r, 0, 0) &= \int_{-\infty}^{\infty} \exp(ik_1 r) F_{22}(k_1) dk_1 \end{aligned} \quad (3.5)$$

Two relations are given between $E(k)$ and $F_{11}(k_1)$, $F_{22}(k_1)$ spectrum by Batchelor (1953) and Hinze (1959), assuming that the turbulent field is isotropic:

$$E(k) = k^3 \frac{d}{dk} \left(\frac{1}{k} \frac{dF_{11}}{dk} \right) \quad (3.6)$$

$$\frac{d}{dk_1} F_{22}(k_1) = -\frac{k_1}{2} \frac{d^2}{dk_1^2} F_{11}(k_1) \quad (3.7)$$

Equation 3.6 is generally used for the calculation of $E(k)$ at high wave numbers from the experimentally measured $F_{11}(k_1)$.

The strain rate associated with the large-scale, energy containing eddies is on the same order with the rate of strain of the mean flow. Accordingly, the large-scale eddies are in a continuous anisotropy depending upon the strain rate of the mean flow. Moreover, the strain rate of the small-scale eddies are higher than the ones of the mean flow and the large-scale eddies and thus continuous anisotropy is not observed at small-scales. However, this does not mean that there is isotropy in the small-scales since the energy transfer can only be realised by the lining of the eddies under a certain strain rate. On the other hand, the anisotropy of the flow decreases as the eddy sizes get smaller and smaller and it is expected that the mean strain rate field will be isotropic in average at this smallest scales. This is called the *local isotropy* and only can be observed at high enough Reynolds numbers.

The time-scales in the turbulence spectra where local isotropy is observed are shorter compared to the mean flow and this implies that the small eddies can be accommodating to the changing mean flow conditions very rapidly. Accordingly, it can be said that the small eddies are in equilibrium with the local conditions of the mean flow and thus the wave number range that local isotropy is observed in the turbulence spectra is also called as the *Equilibrium Range*. The lower limit of the equilibrium range starts from the wave number that the strain rate of the associated eddy is larger than the strain rate of the mean flow and all of the higher wave numbers are in this range. The scaling parameters for the equilibrium range of the turbulence spectra are the dissipation rate (ε) and the viscosity (ν) along with the wave number (k) and accordingly the turbulent spectra may be defined as a function of these three parameters as $E = E(k, \varepsilon, \nu)$ at this range. The non-dimensional so-called *Kolmogorov Spectra* of the equilibrium range is given as follows:

$$\frac{E(k)}{\nu^{5/4} \varepsilon^{1/4}} = \frac{E(k)}{\nu^2 \eta} = f(k\eta) \quad (3.8)$$

where $\nu = (\nu\varepsilon)^{1/4}$ is the Kolmogorov velocity scale and $\eta = (\nu^3/\varepsilon)^{1/4}$ is the Kolmogorov micro scale.

The equilibrium range also covers the Dissipation Range. Batchelor (1953) gives a definition for the turbulence spectra in the dissipation range as follows:

$$D(k) = 2\nu k^2 E(k) \quad (3.9)$$

Accordingly, the dissipation rate, ε , may be calculated as:

$$\varepsilon = \int_0^{\infty} D(k) dk = 2\nu \int_0^{\infty} k^2 E dk \quad (3.10)$$

The behaviour of the turbulence spectra at the small wave numbers and thus at the *Large-Scale Range* is also different. The factors that specify the energy transfer from the mean flow to the turbulence and from large-scale eddies to small-scale eddies constitute the important parameters for the turbulence spectra at this range. The energy of turbulence arises from the mean flow strain rate (S) and the transfer of energy to the smaller-scales is recognised with the dissipation rate (ε), accordingly the scaling parameters for the large-scale range turbulence spectra are S and ε along with the wave number so that $E = E(k, \varepsilon, S)$. Accordingly, the non-dimensionalized turbulence spectra at this range can be written as:

$$\frac{E(k)}{\varepsilon^{3/2} S^{-5/2}} = \frac{E(k)}{u^2 \ell} = F(k\ell) \quad (3.11)$$

The region of the turbulence spectra where both the inertial and the viscous scales are effective is referred to as *the Inertial Subrange*. This region may be thought as the overlap of the two regions either dominated by the viscous effects or inertial effects. The turbulence spectrum at this region is given as:

$$E(k) = \alpha \varepsilon^{2/3} k^{-5/3} \quad (3.12)$$

Equation 3.12 is valid for $kl \rightarrow \infty$, $k\eta \rightarrow 0$, and $R_\ell \rightarrow \infty$ where ℓ is the size of an eddy and R_ℓ is the associated Reynolds number. The constant of α is given as 1.5 depending upon the experimental measurements.

3.3 Time Spectrum

The time spectra of turbulent data may be calculated by the measurement of the fluctuating velocity components in time at one spatial point in the flow field. The autocorrelation of a selected velocity component or cross-correlations of two velocity components may be calculated accordingly, and hence the one-dimensional Fourier transform of these correlation functions will define the related turbulence spectra. Since time is one-dimensional the calculated turbulence spectra will also be one dimensional. Under these circumstances, the transform parameter will be the frequency (ω) due to the dependence of the correlation function on the time lag. Such a turbulence spectrum is also known as *Euler time spectra*.

The correlation tensor that can be calculated by the measurement of the velocity components with a time lag of τ may be defined as:

$$R_{ij}(\tau) = \overline{u_i(x,t)u_j(x,t+\tau)} \quad (3.13)$$

The time spectra $\Psi_{ij}(\omega)$ and the correlation function given in Equation (3.13) are Fourier couples.

$$\begin{aligned} R_{ij}(\tau) &= \int_{-\infty}^{\infty} \exp(i\omega\tau)\Psi_{ij}(\omega)d\omega \\ \Psi_{ij}(\omega) &= \frac{1}{2\pi} \int_{-\infty}^{\infty} \exp(-i\omega\tau)R_{ij}(\tau)d\tau \end{aligned} \quad (3.14)$$

The value of the time spectra at zero frequency ($\omega=0$) defines the integral time scale (T) as given in the below equation:

$$\Psi_{ij}(0) = \frac{1}{2\pi} \int_{-\infty}^{\infty} R_{ij}(\tau)d\tau = \frac{\overline{u_i u_i}}{\pi} T \quad (3.15)$$

The time spectra may be considered as the regenerated spatial spectra depending upon the time scale, since every eddy has an associated length and time scale and hence eddies in different sizes and wave number are associated with a time scale. However, the relation of the length and time scales is not constant in a spatial spectrum. Whilst the time scale decreases as the wave number increases until the peak point of the dissipation region, time scale begins to increase after this point as the wave number further increases. Accordingly, if the spatial spectrum is regenerated depending upon the time scale, the effect of two eddies at different sizes will be present at one frequency. One of these effects will be arising from the lower wave number but high energy containing eddy and the other will depend on the lower energy containing eddy from the dissipation range which has a high wave number. Since the energy level at the dissipation range is considerably small, the related effect of the high wave number eddy may be considered as ignorable. (Tennekes and Lumley, 1972)

The equilibrium range can also be observed in a time spectrum, provided that the Reynolds number is high enough, at the high frequency region where local isotropy exists. The scaling parameters for the time spectra at this region are the dissipation rate and the viscosity as for the spatial turbulence spectra and accordingly the suitable normalisation of the time turbulence spectra is given as:

$$\Psi_{ii}(\omega) = \nu \eta f(\omega \eta / \nu) \quad (3.16)$$

The scaling parameters for the time spectra at the *Energy-Containing Range (Large-Scale Range)* are the mean flow velocity U and the eddy size ℓ . For $\omega(\nu/\varepsilon)^{1/2} \ll 1$ the time spectra can be re-written as:

$$\Psi_{ii}(\omega) = U \ell F(\omega \ell / U) \quad (3.17)$$

Provided that the Reynolds number is rather high, the low-frequency end of the equilibrium range and the high-frequency end of the energy-containing range overlaps and defines the *inertial subrange* for the time spectra. The time spectra is independent both from the frequency of the large eddies (U/ℓ) and the frequency of the small eddies ($(\nu/\varepsilon)^{1/2}$) in this range, so that the spectra can be defined as:

$$\Psi_{ii}(\omega) = B\epsilon\omega^{-2} \quad (3.18)$$

The constant B is given as 1.8 based upon the relation of time spectra and spatial spectra.

The time spectra can be converted into the one-dimensional spatial spectra by using Taylor's hypothesis of frozen turbulence (Taylor, 1938; Tennekes and Lumley, 1972; Reynolds, 1974; Davidson, 2005). According to this hypothesis, if the streamwise turbulent fluctuations are small compared to the mean flow speed, then the temporal response at a fixed point in space can be thought as an unchanging spatial pattern like a cloud convecting uniformly past the fixed point with the mean streamwise velocity. Accordingly, the streamwise wave number may be calculated as;

$$k_1 = 2\pi\omega/U \quad (3.19)$$

and the spatial streamwise turbulence spectra as;

$$E_{11}(k_1) = U/2\pi \Psi_{11}(\omega) \quad (3.20)$$

As it can be observed from the above formulations the mean streamwise velocity, U is used as the convection velocity in the Taylor's hypothesis. Krogstad et al.(1998) state that the instantaneous velocity may also be used as the convection velocity. It should be mentioned here that there is an ongoing research on the convection velocities in a turbulent boundary layer and even the validity of the Taylor's hypothesis is being reconsidered for some flow types (e.g. Leboeuf and Mehta, 1995; del Alamo and Jimenez, 2009; Moin, 2009) .

3.4 Calculation of Turbulence Spectra from Laser Doppler Velocimetry Data

Measurement of the power spectral density (PSD) related to the flow velocity by Laser Doppler Velocimetry (LDV) is complicated and requires special consideration due to the random and intermittent nature of the LDV velocity signals in time. Several advanced algorithms have been introduced for the estimation of autocorrelation function and/or power spectral density from the irregularly sampled velocity data by LDV in the literature during the last years. The fundamental methods for computing power spectral density from LDV signals are summarized

and compared in Britz and Antonia (1996) and Benedict et al. (2000). These fundamental spectral estimation techniques can be classified into three general groups:

- *Direct transform methods*
- *Slotting methods*
- *Interpolation (or Reconstruction) methods*

Direct transform methods for PSD estimation are based on the adaptation of the discrete Fourier transform to the randomly spaced data. The standard estimator for this method is given by Gaster and Roberts (1977). Negative aspects of this standard estimator were mentioned as high frequency contamination and negative bias in the PSD estimates by Britz and Antonia (1996) and Benedict et al. (2000). However, several authors developed modifications to the periodogram such as Scargle (1982), Marquardt and Acuff (1983) and Britz and Antonia (1996).

The slotting method, which was introduced by Mayo et al. (1974), consists of the estimation of the autocorrelation function (ACF) by discretizing the ACF lag time into bins that are not necessarily equally spaced. This procedure is followed by the Fourier transform of the estimated ACF which yields the PSD (Benedict et al., 2000). The slotting technique was improved by local normalisation (van Maanen and Tummers, 1996), fuzzy slotting (Nobach et al., 1998a), the combination of the two (van Maanen et al., 1999), weighting algorithms (Nobach, 1999) and local time estimation (Nobach, 2002). Especially, the latter two in the improved versions yield good estimations of PSD (Benedict et al, 2000 and Nobach, 1999).

Interpolation (or Reconstruction) methods construct equidistantly spaced time series by re-sampling with various interpolation schemes and therefore enable the use of a fast Fourier transform (FFT) in producing the PSD estimates. The new sequence of data at regular intervals can be obtained either by low or high-ordered polynomials (Müller et al., 1998; Adrian and Yao, 1987; Müller et al., 1994), Shannon interpolation (Veynante and Candel 1988), fractal interpolation (Chao and Leu, 1992) or exponential interpolation (Host-Madsen, 1994). The most common and convenient polynomial class algorithm is the zero-order Sample and Hold reconstruction (Adrian and Yao, 1987; Britz and Antonia, 1996; Benedict et al., 2000). However, most of the reconstruction schemes have filtering effects on the

PSD. Adrian and Yao (1987) were the first to call attention to this filtering effect that caused the PSD to be reliable only up to a frequency of $\dot{n}/2\pi$, which becomes a substitute for the Nyquist Theorem concerning regularly sampled data. It was observed by van Maanen and Tulleken (1994) that this filtering effect was even significant at frequencies below $\dot{n}/2\pi$. However, later on, refinement procedures were developed in order to recover from this avoidable filtering effect of the Sample and Hold reconstruction by Nobach et al. (1998b). Moreover, noise suppression techniques have also been developed to account for the white noise and interpolation errors that occur in the PSD by Benedict and Gould (1995), van Maanen and Tulleken (1994) and Nobach et al. (1998b).

The Refined Sample and Hold reconstruction of Nobach et al. (1998b) was used in this Ph.D. study along with the block splitting and averaging procedure which was introduced by Gaster and Roberts (1977) and recommended by Benedict et al. (2000) for reducing the estimator variance. Noise suppression techniques were not needed to be employed since the methods of Benedict and Gould (1995) and van Maanen and Tulleken (1994) are only capable of eliminating the white noise at high frequency data whereas the method of Nobach et al. (1998b) is not working well for low frequency data (e.g. below app. 500 Hz.) although it is capable of reducing the interpolation noise along with the white noise (Nobach et al. (1998b)). The PSD estimation method used in this thesis is explained in detail in the following section.

3.5 Refined Sample and Hold Method for Power Spectral Density Estimation from LDV Data

The power spectral density and autocorrelation function estimation process that is used in this study is based on the recommendations of Benedict et al. (2000) and Nobach (2000). The steps of this analysis procedure are explained thoroughly during this section. The entire processing algorithm from the flow velocity data collected from a LDV to the ACF and PSD estimates is shown in Figure 3.1.

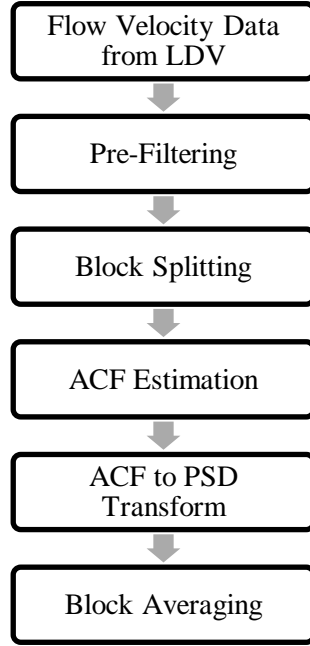


Figure 3.1 : Processing steps of ACF and PSD estimation from LDV data.

3.5.1 Pre-filtering

An appropriate filtering applied to the LDV flow velocity data prior to the ACF estimation eliminates the large-scale uncertainty in ACF and reduces the variability of the PSD estimation. The parameters of the filtering technique are chosen so that the mean velocity and large-scale periodicities are subtracted from the data with negligible influence on the ACF and thus on the PSD (Benedict et al., 2000). A symmetric filter (Nobach, 2000 and Sree et al., 1994) is used to calculate the local mean, μ_i , by using weighting factors w_i to reduce the influence of velocity bias by weighting technique, so that:

$$\mu_i = \frac{\sum_{j=i-M}^{i+M} U_j w_j}{\sum_{j=i-M}^{i+M} w_j} \quad (3.21)$$

The weighting factors may be chosen relying on several weighting techniques (Fuchs et al., 1994), however the transit time weighting of Hösel and Rodi (1977) is used depending on the recommendation of Nobach (2000) and the weighting factors are chosen as the transit times (τ_i) of the particles.

$$w_i = \tau_i \quad (3.22)$$

The pre-filtered velocity sample is calculated as follows:

$$u_i = U_i - \mu_i \quad (3.23)$$

3.5.2 Block splitting

The velocity data set is divided into a number of blocks prior to the reconstruction process. Using block splitting and increasing the number of blocks for a given LDV data set reduces the variances of the ACF and PSD estimates (Benedict et al., 2000). However, it should be born in mind that the block length should be chosen so that it would be large enough to resolve the correlation interval (integral time scale). The block length gives the maximum time lag of the ACF and the resolution of PSD.

3.5.3 ACF estimation

The refined reconstruction method for the ACF estimation consists of six steps as follows:

The reconstruction of the continuous velocity signal from the LDV data set by Sample and Hold,

1. the equidistant resampling,
2. the PSD estimation using the Fourier transform,
3. the ACF estimation using the inverse Fourier transform,
4. the limitation to a maximum time lag that is independent of the block length, and
5. the application of the refinement filter.

The Sample and Hold reconstruction (zero-order polynomial) is used to extract the continuous velocity signal from the LDV data set by using the below formula:

$$u'(t) = u_i \quad \text{for } t_i \leq t < t_{i+1} \text{ and } i = 1, \dots, N \quad (3.24)$$

where N is the total number of samples for a selected block. The equidistant resampling with time steps of $\Delta\tau$ is performed by

$$u'_i = u'(i\Delta\tau) \quad \text{for } i = 0, \dots, N_R - 1 \quad (3.25)$$

where N_R is the number of resamples within one block. Equation 3.5 leads to a data set that can be processed with FFT. The number of resamples should be a power of 2, since zero-padding is not recommended during FFT. The FFT,

$$U_j' = \sum_{i=0}^{N_R-1} u_i' e^{-2\pi i j i / N_R} \quad \text{for } j = 0, \dots, N_R - 1 \quad (3.26)$$

leads to the block PSD:

$$S_j' = \frac{\Delta\tau}{N_R} |U_j'|^2 \quad \text{for } j = 0, \dots, N_R-1 \quad (3.27)$$

and by using the inverse FFT;

$$X_k' = \frac{1}{N_R} \sum_{j=0}^{N_R-1} S_j' e^{-2\pi j k i / N_R} \quad \text{for } k = 0, \dots, N_R - 1 \quad (3.28)$$

to the block ACF:

$$R_k' = \frac{1}{\Delta\tau} X_k' \quad \text{for } k = 0, \dots, N_R - 1 \quad (3.29)$$

Only $K + 2 < N_R$ values of the block ACF are used in the refinement analysis, in order to reduce the variance of the final PSD estimate. The refinement filter for sample and hold reconstruction is given below:

$$R_k = \begin{cases} R_0' & \text{for } k = 0 \\ (2c + 1)R_k' - c(R_{k-1}' + R_{k+1}') & \text{for } k = 1, \dots, K \end{cases} \quad (3.30)$$

with the filter parameter c , defined as:

$$c = \frac{e^{-\dot{n}\Delta\tau}}{(1 - e^{-\dot{n}\Delta\tau})^2} \quad (3.31)$$

where \dot{n} is the mean particle rate.

The refined block ACF R_k is used in the subsequent steps.

3.5.4 ACF to PSD transform

A set of $K + 1$ values is obtained after the refinement process as the ACF estimation. The FFT algorithm requires a data set that extends from 0 to $2K - 1$ with symmetry at K . Therefore, an expansion of the ACF is necessary as below:

$$R_k = R_{2K-k} \quad \text{for } k = K, \dots, 2K - 1 \quad (3.32)$$

The FFT of this data set yields

$$X_j = \sum_{k=0}^{2K-1} R_k \cos\left(\frac{2\pi jk}{2K}\right) \quad \text{for } j = 0, \dots, 2K - 1 \quad (3.33)$$

and the power spectral density is

$$S_j = \Delta\tau X_j \quad \text{for } j = 0, \dots, 2K - 1 \quad (3.34)$$

3.5.5 Block Averaging

Each block of LDV data leads to an independent ACF and PSD estimate. The mean ACF, \bar{R} , and the mean PSD, \bar{S} , can be calculated as follows:

$$\bar{R} = \frac{1}{N_B} \sum_{i=1}^{N_B} R^{(i)} \quad (3.35)$$

$$\bar{S} = \frac{1}{N_B} \sum_{i=1}^{N_B} S^{(i)} \quad (3.36)$$

where the upper index (i) represents the estimate of the i -th block.

3.6 Transfer Functions

A transfer function is a mathematical representation, in terms of spatial or temporal frequency, of the relation between the input and output of linear time-invariant systems. Transfer functions are also referred to as the frequency response functions.

Linear time-invariant system behaviour can be described by linear integro-differential equations with constant coefficients. In general, the solution to such an equation may be written as a convolution integral:

$$y(t) = \int_{-\infty}^{\infty} h(u)x(t-u)du \quad (3.37)$$

where, $y(t)$ is the solution, $h(u)$ is the impulse response function and $x(t)$ is the forcing function. The solution is simplified by Fourier transforms and the transform of the solution becomes:

$$Y(f) = H(f)X(f) \quad (3.38)$$

where $Y(f)$, $H(f)$ and $X(f)$ are the Fourier transforms of $y(t)$, $h(t)$ and $x(t)$ respectively. Thus, the convolution in the time domain transforms to multiplication in the frequency domain.

The frequency response function (transfer function) of such a system may be calculated by spectral analysis if the input and corresponding output of the system are available. The transfer function can be defined as:

$$H(f) = \int_0^{\infty} h(u)e^{-j2\pi fu} du \quad (3.39)$$

The estimation of the transfer function is calculated as:

$$H(f) = \frac{PSD_{22}(f)}{PSD_{11}(f)} \quad (3.40)$$

where, $PSD_{22}(f)$ and $PSD_{11}(f)$ are the power spectral density functions of the output and input variables respectively. This can be achieved by dividing the two spectra at each frequency. In this study, the input variable is the surface roughness whilst the output is the turbulent fluctuations.

The estimation of the transfer function can also be performed by using cross spectral analysis (Jenkins and Watts, 1968). In this approach, the cross spectra between the input and the output variables are calculated and divided by the spectrum of the input variable.

In this study, the above mentioned first method which is also used by for e.g. Volino and Simon (2000) in transfer function calculation between the freestream and boundary layer turbulence was adopted rather than the one of Jenkins and Watts (1968).

3.7 Summary

The turbulence time (frequency) spectra and spatial (wave number) spectra can be calculated from the turbulent boundary layer data which may be collected using a two-dimensional LDV system for the two components of the measured velocity fluctuations. However, the calculation of the turbulence spectra from the LDV data requires a complex procedure due to the irregular sampling of the velocity. Moreover, the high sampling rate which is needed in order to resolve the dissipation range of the spectra, large and long-time sample populations that are needed for reducing the variance of the calculated spectra and resolving the large wavelength components should be taken into account in the design of the experiments. The above requirements constitute a difficult task in a boundary layer LDV measurement due to the very low data rates that will be encountered in the vicinity of the wall. A dedicated experimental campaign was carried out in Chapter 6 for the purpose of the turbulence spectra and transfer function calculations, and the associated turbulence time spectra are calculated by the refined sample and hold reconstruction technique as described earlier in this chapter.

4. SURFACE ROUGHNESS MEASUREMENT AND ANALYSIS

4.1 Introduction

The main objective of this chapter is to develop an understanding of the surface roughness concept along with the characterization, measurement and analysis of the irregularly rough surfaces.

In order to meet the above objective, the work carried out in this chapter is presented as follows: in Section 4.2, the definition of the surface roughness is given and the categorization of the surface roughness measurement devices is made in Section 4.3. Detailed information about the roughness measurement devices, which were used in this thesis, is also presented in the latter. Extensive summary of the surface roughness analysis procedures, the essential roughness parameters and the use of autocorrelation and power spectral density functions in roughness characterization are discussed in Sections 4.4 and 4.5, respectively.

4.2 Definition of Surface Roughness

Surface roughness can be defined as the deviation of a solid's actual topography from its nominal surface (Thomas, 1982). Although, usually the vertical deviations of the surface are the first thing to spring to mind about the characterization of surface roughness, it is actually a three-dimensional topography which should be considered and projected at two principle planes: one at a plane normal to the surface and other in the plane of the surface. The behaviour of the surface at planes normal to the surface is represented by the roughness amplitude parameters whereas the latter is characterized with the wavelength (or texture) parameters.

Within the context of machined surface definition, the deviations of machined surfaces are divided in three groups: *roughness*, *waviness* and *errors of form* depending upon the causes of the surface deviations. *Roughness* results from the manufacturing processing such as a tool mark or impression of polishing. *Waviness* is a longer wavelength defect caused by improper manufacture, e.g. caused by the

vibration between the surface being machined and the machining tool. *Errors of form* with very long wavelengths may be caused due to thermal distortion or rotating parts of the machine (Whitehouse, 2011). An example of roughness and waviness, superimposed on the nominal shape of a surface can be observed in Figure 4.1.

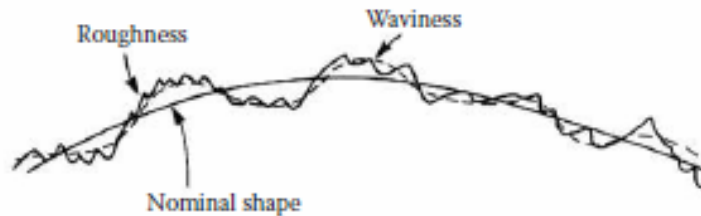


Figure 4.1 : Types of surface deviations (from Whitehouse, 2011).

Hull surface deviation is also defined in a similar way using the above described three regimes: roughness, waviness and error of form. Waviness and error of form are generally regarded together as structural roughness (Lackenby, 1962). For a hull with newly applied paint, Howell and Behrends (2006) propose a slightly different categorization. Accordingly, they define the longest wavelength defect as the structural roughness due to construction processes which is similar to form error. Their definition designate the second level of hull roughness being caused by the effect of the coating/paint application process (e.g. spray, roller) whilst the third level, namely micro-roughness is a function of the components and structure of the coating system.

The characterization of hull roughness has been prevalently relying on one roughness height parameter (Rt_{50}) measured with either British Maritime Technology (BMT) Hull Roughness Analyser or its predecessors (BSRA Wall Gauge) for the last 6 decades. The Rt_{50} parameter is defined as the maximum peak to lowest trough height for a given length of 50 mm along the hull. Conventionally, the ship hull is divided into ten sections longitudinally and usually 10 measurements are carried out at each section at the port, starboard and bottom sides. The average of a total of 100 readings is called the Average Hull Roughness (AHR) which is accepted as the roughness parameter for the characterization of ship hulls (ITTC, 1990).

4.3 Surface Roughness Measurement Devices

The roughness measurement devices can be investigated under two groups: *the stylus instruments* and *optical instruments*. The stylus instruments are contact type devices

which have mechanical probes called stylus. The stylus of various devices may have tips with different geometries such as a cone, pyramid or sphere as seen in Figure 4.2. The angle of the stylus tip defined by its geometry has an effect on the roughness measurements no matter how sharp the tip is, since it is not possible for the tip to fully penetrate into the valley or groove. Whitehouse (2011) states that this is a more crucial problem for fine surfaces with an average roughness height that is below 0.1 μm .

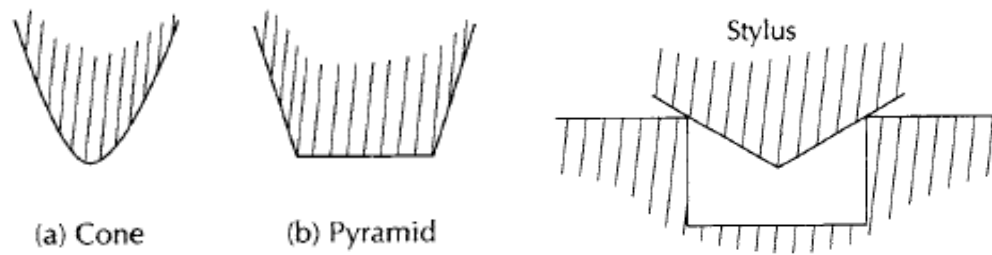


Figure 4.2 : The geometries of stylus and stylus geometry effect on roughness measurement (from Whitehouse, 2011).

The BMT hull roughness analyser (BMT-HRA), which is one of the devices used for the roughness measurements conducted in this study, is a stylus type instrument. The lowest valley to highest crest value is measured over 50 mm intervals (Rt_{50}). The instrument can measure an Rt_{50} value of up to 1999 μm with an accuracy of $\pm 15 \mu\text{m}$ or $\pm 5\%$, whichever is larger. The device prints out 12 Rt_{50} values when an approx. 750 mm distance on the surface is traversed. BMT-HRA is composed of two parts: the measurement head and the analyser box as seen in Figure 4.3. The measurement head is similar to a trolley with two wheels at the front and one at the rear. Connected to the front left wheel, there is an encoder that sends signal depending upon the rotation of the wheel for the measurement of the distance travelled. Accordingly, it is crucial that the wheels rotate rather than slipping on the surface during the measurement. There is also an arm for the user to hold the trolley and move it through the measurement direction. The trolley should ideally be driven with a constant velocity of 50 mm/s. Underneath the trolley, there is a skid that also houses the 1.56 mm diameter sphere steel stylus. The skid freely moves in the vertical direction and enables the removal of the large wavelength curvatures with a radius of 2.5 m and above. Moreover, it acts like a reference surface to the stylus so that the difference between the skid and the stylus is measured as the surface profile. Detailed information about the working principle of stylus instruments with skids can

be found in Whitehouse (2002). Recently, Newcastle University and BMT are working on an advanced version of this device which will operate as a non-contact instrument (with a laser probe) and transfer the whole measured surface profile to a portable computer that may be analysed in any software (Atlar et al., 2010 and 2012).

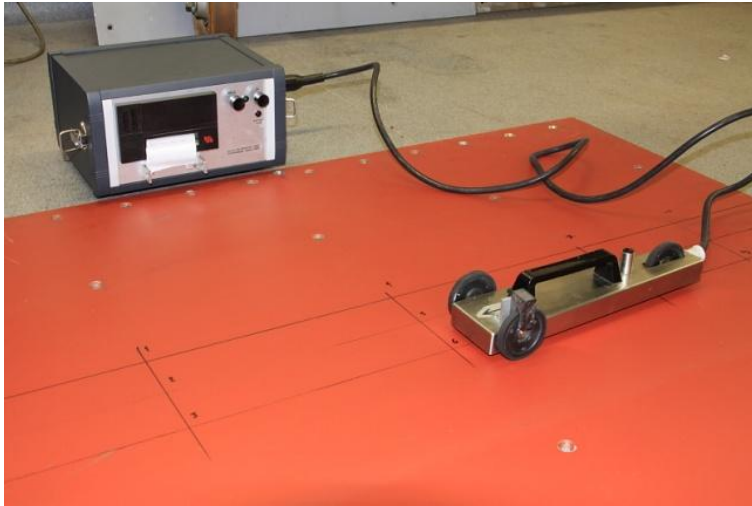


Figure 4.3 : The BMT hull roughness analyser.

The optical roughness measurement instruments rely on the several optical measurement techniques which are well documented in Thomas (1999) and Whitehouse (2002). When a light beam is incident on a surface, a part of its energy will be reflected depending upon the surface properties. The main idea behind the optical methods is based on the expected combined effect of the surface texture and wavelength of the incident beam on the physics of reflection (Thomas, 1999). Optical methods are divided into two between themselves as profiling and parametric techniques. Profiling techniques involve specular reflection whereas the latter are mainly associated with diffused reflection. The Omniscan Uniscan OSP100A laser profilometer is the second roughness measurement device used in this study. It is an optical high accuracy non-contact instrument that works by profiling techniques and utilises a laser displacement sensor. The OSP100A is capable of measuring surface topography in the range 10's of millimetres to sub-micrometers over areas up to 100mm x 75mm. The components of the OSP100A can be observed in Figure 4.4. The instrument is composed of a traversing unit which also houses the laser head and displacement sensor located on a rigid granite tray, a processor and a personal computer for data acquisition.



Figure 4.4 : The Omnican Uniscan OSP100A laser profilometer.

The relative advantages and disadvantages of the optical and stylus instruments are listed in Whitehouse (2002). The main advantage of using an optical instrument for the surface roughness measurement of fouling-release coated surfaces is that such instruments are non-contact and thus possible damage of these soft coatings is eliminated by avoiding the contact of stylus to the surface. Moreover, the Author's experience with the BMT-HRA on silicone based fouling-release coatings indicated that the stylus and skid of this device tend to stick on the surface and it was rather difficult to retain the continuous movement of the measurement head when the surface is dry. Similar behaviour was also observed while examining the use of the self-propelled stylus instrument Taylor Hobson's Surtronic 3+ on such surfaces which ended with the breakdown of the propulsion mechanism of the device. It is obvious that such behaviour of the stylus instrument may give damage to the surface as well as leading to questionable roughness measurement. It should also be noted here that the surfaces coated with the fouling-release coatings were slightly wetted with water prior to the roughness measurements with BMT-HRA in order to prevent the stuttering of the stylus.

4.4 Analysis of Surface Roughness and Roughness Parameters

The representation and interpretation of the surface roughness and associated parameters strongly depend on the length scales imposed by the roughness measurement device or selected by the user for the analysis. Whichever the case, there are four main length scales or wavelength cut-offs in roughness characterization. Three of them, which are associated with the long wavelength cut-off, are presented in Figure 4.5. *Traverse length* is the maximum length over which the probe of the measurement device travels across the surface and may vary from

one instrument to another. It is obvious that it will not possible to measure the wavelengths that are longer than the traverse length of the instrument. In some devices surface data is not collected over the entire traverse length; especially in self-propelled ones a part of the traversing length is needed for the mechanism to achieve constant speed. *The assessment length (or evaluation length)* is the length of data that is used in the analysis. It is usually shorter than the traverse length. On the other hand, *the sampling length (or cut-off length)* is the smallest distance over which the surface roughness parameters are assessed. The cut-off length selection can usually be made by the user prior to the analysis of the surface data. The selected cut-off length should include enough surface data within it to ensure reliable calculation of the roughness characteristics whilst precluding the waviness. The first typical cut-off length was established by the Taylor Hobson company as 0.8 mm which is also one of the ISO standards together with 0.08 mm, 0.25 mm, 2.5 mm and 8 mm (ISO, 1998). Whitehouse (2002) recommends that the evaluation length should better to include 5 sampling lengths for reliable statistics whilst according to ISO4288 it should compose of at least one cut-off length. ISO4288 also defines the recommended cut-off lengths for various expected roughness height or spatial parameters of the surfaces (Whitehouse, 2011).

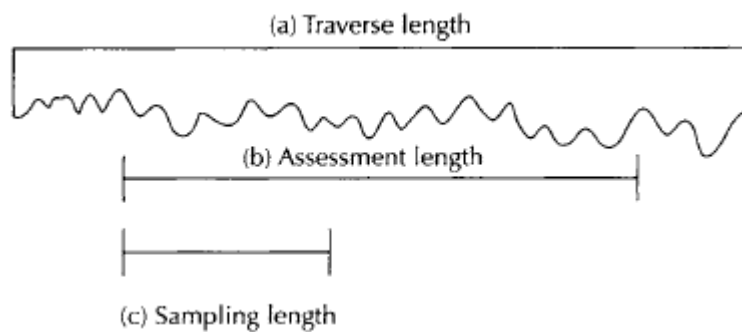


Figure 4.5 : The lengths used in surface characterization (from Whitehouse, 2002).

On the other hand, the fourth important length scale is *the sampling interval* which determine the short wavelength cut-off as it is not possible to observe the wavelengths smaller than the twice of the sampling interval according to the Nyquist theorem (Bendat and Piersol, 1998; Thomas, 1999).

It is important that the long and short wavelength cut-offs are specified together with the roughness characteristics since most of the roughness parameters show variation depending upon the cut-off lengths.

For the analysis of the raw surface profiles or areas, a filtering procedure is needed in order to specify the waviness and subtract it from the raw data to acquire the roughness. In Figure 4.6, a sample raw surface profile data, the waviness and the associated roughness profiles may be observed. The waviness is sometimes called as the mean line as in the figure. In some cases a levelling procedure may also be needed in order to correct the tilt in the raw profile as seen in Figure 4.7. The levelling line is considered as the reference line for the surface profile. The reference line may be calculated by using straight lines (as in the best-fit least-squares line in Figure 4.7), polynomial fitting or spline functions (Whitehouse, 2011).

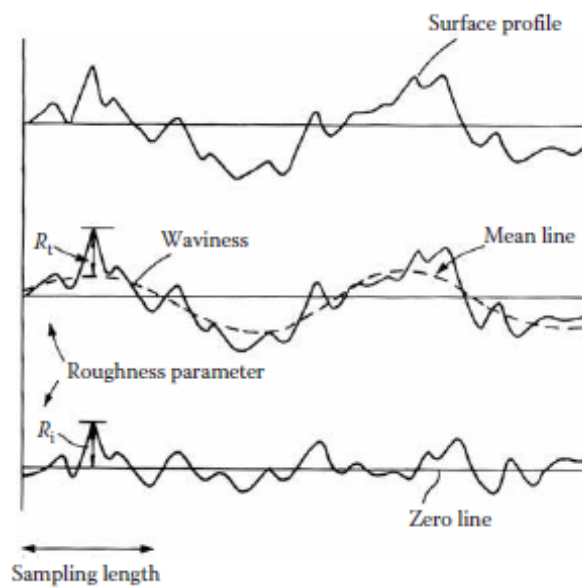


Figure 4.6 : The surface profile, waviness and roughness (from Whitehouse, 2011).

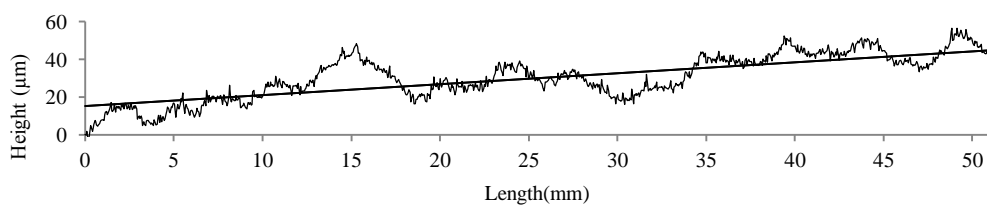


Figure 4.7 : Levelling of the raw surface profile (from Politis et al., 2011).

The filtering methods used in surface roughness analyses are well documented in the fundamental books about surface roughness such as Whitehouse (1994, 2002 and 2011) and Thomas (1999). High-pass filtering is needed in order to subtract the long wavelength (or low frequency) components from the surface profile. Both recursive (infinite impulse response- IIR) and non-recursive (finite impulse response- FIR)

filter types can be used for this purpose (Smith, 2003). Medhurst (1989) discusses the relative advantage and disadvantages of such filter types. Although Gaussian type high-pass filters are used as a standard (DIN4777, 1990) in roughness analysis, several other methods are also employed such as valley suppression filter (Mummery, 1990), polynomial fits (such as least-squares), moving-average boxcar method (Dey,1989; Medhurst, 1989; Candries, 2001), motif analysis (ISO12085, 1996; Fahl, 1982) and envelope filters (Thomas, 1999).

The roughness parameters are usually grouped into two as the profile and area parameters. They are basically the same parameters defined in 2-D and 3-D respectively. Three sub-groups exist being the amplitude parameters, spacing parameters and hybrid parameters for both the 2-D and 3-D roughness parameters. The definitions of only the profile parameters will be explained herein, however the reader may refer to Whitehouse (2011) for the formulations of the area parameters.

A total of five amplitude parameters were used in this study, being the average and root-mean-square roughness, the highest peak to lowest valley, and the skewness and kurtosis of the roughness height distribution. The average roughness height is denoted with Ra which is calculated as:

$$Ra = \frac{1}{n} \sum_{i=1}^n |z_i| \quad (4.1)$$

where n is the total number of surface height samples and z_i is the i^{th} sample. The root-mean-square roughness height Rq is given as:

$$Rq = \sqrt{\frac{1}{n} \sum_{i=1}^n z_i^2} \quad (4.2)$$

The Rt value is known as the largest peak to valley height within each cut-off length. The skewness (Sk) and kurtosis (Ku) are defined respectively as:

$$Sk = \frac{1}{n\sigma^3} \sum_{i=1}^n z_i^3 \quad (4.3)$$

$$Ku = \frac{1}{n\sigma^4} \sum_{i=1}^n z_i^4 \quad (4.4)$$

Three widely used spacing parameters are associated with the mean spacing of the roughness elements (Sm , S) and number of peaks per unit surface profile (De). Sm is defined as the mean spacing between profile peaks at the mean line, measured over the assessment length. Profile peak is defined as the highest part of the profile between an upwards and downwards crossing of the mean line. Accordingly,

$$Sm = \frac{1}{n-1} \sum_{i=1}^{n-1} S_i \quad (4.5)$$

where S_i is the mean spacing between the i^{th} and $(i+1)^{\text{th}}$ profile peak. Another parameter that relies on the mean spacing is S , which is the mean spacing between the local peaks. The selection of the local peaks is highly effective on this parameter. In this study the peaks that are larger than the $1/4^{\text{th}}$ of the Rt value is accepted as local peaks. The third parameter, De is the number of local peaks per unit length of the surface profile. The texture parameters about the autocorrelation and power spectral density functions are defined in the following section.

4.5 Autocorrelation and Power Spectral Density Functions for Surface Roughness

Womersley and Hopkins (1945) were the first to suggest the use of a correlogram in investigating the surface texture. However, at that time it was not possible to realize such a calculation and Peklenik (1967) became the first researcher to use the autocorrelation function and its Fourier transform, the power spectral density function for surface roughness analyses. For a surface profile the autocorrelation function is given as:

$$R(\tau) = \overline{z(x)z(x+\tau)} \quad (4.6)$$

where $z(x)$ defines the measured surface profile after the subtraction of the mean value and τ is the spacing lag in the measurement direction. The calculation of the autocorrelation function is explained with a sketch in Figure 4.8.

The autocorrelation function is generally used in its non-dimensional form, $\rho(\tau)$. The non-dimensionalization is done by $R(0)$ which is theoretically equal to the variance of the roughness height distribution. The correlation length is used as a roughness texture parameter. Although, the correlation length is statistically defined as the distance needed in spacing (or time) lag axis for the ACF to cross this axis, in surface roughness analyses it is the length over which ACF decays to some fraction of its maximum value, taken as the tenth, $1/e$ or 0.5 . In this study the 0.5 value is used for the roughness correlation length $\tau_{0.5}$.

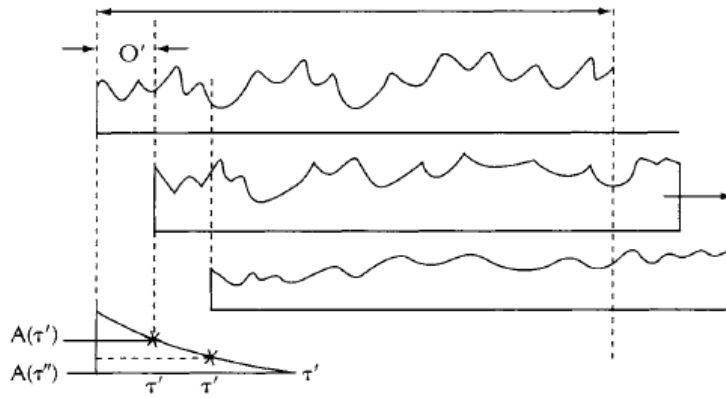


Figure 4.8 : Calculation of the autocorrelation function (from Whitehouse, 2011).

The ACF and the power spectral density function (PSD) are Fourier couples:

$$R(\tau) = \int_{-\infty}^{\infty} \exp(i\omega\tau)\Psi(\omega)d\omega$$

$$\Psi(\omega) = \frac{1}{2\pi} \int_{-\infty}^{\infty} \exp(-i\omega\tau)R(\tau)d\tau$$
(4.7)

The calculation of the PSD is rather straightforward via Fourier transform in surface roughness analyses since the surface profile is measured at equidistant spacings. Certain moments of the PSD are also used as roughness parameters. The zeroth moment gives the variance of the roughness height distribution whereas the second and fourth moments give the variances of the slope and curvature distributions respectively. The moments of the PSD are calculated as:

$$m_n = \int_{-\infty}^{\infty} \omega^n \Psi(\omega)d\omega$$
(4.8)

The non-dimensional bandwidth parameter (α) is calculated depending upon these three moments of the PSD:

$$\alpha = \frac{m_0 m_4}{m_2^2} \quad (4.9)$$

4.6 Summary

Since the surface roughness is the most critical input to the turbulence phenomenon on rough wall boundaries, an insight towards the definition, measurement, characterization and analysis of surface roughness was provided in this chapter based mainly upon the basic textbooks.

As well as a brief review of the relevant roughness measurement instruments, the definitions of the roughness parameters that are widely used in the literature and in this thesis for the roughness characterization of the tested surfaces are given in details.

The selection of an appropriate instrument for the roughness measurement on soft coating surfaces requires particular attention and hence the use of optical instruments. An important keynote may be about the long and short wavelength cut-off lengths that are used in the analysis of the surface roughness or forced by the measurement devices since these wavelengths have strong effects on the revealed roughness characteristics. It is of vital importance that the calculated roughness characteristics should be considered together with these cut-off lengths. Thus, the roughness properties of different surfaces can be comparable provided that they are sampled and analysed with the same cut-off lengths.

5. TURBULENT BOUNDARY LAYER MEASUREMENTS ON FLAT PLATES WITH ZERO-PRESSURE GRADIENT

5.1 Introduction

In order to capture a basic understanding towards the relationship of the roughness characteristics with the turbulent boundary layers developing on transitionally rough surfaces, a detailed experimental research was carried out with four recently developed nanostructured antifouling coated flat plate surfaces along with three reference surfaces. One of the reference surfaces was coated with a state-of-the-art commercially in use foul-release (FR) coating scheme whilst the other two consisted of a smooth and a fully-rough reference. The experimental campaign covered carefully conducted turbulent boundary layer tests on these surfaces fitted to a zero-pressure-gradient flat test bed using a two-dimensional Laser Doppler Velocimetry (LDV) system as well as conducting the roughness measurements of the tested surfaces. The roughness parameters and spectra, mean velocity profiles, boundary layer parameters, local skin friction drag, roughness functions and Reynolds stresses were presented and discussed.

This chapter presents the experimental details, analyses procedures and results of the above mentioned flat plate boundary layer experiments which were carried out in the Emerson Cavitation Tunnel of Newcastle University as well as the related roughness measurements. Most of the conducted tests were also part of the EU FP6 AMBIO Project where the Author participated as a visiting researcher to collect data for her PhD study. This experimental campaign was carried out during the year 2009.

This chapter begins with the presentation of the specifications of Emerson Cavitation Tunnel in Section 5.2 which is followed by the details of the experimental set-up and test plates in Section 5.3. Presented in Section 5.4 are the specifications of the LDV system that was used in the boundary layer experiments. The details and results of the roughness measurements of the test specimens are explained and discussed in Section 5.5. Given in Section 5.6 and Section 5.7 are the inflow measurements and

uncertainty analysis, respectively. The data analysis methods are explained in Section 5.8. The results of the boundary layer experiments are presented in detail and discussed with comparisons with the relevant data published in the open literature in Section 5.9. An overall summary of this chapter is given in Section 5.10 along with the main conclusions of the boundary layer experiments.

5.2 Emerson Cavitation Tunnel

The experiments were conducted in the Emerson Cavitation Tunnel (ECT) of Newcastle University in Newcastle upon Tyne, UK. The ECT is a closed circuit depressurized tunnel, which has a measuring section of 3.10 m x 1.22 m x 0.81 m and a contraction ratio of 4.271:1. The tunnel contains 60 tonnes of water which is circulated using a 400 HP DC motor driving a 1.4 m diameter and 4-bladed impeller. The maximum attainable water speed in the measuring section is 8 m/s. The large observation windows on the side walls and floor of the measuring section of this facility provide a good laser and camera access and make it an ideal facility for measuring flow around various test bodies. Figure 5.1 shows a schematic of the cavitation tunnel circuit. The longitudinal and transverse turbulence intensity of the tunnel flow between 1 m/s and 6 m/s flow speeds are about 2.1% - 2.3% and 2.1% - 3.1%, respectively. The full specification of ECT including the details of the recent modernization can be found in Atlar (2011).

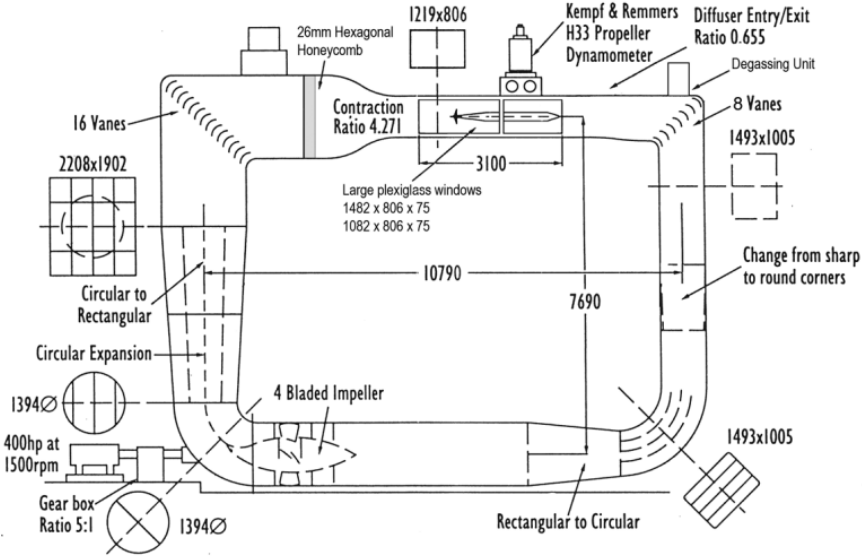


Figure 5.1 : Schematic of the Emerson Cavitation Tunnel.

5.3 Experimental Set-up

In order to have a sufficient length for the development of the turbulent boundary layer, a specially constructed flat base plate made of mild steel as a test bed with a total length of 2.880 m was used in the flat plate boundary layer experiments. The plate had a 0.8 m height and 12 mm thickness and an adjustable angle of attack so that it was possible to obtain a zero pressure gradient flow. An interchangeable test section of 1.0 m was adopted at the tail end of this large plate. Tapered, 52 mm long leading and trailing edges were used at the beginning and end of the plate for preventing the deterioration of the flow. A 3 mm thick 120 grid sanded mild steel plate which was 1776 mm in length was used to cover the front part of the base plate. This thinner plate and the test specimens were mounted on the base plate by using countersunk screws around the edges. Extra screws were used both on the front thin plate (14 screws) and test specimen (10 screws) 250 mm below and above the centreline (CL) for reducing the vibration at higher speeds.

Following the leading edge, 300 mm long sand paper (40 grid) was used in order to artificially thicken the boundary layer as well as accelerating the transition to turbulence. This grade of sand paper was selected by relying on the various works on turbulent boundary layer by several researchers (e.g. Schultz and Swain 1998, Flack et al. 2007, Candries and Atlar 2005). The details of the test plate and the test positions can be seen in Figure 5.2.

The test plate was arranged in the test section of the tunnel so that a distance of 700 mm was achieved between the measurement wall and the tunnel window in Y direction. In the streamwise direction(x), the leading edge of the test plate was beginning from the beginning of the test section. The plate was held in place by using 6 corner brackets at the back which supported the plate in pairs (bottom and top). The brackets were adjustable until they were fixed firmly so that it was possible to obtain a zero-pressure gradient through the plate. A photograph of the base plate before and after being arranged into the tunnel with one of the test specimens mounted on it may be seen in Figure 5.3 and Figure 5.4, respectively.

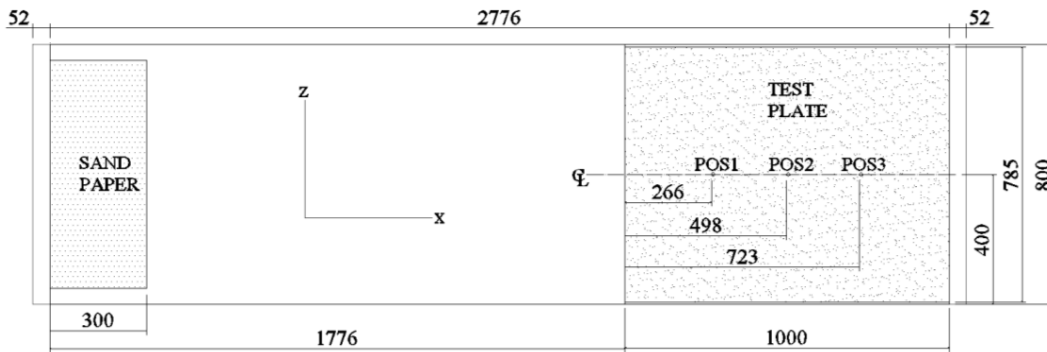


Figure 5.2 : Testing bed plate sketch showing the measurement positions and dimensions of the test plate in mm.

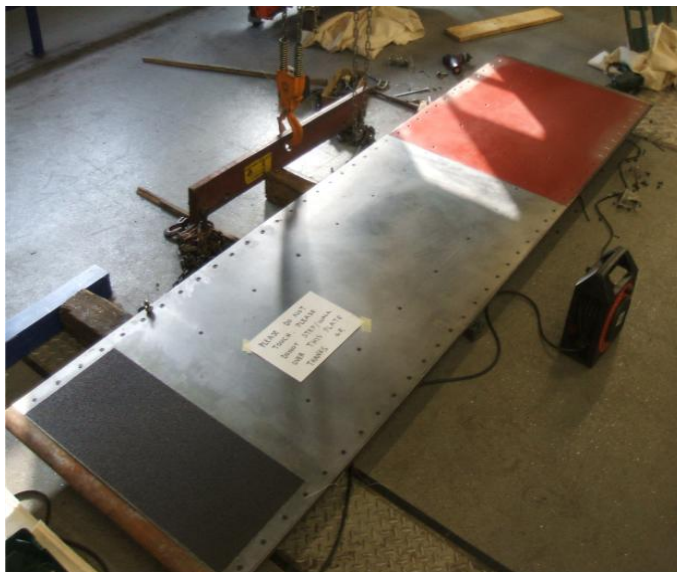


Figure 5.3 : Test plate before being adjusted into the tunnel with FR specimen (red coloured) fitted on it.



Figure 5.4 : The test plate mounted in the tunnel test section, photograph taken just after the changing of the test specimen (pink coloured).

The boundary layer tests were carried out for three reference plates and four selected nanostructured (or nanopatterned) coatings developed in the AMBIO project. The reference plates consisted of a mild steel sanded with 120 grid sandpaper (STEEL), a commercially in use and state-of-the-art foul-release coating (FR), and a steel surface covered with 40 grid sand paper (SAND40). The four coatings from the AMBIO project were selected regarding their performances in terms of their antifouling characteristics. These coatings were namely CNT, FCP1, FCP2 and FCP3. FCP1 and FCP2 are basically condensation-cured silicone containing 1% and 4% fluorocopolymers, respectively. These products include amphiphilic, fluorinated and PEGylated copolymer for their surface nanopatterning in creating a complex topology that fouling organisms find it difficult to adhere to. Further details of these coatings can be found in Martinelli et al. (2008, 2009a, 2009b) and Marabotti et al. (2009). FCP3 is a condensation-cured silicone reference coating with no fluoropolymer. CNT is another condensation-cured silicone but containing 0.1% carbon-nanotubes (CNT). Controlled nanoscale roughness of this novel nanocomposite coating incorporates polysiloxane and small amounts of multi-wall carbon nanotubes. The coating matrix therefore displays strong affinity between the polysiloxane and CNT which changes the dynamics of surface reorganisation of PDMS chain underwater resulting in a characteristic rugosity that enhances the fouling release. Although CNT's are recognised to be toxic, the matrix does not release CNT which is a significant feature in relation to any ecotoxicological issues associated with CNTs. Further details of these coatings can be found in Beigbeder et al. (2008a, 2008b, 2009, and 2010).

The photographs of the test specimens that were coated with different antifouling paints along with the smooth reference STEEL specimen and the fully rough reference sand roughness specimen (SAND40) may be seen in Figure 5.5. All of the test specimens were 1000 mm in length and 785 mm in width. One layer of anticorrosive and one layer of tie coat were applied on 120 grid sanded steel surfaces prior to the paint application in the preparation of the specimens. In Figure 5.6, a photograph that was taken during the drying period of the test specimens is observed.

All of the measurements were done at the middle of the test plate, which corresponds to 400 mm from the bottom tunnel window, and at three different streamwise positions. Position 1 (POS1) was selected at a distance of 266 mm from the

beginning of the test specimen which led to a distance of 2042 mm from the leading edge.

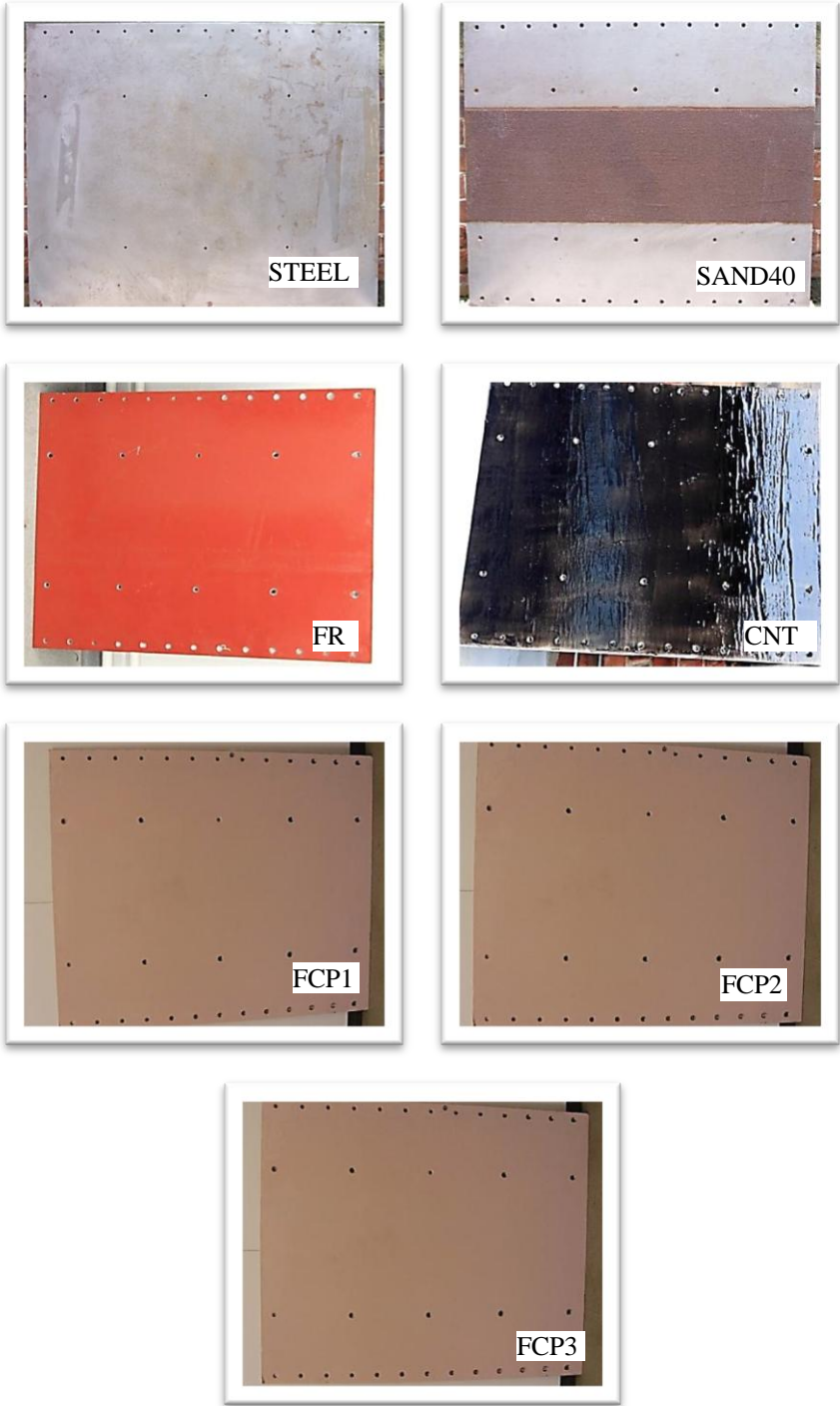


Figure 5.5 : The test specimens

Position 2 (POS2) was located at 498 mm from the beginning of the test specimen and 2274 mm from the leading edge. The distance between the position 3 (POS3) and the leading edge was 2499 mm. The location of these three positions may also be observed from Figure 5.2. The measurements were carried out for three freestream

velocities; 1 m/s, 2 m/s and 3 m/s, so that it was possible to cover a range of Reynolds numbers for acquiring fully turbulent boundary layer flow. Accordingly, the length based local Reynolds number (R_{ex}) varied between 2.04×10^6 and 7.53×10^6 during the tests. Velocity- time data were collected for 170 points in the boundary layer up to a distance of $y = 59.24$ mm from the wall. In order to measure the free-stream velocity for each case, measurements were performed at one more point outside the boundary layer, at $y = 200$ mm.

The combination of the test surfaces, positions and freestream velocities were used for describing the test cases by using the abbreviation of the test surface and position and velocity in order. For example, a measurement for STEEL surface at position 1 with 2 m/s freestream velocity is shortly named as STEEL_POS1_2.

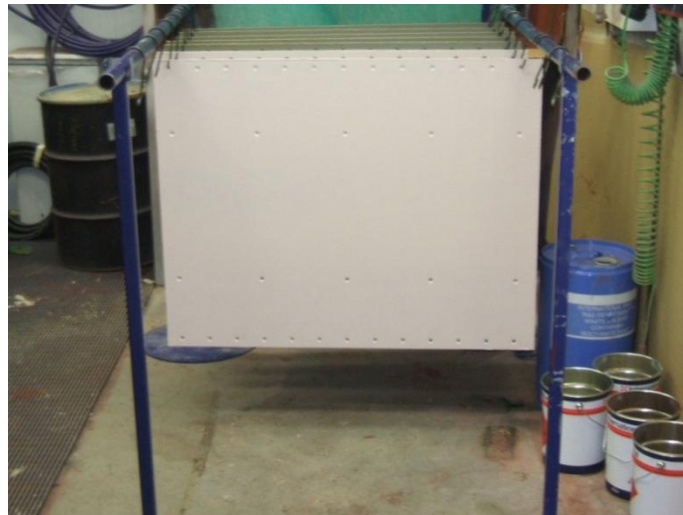


Figure 5.6 : Test specimens drying after coating application.

5.4 LDV System

Two-dimensional DANTEC Laser Doppler Velocimetry (LDV) measurement system was used for the measurement of the velocity-time data during the boundary layer experiments. The LDV system consists of a laser light source (Spectra Physics), a beam separator, fibre-optic couplers, a multi-colour receiver, a signal processor, a fibre-optic probe, a chiller, traverse controller and a three-axis traverse (Lightweight) which are controlled by a high performance personal computer by the aid of a dedicated software, namely BSA Flow Software 4.11. Figure 5.7 and 5.8 show overviews of the LDV set-up and the ECT test section during the tests. In Figure 5.8, the multi-colour receiver and the signal processor which are located on the top tray

of a small table can be observed at the left corner of the photograph whilst the traverse controller is located at the lower tray of the same table. In Figure 5.9, a closer look of the beam separator and the laser light source is presented.

The laser beam is separated into two green ($\lambda = 514.5 \text{ nm}$) and two blue ($\lambda = 488 \text{ nm}$) laser beams by the DANTEC beam separator. 40 MHz Bragg cell removes the directional ambiguity. The system includes a 60 mm probe which can be used with a beam expander by the help of an adaptor. The present experiments were conducted with the beam expander which had a ratio of 1.98 and a 500 mm focal length lens so that it was possible to make the probe volume as small as possible within the limitations of the experimental set-up. The probe was tilted with an angle of 7° so that it was possible to approach to the wall as desired without one of the beams hitting the wall. Correction needed due to this tilt angle was performed in the BSA flow Software. A photograph of the tilted probe with the beam expander mounted on it and the traversing mechanism may be seen in Figure 5.10.

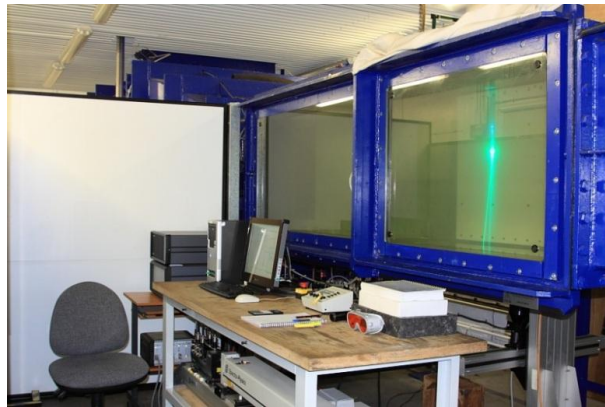


Figure 5.7 : ECT test section and 2D LDV set-up during the tests of FCP1 coated surface.



Figure 5.8 : The components of the 2D LDV system

Silver coated glass spheres with a mean particle size of 10 μm , provided by Potters Industries Inc., were used as a seeding material (Figure 5.11). About 3 tea spoonful of seeding were added to the tunnel water every second day (After changing the test specimen).

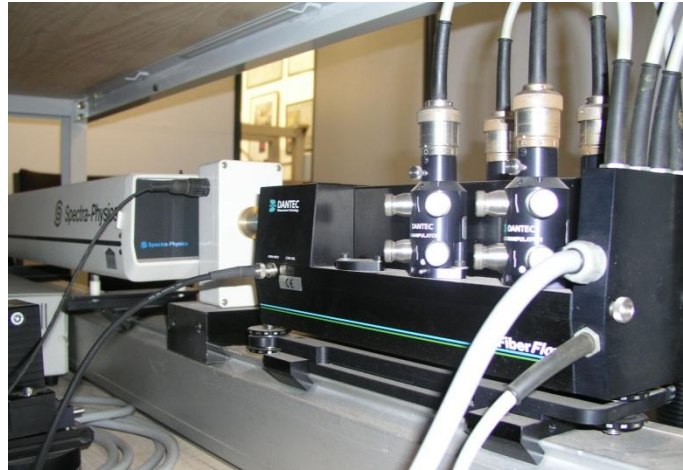


Figure 5.9 : The beam separator (located at the front right) and the laser light source

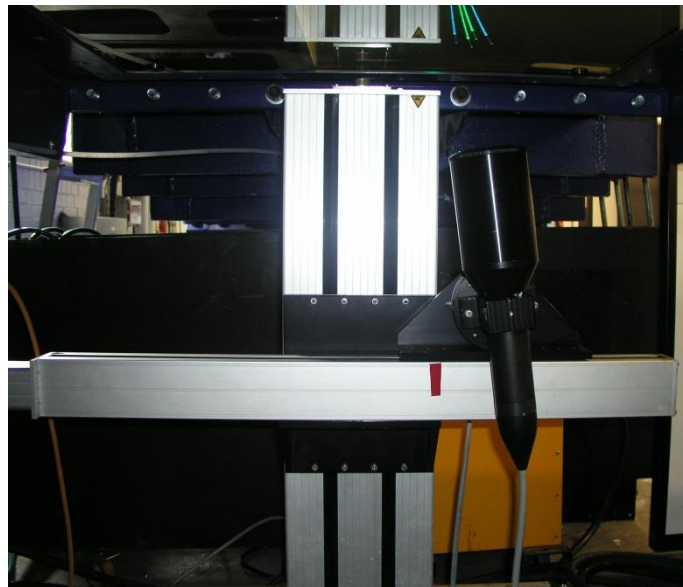


Figure 5.10 : 60 mm probe tilted by 7° with the beam expander and 500 mm focus length lens

Velocity measurements were conducted in the backscatter mode. The beam diameter was 1.35 mm, the beam spacing was 38 mm and the beam half angle was 4.303 degrees both for green and blue beams. The probe volumes were 0.1229 mm for dx and 0.1225 mm for dy for green beams whereas these values were 0.1166 mm and 0.1162 mm for the blue beams, respectively. The number of fringes was 35 for both beams with a fringe spacing of 3.429 μm and 3.252 μm for green and blue beams, respectively.

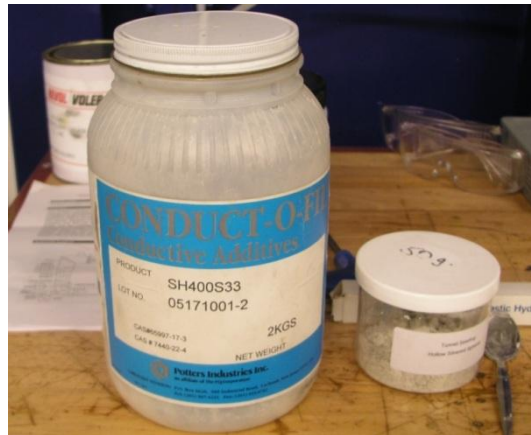


Figure 5.11 : The seeding material

Velocity-time data were collected for 30 seconds or until achieving 10000 samples, whichever came first, for each velocity channel and measurement location in coincidence mode. The validated data rate had a non-monotonous character depending on the location being measured through the boundary layer, which varied in the range of approximately 10 Hz to 0.6 KHz with a high validation.

5.5 Surface Roughness Characterization of the Test Plates

The surface characteristics of the tested surfaces were measured by using a non-contact optical and a contact stylus type roughness measurement device which were the Uniscan OSP 100 Laser Profilometer and the BMT Hull Roughness Analyser (BMT-HRA), respectively.

The BMT-HRA which has been accepted as a standard instrument for the measurement of hull roughness can be observed in Figure 5.12. This device (in its standard form) is only capable of measuring the R_{t50} parameter. The trolley part of the device (seen at the right hand side in Figure 5.12) is operated by hand, and thus it can be said that the effect of the operator is inevitable while using the device. A traversing length of more than at least 600 mm is needed for roughness measurement with BMT-HRA. The device calculates and prints out 12 R_{t50} values for a 600 mm assessment length.

The measurements with the BMT-HRA device were performed on the large actual flat plate specimens. The data were collected along 3 different lines in the longitudinal direction from upstream to downstream for each test specimen. One of the data collection lines was located at the vertical centreline of the plate whilst the

other two lines were selected at 0.05 m above and below the centreline as seen in Figure 5.13. 7 runs of measurement were carried out on each of the lines. Accordingly, it was possible to measure a total of 252 Rt_{50} values for each test specimen. Great care was taken during the measurements in order to minimize the effect of the operator. For example the trolley was run with an almost constant speed and in order to achieve this, the time needed for running the trolley on a 750 mm length was calculated before the measurements by using the recommended average trolley speed of the designer and it was kept constant in each measurement. The surfaces coated with silicone based coatings were slightly wetted with water prior to the measurements in order to prevent the sticking of the ball head of the device and the scratching of the surface.



Figure 5.12 : BMT Hull Roughness Analyser.

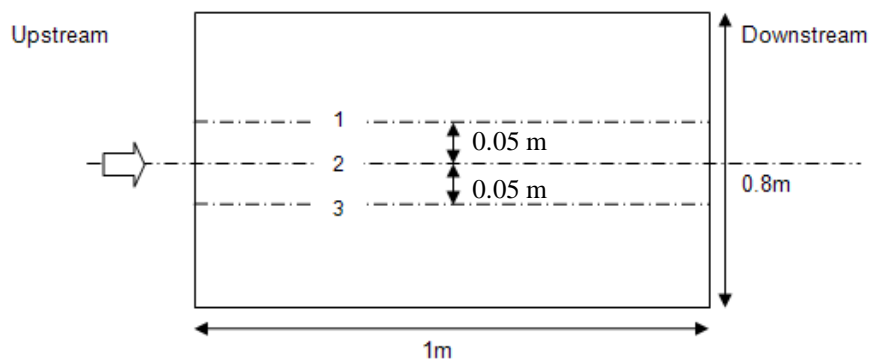


Figure 5.13 : The locations of the three data-collection lines on the actual test specimens (from Ünal et al., 2010 report).

The averages of the measured Rt_{50} values are presented in Table 5.1 for each test specimen. It can be said that the smooth reference STEEL surface was rather smoother than the other test specimens, as expected. FCP2 and FCP3 coated test plates had very similar Rt_{50} values which were also the lowest ones between the coated surfaces. FCP1 coated test plate had an almost double average Rt_{50} value

compared to the FCP2 and FCP3 coated ones. It was followed by the FR coated surface with a 44.87 μm average Rt_{50} value. CNT coated surface appeared to be the roughest one along the coated test specimens. The measured average Rt_{50} value of the SAND40 surface can be said to agree quite well with the one given by the Federation of European Producers of Abrasives (FEPA) which is 425 μm for a standard grid 40 sandpaper, if the relation given by Canham (1975) is considered.

Table 5.1 : Rt_{50} parameter of the test specimens, from BMT-HRA

Test Specimens	STEEL	FR	FCP1	FCP2	FCP3	SAND40	CNT
Rt_{50}	8.54	44.87	26.38	13.06	13.71	615.30	54.32

According to Canham (1975) the average height of the sand grains can be calculated as below, by using the average hull roughness (AHR) value:

$$k_s = 4.65(AHR)^{0.7} \quad (5.1)$$

The k_s value, which is known to be the equivalent sand roughness, is calculated as 416.7 μm from the above equation for the SAND40 surface.

The other device used for the roughness characterization was the Uniscan OSP100 laser profilometer which is a modular instrument for non-contact optical 3-dimensional surface roughness measurement. A photograph of the OSP100 is presented in Figure 5.14. The instrument consists of a rigid granite tray, a traversing unit with a laser probe located on the tray with four adjustable legs, a processor and a personal computer for data acquisition and processing. The tray size and the distance between the legs restrict the size of the surface to be measured. This kind of laser profilometer is only suitable for scanning flat surfaces in the laboratory environment. Basic difference between the BMT-HRA and Uniscan OSP100 is that the latter is a non-contact and non-portable device. Such a non-contact instrument has a great advantage since there is not any contact to the surface and no harm (e.g. scratching) is done to the surface being measured. This property gains even more importance for the roughness measurement of surfaces coated with silicone based antifouling where stylus tips often scratch the coatings and skids tend to stick.



Figure 5.14 : Uniscan OSP100 laser profilometer.

Sample plates of all of the test specimens, with a size of 300 mm by 150 mm, were prepared alongside the large flat plates for the roughness measurements with the laser profilometer due to the tray size limitations of this device. Roughness measurements of the prepared samples were carried out on 60 mm by 60 mm areas with a spatial resolution of 50 μm with the use of the OSP100 laser profilometer. In Figure 5.15 and 5.16 the roughness topographies of the tested reference surfaces and surfaces coated with nanostructured antifouling are presented, respectively.

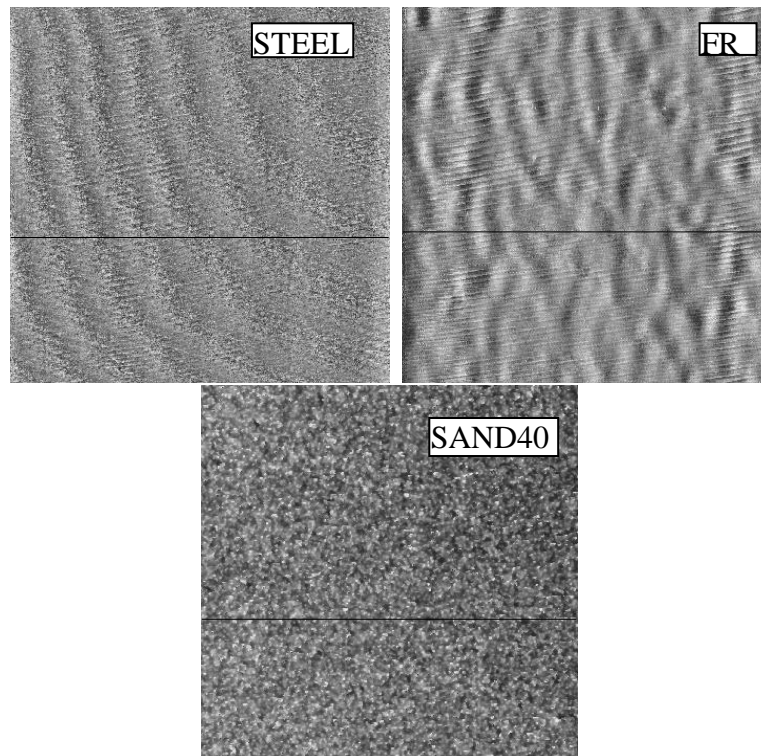


Figure 5.15 : Roughness topographies of the tested reference surfaces.

A data matrix of 1201 by 1201 was acquired meaning 1201 profiles of 60 mm length were measured. Two line averages were used in the measurements for each profile. The spatial resolution was chosen by taking the size of the laser beam, the studies in the literature (e.g. Candries 2001, Medhurst 1990) and the sampling resolution of BMT-HRA into consideration. The laser beam of the instrument's probe had a diameter of approx. 20 μm and using a lower sampling rate than this would lead to oversampling. The spatial sampling resolution of BMT-HRA was also 50 μm . The gathered data were saved in ".txt" format and analysed with a separate MATLAB code. 50 mm assessment length was used for the analysis of the data. A noise reduction procedure according to the Chauvenet criteria was applied to the raw data and the same procedure was repeated after the tilt correction of the raw profiles. The noise reduction winnowed out the rare anomalies in the profiles which are capable of increasing the extreme height parameters (e.g. Rt) unrealistically. In Figure 5.17 a sample roughness profile is given before and after the noise reduction as an example. The blue peaks are the ones rejected depending upon the Chauvenet criteria and red profile is the one that is used for further analysis.

For the filtering of the roughness data, which is needed for separating the waviness from the actual roughness, a low-pass moving average filter was used as was described in Dey (1989), Medhurst (1989), Bryne (1980) and Candries (2001). Accordingly the width of the filter window was set to $0.8L_c$, L_c being the cut-off length and number of ordinates over the cut-off length was calculated based upon this criteria. Three different cut-off lengths were used in the analysis: 2.5 mm, 5 mm and 8 mm. The numbers of ordinates for the selected cut-off lengths were 41, 81 and 129, respectively. It should be noted here that 2.5 mm and 8 mm are two of the standard cut-off lengths determined by the International Organization for Standardization (ISO).

The effect of the cut-off length on the relativistic waviness concept and the change in the resulting roughness profiles may be observed in Figure 5.18. As the cut-off length gets smaller the waviness tends to follow the raw profile more closely, meaning the smaller wavelengths (e.g. bigger than 2 mm for 2.5 mm cut-off length) are also considered as waviness. There is no doubt about the effect of the cut-off length on the calculated roughness parameters. Especially the height parameters are sensitive to the long wavelength cut-off (Thomas, 1999).

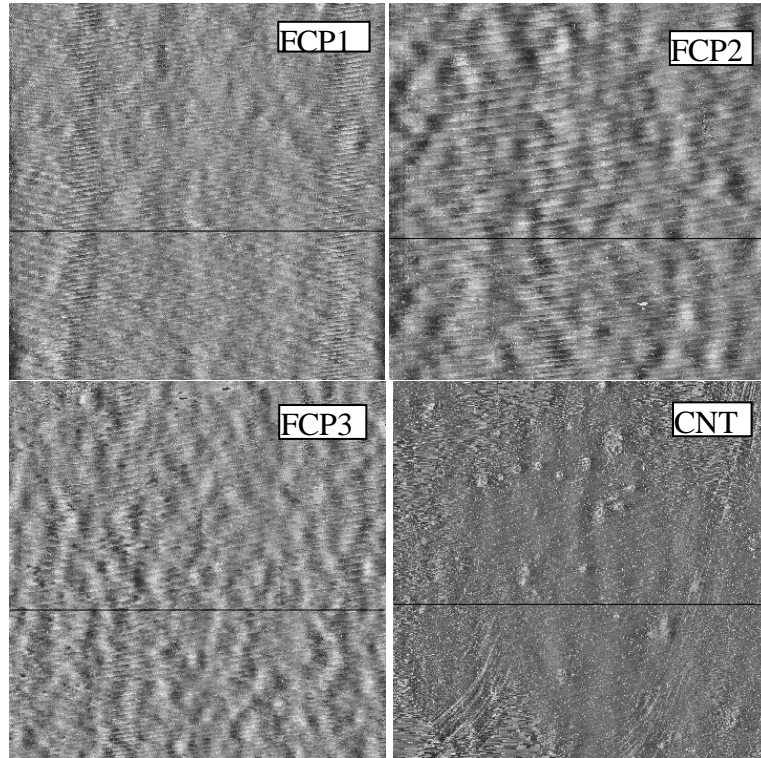


Figure 5.16 : Roughness topographies of the tested surfaces coated with nanostructured antifoulings.

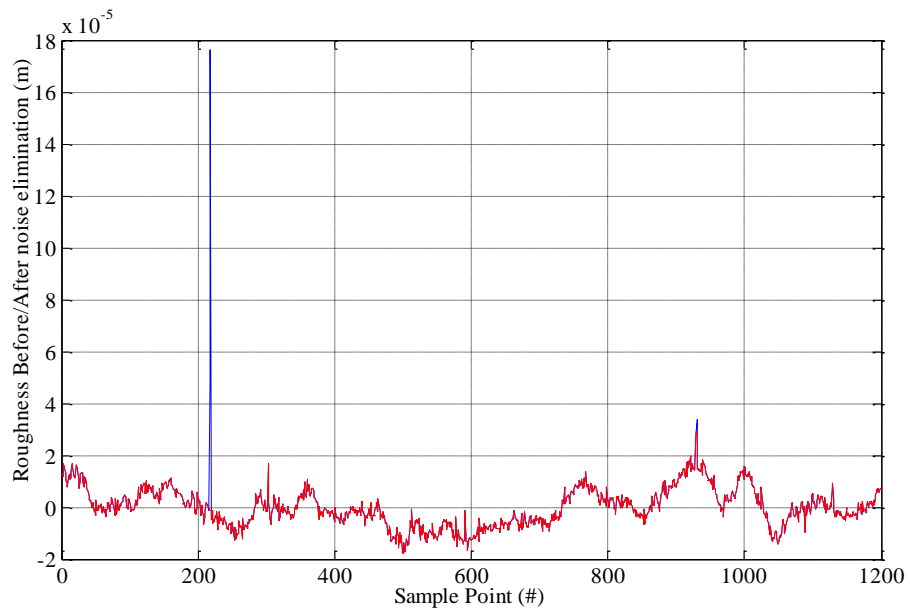


Figure 5.17 : An example to noise reduction results.

The histograms of the measured profiles are also calculated in the MATLAB code. In Figure 5.19 and Figure 5.20, representative roughness histograms are presented for the reference surfaces and the surfaces coated with the nanostructured antifouling paints, respectively. As seen from Figure 5.19, the smooth reference STEEL surface has a rather broad band roughness height distribution changing between almost ± 14

μm . The height distribution of the STEEL sample seems to be almost symmetric around the meanline. The histograms of the FR coated sample and the samples coated with fluorinated co-polymers (FCP1, FCP2 and FCP3) are rather similar with a narrower band distribution compared to that of the STEEL, with changing roughness heights between approx. ± 7 to $\pm 9 \mu\text{m}$. SAND40 sample plate has a rather different roughness height distribution compared to the others, with two humps, and extending to a much broader band ranging between about $-300 \mu\text{m}$ and $400 \mu\text{m}$.

CNT coated sample presents a roughness histogram with a rather sharp peak with roughness height values spreading in a wide range of approx. $\pm 50 \mu\text{m}$. The symmetry and the peak sharpness of the height distributions may be more precisely evaluated by the investigation of the skewness and kurtosis parameters which are presented in Table 5.2 along with the other roughness parameters.

The roughness parameters, presented in Table 5.2, were calculated in the MATLAB code after the filtering procedure with various cut-off lengths. The definitions of the calculated roughness parameters were given in Chapter 4.

If the presented roughness amplitude parameters (R_t , R_a , R_q) are observed, it is seen that the SAND40 surface is much more rougher than the others, as expected. The roughest coated surface, on the other hand, is the CNT coated one which displays rather higher amplitude parameters compared to the other coated surfaces. The STEEL surface can be considered to be rougher than the surfaces coated with FR and FCPs by looking at the results of the 2.5 mm cut-off length. However, this statement loses its validity due to the higher amplitude parameters of FCP2 and FCP3 coated surfaces as the cut-off length increases. FR and FCP1 coated flat plate samples consistently appear to be smoother than the STEEL sample according to all cut-off length results. Even so, it can be generally said that the roughness amplitude parameters of the STEEL, FR and FCPs are coherently in the same magnitude for all the considered cut-offs.

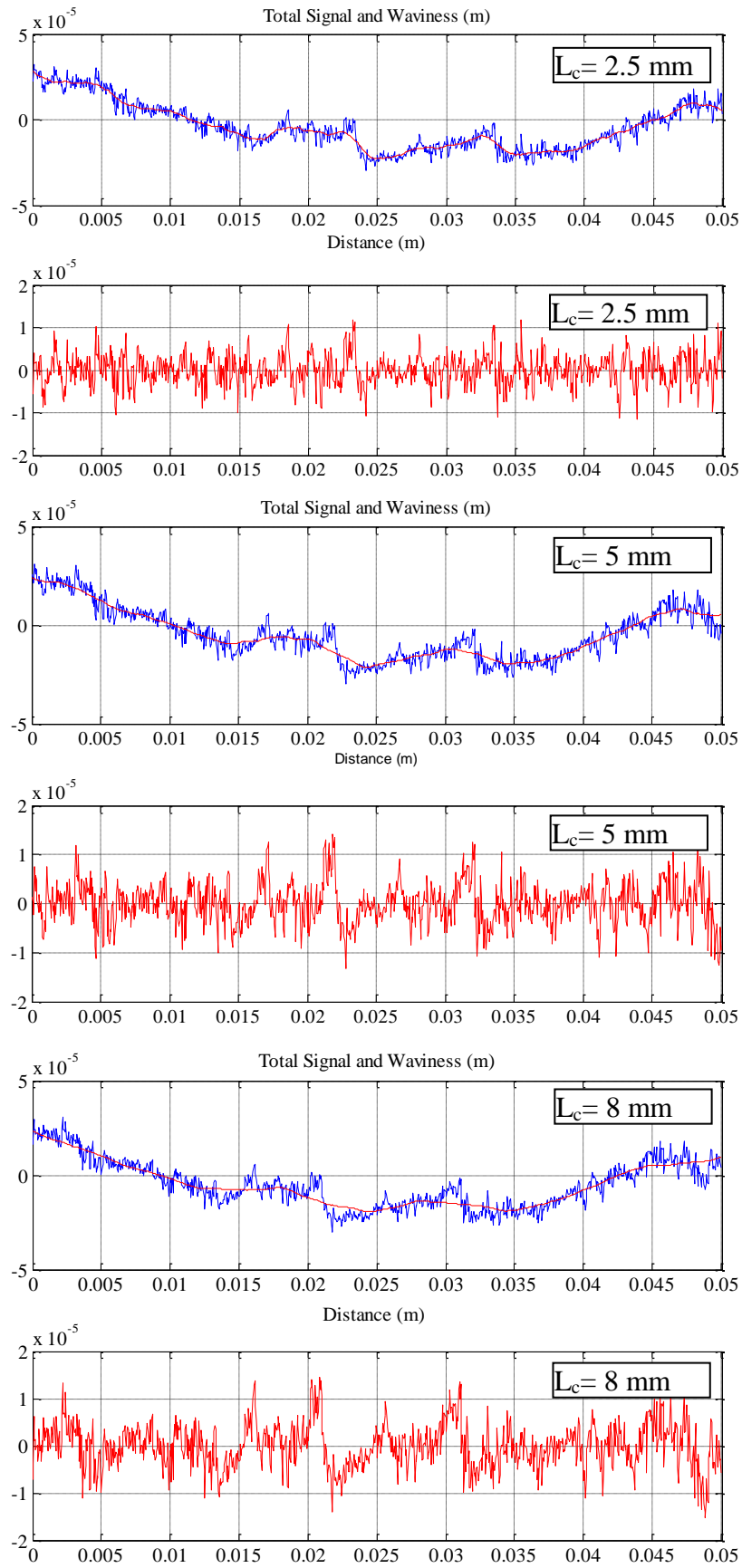


Figure 5.18 : Sample raw profiles (blue) and waviness (red on blue) and roughness profiles (red) for the same profile for various cut-off lengths.

The skewness parameter (Sk) is an indicative of the asymmetry of the roughness height probability density function (PDF). It is observed that the skewness values of the STEEL and the FCP3 coated sample plates are very close to zero, implying that the roughness height PDFs are very close to being evenly distributed around the mean. All of the other measured sample flat plates have positive skewness, with CNT and SAND40 surfaces having rather higher values (above 0.5) compared to the ones of others. A positive skewness value indicates that the tail of the PDF on the right side is longer than the left side and the bulk of the values lie to the left of the mean value.

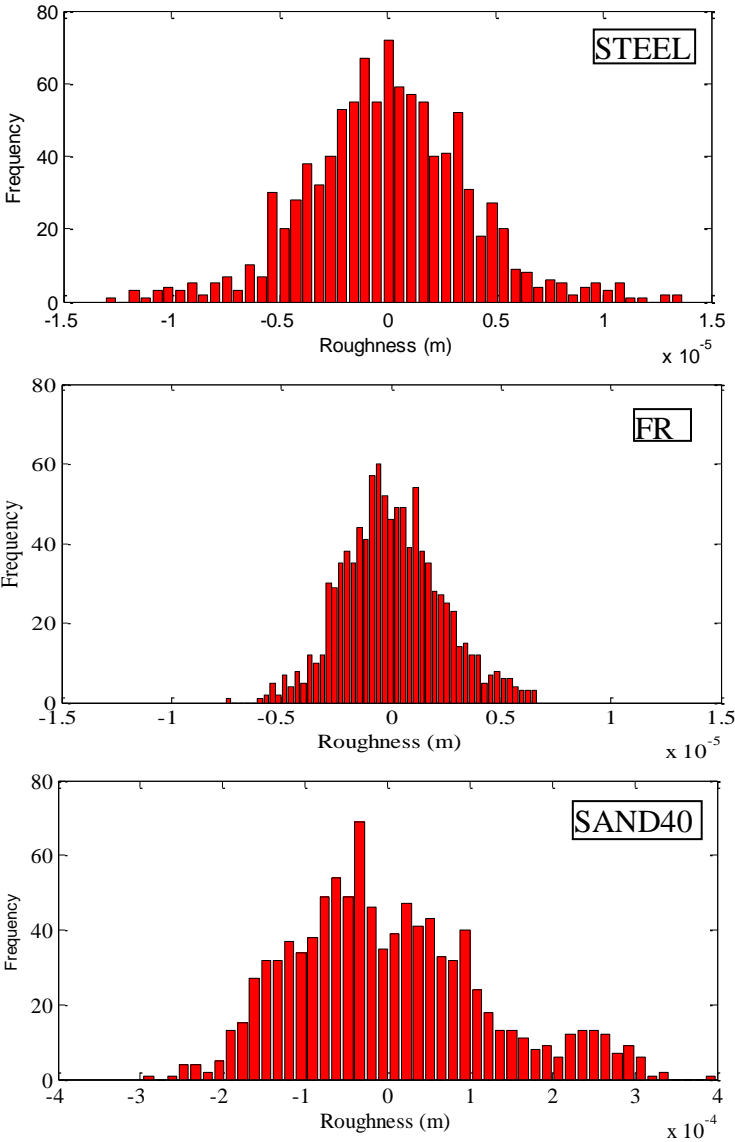


Figure 5.19 : Roughness histograms of the reference sample test plates (cut-off=2.5 mm).

On the other hand, the kurtosis parameter (Ku) is a measure of the peakedness of the roughness height PDF. Most of the tested surfaces have kurtosis values more or less close to 3, meaning that their peakednesses are similar to that of a Normal distribution. However, the CNT coated sample has rather higher Ku parameter, higher than 4 for the entire considered cut-offs, which means that the roughness height PDF of this surface has a sharp peak with thinner tails.

The Sm , De and S parameters presented in the table are all indicators about the openness of the surface. Sm parameter was calculated by taking the average of the distances between the zero-crossings of the roughness profile whilst S is the mean distance between local peaks. The selection of a local peak is very influential on this parameter. In this study, the peaks higher than the $1/4^{\text{th}}$ of the Rt parameter were identified as local peaks. D is the reciprocal of S , showing the number of local peaks per unit length of the roughness profile and is presented here as number per mm. Since the mean values for 100 profiles are given for every parameter in Table 5.2, the S parameter may not be equal to the exact reciprocal of the D parameter, but it is exactly the reciprocal of D for each profile considered. SAND40 and the CNT coated surface appears to be the most open surfaces if the Sm parameter is considered. On the other hand, if the S parameter is evaluated FCP2 and FCP3 coated samples are generally have the most open texture properties.

m_0 , m_2 , and m_4 are the zeroth, second and fourth spectral moments, respectively. In other words, they are the moments of the power spectral density function (PSD). The zeroth moment is theoretically equal to the variance of the roughness height distribution, Rq^2 whilst the second and fourth moments are the variances of the slope and curvature distribution, respectively. α is an important texture parameter referred to as the bandwidth parameter which is a non-dimensional combination of the m_0 , m_2 , and m_4 : $\alpha = (m_0 m_4) / (m_2^2)$.

$\tau_{0.5}$ parameter is one of the widely used correlation lengths and specifies the length that the autocorrelation function decays from 1 to 0.5. A greater correlation length implies a more open texture. However, this parameter depends on the long wave cut-off and increases as the cut-off length increases. This property can also be observed in Table 5.2. It is interesting to note that while the correlation lengths of FR and FCPs increase dramatically as the cut-off length increases, those of the SAND40, CNT and STEEL surfaces show much less reaction compared to others.

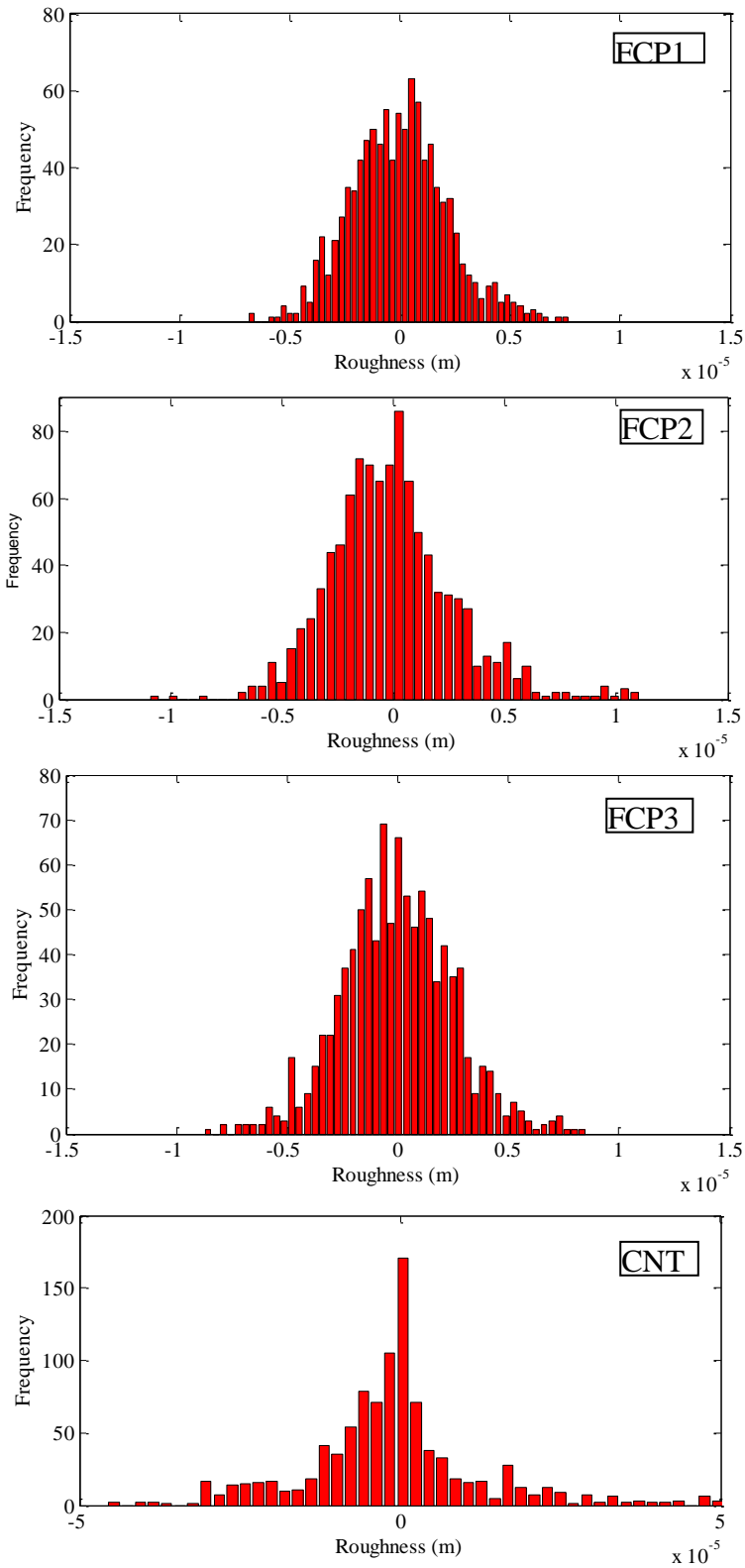


Figure 5.20 : Sample roughness histograms of the sample test plates coated with nanostructured antifoulings (cut-off=2.5 mm).

Table 5.2 : Roughness parameters of the flat plate samples at various cut-off lengths.

		$Rt(\mu\text{m})$	$Ra(\mu\text{m})$	$Rq(\mu\text{m})$	Sk	Ku	$Sm(\mu\text{m})$	$De (\#/mm)$	$S (\mu\text{m})$	$m_0(\mu\text{m}^2)$	m_2	$m_4(1/\mu\text{m}^2)$	α	$\tau_{0.5}(\mu\text{m})$
Cut-off = 2.5 mm	STEEL	23.30	2.75	3.54	0.04	3.42	281.00	1035.00	991.26	12.59	2.13E-04	1.11E-08	3.07	45.60
	FCP1	15.40	1.75	2.25	0.19	3.48	305.16	1006.00	1061.34	5.08	9.16E-05	5.67E-09	3.43	46.71
	FCP2	19.00	2.09	2.70	0.39	3.91	352.72	905.40	1172.54	7.36	9.89E-05	5.32E-09	4.00	73.41
	FCP3	17.69	2.05	2.61	0.09	3.38	392.57	914.40	1159.10	6.84	7.17E-05	3.85E-09	5.12	113.65
	FR	14.03	1.69	2.16	0.14	3.35	342.86	1153.00	890.91	4.72	6.63E-05	3.97E-09	4.26	74.04
	SAND40	685.79	82.17	105.41	0.41	3.54	1020.40	1313.60	803.55	11207.09	3.28E-02	1.09E-06	11.31	168.08
	CNT	99.51	9.47	14.38	0.51	5.28	507.41	1166.80	918.48	213.05	1.08E-03	4.62E-08	8.45	157.09
Cut-off = 5 mm	STEEL	25.98	3.09	3.96	0.06	3.35	320.15	1031.20	992.13	15.81	2.13E-04	1.10E-08	3.84	68.53
	FCP1	20.24	2.49	3.16	0.16	3.23	437.82	1259.00	835.83	10.04	9.48E-05	5.83E-09	6.52	354.32
	FCP2	25.95	3.20	4.06	0.19	3.28	532.15	1144.60	947.13	16.71	1.07E-04	5.67E-09	8.32	395.28
	FCP3	24.78	3.08	3.91	0.03	3.22	568.43	1098.80	988.70	15.43	7.71E-05	4.09E-09	10.61	405.88
	FR	21.59	2.81	3.52	0.05	3.01	572.20	1317.20	799.21	12.52	6.76E-05	4.03E-09	11.04	446.54
	SAND40	747.06	91.32	116.66	0.49	3.52	1129.38	1349.20	773.60	13720.64	3.42E-02	1.14E-06	13.42	198.60
	CNT	115.04	12.79	18.21	0.63	4.56	712.73	1484.40	719.24	342.92	1.16E-03	4.92E-08	12.59	266.67
Cut-off = 8 mm	STEEL	28.38	3.51	4.45	0.04	3.19	367.88	1055.20	977.62	20.00	2.15E-04	1.11E-08	4.82	111.19
	FCP1	25.25	3.23	4.09	0.22	3.20	559.53	1493.60	698.98	16.90	9.75E-05	5.98E-09	10.63	612.61
	FCP2	30.36	3.91	4.92	0.14	3.11	658.44	1260.00	869.38	24.74	1.13E-04	5.94E-09	11.56	567.24
	FCP3	29.02	3.76	4.73	0.06	3.05	718.31	1304.80	815.00	22.58	8.12E-05	4.28E-09	14.67	572.35
	FR	27.60	3.85	4.80	0.11	2.88	795.78	1742.20	607.33	23.24	6.87E-05	4.06E-09	19.97	720.72
	SAND40	781.36	95.10	122.05	0.51	3.60	1192.52	1390.40	754.78	15019.72	3.51E-02	1.17E-06	14.30	212.43
	CNT	124.72	15.61	21.28	0.65	4.11	970.49	1741.60	626.56	470.93	1.22E-03	5.16E-08	16.20	384.08

From Figure 5.21 to Figure 5.23, the autocorrelation functions of the sample flat plate surfaces are shown for 2.5 mm, 5 mm and 8 mm cut-off lengths respectively. Two plots are given in each figure, and the plots located at the bottom of each figure include a closer look of the part of the autocorrelation function (AC) that specifies the correlation length. At a first glance, it can be said that the FR and FCPs have similar AC trends at all investigated cut-off lengths whilst CNT and SAND40 surfaces display entirely different trends.

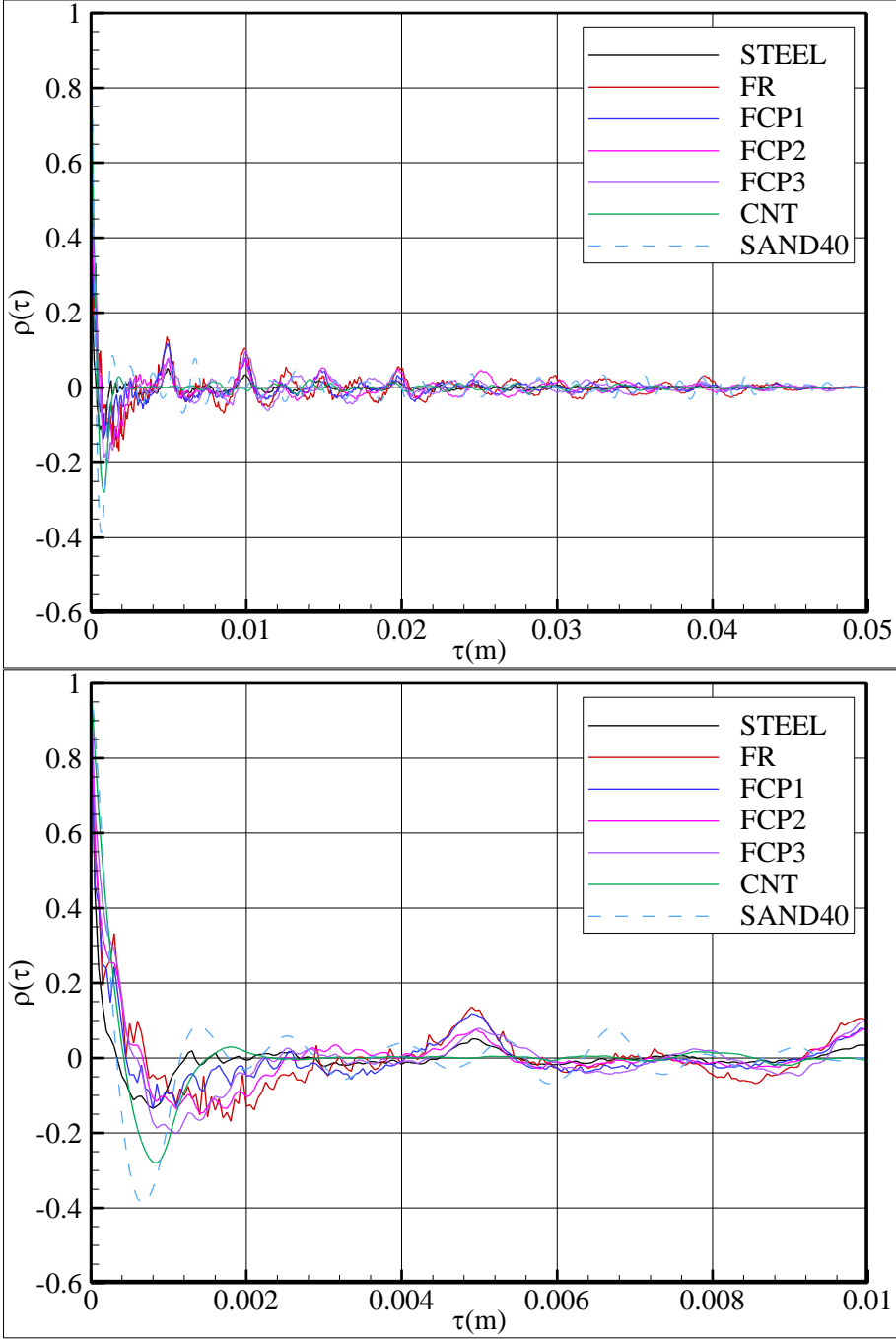


Figure 5.21 : Autocorrelation functions of the tested surfaces, cut-off 2.5 mm.

The AC of the STEEL surface also follows a distinctive trend for all the considered cut-off lengths. However, it resembles the trends of the FCP coated surfaces for higher wavelengths (e.g. $\tau > 0.04\text{m}$). On the other hand, it is certainly remarkable that all of the measured coated surfaces except CNT coated one have an important contribution from the long wave-lengths.

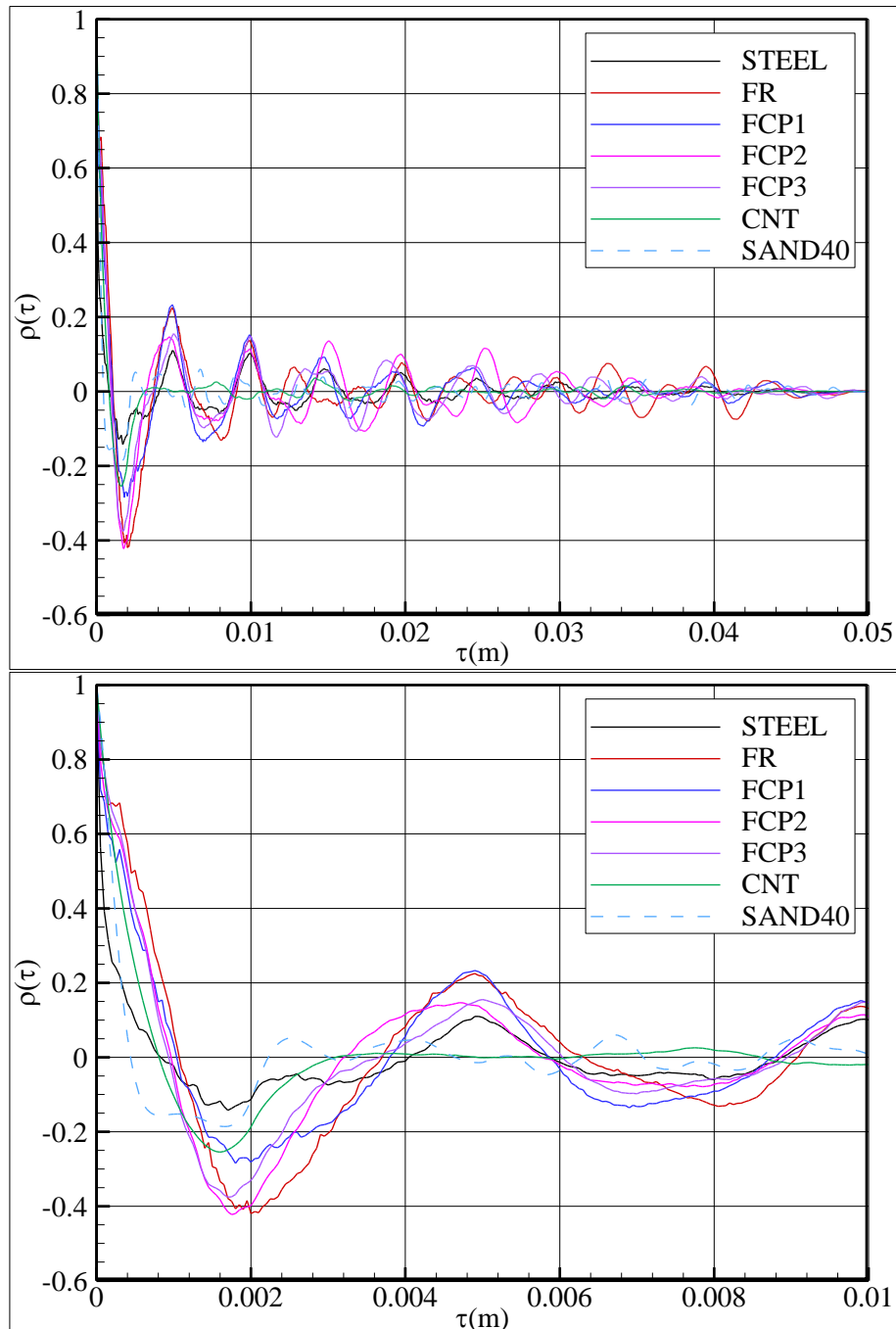


Figure 5.22 : Autocorrelation functions of the tested surfaces, cut-off 5 mm.

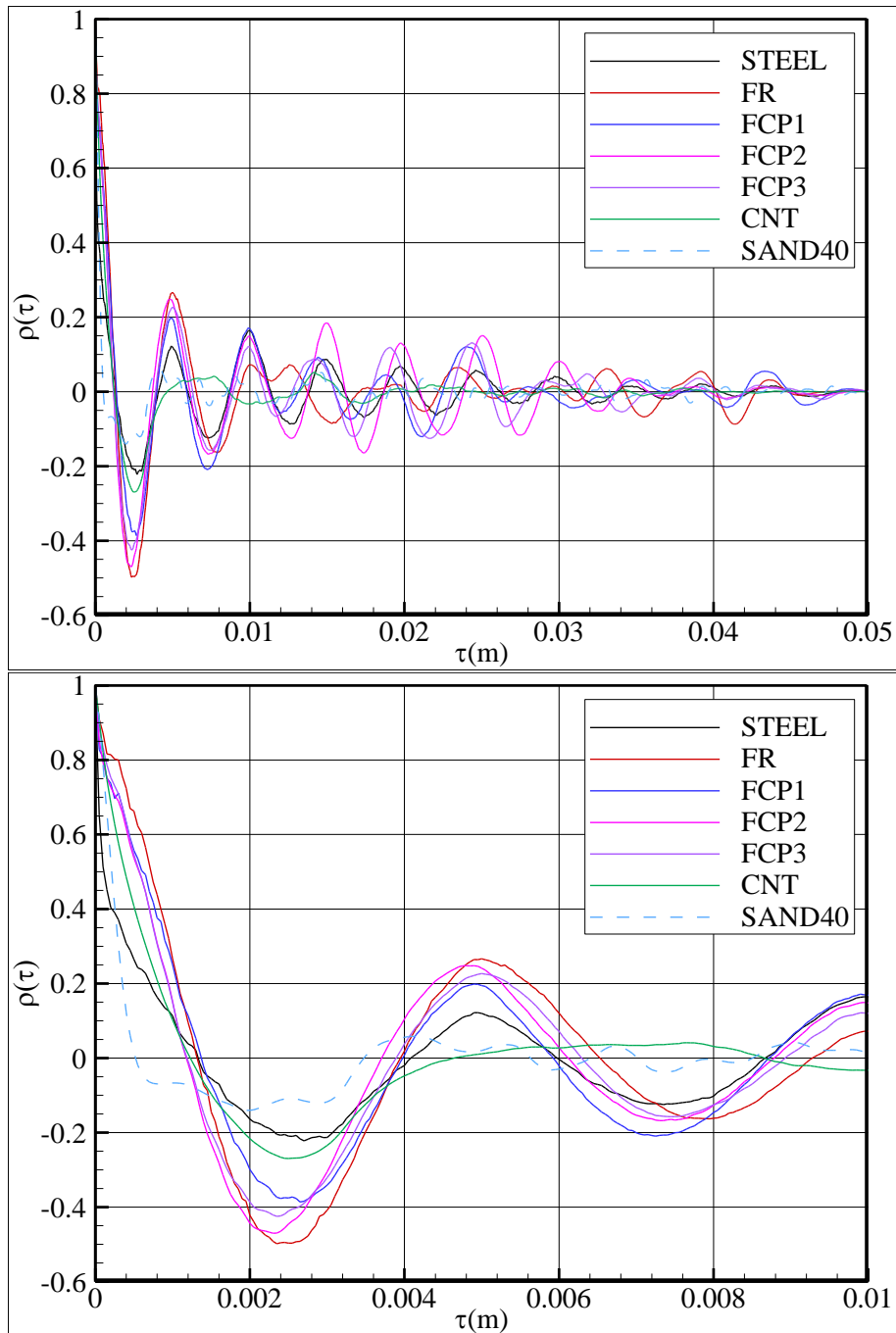


Figure 5.23 : Autocorrelation functions of the tested surfaces, cut-off 8 mm.

In Figure 5.24 the autocorrelation functions of the sample surface coated with FR calculated at different cut-off lengths are presented for comparison. From this figure, it is visually observed that the correlation length increases as the cut-off length increases as was realised from the change in $\tau_{0.5}$ parameter. From Figure 5.25 to Figure 5.27 the power spectral density functions (PSD) of the surfaces are shown comparatively for 2.5 mm, 5 mm and 8 mm cut-off lengths respectively. The maximum wave number (k) in the plots were selected by taking the Nyquist theorem

into account and given maximum wave number is the half of the sampling wave number ($1/50 \text{ 1}/\mu\text{m}$). Two plots were given in both Figure 5.25 and 5.27 in order to present different perspectives with using log-log scales in the top plots and log scale only in the y axis in the plots located at the bottom. The PSD and the AC of the measured roughness heights actually have the same information. However, investigation in the frequency domain may give a more pronounced graphic that may be easier to follow. If Figure 5.28 is considered, in which a comparison of the PSDs of SAND40, CNT and FR sample plates are given at different cut-off lengths in order to compare the cut-off length effect on the PSD, it is obviously seen that the increasing long wavelength cut-off only has an effect on the power of the long and middle range wavelength (or small and mid-range wave number $-k-$) part of the spectrum. This effect completely loses its influence for $k > 400-500$ (or for wavelengths smaller than 2 - 2.5 mm). Moreover, the location of the plateau of the CNT coated surface also changes whilst the width of the plateau increases towards the shorter wave numbers with increasing cut-off length. The location of the peaks does not change for the FR coated surface or the other surfaces which are not shown in this plot for clarity of the figure.

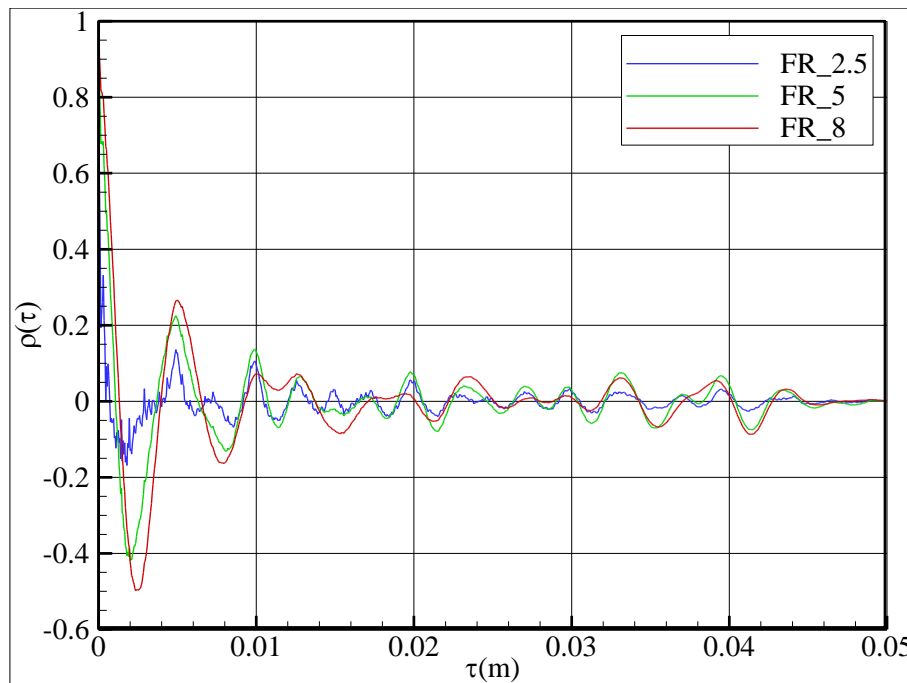


Figure 5.24 : The effect of cut-off length on the autocorrelation functions.

From Figure 5.25 and 5.27, it is clearly observed that the spectrum of SAND40 sample and the CNT coated surface are totally different than the others by containing much more power in all wavelength ranges due to their much larger roughness

heights. These surfaces are also different since both of them present small flat plateaus in a wave number range -rather than sharp peaks- followed by a gradually decaying trend. In these two figures, it is harder to distinguish the differences between the STEEL, FR and FCPs.

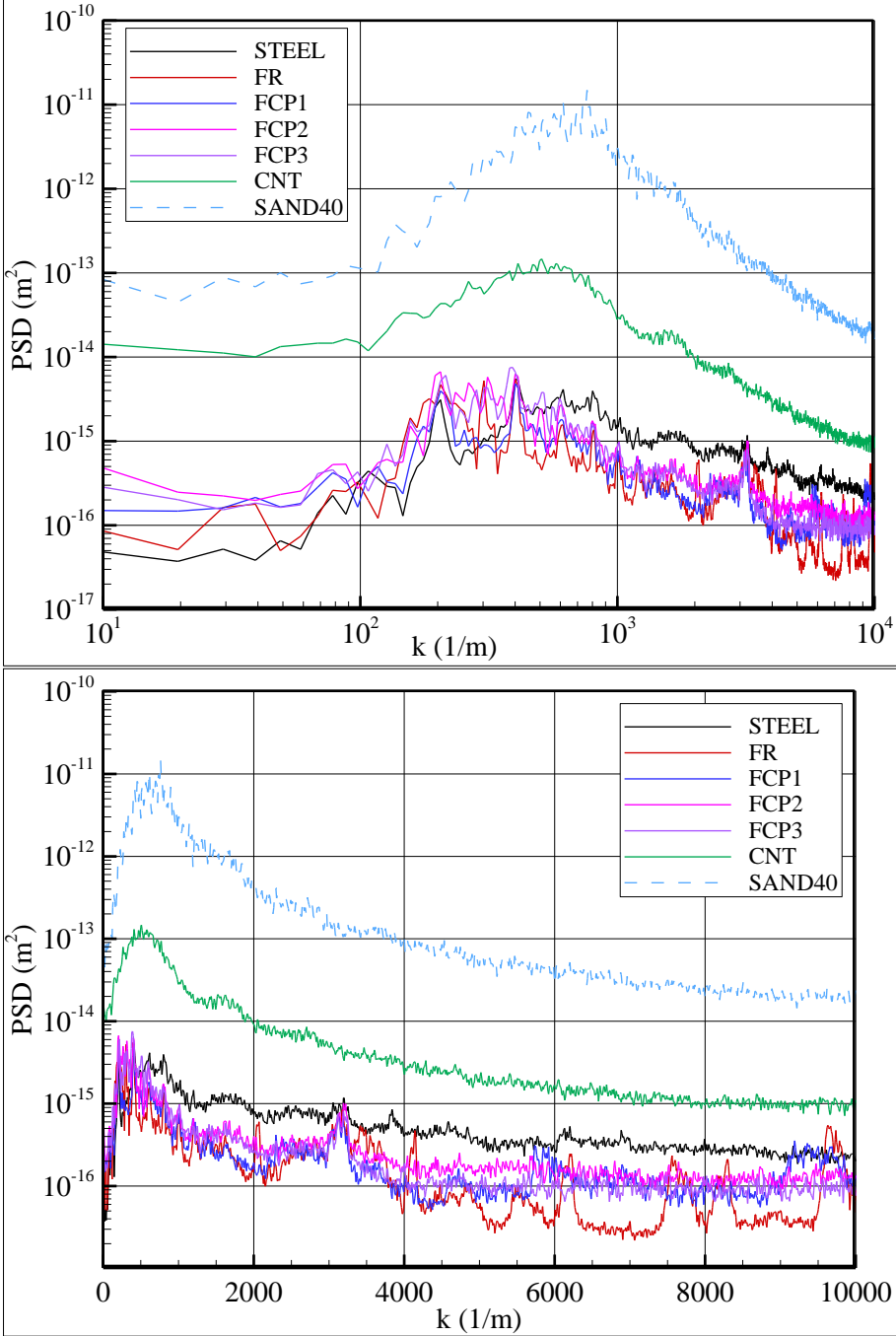


Figure 5.25 : Comparison of PSD at a cut-off length of 2.5 mm.

Accordingly, in Figure 5.26 for cut-off length of 5 mm, the PSDs of tested surfaces are plotted in small groups in order to emphasize the similarities or dissimilarities in their trends. At the top left plot, it is seen that FCP2 and FCP3 coated surfaces have

almost the same PSD except, the one of FCP2 displaying slightly higher power at the smaller wavelengths. Both of the mentioned surfaces show only two dominant peaks corresponding to approx. 5 - 2.5 mm and 0.3 mm wavelengths. The dominant longer wavelength part shows itself with a very small plateau for the 2.5 mm and 5 mm cut-offs and leaves its place to a significant peak located at 3.3 mm wavelength for 8 mm cut-off both for FCP2 and FCP3. The PSD of the FCP1 coated surface is slightly different than the ones of the FCP2 and PCP3 coated surfaces as seen from the bottom right plot in Figure 5.26 whilst it shares almost every peak that the PSD of the FR coated surface displays up to approx. $k=3200$ (or approx. 0.3 mm wavelength). However, the FR coated surface appears to reserve much shorter wavelength components, such as 0.24 mm, 0.16 mm, 0.14-0.12 mm, and 0.1 mm in the measured wavelength range.

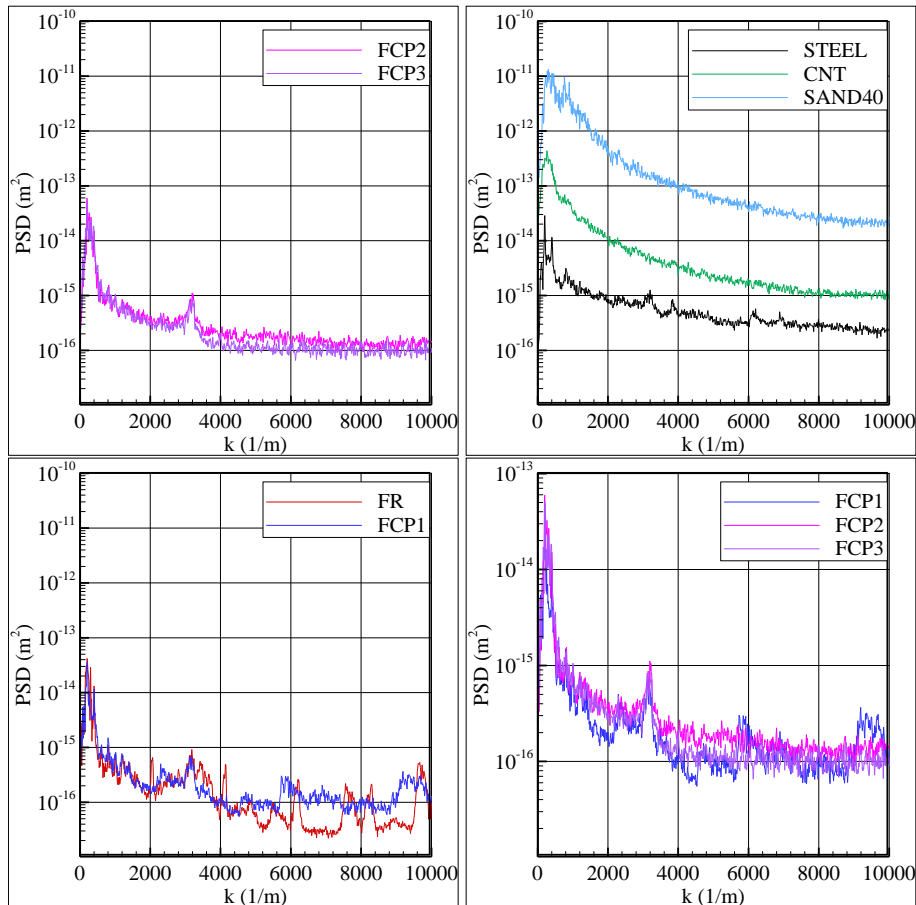


Figure 5.26 : Comparison of PSD at a cut-off length of 5 mm.

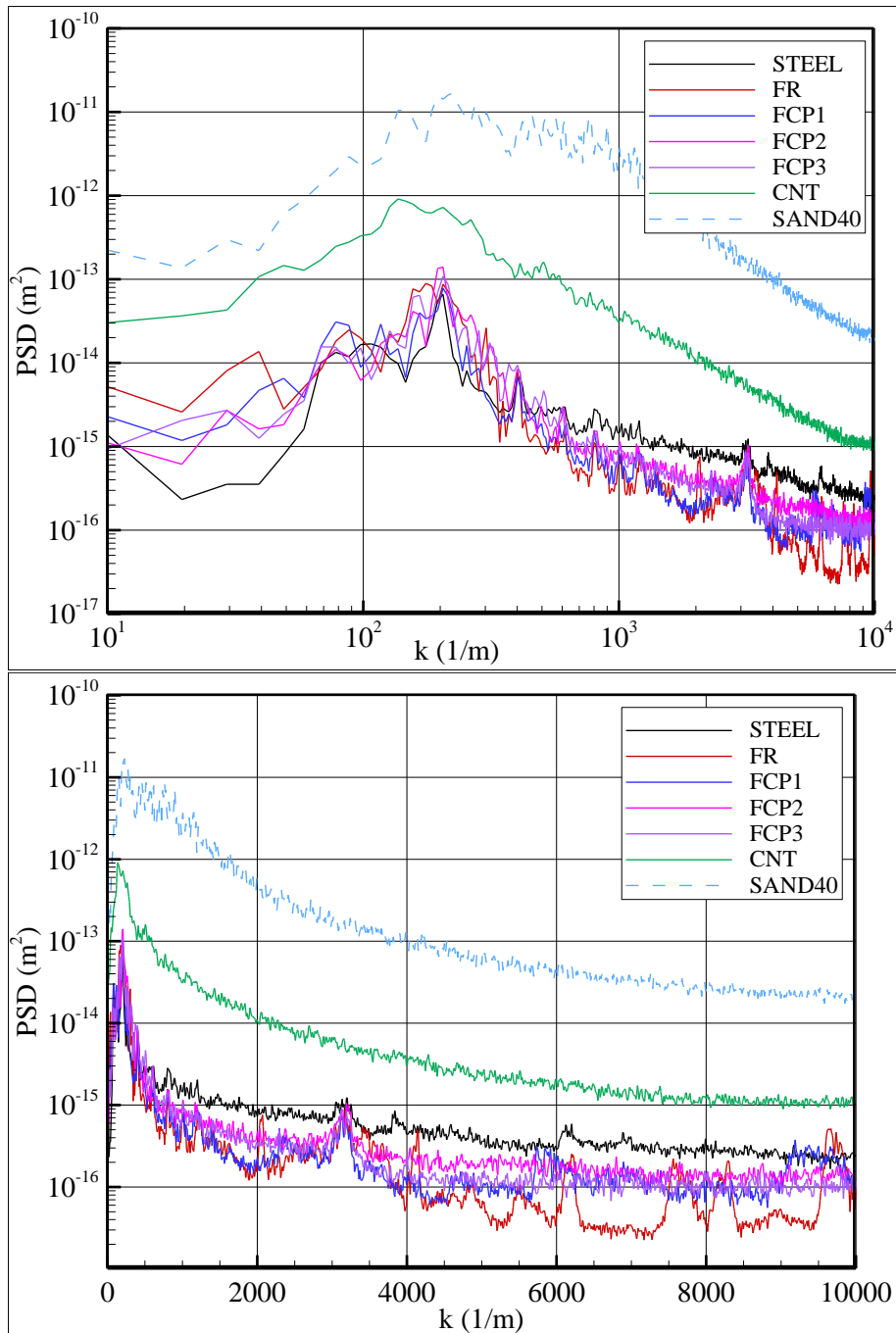


Figure 5.27 : Comparison of PSD at a cut-off length of 8 mm.

FCP1 shares the 0.11-0.1 mm wavelength range with FR and also displays a very small plateau at approx. 0.17 mm. On the other hand, the STEEL surface show a similar PSD trend to those of SAND40 and CNT, with the difference of significant peaks at $k= 100, 200, 400$ and 800 (corresponding to 10 mm, 5 mm, 2.5 mm and 1.25 mm wavelengths). SAND40 surface has a broad plateau around 1.3 -2.4 mm at 2.5 mm cut-off and this plateau extends up to 7 mm at 8 mm cut-off length. CNT coated

sample plate has smaller plateaus compared to SAND40, at wavelengths of around 2.1 mm, 3.8 mm and 7 mm, increasing with the increasing cut-off length.

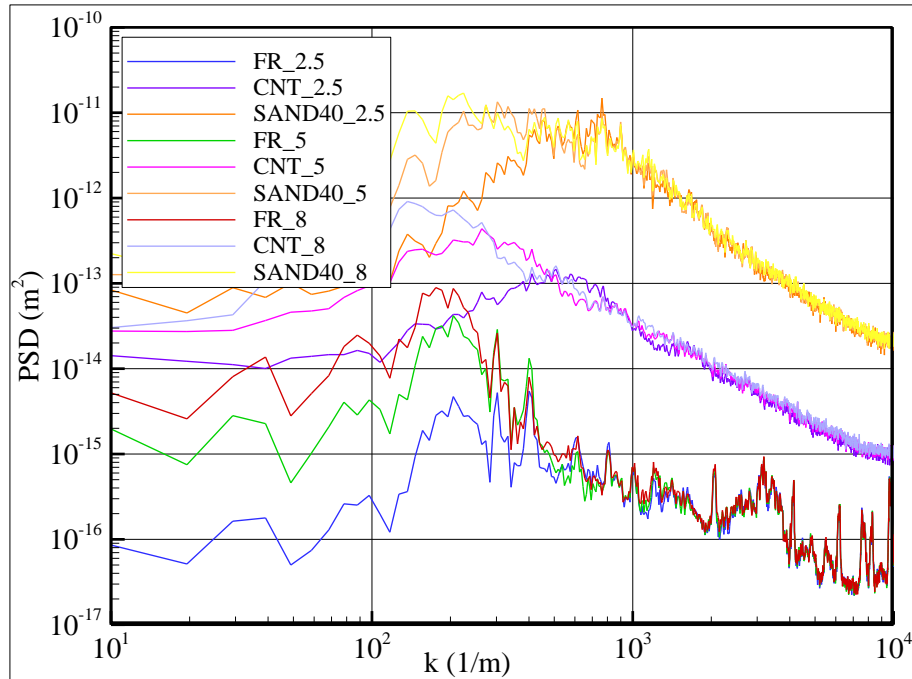


Figure 5.28 : Cut-off length effect on PSD.

5.6 Inflow Measurements

Prior to the boundary layer tests for the plates, preliminary measurements were performed for the tunnel in the presence of no test bed, in order to investigate the inflow stream properties such as the fluctuations around the mean tunnel velocity and turbulence intensity.

The background flow measurements in the tunnel were performed over the range of 1-3 m/s which also represents the velocity values adopted for the boundary layer measurements. The measurements were taken at two different cross-sections of the test section. The positions of these cross-sections were at a distance of 715 mm (IN1) and of 745 mm (IN2) from the entrance of the test section.

The velocity distributions at the above described two cross sections were measured in the axial direction, which is parallel to the incoming flow and in the transverse direction by using the 2-D DANTEC LDV system whose details were given in Section 5.4. The measurement area was chosen as 600 mm x 460 mm. This area was determined according to the limit of the traversing system used and of the laser probe. The 60 mm laser probe was used with an optical lens with a focal length of

600 mm for the inflow measurements in order to increase the possible measurement area as much as possible. The intervals between the locations of the measurement points were 50 mm and 46 mm in transverse and vertical directions respectively.

For each measurement point, 10000 samples were collected or the samples were recorded during 30 seconds, whichever came first, for each velocity channel. The data rate varied between 80 and 1000 Hz depending on the measurement point. Generally, 5000-10000 velocity samples for each component were collected at each point.

Table 5.3 shows the averaged values across both measurement area for each freestream velocity considered. It can be seen that the difference of the measured streamwise velocity displayed only very slight variations from the adjusted velocity in each case. The results for the transverse component indicated a slight cross-flow across the tunnel which is around 1% of the streamwise velocity. The turbulence intensity for both components was around 1.3-1.5% for 2 and 3 m/s whilst much lower values were obtained for 1 m/s.

Table 5.3 : Characteristics of the freestream.

	1 m/s				2 m/s				3 m/s			
	\bar{U}	\bar{V}	TI_x	TI_y	\bar{U}	\bar{V}	TI_x	TI_y	\bar{U}	\bar{V}	TI_x	TI_y
IN1	-	-	-	-	1.999	-0.030	1.487	1.356	2.999	-0.053	1.517	1.441
IN2	1.001	-0.003	0.340	0.950	2.006	-0.021	1.516	1.330	3.011	-0.039	1.562	1.444

The contours of the streamwise and transverse velocity components for a speed of 2 m/s at IN1 and IN2 are presented in Figure 5.29 as an example. As seen in the figures, very similar characters were obtained for both sections as expected. The flow shows slight variations around the mean across the measurement area. There is an increase in the magnitude of the streamwise component from the bottom of the tunnel to the top whilst the transverse component exhibits a non-uniform character towards the bottom of the tunnel. This variation in the velocity distribution can be accepted as a typical characteristic of the velocity pattern of a vertically oriented water/air tunnel measuring section following a symmetrical and short contraction section. On the other hand, the uniformity of the flow reaches to high levels at the plane around $z=0$ where the boundary layer measurements were taken. At this height level the velocity variations are such small that the values in this range would not jeopardise the quality of the experiments and hence can be definitely neglected.

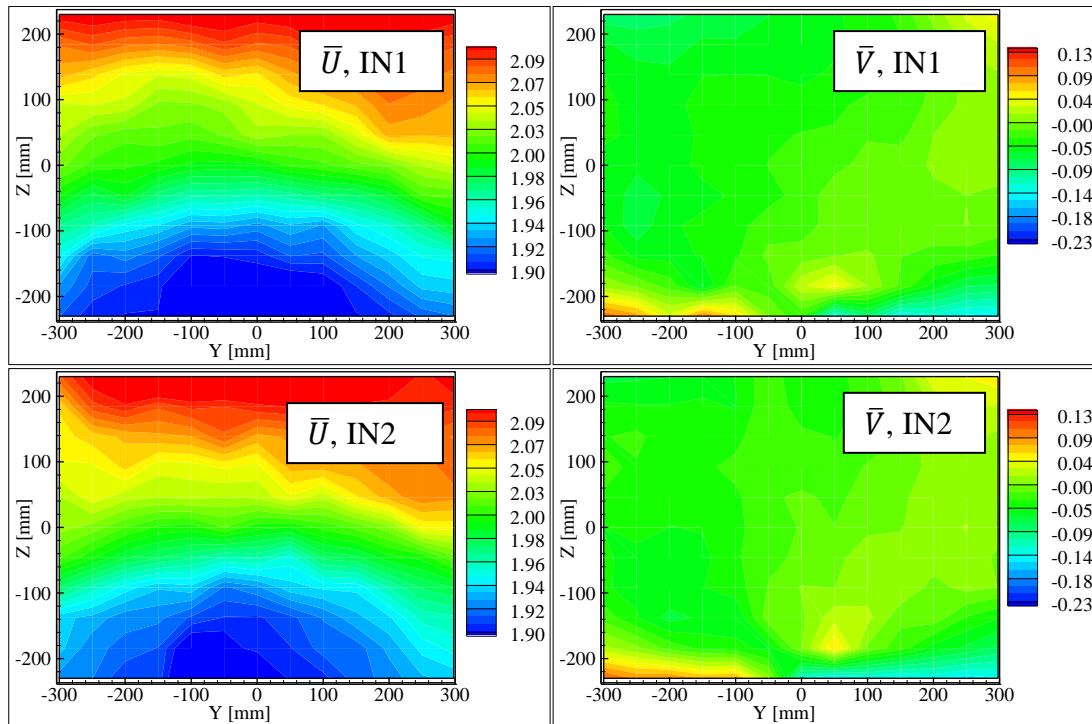


Figure 5.29 : Streamwise and transverse mean velocities for freestream velocity of 2 m/s at IN1 and IN2 sections

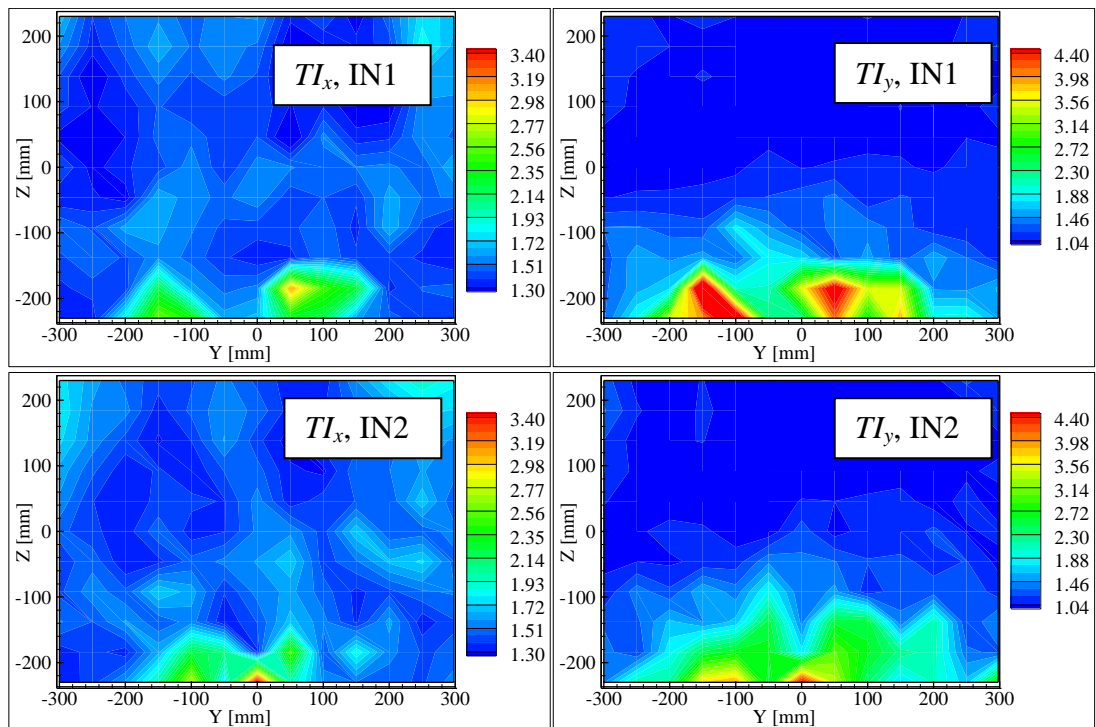


Figure 5.30 : Streamwise and transverse turbulent intensities for freestream velocity of 2 m/s at IN1 and IN2 sections

The measured streamwise (TI_x) and transverse (TI_y) turbulence intensities are shown in Figure 5.30 for both cross-sections. Likewise to the velocity distributions, the general trend of the results was very similar for both sections. Both components

exhibited a local increase towards the bottom end of the measurement area. Although the extreme values of the transverse components were higher than the streamwise component, the transverse turbulence intensity distribution was much more uniform in most part of the measurement area.

5.7 Uncertainty

The uncertainty analysis of the turbulent velocity data from LDV was performed with two different methods. Both methods account for the precision errors and the overall experimental uncertainties may be calculated by considering the bias error as well as the precision errors according to Moffat (1988). One of these methods aims the calculation of the statistical uncertainty associated with the sampling of a random process which is explained in detail in Benedict and Gould (1996). Table 5.4 presents the estimator variances of the statistics considered which are valid for any type of statistical distribution. N represents the number of the samples in Table 5.4. By using the estimator variances given in the table, the 95% confidence bounds for a statistical variable can be calculated as $\pm \sqrt{1.96} \sigma$, where σ is the estimator variance.

Table 5.4 : Estimator variances

Statistics	Variances (σ)
\bar{U}	$\frac{\overline{U'^2}}{N}$
$\sqrt{\overline{U'^2}}$	$\frac{[\overline{U'^4} - (\overline{U'^2})^2]}{4\overline{U'^2}N}$

Figure 5.31 present the distribution of the uncertainty percentages of the mean variables calculated with the aforementioned procedure throughout the boundary layer for all experimental cases. The distribution of the uncertainty level is much more scattered for the transverse velocity component, as may be expected, which exhibits very close velocities to zero. At the first third of the boundary layer where the irregularities due to the passage to the viscosity-dominated region and intermittent turbulence characteristics the uncertainty is higher than the other parts of the boundary layer. Moreover, the measurements in the vicinity of the wall are the ones that are most effected from the reflections of the laser from the wall which also

increases the uncertainty. The uncertainty level up to $y/\delta = 0.5$ is roughly $\pm 0.5\%$ and $\pm 8\%$ in average for streamwise and transverse velocity components, respectively. The uncertainty levels reach to much smaller values getting closer to the edge of the layer. The uncertainties of the RMS velocities are presented in Figure 5.32. With the exception of the vicinity of the surface the values are below $\pm 5\%$ for most cases and the average uncertainties for RMSU, RMSV and Reynolds shear stresses in the $y^+ > 30$ range were $\pm 2.5\%$, $\pm 3.1\%$, and $\pm 17\%$, respectively.

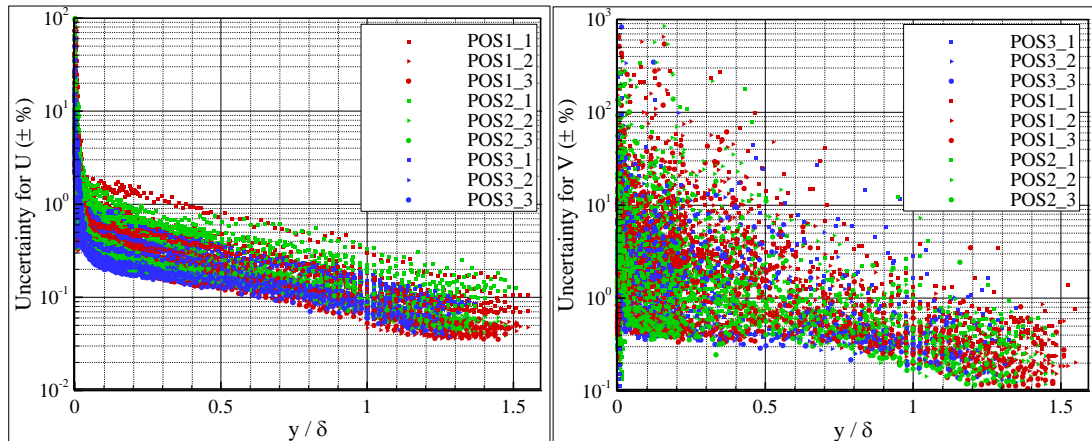


Figure 5.31 : Uncertainties (%) in the mean streamwise and transverse (right) velocities

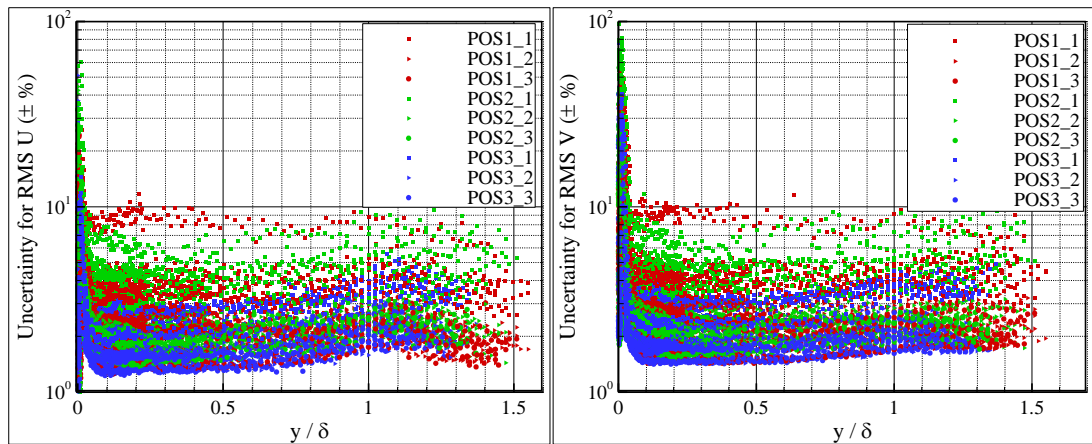


Figure 5.32 : Uncertainties (%) in root-mean-square streamwise and transverse (right) velocities

The second method that was adopted for the estimation of the uncertainty level of the sample data is based on the repetitive tests in order to include the inconsistencies of the experimental setup, such as very slight vibrations, temperatures fluctuations causing inexact Reynolds numbers, probe alignment errors etc., in the calculation procedure. Accordingly, 6 replicate tests were performed at an inflow velocity of 2 m/s for FR and SAND40 test plates at POS2. The 95% confidence bounds of the

statistics were determined via the multiplication of the standard deviation of the statistical variables by the related two-tailed t value ($t=2.571$) for 5 degrees of freedom as given in Coleman and Steele (2009). Shown in Figure 5.33 are the uncertainty percentages of the mean velocity variables at each sampled point for FR coated test plate. The results are slightly higher than those calculated with the adopted aforementioned method. This is highly expected, due to the inclusion of the other factors contributing to the values of the sampled data in the estimation procedure. Moreover, it was possible to carry out only 6 replicate tests due to the time restrictions arising from the desire of taking the replicate measurements in one day for avoiding the unwanted water temperature fluctuations (up to 3°C) between consecutive days. The relatively less number of replicate tests increases the two-tailed t value and thus the calculated uncertainty level. The calculated uncertainty level is approximately $\pm 1.5\%$ in most part of the boundary layer for the streamwise velocity component whilst the transverse component, exhibiting more scattered distribution, remains generally in the range of $\pm 2-50\%$. In other words, the average uncertainty level of the mean streamwise and transverse velocity were $\pm 1.1\%$ and $\pm 9\%$ in $y^+ > 30$ region, respectively.

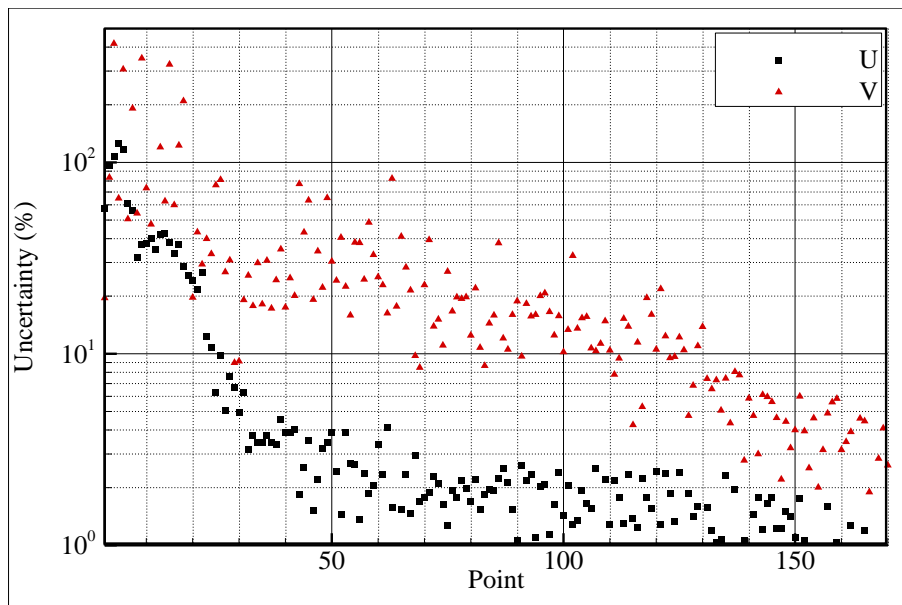


Figure 5.33 : Uncertainty (%) in mean streamwise and transverse velocities calculated with repetitive measurements for the FR coated surface.

The uncertainty propagation of the RMS velocities along with that of the shear stresses is plotted in Figure 5.34. It can be said that the uncertainty level for the streamwise RMS velocities varies between $\pm 2.9\%$ and $\pm 50\%$ whereas it changes

between $\pm 2.5\%$ and $\pm 87\%$ for the transverse RMS velocities. The uncertainty calculated for the turbulent shear stresses is $\pm 2.6\%$ in minimum and increases to a maximum of $\pm 120\%$ near the wall. The average uncertainty level of the streamwise and wall-normal Reynolds stresses and Reynolds shear stresses were $\pm 9\%$, $\pm 10\%$ and $\pm 21\%$ in $y^+ > 30$ region, respectively.

It should be noted here that very similar results were obtained for the SAND40 case and hence the graphical presentation was not considered to be necessary.

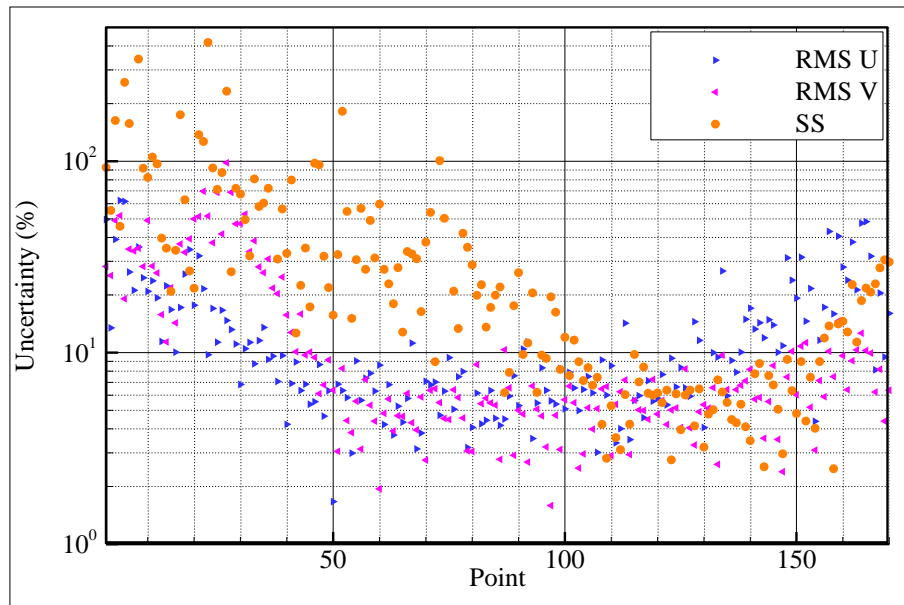


Figure 5.34 : Uncertainty (%) in root-mean-square streamwise and transverse velocities and shear stresses calculated with repetitive measurements for the FR coated surface.

5.8 Data Analysis Methods and Method Description

The collected time data for every measurement point in the boundary layer were saved as a text file. The analysis of the data was carried out with a couple of MATLAB codes and MS Excel sheets. The moments of the time data were calculated by using transit time averaging technique in order to eliminate the velocity bias. A noise elimination procedure by using Chauvenet criteria (Coleman and Steele 2009) was applied to the raw data along with a data filtering process which eliminated the sample populations that consisted of less than 500 samples considering the high uncertainty levels for $y^+ < 30$. This resulted in much smoother moment profiles and decreased the average uncertainty level in the vicinity of the wall. Mean, root-mean-square (RMS) velocities, turbulent normal and shear stresses

and boundary layer parameters, and uncertainties related to the moments are calculated at this stage. The calculated mean streamwise velocity profiles are used in a MATLAB code for the calculation of the friction velocities and skin friction coefficients. The roughness functions related to the test specimens were calculated in MS Excel 2007. In order to determine the effect of the tested surfaces, two-factor analysis of variance (ANOVA) with Re_x and the test surface selected as factors was carried out by using MATLAB. When ANOVA indicated significant differences between the test surfaces, multiple pairwise comparisons were conducted (Mason et al., 1989). The significance level for all tests was set to 0.05 which led to a confidence interval of 95%.

The Hama Method (HM) and the Modified Clauser Chart Method (MCCM) was used for the determination of the friction velocities for SAND40 and the coated surfaces whereas the Standard Clauser Chart Method (SCCM) was adopted for the smooth reference STEEL surface. The mentioned three methods were already explained in Chapter 2.8.

5.9 Results

The results of two-dimensional LDV boundary layer measurements, which were conducted over transitionally rough surfaces coated with novel nanostructured marine antifouling as well as a commercially-in-use foul-release antifouling are presented in this section. Hydraulically smooth and fully rough surfaces were also included as references in the boundary layer tests. The basic findings about the boundary layer properties such as the boundary layer and integral thickness parameters along with the mean velocity profiles, local skin friction drag coefficients, roughness functions and Reynolds stresses are discussed along with the relevant comparative data published in the open literature.

The calculated basic boundary layer parameters of the reference surfaces and the surfaces coated with nano-structured antifouling are presented in Table 5.5 and Table 5.6, respectively, including the entire test positions and inflow velocities. In this table, δ represents the thickness of the boundary layer, δ_1 and θ are the displacement and momentum thicknesses, respectively, whereas H is the shape factor and Re_{δ_1} and Re_{θ} are the Reynolds numbers calculated by using the displacement thickness and momentum thickness, respectively.

Table 5.5 : Variation of the boundary layer parameters for reference surfaces.

Surface	U_e	δ	δ_1	θ	H	Re_{δ_1}	Re_{θ}
STEEL_POS1_1	1.00	41	6.7	4.8	1.39	6475	4658
STEEL_POS1_2	2.00	39	6.1	4.5	1.35	11839	8786
STEEL_POS1_3	3.00	39	6.0	4.5	1.35	17616	13090
STEEL_POS2_1	1.01	40	6.7	5.0	1.35	6779	5039
STEEL_POS2_2	2.01	42	6.5	4.9	1.32	12797	9675
STEEL_POS2_3	3.01	44	6.5	5.0	1.31	19750	15102
STEEL_POS3_1	1.00	46	7.2	5.3	1.36	7236	5307
STEEL_POS3_2	2.01	48	7.2	5.4	1.33	14701	11048
STEEL_POS3_3	3.01	47	7.1	5.4	1.32	21653	16453
FR_POS1_1	1.01	40	6.5	4.8	1.37	6670	4860
FR_POS1_2	2.00	39	6.1	4.5	1.35	12400	9220
FR_POS1_3	3.01	40	6.1	4.6	1.32	18700	14100
FR_POS2_1	1.00	40	6.9	5.0	1.37	6890	5050
FR_POS2_2	2.00	40	6.4	4.8	1.33	12900	9720
FR_POS2_3	3.01	44	6.5	5.0	1.30	19900	15300
FR_POS3_1	1.01	43	7.2	5.4	1.34	7330	5460
FR_POS3_2	2.01	46	7.0	5.3	1.31	14300	10900
FR_POS3_3	3.01	50	7.1	5.5	1.29	21700	16900
SAND40_POS1_1	1.00	38	7.6	5.0	1.53	7590	4970
SAND40_POS1_2	2.01	41	7.1	5.0	1.43	14300	9940
SAND40_POS1_3	3.01	41	7.1	4.9	1.43	21200	14800
SAND40_POS2_1	1.01	43	8.9	5.7	1.57	8920	5690
SAND40_POS2_2	2.00	43	8.2	5.5	1.50	16500	11100
SAND40_POS2_3	3.01	44	8.4	5.7	1.48	25300	17100
SAND40_POS3_1	1.01	45	9.7	6.3	1.54	9900	6420
SAND40_POS3_2	2.01	51	9.2	6.3	1.47	18800	12800
SAND40_POS3_3	3.01	52	9.5	6.5	1.47	28900	19700

As seen from the tables, the boundary layer thickness varied between 39 mm (STEEL) and 52 mm (SAND40) for the reference surfaces, whereas the minimum and maximum boundary layer thickness values were 38 mm (FCP1) and 51 mm (CNT) for the nano-structured antifouling coated test surfaces. The displacement thickness varied between 5.9 mm (FCP1) and 9.7 mm (SAND40) whilst the momentum thickness had a variety range from 4.5 mm to 6.5 mm (SAND40). The shape factor varied between 1.30 and 1.57 (SAND40). The Reynolds number based on the displacement thickness changed between 6110 (FCP1) and 28900 (SAND40), whereas the one based on the momentum thickness varied between 4480 (FCP1) and 19700 (SAND40).

Table 5.6 : Variation of the boundary layer parameters for nanostructured surfaces.

Surface	U_e	δ	δ_1	θ	H	Re_{δ_1}	Re_{θ}
FCP1_POS1_1	1.00	38	6.3	4.6	1.37	6110	4480
FCP1_POS1_2	2.01	40	6.2	4.6	1.34	12200	9080
FCP1_POS1_3	3.00	41	5.9	4.5	1.31	17500	13400
FCP1_POS2_1	1.01	42	6.9	5.1	1.36	6690	4930
FCP1_POS2_2	2.01	41	6.5	4.9	1.33	12600	9480
FCP1_POS2_3	3.00	47	6.5	5.0	1.30	18900	14500
FCP1_POS3_1	1.01	46	7.5	5.6	1.35	7520	5580
FCP1_POS3_2	2.00	45	6.8	5.2	1.33	13500	10200
FCP1_POS3_3	2.99	44	6.7	5.1	1.31	19900	15100
FCP2_POS1_1	1.00	41	6.4	4.8	1.34	6210	4640
FCP2_POS1_2	2.00	39	6.0	4.5	1.32	11700	8830
FCP2_POS1_3	3.01	41	6.1	4.6	1.32	17900	13600
FCP2_POS2_1	1.00	39	6.6	4.8	1.36	6330	4640
FCP2_POS2_2	2.00	40	6.3	4.7	1.32	12000	9060
FCP2_POS2_3	3.01	43	6.4	4.9	1.30	18300	14100
FCP2_POS3_1	1.01	47	7.2	5.5	1.33	7080	5320
FCP2_POS3_2	2.00	43	6.7	5.1	1.31	12900	9860
FCP2_POS3_3	3.01	46	6.9	5.3	1.30	20000	15400
FCP3_POS1_1	1.01	41	6.5	4.8	1.35	6390	4730
FCP3_POS1_2	2.00	41	6.1	4.7	1.32	11900	9040
FCP3_POS1_3	3.01	43	6.1	4.7	1.31	17900	13700
FCP3_POS2_1	1.00	42	6.8	5.0	1.35	6620	4890
FCP3_POS2_2	1.99	40	6.3	4.8	1.32	12300	9320
FCP3_POS2_3	3.01	44	6.6	5.0	1.32	19300	14600
FCP3_POS3_1	1.00	47	7.3	5.4	1.35	7230	5350
FCP3_POS3_2	2.01	46	7.0	5.3	1.33	13800	10400
FCP3_POS3_3	3.01	46	7.0	5.4	1.31	20800	15900
CNT_POS1_1	1.00	39	6.5	4.8	1.36	6370	4680
CNT_POS1_2	1.98	38	5.9	4.5	1.32	11400	8630
CNT_POS1_3	3.01	42	6.4	4.8	1.33	18800	14100
CNT_POS2_1	1.00	43	7.0	5.2	1.34	6790	5060
CNT_POS2_2	2.00	45	6.7	5.1	1.31	13000	9970
CNT_POS2_3	2.99	48	6.6	5.2	1.29	19400	15100
CNT_POS3_1	1.00	44	7.5	5.5	1.35	7330	5420
CNT_POS3_2	1.99	44	7.0	5.2	1.33	13500	10200
CNT_POS3_3	3.00	51	7.6	5.8	1.31	22200	17000

In order to get a better understanding of the effect of surfaces on the boundary layer parameters, two-factor ANOVA was performed with Re_x and test surface as the analysis factors. When ANOVA analysis indicated significant differences between the test surfaces, multiple pairwise comparisons were conducted (Mason et al., 1989). The significance level for all the tests was set to 0.05 which led to a confidence interval of 95%.

For the boundary layer thicknesses values, the analysis indicated that the only significant parameter was the Re_x , not the test specimens. Likewise, the other boundary layer parameter was not significantly affected by the variation of the test surfaces with the exception of the SAND surface. The displacement and momentum thicknesses along with the shape factor H , presented a significant increase for the SAND surface which is expected depending upon the surface properties.

In Figure 5.35, mean streamwise velocity profiles of the tested surfaces are plotted in outer variables for test position 2 and 3 m/s freestream velocity. The streamwise velocity component U is non-dimensionalized with the outer flow velocity U_e and the wall normal distance y is non-dimensionalized with the boundary layer thickness δ in this figure. The velocity profile of SAND40 test surface is eye-catching with a much higher velocity defect whilst the others generally collapse within the uncertainty. Since the surface roughness properties of the SAND40 surface is highly different (and rough) than the other surfaces, this surface is expected to exhibit rather larger skin friction drag and thus has a much less full profile compared to others. The flow over such a rough surface at the tested Reynolds numbers is expected to be in the fully rough regime whereas the flow over the other tested surfaces most probably be undergoing the transitionally rough regime. Accordingly, much less difference is expected in the velocity profiles of these surfaces compared to the smooth reference STEEL. Figure 5.36 shows the mean streamwise velocity profiles of the tested surfaces for the entire test cases, while Figure 5.35 represents the behaviour of the comparative mean streamwise velocity profiles of the tested surfaces in all test cases.

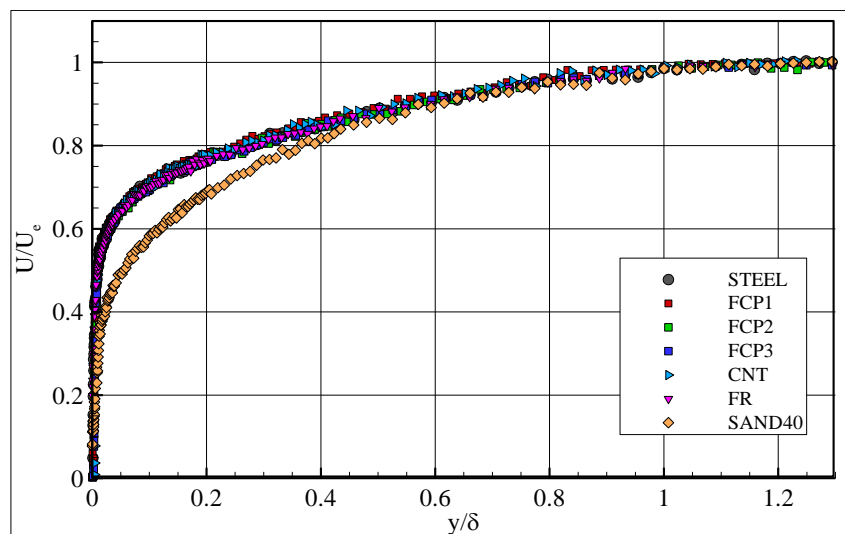


Figure 5.35 : Streamwise velocity in outer variables at POS2, 3m/s.

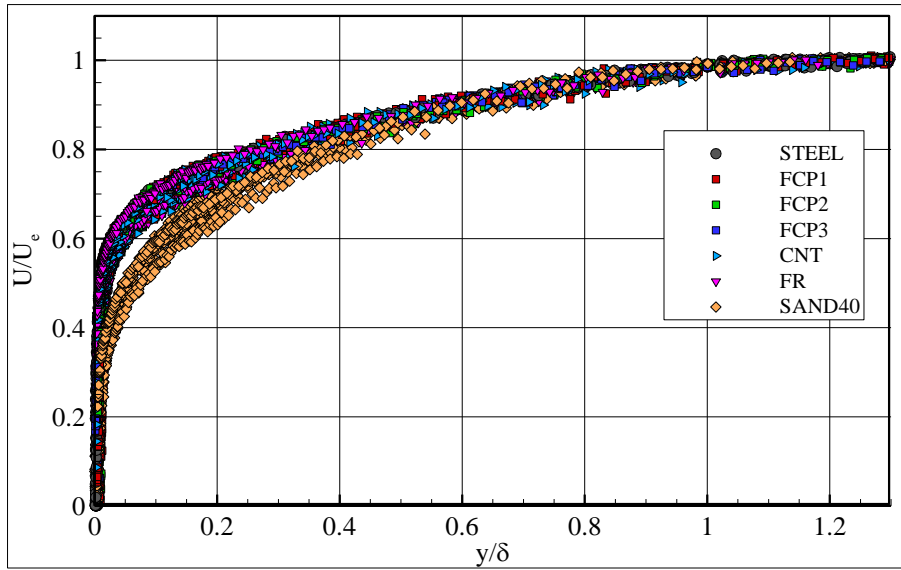


Figure 5.36 : Streamwise velocity in outer variables for all test cases.

The calculated friction velocities (u_τ), local skin friction drag coefficients (c_f) and roughness functions (ΔU^+) are presented in Table 5.7 and Table 5.8 along with the roughness Reynolds numbers (k_s^+) for the tested reference and nanostructured surfaces respectively. The given friction velocities were calculated with the HM and MCCM for the rough and coated surfaces whereas they were calculated according to SCCM and HM for the STEEL surface. The methods used (SCCM and HM) for the calculation of the friction velocity for the STEEL surface provided very close results within a maximum difference of 2.4% (and 1.35% in average). Good agreement was also found between MCCM and HM methods which were used in the calculation of the friction velocities for all surfaces other than the STEEL surface. The latter two methods led to a maximum difference of 3% in the calculated friction velocities. In Figure 5.37 and Figure 5.38, shown are the velocity profiles of the FCP1 coated surface at POS3 with 3m/s freestream velocity along with the optimized curves according to HM and MCCM, respectively. As observed, the agreement of the curves and the profiles in both cases is very well.

Local skin friction drag coefficients determined by the SCCM for the STEEL surface are plotted against Re_{δ_l} in Figure 5.39, including the solid line representing the local surface-resistance formula derived by Clauser (1954). The Clauser's model equation can be expressed as:

$$\sqrt{\frac{2}{C_f}} = A \log(Re_{\delta_1}) + B \quad (5.2)$$

where A and B coefficients are equal to 5.6 and 4.3, respectively.

Table 5.7 : Variation of the inner variables for the reference surfaces.

Surface	Re_{δ_1}	u_τ (CCM)	$c_f \times 10^3$ (CCM)	$c_f \times 10^3$ (HM)	ΔU^+ (MCCM)	k_s^+ (MCCM)
STEEL_POS1_1	6475	0.0389	3.01	3.08	-	-
STEEL_POS1_2	11839	0.0734	2.69	2.70	-	-
STEEL_POS1_3	17616	0.1057	2.48	2.47	-	-
STEEL_POS2_1	6779	0.0392	3.04	3.03	-	-
STEEL_POS2_2	12797	0.0738	2.71	2.69	-	-
STEEL_POS2_3	19750	0.1067	2.51	2.38	-	-
STEEL_POS3_1	7236	0.0387	2.98	3.02	-	-
STEEL_POS3_2	14701	0.0729	2.63	2.56	-	-
STEEL_POS3_3	21653	0.1054	2.45	2.31	-	-
FR_POS1_1	6670	0.0406	3.24	3.11	0.88	1.5
FR_POS1_2	12400	0.0759	2.87	2.74	0.86	2.8
FR_POS1_3	18700	0.1100	2.68	2.55	0.92	4.1
FR_POS2_1	6890	0.0404	3.26	3.10	1.05	1.5
FR_POS2_2	12900	0.0754	2.85	2.69	0.87	2.8
FR_POS2_3	19900	0.1080	2.56	2.45	0.46	4.0
FR_POS3_1	7330	0.0394	3.06	2.94	0.38	1.5
FR_POS3_2	14300	0.0744	2.74	2.60	0.55	2.8
FR_POS3_3	21700	0.1050	2.45	2.33	0.06	3.9
SAND40_POS1_1	7590	0.0567	6.44	5.98	8.42	54.0
SAND40_POS1_2	14300	0.1060	5.51	4.76	8.54	100.9
SAND40_POS1_3	21200	0.1570	5.46	4.99	9.42	149.4
SAND40_POS2_1	8920	0.0562	6.24	6.10	8.54	53.5
SAND40_POS2_2	16500	0.1040	5.42	5.15	8.73	99.0
SAND40_POS2_3	25300	0.1550	5.29	5.05	9.54	147.5
SAND40_POS3_1	9900	0.0565	6.27	6.04	8.84	53.8
SAND40_POS3_2	18800	0.1030	5.23	5.03	8.71	98.0
SAND40_POS3_3	28900	0.1520	5.07	4.87	9.45	144.6

The figure also includes the dashed line plotted using the model Equation 5.2 with the new coefficients that were calculated with a non-linear-least-squares-based optimization process. The values of the coefficients A and B were found as 5.62 and 4.23, respectively. As can be observed from the figure, the proposed regression line for the smooth reference surface is in perfect agreement with the original line. Accordingly, the model Equation 5.2 with the calculated new coefficients was used

for the calculation of the associated roughness functions of the coated surfaces and the SAND40 surface.

Table 5.8 : Variation of the inner variables for nanostructured surfaces.

Surface	Re_{δ_1}	u_τ (CCM)	$c_f \times 10^3$ (CCM)	$c_f \times 10^3$ (HM)	ΔU^+ (MCCM)	k_s^+ (MCCM)
FCP1_POS1_1	6110	0.0402	3.23	3.07	0.64	1.5
FCP1_POS1_2	12200	0.0759	2.86	2.70	0.74	2.9
FCP1_POS1_3	17500	0.1040	2.43	2.33	-0.61	4.0
FCP1_POS2_1	6690	0.0402	3.19	3.03	0.72	1.5
FCP1_POS2_2	12600	0.0738	2.70	2.61	0.09	2.8
FCP1_POS2_3	18900	0.1040	2.41	2.29	-0.55	4.0
FCP1_POS3_1	7520	0.0407	3.24	3.06	1.17	1.6
FCP1_POS3_2	13500	0.0735	2.70	2.59	0.21	2.8
FCP1_POS3_3	19900	0.1050	2.47	2.33	-0.07	4.0
FCP2_POS1_1	6210	0.0402	3.24	3.03	0.70	1.0
FCP2_POS1_2	11700	0.0743	2.76	2.62	0.18	1.9
FCP2_POS1_3	17900	0.1070	2.51	2.46	-0.06	2.7
FCP2_POS2_1	6330	0.0398	3.17	3.04	0.49	1.0
FCP2_POS2_2	12000	0.0745	2.78	2.64	0.35	1.9
FCP2_POS2_3	18300	0.1070	2.54	2.41	0.12	2.7
FCP2_POS3_1	7080	0.0399	3.14	2.95	0.63	1.0
FCP2_POS3_2	12900	0.0739	2.73	2.59	0.28	1.9
FCP2_POS3_3	20000	0.1050	2.43	2.31	-0.30	2.7
FCP3_POS1_1	6390	0.0414	3.40	3.16	1.36	1.0
FCP3_POS1_2	11900	0.0782	3.05	2.91	1.55	1.8
FCP3_POS1_3	17900	0.1110	2.71	2.60	0.95	2.6
FCP3_POS2_1	6620	0.0403	3.22	3.07	0.79	0.9
FCP3_POS2_2	12300	0.0766	2.95	2.76	1.19	1.8
FCP3_POS2_3	19300	0.1070	2.52	2.43	0.16	2.5
FCP3_POS3_1	7230	0.0390	3.02	2.93	0.20	0.9
FCP3_POS3_2	13800	0.0736	2.70	2.62	0.26	1.7
FCP3_POS3_3	20800	0.1060	2.45	2.37	-0.05	2.5
CNT_POS1_1	6370	0.0406	3.26	3.14	0.86	9.0
CNT_POS1_2	11400	0.0755	2.90	2.73	0.79	16.8
CNT_POS1_3	18800	0.1130	2.81	2.69	1.59	25.1
CNT_POS2_1	6790	0.0400	3.20	3.05	0.76	8.9
CNT_POS2_2	13000	0.0752	2.82	2.67	0.71	16.7
CNT_POS2_3	19400	0.1070	2.54	2.42	0.29	23.8
CNT_POS3_1	7330	0.0400	3.19	3.03	0.92	8.9
CNT_POS3_2	13500	0.0751	2.84	2.69	0.92	16.7
CNT_POS3_3	22200	0.1080	2.57	2.49	0.78	24.0

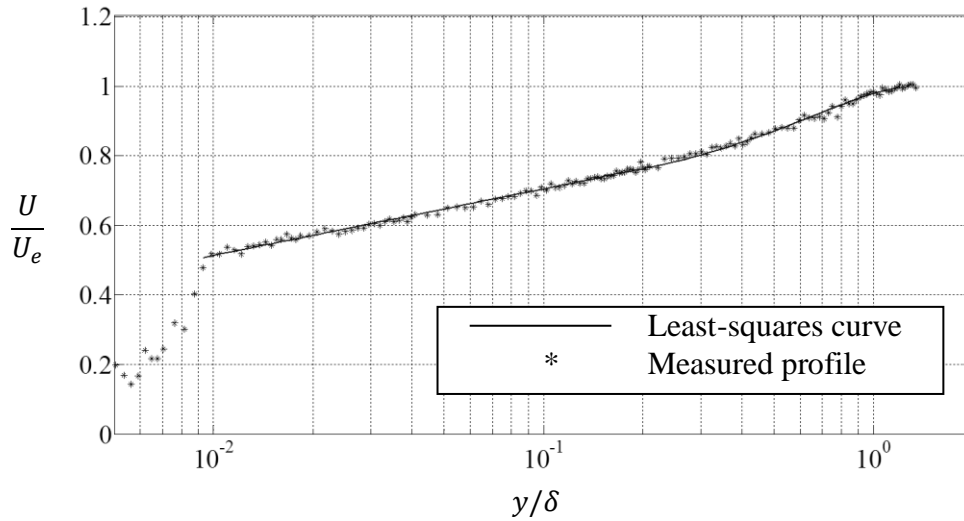


Figure 5.37 : Least-squares curves and measured velocity profiles for FCP1_POS3_3 with HM (Uncertainty in U/U_e : $\pm 0.6\%$).

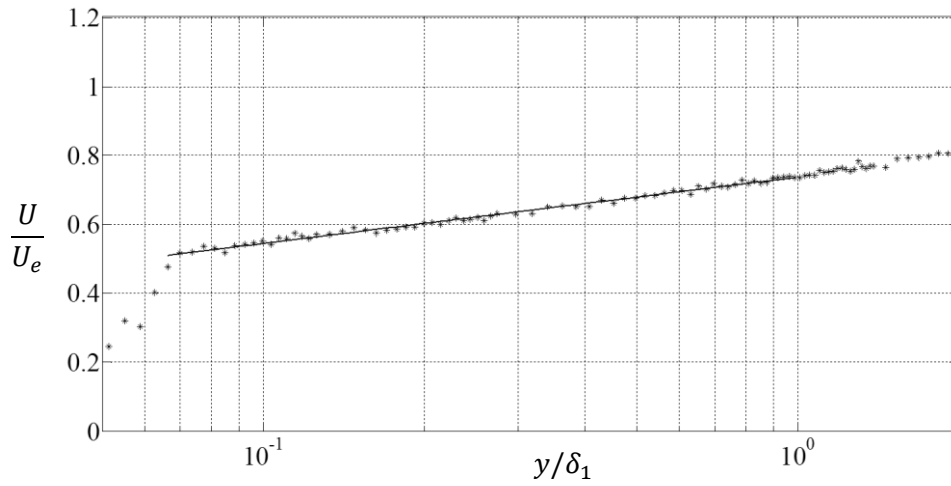


Figure 5.38 : Least-squares curves and measured velocity profiles for FCP1_POS3_3 with MCCM (Uncertainty in U/U_e : $\pm 0.6\%$).

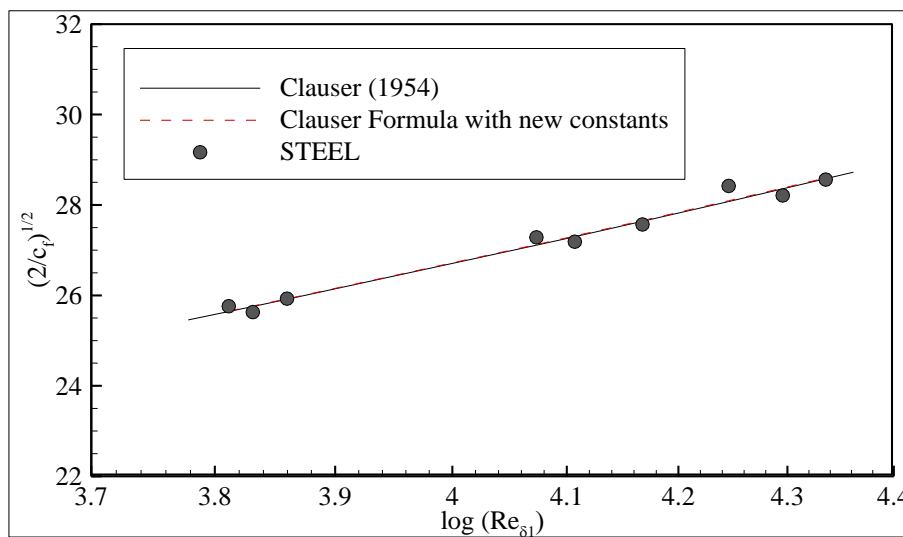


Figure 5.39 : Comparison of local frictional drag for STEEL.

The k_s values that were presented in Table 5.7 and Table 5.8 were calculated according to Flack and Schultz (2010) formula:

$$k_s = 4.43Rq(1 + Sk)^{1.37} \quad (5.3)$$

where Rq represents the root-mean square roughness height and Sk is the skewness of the roughness height probability density function. The mentioned two parameters calculated at a cut-off length of 8 mm were used in the formula. These roughness parameters were presented in Chapter 5.5. The formula of Flack and Schultz (2010) was derived by using surface statistics and roughness parameters measured with a sampling length of 50 mm and sampling interval of 25 μm (Flack and Schultz, 2010), which are rather similar values to those applied in the present roughness measurements. Although Flack and Schultz (2010) state that their formula was originally developed for the fully-rough surfaces, it is observed from their study that their formula also show good correlation for the transitionally rough surfaces. Roughness Reynolds number was calculated accordingly, as given below:

$$k_s^+ = \frac{k_s u_\tau}{\nu} \quad (5.4)$$

Figure 5.40 presents the mean velocity profiles of the tested surfaces at various positions and freestream velocities of 1 m/s, 2 m/s and 3 m/s, using inner scaling. The friction velocities, which were calculated with SCCM for STEEL and with MCCM for the others, were used for the non-dimensionalisation. It is observed that the smooth reference STEEL surface closely follows the smooth logarithmic law (log-law) line as expected. The surface roughness effects causes a downwards shift in the velocity profiles of the coated and rough surfaces in the vertical axis. Although a significant shift is not observed for the FR, FCP and CNT coated surfaces and the variation between the surfaces are actually at minor levels, the difference is still obvious with spreading values of U^+ over a broad band. On the other hand, the velocity profile of the SAND40 surface displays a large deviation from the smooth log-law and the ones of the coated surfaces with an obvious large downwards shift as expected in a fully rough flow regime.

Presented in Figure 5.41 are the mean velocity profiles of the tested surfaces for various test positions and inflow velocities, plotted in velocity defect form using

Rotta outer length scale (Clauser, 1956). In this type of scaling, the displacement thickness, which is an integral length parameter, is used as the length scale rather than the boundary layer thickness. The use of an integral length scale increases the quality of the expected collapse of the velocity defect profiles compared to the boundary layer thickness since it is rather difficult to be determined accurately and has a relatively arbitrary definition. In this plot, velocity scaling is performed taking both outer and inner velocity scales (freestream and friction velocities) into account. The presented velocity defect profiles display very good collapse throughout the logarithmic and outer part of the boundary layer, within the uncertainty level. This finding is in accordance with for e.g. Connely et al. (2006) or Schultz and Flack (2009) and obviously provides support to the universality of the wall similarity of the mean flow as indicated in Hama (1954). Since the velocity defect law is accepted to be universal, it is possible to relate the shape parameter with the local skin friction coefficient by introducing a universal form parameter G , which is equal to 6.1 for zero-pressure-gradient flat-plate turbulent boundary layer flows (Hama, 1954). The relation is expressed as:

$$H = \left(1 - G \left(\sqrt{\frac{c_f}{2}} \right) \right)^{-1} \quad (5.5)$$

In Figure 5.42 the local skin friction results of the smooth, coated and rough cases are plotted against the shape factor along with Equation 5.5. It is seen that the measured values of most of the tested surfaces accumulate in the right part of the figure. However, the values of the SAND40 surface form a separate group due to the high H and c_f values associated with this highly rough surface. Generally, it is possible to state that the agreement of the experimental results with the given relationship is good and provides support to the universality of the velocity defect law. Shown in Figure 5.43 are the local skin friction coefficient results for all test cases except the SAND40 surface which displayed much higher frictional drag coefficient values and was not included in this figure in order to preserve the distinguishability of the trends of the other tested surfaces. The presented values were obtained by SCCM for STEEL and MCCM for others. Non-linear-least-squares-based interpolation lines shown in Figure 5.43 were constructed based on the model equation given in Equation 5.2.

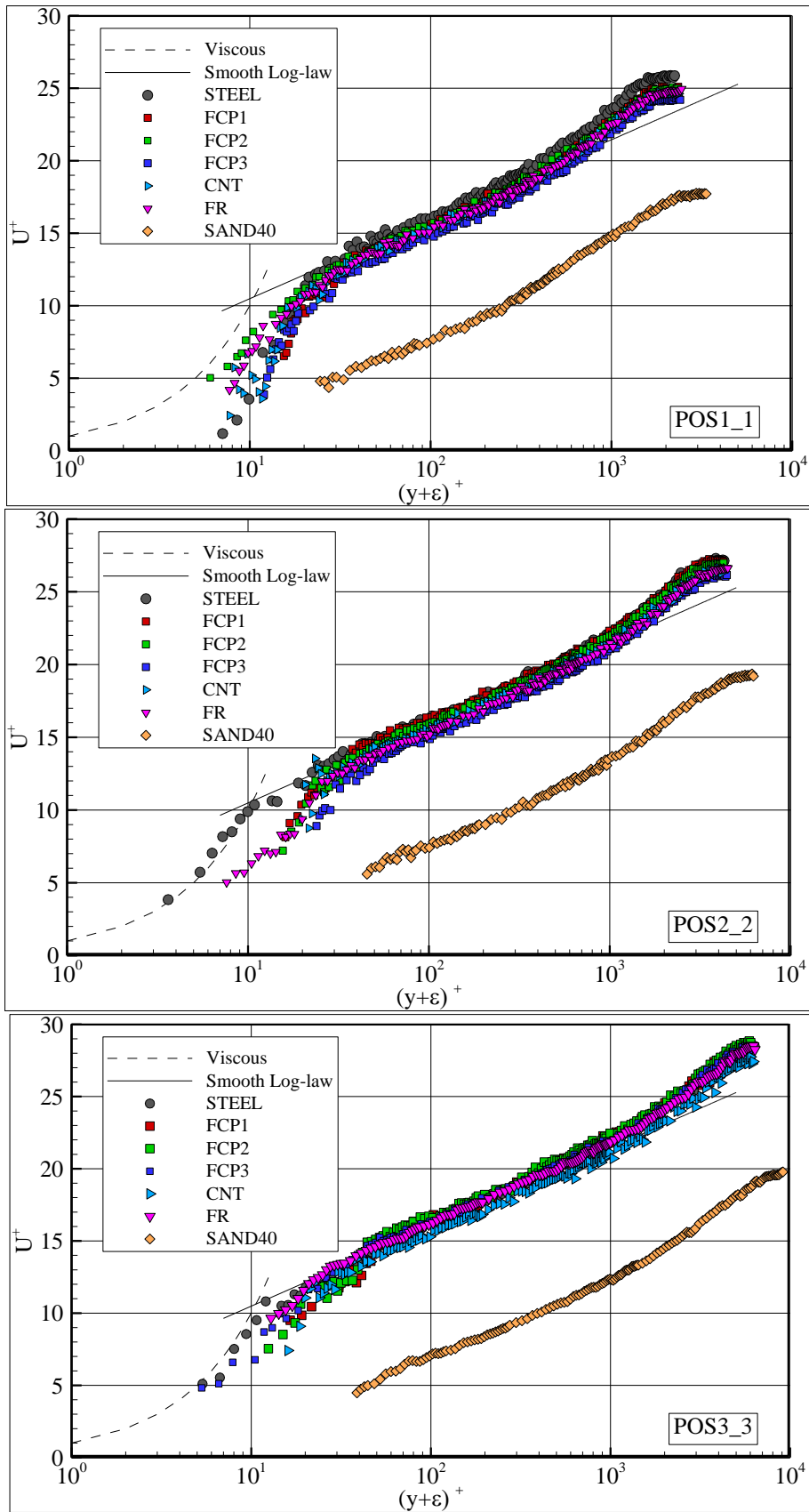


Figure 5.40 : Streamwise velocity in inner variables at various test positions and inflow velocities.

The different character of the FCP1 and FCP2's trendlines are immediately noticeable, which advance in a much steeper angle, whilst the rest display roughly a downward shift with respect to the STEEL's. The results of the FCP3 and CNT coated surfaces appeared to be highly sensitive to the test position and the freestream velocity and they displayed rather scattered results as seen from the figure. It seems that, for the lower Reynolds number values, the coated plates display similar drag performance, within the uncertainty, and they all present slightly higher frictional resistance than the smooth reference STEEL. The difference is higher than 6%, which is clearly above the uncertainty level, for most cases in the low Reynolds number range. As the Reynolds number increases towards the moderate range, FCP1 and FCP2 coated surfaces present better frictional characteristics which are almost equal to the smooth STEEL's performance.

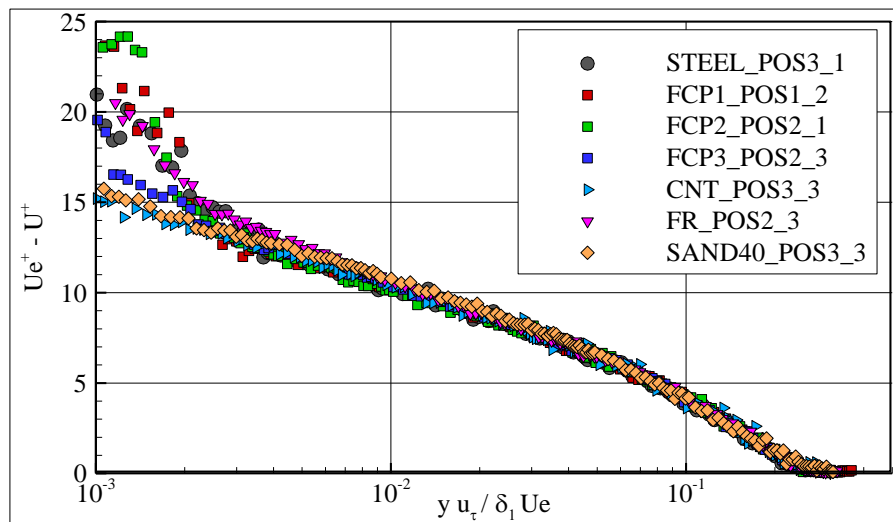


Figure 5.41 : Streamwise velocity in velocity defect form.

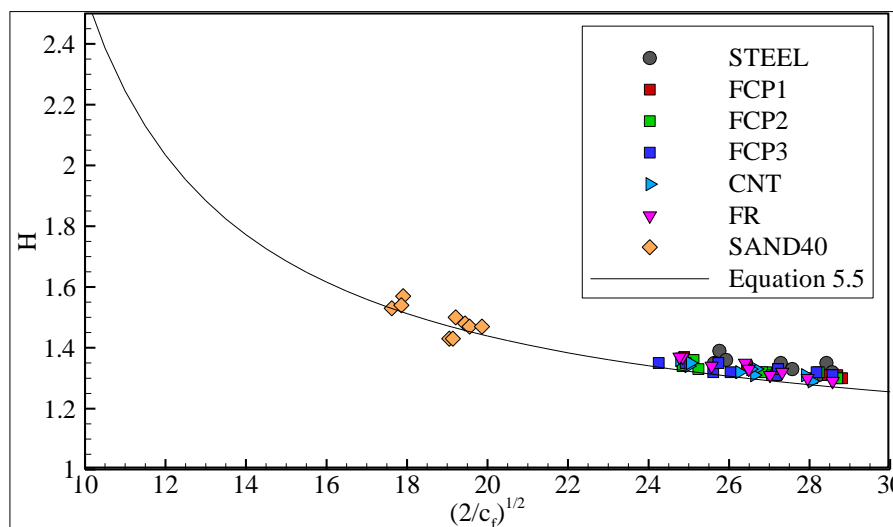


Figure 5.42 : Shape parameter and local skin friction drag correlation.

The difference in c_f with the rest of the coated surfaces is generally more than 5% for the moderate Reynolds number values. The most interesting finding was that FCP1 and FCP2 coated surfaces displayed even better frictional resistance performances than they did at moderate Reynolds numbers, as the Reynolds number further increased. The local frictional drag coefficient values of these coatings, which indicated very close results to that of the smooth STEEL, were at least ~4% (and ~8% at most) lower than those of the other tested coated surfaces at $Re_{\delta_1}=20000$ according to the trendlines given in the figure. At the same Reynolds number, FCP1 also indicated a reduction of local skin friction with respect to the STEEL that may be calculated as 2.2% from the trendlines. This ratio, however, is only slightly larger than the uncertainty level for the MCCM, which was calculated as 1.5%.

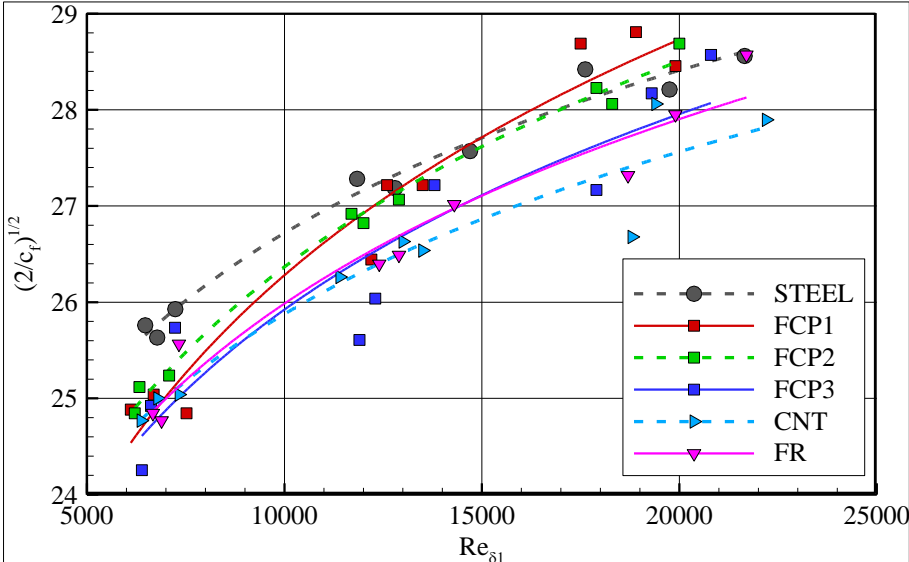


Figure 5.43 : Local frictional drag coefficient of the tested surfaces.

The variation of the roughness functions (calculated with the MCCM method) of the reference surfaces and nanostructured surfaces with respect to the displacement thickness Reynolds number is presented in Figure 5.44. It appears that the results of the skin friction coefficient calculated were well reflected to the roughness functions. The negative values of FCP1’s roughness functions compared to the smooth reference STEEL are immediately apparent for high Reynolds numbers, warranting further investigation. This shows a similarity to the study of Choi et al. (1997) who found a negative roughness function for a compliant surface. The figure also shows that, as the Reynolds number increases, the FCP1 and FCP2 coated surfaces display a decreasing trend in the roughness functions, which is opposite to the fully rough

reference SAND40. Whilst the roughness function rapidly decreases with increasing Reynolds numbers for the FCP1 and FCP2 coated surfaces, it increases for the SAND40. On the other hand, the average trends of the roughness function values associated with the FR and FCP3 coated tested surfaces generally show an almost constant trend for the first two inflow velocities followed by a drop for the 3 m/s cases although FCP3 has rather scattered roughness function values. CNT coated test plate display a constant trend in average throughout the changing test velocities, although it presents highly scattered values at 3 m/s for changing test positions.

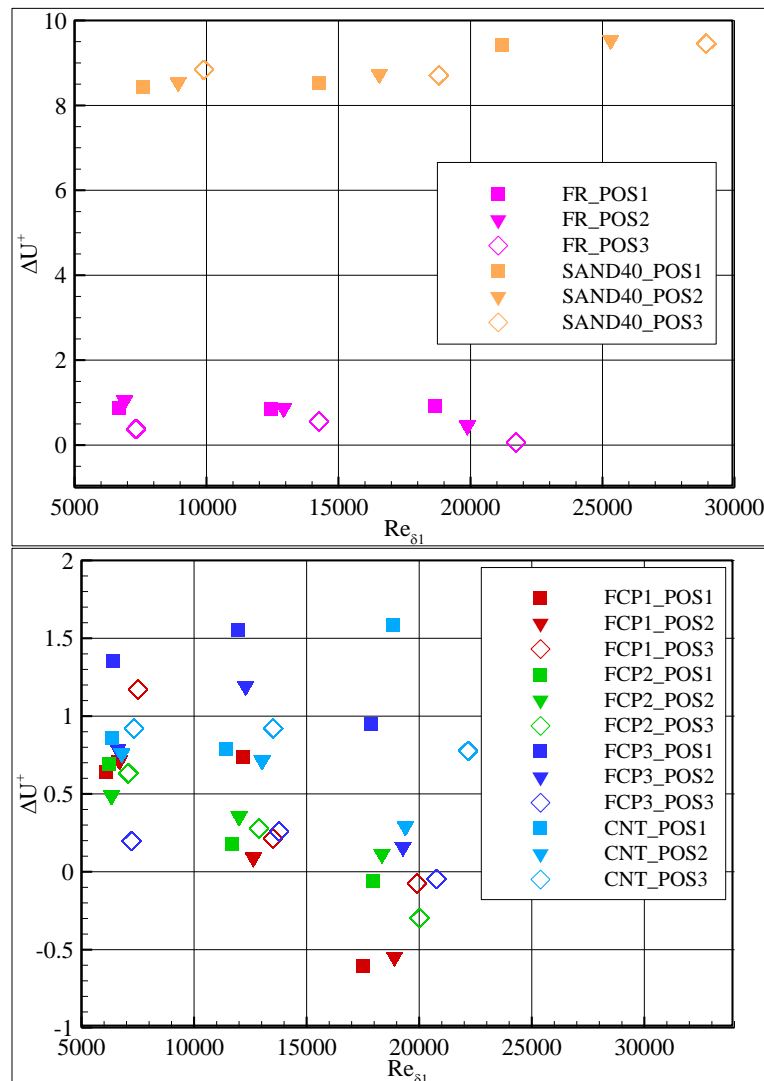


Figure 5.44 : Variation of the roughness function values for reference (top) and nanostructured surfaces.

Another way of presenting the roughness function results is the use of k_s^+ as the independent variable. Figure 5.45 presents the ΔU^+ values of the surfaces for each test case against k_s^+ values. The average roughness function values were plotted on the graph for the present study. The figure also includes the correlation of Dey

(1989), which relies on a sizeable collection of data for rough ship surfaces, the well-known Colebrook-White formula (Colebrook, 1939), which was specifically developed for engineering-surfaces, and the relationship recommended by Ligrani and Moffat (1986). The experimental data of Candries (2001), plotted in the same figure, are the results of the zero-pressure gradient flat plate boundary layer experiments for surfaces coated with marine antifouling paints whilst the data of Schultz and Flack (2007) are transitionally rough regime data gathered from boundary layer experiments on a bi-directionally sanded cast acrylic plate coated with silica-filled epoxy.

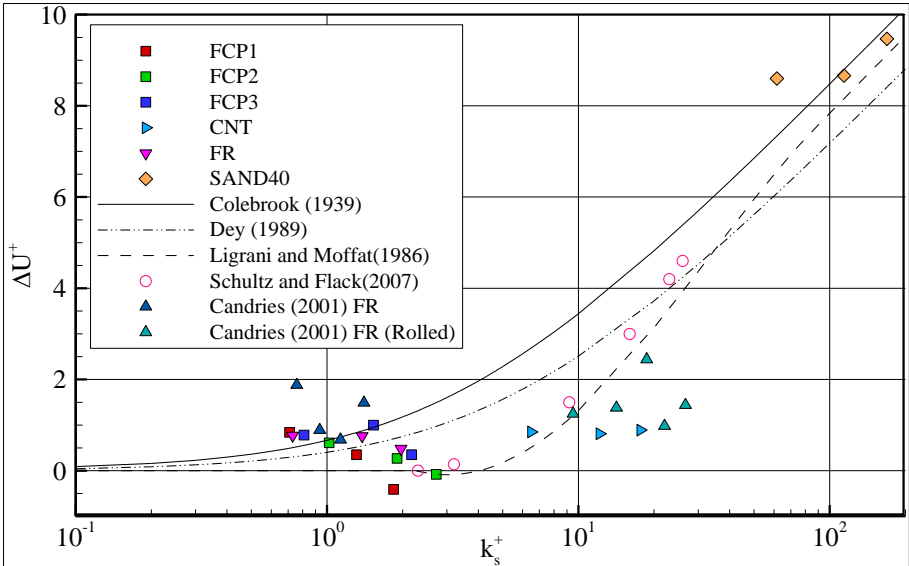


Figure 5.45 : Correlation of the roughness functions and the roughness Reynolds number.

A single regular roughness type data of Schultz and Flack (2007) obtained with varying flow velocities exhibit a well ordered curvy character and a slow departure from the smooth behaviour beginning from $k_s^+=2.5$, in Figure 5.45. Instead, the present data including various roughness and texture types displayed rather scattered character depending on the surface type, testing position and freestream velocity. Since the positional variation hardly affected the k_s^+ values, the averaged values are plotted in the figure. As seen, the results of different surfaces displayed their own trends and the overall observation of the results led to no significant form in roughness functions. The roughness function values in the low roughness Reynolds number range were generally spread around Colebrook’s and Dey’s curves, however no correlation with the suggested relations was observed. The results were, however, in reasonable agreement with those of Candries (2001)’s FR antifouling coating

experiments when the k_s^+ values of his surfaces were calculated in the same manner, using Equation 5.3. It should be mentioned here that the FR surface tested by Candries (2001) was a coated with a different slightly older foul-release type coating scheme compared to the FR coating used in the present study. Candries' boundary layer experiments on the surfaces coated with marine antifouling paints did not suggest that the coated surfaces obey the Colebrook-White law (Candries 2001, Candries and Atlar 2005). The rapidly decreasing trends of FCP1 and FCP2 as the k_s^+ increases are remarkable in Figure 5.45. The narrow k_s^+ range investigated somewhat obscures the global trend of the results of these coatings; however the appearing tendency is the opposite of what the global correlations suggest. In fact, a similar behaviour was observed in Candries (2001), as seen in Figure 5.45, which was then followed by an increase in ΔU^+ at a k_s^+ value of 1.5 which corresponded to a rather higher freestream velocity of 6 m/s. Further research is obviously needed to investigate the following behaviour of the present data at a higher Reynolds number range. Slowly fluctuating values of both FCP3 and FR coated surfaces are also apparent in the figure. CNT presented the highest k_s^+ range ($6.5 < k_s^+ < 18.2$) amongst the tested coatings and showed almost no reaction to the increase of the k_s^+ values displaying a horizontal trend with an almost constant average ΔU^+ value. These values showed a similarity to those obtained by Candries (2001) for a FR coating applied by rollering. Although the former and CNT represent different surface types, the agreement indicates that a much lower order of ΔU^+ values compared to the regression lines of Colebrook and Dey may be obtained with FR marine antifouling in this k_s^+ range. On the other hand, the results of the fully rough SAND40 surface cases, with k_s^+ values higher than 100, fell between the fully rough asymptotic lines of Colebrook and Ligrani and Moffat.

According to the closed-packed uniform grain sand roughness measurements of Nikuradse (1933), the hydrodynamically smooth state extends up to $k_s^+=5$. Whilst this critical Reynolds number was reported as 2.5 by Schultz and Flack (2007) and may be as low as 1.4 for a commercial steel pipe according to Langelandsvik et al. (2008), Ligrani and Moffat (1986) recommended a value of 15 for uniform spheres roughness and of 2.25 for sand grain. As also pointed out in Flack and Schultz (2010), the transitional roughness regime is defined by a varying range depending on the roughness type. Present data, with the exception of CNT and the SAND40

surface, was generally accumulated in the range of $0.7 < k_s^+ < 2.8$. Consequently, most of the test cases investigated should have fallen into the hydrodynamically smooth state according to the open literature. However, the results clearly indicated that the complex engineering surfaces, such as marine antifouling coatings, may produce non-zero ΔU^+ values despite their very low k_s^+ values. Apparently, there is a great need to develop new correlations, whose validity includes (old or new generation) marine antifouling, which are basically complex irregular engineering surfaces, by substantially expanding the present data.

Figure 5.46 shows the streamwise Reynolds stresses, \overline{uu}/u_τ^2 or \overline{uu}^+ , in inner (top plot) and outer (bottom plot) variables for all tested surfaces with varying displacement thickness Reynolds number between $19900 < Re_{\delta_1} < 28900$. The results in inner variables indicate that there exists almost no difference in the profiles of the coated and smooth surfaces being valid from $(y + \varepsilon)^+ \approx 40$. \overline{uu}^+ value of all surfaces is around 4 for $(y + \varepsilon)^+ \approx 1000$ corresponding to y/δ value of approximately 0.1 which presents good agreements with Schultz and Flack (2007), Raupach et al. (1991) and Candries and Atlar (2005). A lower stress region is apparent for the SAND40 surface over the band $30 < (y + \varepsilon)^+ < 300$. This region consistently produced lower streamwise fluctuations for all testing positions and freestream velocities for the SAND40 surface compared to the rest of the surfaces. This is in accordance with Candries and Atlar (2005) who also reported lower \overline{uu}^+ values in a similar but wider range for a grid 40 sandpaper compared to a smooth steel surface. This may be attributed to the high streamwise turbulence energy production of fully rough surfaces in these regions (Ligrani and Moffat, 1986). In the outer region, the effects due to both Reynolds number and very high roughness may be observed for the SAND40 profile. A near-wall peak of around 6.9 to 9.9 was observed at $(y + \varepsilon)^+ \approx 18 - 20$ for all surfaces except the SAND40 surface, which presented almost no peak value. The peak values are in agreement with, for example, Schultz and Swain (1999), DeGraff and Eaton (2000), Brzek et al. (2008). The highest peak values were displayed by FCP1 and FCP2 which presented the best frictional properties amongst the other coated surfaces. According to Grass (1971), these peaks are associated with the streamwise vortical structures. Probably due to the breakup of these structures by the roughness elements (see for example Schultz and Flack, 2007), a reductive trend of the peak values were observed for the CNT

until the peaks eventually almost disappeared for the SAND40 surface. A similar trend was also observed by e.g. Ligrani and Moffat (1986), Jimenez (2004), Brzek et al. (2008) with reducing and disappearing \overline{uu}^+ values as the k_s^+ values increases.

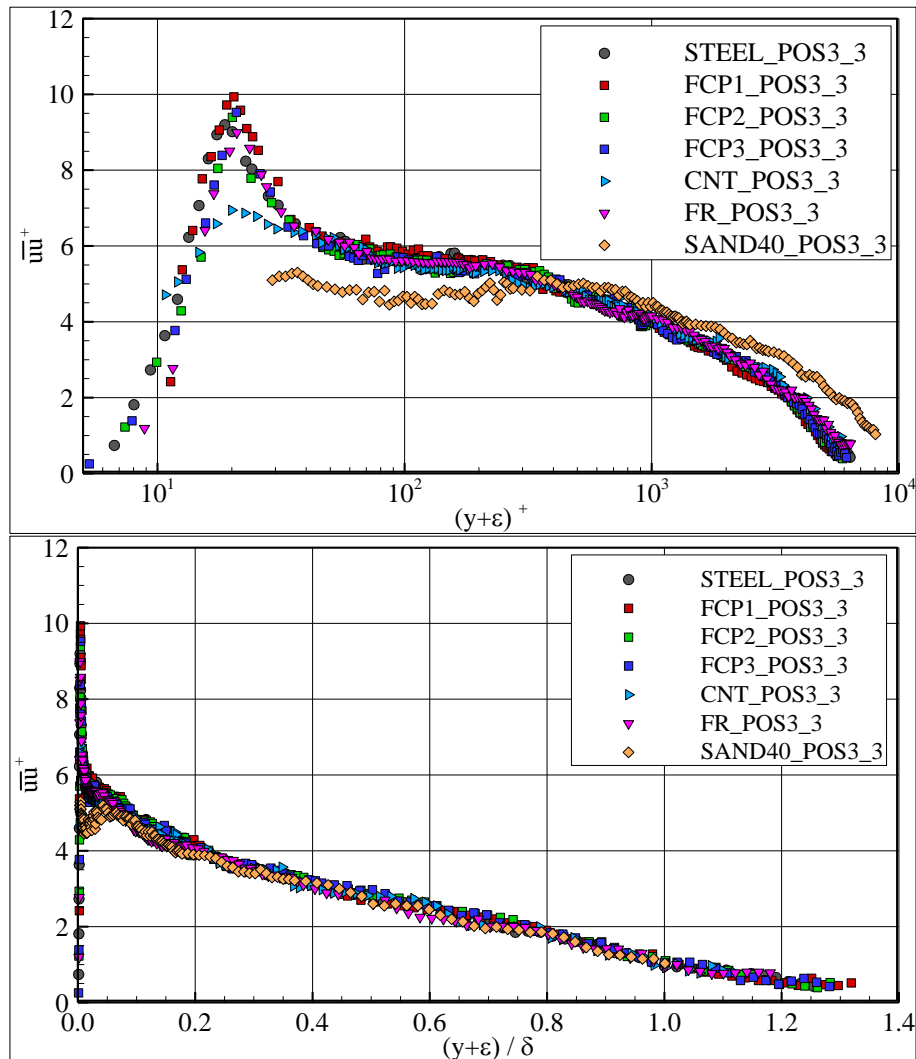


Figure 5.46 : Streamwise normal Reynolds stresses in inner (top) and outer scales.

The \overline{uu}^+ variation through the boundary layer for all tested surfaces is also alternatively plotted against wall distances non-dimensionalized via boundary layer thickness (in outer scaling) in Figure 5.46 at the bottom plot. There is a good agreement of the smooth, rough and coated surface profiles in the outer layer where they collapsed within the uncertainty. Schultz and Flack (2007) pointed out more distinctive differences in the overlap region; this was probably due to the higher differences in Reynolds numbers of their test cases. However the effect of the high roughness of the SAND40 surface is clearly visible in the overlap region. The near wall peaks stated in the previous paragraph may also be observed at approximately $y / \delta \approx 0.001-0.01$ with varying values for the different cases in this figure.

The profiles of wall-normal Reynolds stresses, $\overline{v'v'}/u_\tau^2$ or $\overline{v'v'}^+$, in inner scaling for the smooth and rough surfaces are presented in Figure 5.47 at the top graphic. Rapidly increasing trend of the profiles is visible up to $(y + \varepsilon)^+ \approx 70 - 80$. Although not definite as the $\overline{u'u'}^+$ profiles, a slight roughness Reynolds number dependence up to $(y + \varepsilon)^+ \approx 100$ was displayed by the smooth and rough profiles with somewhat decreasing values of $\overline{v'v'}^+$ as k_s^+ increases. The large plateau of almost constant value of 1.35 which was observed in the overlap region is in good agreement with Degraff & Eaton (2000) and Schultz & Flack (2007). As seen from the figure, there exists no distinctive difference between the profiles due to the surface roughness in the overlap and outer region of the boundary layer when they are expressed in inner scaling. The wall similarity concept about the wall-normal fluctuations has been extensively discussed by several researchers. In the literature, there are highly conflicting views about the effect of the surface roughness on the wall-normal fluctuations. There are several works which show that the surface roughness does not affect the wall-normal fluctuations outside the viscous sublayer. For instance, the channel flow experiments of Grass (1971), both computational and experimental work by Krogstad et al. (2005), the work by Raupach et al. (1991) and Flack et al. (2005), all reported minor or no effect of the surface roughness on the outer region of the boundary layer. Conversely, Musker (1990), Krogstad et al. (1992), Krogstad and Antonia (1999), Antonia and Krogstad (2001) observed significant increases in transverse turbulence intensities with the effect of the different surface roughness types. Figure 5.47 middle graphic presents the wall-normal Reynolds stresses for each surface against normalized wall distance. It is clear that, the profiles of the smooth and coated surfaces collapse within the uncertainty, strongly supporting the wall similarity concept for this particular flow property. However, the SAND40 profile displays lower values over the range $(y + \varepsilon)/\delta > 0.15$. This presents a discrepancy with, for example, Schultz and Flack (2007) who showed the wall similarity of the smooth and rough surfaces with different roughness Reynolds number. This may probably be attributed to the very high roughness Reynolds number values and texture properties of the SAND40 surface. On the other hand, Schultz and Swain (1999) also reported lower wall-normal fluctuations for some of their fouled specimens. It is also of note that when the inner scaling is used, the friction velocity has an effect on the results.

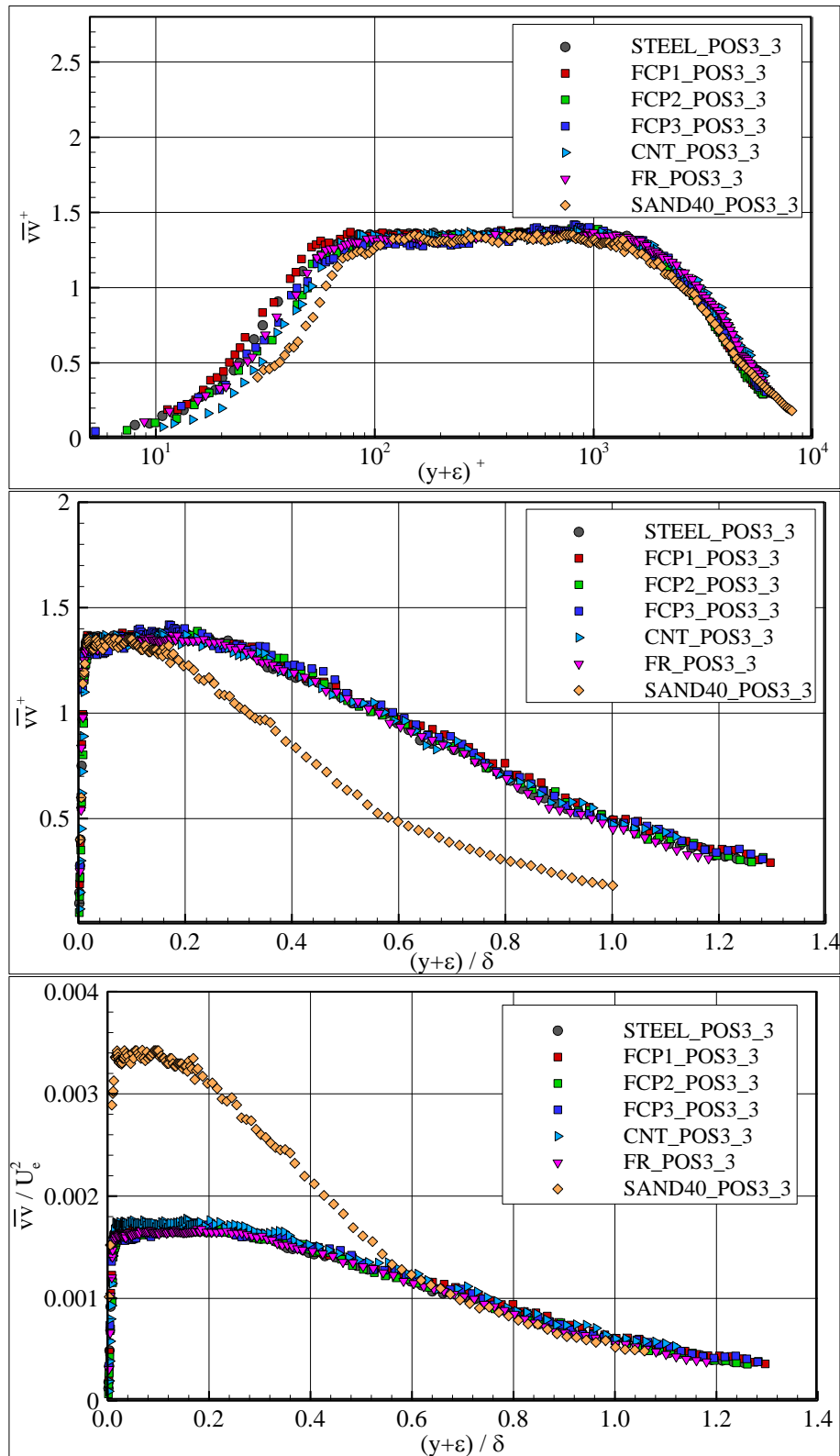


Figure 5.47 : Transverse normal Reynolds stresses in inner (top), outer (middle) and George and Castillo (1997) scaling.

Another way of presenting the results is the scaling of George and Castillo (1997) which is based on the normalization with the U_e rather than u_τ . Figure 5.47 bottom plot presents the same variable by using the freestream velocity as the normalization

parameter. As clearly seen, the profiles collapse within the uncertainty for the range of approximately $(y + \epsilon)/\delta > 0.6$. The effect of the very high roughness characteristics of the SAND40 surface may be clearly observed and extends up to the outer layer. These results are in good agreement with Candries and Atlar (2005). As the numerous studies with conflicting findings conducted by now suggest, further research is needed to provide support to the concept of wall similarity of the $\overline{v}v^+$ profiles. However, the present work, at least, validate this view for the transitionally rough surfaces from $(y + \epsilon)^+ \approx 100$ up to the end of the boundary layer.

The Reynolds shear stress profiles for the smooth, rough and coated surfaces in inner scaling are shown in Figure 5.48. The $-\overline{uv}$ profiles were non-dimensionalized by the square of the friction velocities calculated by the MCCM for the rough and coated surfaces and the SCCM for the STEEL surface at the top graphic. All of the Reynolds shear stress profiles had a plateau at the constant stress region with a peak value around 0.95 to 1 at about $0.03 < (y + \epsilon)/\delta < 0.16$. This peak values validated the friction velocities calculated with the MCCM and SCCM. No significant difference was observed between the tested surfaces in the outer layer of the boundary layer. Although the shear stress profile of the SAND40 surface seemed to display slightly lower values compared to the other tested surfaces, the results stayed within the uncertainty level. This is in agreement with Ligrani and Moffat (1986) and Schultz and Flack (2007) who did not find any influence of roughness on the Reynolds shear stresses.

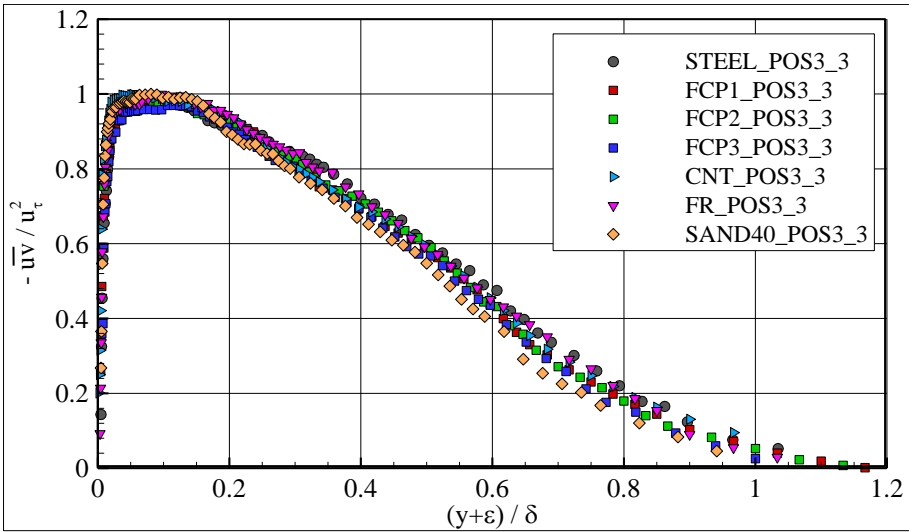


Figure 5.48 : Reynolds shear stresses in inner scales.

5.10 Conclusions

Turbulent boundary layers of the antifouling (fouling-release and nanostructured fouling-release) coated surfaces along with smooth and rough reference surfaces growing in zero-pressure-gradient condition were measured by 2D LDV and the characteristic findings were presented. The main objectives of these measurements were to investigate the turbulent boundary layer characteristics of the fouling-release coatings and the effect of their roughness properties on their boundary layers and frictional drags using consistent analysis methods across all tested surfaces.

In terms of the roughness properties, the entire tested coated surfaces other than the CNT coated one had rather small roughness amplitude parameters; some of them even being smoother than the smooth reference STEEL surface. All of the measured fouling-release surfaces except CNT had an important contribution from the long wave-lengths. The FR coated surface appeared to reserve much shorter wavelength components in addition to the long wavelengths. FCP2 and FCP3 were very similar in terms of their spectral properties whereas FCP1 had a similar power spectral density function to the one of the FR in the long and middle wavelength part of the spectra. On the other hand, the Rt_{50} values of the FCPs were rather lower than the other tested surfaces except the smooth reference. However, it was observed that the Rt_{50} parameter did not show any correlation with the frictional drag properties of the FCP and FR coated surfaces.

The results showed that the frictional drag properties of all coatings tested were exceptionally good, displaying at most 6.6% higher local frictional drag coefficient compared to the smooth reference STEEL. In particular, the drag benefit provided by two of the nanostructured amphiphilic coatings, FCP1 and FCP2, with fluorinated copolymer, compared to the other tested coatings, was remarkable. The general trend in the frictional characteristics of these superior coatings over the tested Reynolds number range were found to be relatively different than the other surfaces tested, in particular at higher Re number warranting further investigations.

The basic boundary layer parameters (e.g. displacement and momentum thicknesses), on the other hand, were found to be insensitive to the texture types of the coatings.

The universality of the velocity defect law was validated with the present data. A good correlation was obtained between the local skin friction coefficients and the

shape parameters of the test surfaces. The mean velocity profiles in velocity defect form presented using Rotta outer length scale also displayed good collapse through the logarithmic and outer part of the boundary layer, within the uncertainty level, providing support to the universality of the velocity defect law.

The rapidly decreasing roughness function, ΔU^+ , trends of FCP1 and FCP2 as k_s^+ increases were remarkable. However, the narrow k_s^+ range investigated somewhat obscured the global trend of the results of these coatings; warranting further investigations at a higher Reynolds number range. The ΔU^+ values in the low roughness Reynolds number range were generally spread around Colebrook's and Dey's curves; however no correlation with the suggested relations was observed. Much lower values of ΔU^+ were obtained compared to the regression lines of Colebrook and Dey with the fouling-release marine antifouling in the examined higher k_s^+ range. The results showed that the complex engineering surfaces, such as marine antifouling coatings, may produce non-zero ΔU^+ values despite their very low k_s^+ values and there is a great need to develop new correlations, whose validity includes (old or new generation) marine antifouling by substantially expanding the present data.

The results indicated that there exists no difference in the streamwise normal Reynolds stresses, \overline{uu}^+ of the coated and smooth surfaces being valid from $(y + \varepsilon)^+ \cong 40$, except the Reynolds number dependency observed for the SAND40 surface. A decreasing trend of the near wall peaks at $(y + \varepsilon)^+ \cong 18-20$ was generally observed as the k_s^+ values increased. No distinctive differences were observed between the \overline{uu}^+ profiles due to the surface roughness in the overlap and outer region of the boundary layer when they were expressed in outer scaling. The \overline{vv}^+ profiles presented a large plateau with a constant value for approximately $100 < (y + \varepsilon)^+ < 1000$ for all cases. A slight roughness Reynolds number dependency up to $(y + \varepsilon)^+ \approx 100$ was also present in the wall-normal fluctuations when the data were expressed in inner scaling. However, very high roughness Reynolds number values and highly different texture properties of the SAND40 surface compared to the other tested surfaces led to lower \overline{vv}^+ values over the range $(y + \varepsilon)/\delta > 0.15$, when the data were expressed in outer scaling. All of the Reynolds shear stress profiles had a plateau with a peak value around 0.95 to 1 at $0.03 < (y + \varepsilon)/\delta < 0.16$ and no significant difference was observed between the tested surfaces in the

outer layer of the boundary layer. Accordingly, it can be said that the present work generally validate the outer layer similarity for the transitionally rough surfaces.

6. ZERO-PRESSURE GRADIENT FLAT PLATE TURBULENT BOUNDARY LAYER MEASUREMENTS FOR TURBULENCE SPECTRUM CALCULATION

6.1 Introduction

An additional set of zero-pressure gradient turbulent boundary layer experiments was carried out by using 2-dimensional Laser Doppler Velocimetry (LDV) for collecting data that is suitable for turbulence spectra calculation. The most important criteria for this purpose were collecting a large and long-time sample data population at the needed locations in the boundary layer with a high enough data rate. A high data rate is essential in order to be able to resolve the turbulent motion and thus obtain the turbulence spectra up to higher frequencies whereas a large sample population serves to reduce the variance of the spectrum providing reliable results.

The experiments were conducted in the Emerson Cavitation Tunnel of Newcastle University by using a new flat plate test set-up and 2D LDV for the investigation of the turbulence spectrum along with the frictional drag and boundary layer properties of the tested surfaces. The experiments were carried out between November 2011 and April 2012. Information about the Emerson Cavitation Tunnel may be found in Chapter 5. The set-up of these experiments was rather similar to that was given in Chapter 5; however several improvements, e.g. reducing vibration with a more rigid model, using a probe rotation for reducing uncertainty and using smaller seeding particles, were done in order to have a test set-up that is more suitable for turbulence spectra measurement.

Six different surfaces were included in the tests, which consist of one smooth reference, one sand grit surface and four surfaces coated with anti-fouling coatings including Self-Polishing Co-polymer (SPC) and Foul(ing) Release (FR) types either by spraying or rolling. In complementing the boundary layer tests, roughness measurements of these surfaces were carried out by using a laser profilometer.

This chapter presents the experimental details, analysis procedure and results of the mentioned flat plate boundary layer experiments and the related roughness measurements. The turbulence properties such as the Reynolds normal and shear stresses, triple correlations, skewness and flatness factors and time scales are also presented in the results as well as the autocorrelation functions, turbulence spectra and transfer functions between roughness and turbulence spectrum.

The chapter starts with the details of the experimental set-up in Section 6.2 and followed by the Section 6.3 summarizing the preliminary measurements which consists of the inflow and pressure gradient measurements results. In Section 6.3, the roughness measurements and the results of the roughness analysis are given whilst boundary layer data collection and analysis procedures are told in Section 6.5. The uncertainty levels of the measured and calculated quantities are presented in Section 6.6. The boundary layer measurement results including the basic boundary layer characteristics and skin friction drag properties along with the spectral analysis of turbulence and transfer functions are investigated in Section 6.7. Section 6.8 includes the summary of the results and main conclusions.

6.2 Experimental Set-Up

A new, much more rigid flat plate test bed with an overall length of 3.924 m was used in the experiments. The test bed had a nose section with an airfoil shaped leading edge that was deployed in order to slowly lead the incoming flow from the contraction part of the tunnel to the front part of the test bed. This set-up helped to reduce the vibration of the test bed by almost eliminating the flow at the behind of it and enabled to use the tunnel at lower impeller speeds for a higher inflow velocity by acting like a smaller test section by decreasing the width of the original test section from 1.22 m to 0.81 m. The seeding density of the tunnel water in the test section was also more easily controllable with this set-up. The new testing bed also had a slightly inclined tail section of 0.9 m that extended into the diffuser end of the tunnel test section preventing separation at the trailing edge of the test bed. The improved properties of the testing bed enabled the use of inflow velocities up to 8 m/s without any vibration. However, the highest selected inflow velocity for the tests was 6 m/s due to the higher temperature changes at higher velocities during the required relatively long time for one boundary layer profile measurement, which took

approximately 2.5 hours. It was aimed to keep the temperature change in one Celsius degrees during one boundary layer profile measurement during the test campaign. The testing bed allowed 600 mm long and 220 mm wide flat plate test specimens to be fitted on it. The test specimens were fitted so that they were on the midline of the testing bed vertically and the trailing edge of the test specimens was located approximately at a distance of 200 mm to the beginning of the tail section. Six toggle screws and handles were used to hold the test specimen plate on the testing bed along with an attachment frame. The test plates were designed to be flush with the surface of the testing bed when not coated and shims were used in order to align the plates with the testing bed after the test specimens were coated. The steel testing bed surface was 120 grid sanded prior to the boundary layer experiments in order to make the surface as smooth as possible. A 36 grid sand paper with a length of 400 mm was used as a turbulent stimulator following the leading edge of the testing bed in order to thicken the boundary layer and hasten the transition to fully turbulent flow near the wall. A schematic of the test bed can be seen in Figure 6.1. Two photographs of the test bed are given in Figure 6.2 where the tail section can be observed at the right hand side and the leading edge, the turbulence stimulator (green colour) and the test specimen located on the test bed (red colour) are seen on the left hand side.

A total of six test specimens were used in the experiments which consisted of one smooth reference, one fully rough reference and four plates coated with several marine anti-fouling. The smooth reference was a perfectly smooth plate made up of acrylic and accordingly it is named as ACRYLIC in the thesis. The fully rough reference, namely SAND40, was prepared by glueing 40 grid sand paper with a special water resistant adhesive to a steel surface. The other four test specimens were arranged by coating 120 grid sanded steel plates, which can be seen in Figure 6.3, with one layer of anticorrosive and with one layer of tiecoat (in only fowl-release coating schemes) prior to the anti-fouling application. A state-of-the-art fowl-release antifouling coating was applied by spraying and rolling after the tiecoat and the acquired two test specimens were named as FR and FRR, respectively. The anticorrosive and tiecoat was also applied with the same type of roller for the FRR surface as can be observed in Figure 6.4. The third coated test specimen, namely HC, was coated with a hard coating, which is generally used in very large pipe systems in

marine environment for antifouling purposes, whilst the last one was coated with a Self-Polishing-Copolymer (SPC). The latter two were also applied by spraying.

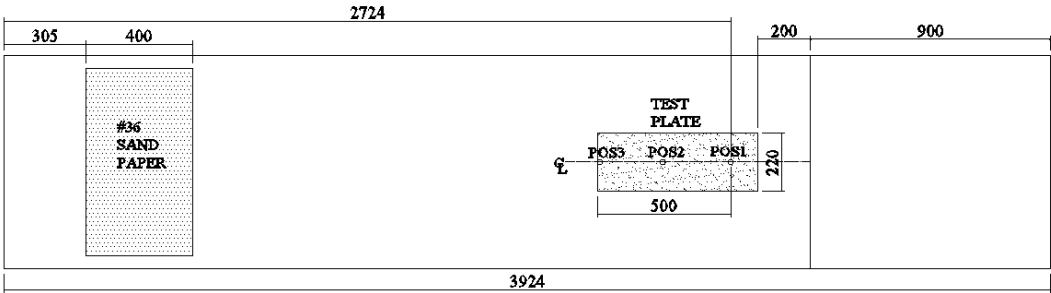


Figure 6.1 : Schematic of the test bed.



Figure 6.2 : Photographs of the test bed; tail section at the right hand side.

It may be mentioned here that all of the coatings used are commercially in use products. All of the test specimens had a testing surface of 600 mm by 220 mm. A groove was circling the plates for housing an “O” ring made of rubber in order to seal the plate and eliminate any flow between the front and back faces. The photographs of the test specimens may be seen in Figure 6.5.

The boundary layer measurements were performed at the midline of the test plates and at 500 mm distances from their leading edges. Accordingly, a distance of 2724 mm was achieved for the boundary layer growth. The measurements were carried out

for three freestream velocities; 2 m/s, 4 m/s and 6 m/s, so that it was possible to cover a relatively large range of Reynolds numbers for acquiring fully turbulent boundary layer flow. Accordingly, the length based local Reynolds number (Re_x) varied between 5.45×10^6 and 1.63×10^7 during the tests.



Figure 6.3 : The steel plates were sanded with 120 grid sandpaper before the anti-fouling application.



Figure 6.4 : The application of anticorrosive with roller.

The DANTEC 2D LDV equipment that was used for the velocity measurements was the same one that was used in the boundary layer experiments reported in Chapter 5 and detailed information about the LDV may be found in Section 5.4. A general view of the tunnel test section and the LDV equipment is presented in Figure 6.6. A different arrangement was used for the LDV probe in the experiments compared to the one explained in Chapter 5 and the probe was fixed with 45° rotation angle and 5° tilt angle, as can be observed in Figure 6.7, in order to reduce the uncertainty in the wall normal velocity component.

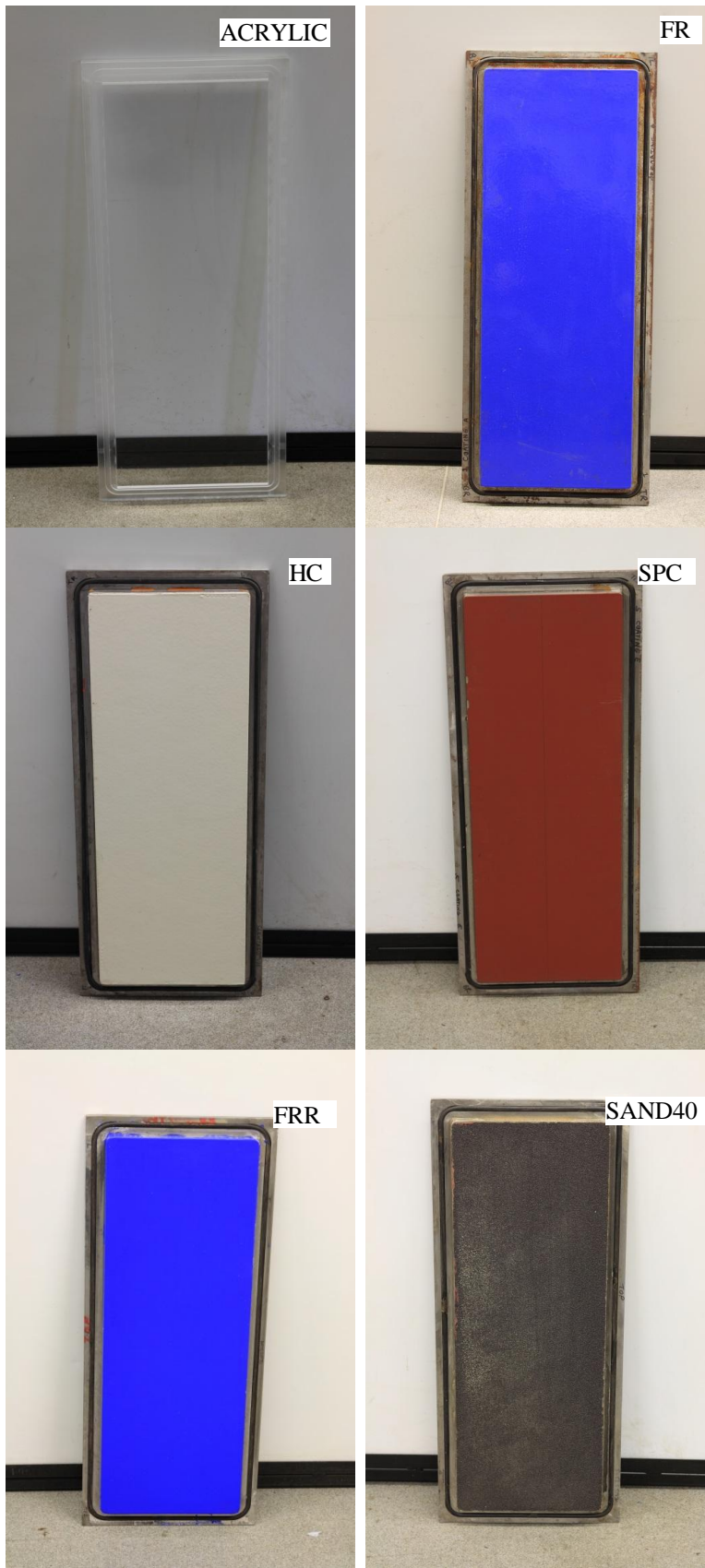


Figure 6.5 : The test specimens.

Smaller seeding particles with a diameter of $2\ \mu\text{m}$ were used in the experiments with the aim of increasing the data rate during the measurements. The particles were supplied by Potters Industries and made of glass with spherical shape which was coated with a higher density of silver. The seeding was injected to the tunnel test section from a valve prior to the measurements. The seeding material and the equipment for adding seeding can be seen in Figure 6.8.

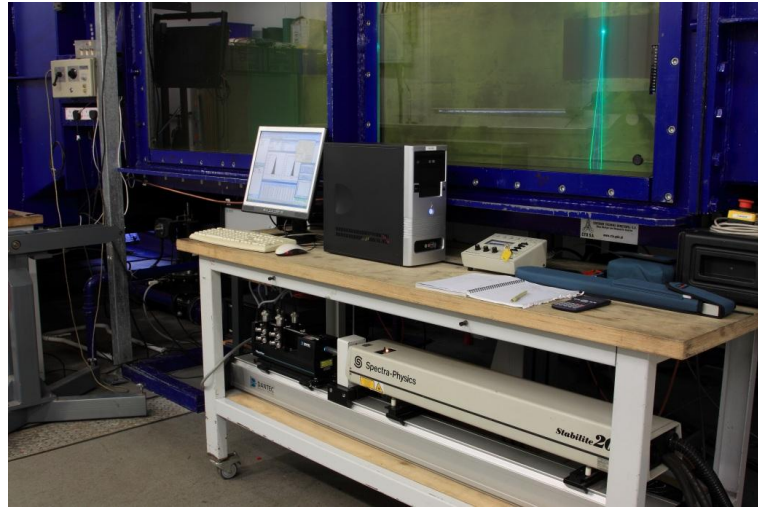


Figure 6.6 : A general view of the tunnel test section and LDV during the measurements.



Figure 6.7 : LDV probe with 5° tilt and 45° rotation.



Figure 6.8 : The equipment used for adding seeding to the tunnel water and the seeding material.

6.3 Preliminary Measurements

Three sets of preliminary measurements were carried out before the experimental campaign. The first set was the inflow measurements performed in order to observe the uniformity of the flow along the test bed and evaluate the inflow turbulence properties. This set was carried out by Mr. G. Politis and a short summary about the inflow properties that was reported in Politis (2010) will be given here.

The second set of measurements was carried out for checking the freestream turbulence properties along the test bed where the test specimens were to be mounted. The details of these experiments will be explained in Section 6.3.1 together with the previous ones.

The purpose of the last set of preliminary measurements was to check the pressure gradient along the test bed and ensure zero-pressure gradient flow during the boundary layer experiments.

6.3.1 Inflow measurements

In order to test the effect of the new testing bed on the inflow properties and to investigate the homogeneity of the flow throughout the test section, a set of LDV measurements were carried out at five different planes, which can be seen in Figure 6.9 (Politis, 2010). As can be observed from the top schematic in Figure 6.9, the testing bed (or insert) decreases the width of the test section from approx. 1.22 m to 0.81 m. This special design also eliminates the flow behind the test bed with a cascade of vanes at the back side. The streamwise (x) and wall-normal (y) flow

velocities were measured for cross-sectional areas of 460 mm (in y direction) by 614 mm (in z direction) on these planes. The properties of the flow were measured between 2 m/s and 8 m/s inflow velocities. Data were gathered for each velocity channel until 10000 samples were collected or for 30 seconds, whichever came first. The data rate changed between 0 and 800 Hz depending on the measurement point. At least 2 and at most 10000 velocity samples for each component were collected at each point (Politis, 2010).

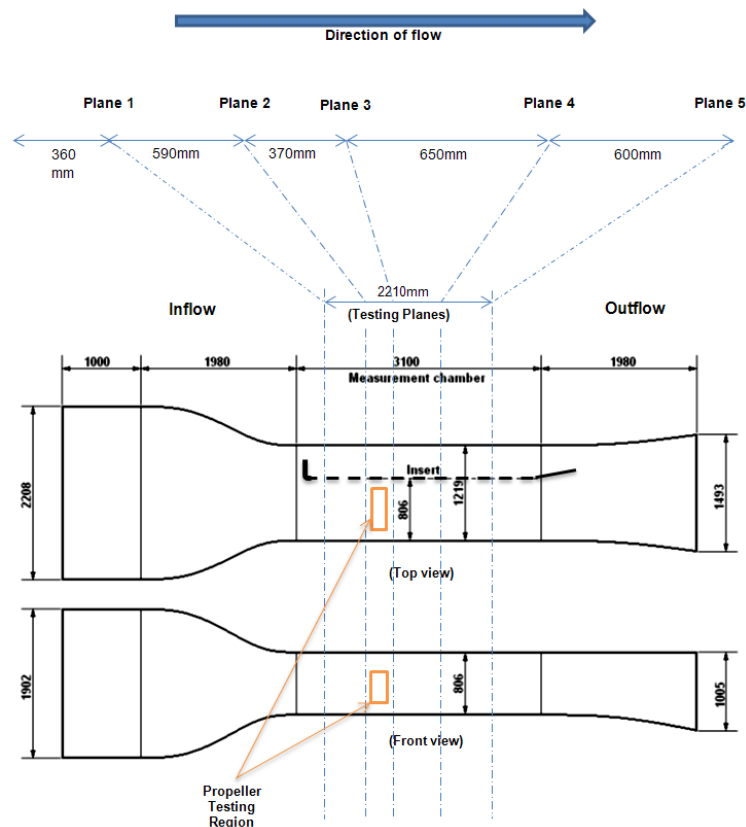


Figure 6.9 : Inflow measurement planes (from Politis, 2010).

In Table 6.1, the average streamwise(U) and transverse(V) velocities are presented along with the streamwise(TI_x) and transverse(TI_y) turbulence intensity percentages. The turbulence intensity percentages were calculated by dividing the root-mean square of the velocity fluctuations multiplied with 100 with the mean velocity at the calculation point. The presented values in the table are the averages of the whole values in one measurement plane. It is observed that the average TI_x changes between 2.14% and 3.51% whilst TI_y varies between 2.07% and 3.58% for 2, 4 and 6 m/s inflow velocities. It can be said that the measured turbulence intensity levels are in a rather acceptable range for a water tunnel. It is observed that there is a slight change in the average streamwise and transverse velocities between the planes. For the

streamwise velocity this variation is quite low and stays below 1.7%, however the difference in the average transverse velocity between the planes may be seen as slightly high. The reason of this variation is the strengthening high velocity field located at the bottom of the test section which was showing the very same behaviour without the testing bed and can also be accepted as normal for water tunnels.

Table 6.1 : The mean velocities and average turbulence intensities across the test section (Data from Politis, 2010).

Plane	U_e (m/s)	U (m/s)	V (m/s)	TI_x (%)	TI_y (%)
1	2	1.99	0.06	2.14	2.07
	4	3.98	0.04	2.75	2.51
	6	6.02	0.11	2.33	2.36
2	2	1.99	0.03	2.83	2.71
	4	3.98	0.03	2.71	2.47
	6	6.00	0.05	2.43	2.29
3	2	2.00	0.02	2.85	3.08
	4	4.00	0.03	2.89	3.17
	6	6.02	0.04	3.07	2.78
4	2	1.99	0.05	3.35	3.58
	4	3.99	0.07	2.93	3.32
	6	5.95	0.09	3.41	3.08
5	2	2.02	0.04	3.45	3.16
	4	3.99	0.08	3.32	3.20
	6	5.92	0.11	3.51	2.87

Presented in Figure 6.10 are the contour plots of the velocity distributions for the measurement planes. The streamwise velocity distributions are plotted at the top figures while the transverse velocity distributions are located at the below ones. It is observed that the flow at the vertical midline of the tunnel ($z=0$), where the boundary layer measurements were taken, are highly uniform across the planes. The flow retains its uniformity while developing along the test section in most part of the cross-sectional planes. High and low velocity fields are observed at restricted areas located just near the top and bottom tunnel walls. There seems to be a low transverse velocity field growing across the planes located at the bottom right between approximately $-50 < y < 100$ mm. However, it does not penetrate to the midpart of the cross-sections and will not jeopardize the experiments.

The second set of inflow measurements was performed just prior to the beginning of the boundary layer experiments. The test were carried out at three different streamwise positions which were located at distances of 2650 mm (POS1), 2395 mm (POS2) and 2160 mm (POS3) respectively from the leading edge of the test bed.

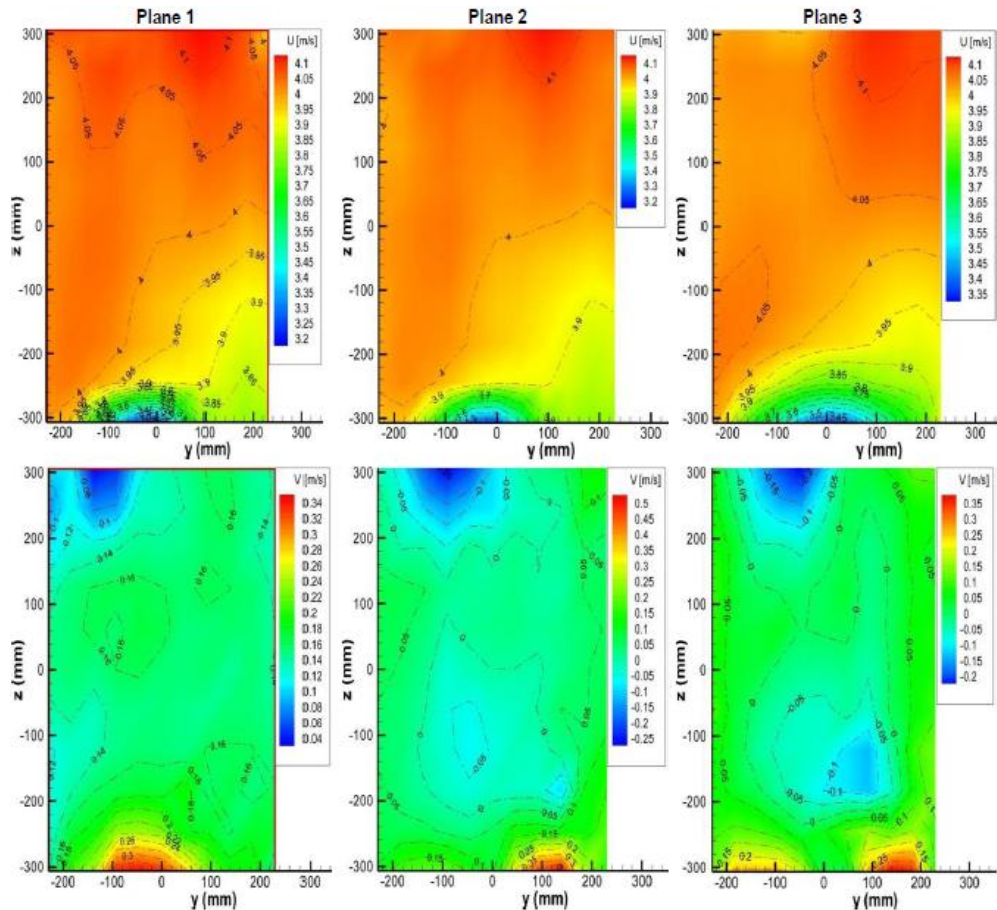


Figure 6.10 : The streamwise (plots located at the top) and transverse velocity distributions across the tunnel test section for the first 3 planes at 4 m/s inflow velocity (from Politis, 2010).

These positions correspond with the streamwise location of the test specimen on the test bed. Data were collected at these streamwise positions for five different vertical locations which were $z = -10, -5, 0, 5$ and 10 mm. The vertical midline of the test bed (and the tunnel test section) corresponded to $z=0$ and z axis was negative towards the bottom wall of the tunnel test section. In the direction normal to the wall (y), data were gathered at 58 points beginning from the outer layer of the test bed boundary layer at 40 mm from the wall and ending at 400 mm. The measurements were done at three inflow velocities of $2, 4$ and 6 m/s which will be used in the boundary layer experiments. The experiments were performed by using the 2D DANTEC LDV system. 50000 data were collected at each measurement point for reliable statistics, with a high validation (above 90%) and relatively high data rate (between 0.2 and 3 kHz).

In Figure 6.11, the nondimensional streamwise and transverse velocities can be observed for $2, 4$ and 6 m/s inflow velocities at the test positions. The plots located at

the left hand side include the streamwise velocity component whilst the transverse one is located at the right. The non-dimensionalization was performed with the mean streamwise velocity at $y=80$ mm and $z=0$ at each streamwise position. The velocity profiles at various z positions are given with the same colour since they are tightly packed together and almost no difference is observed at different z positions for a fixed streamwise location.

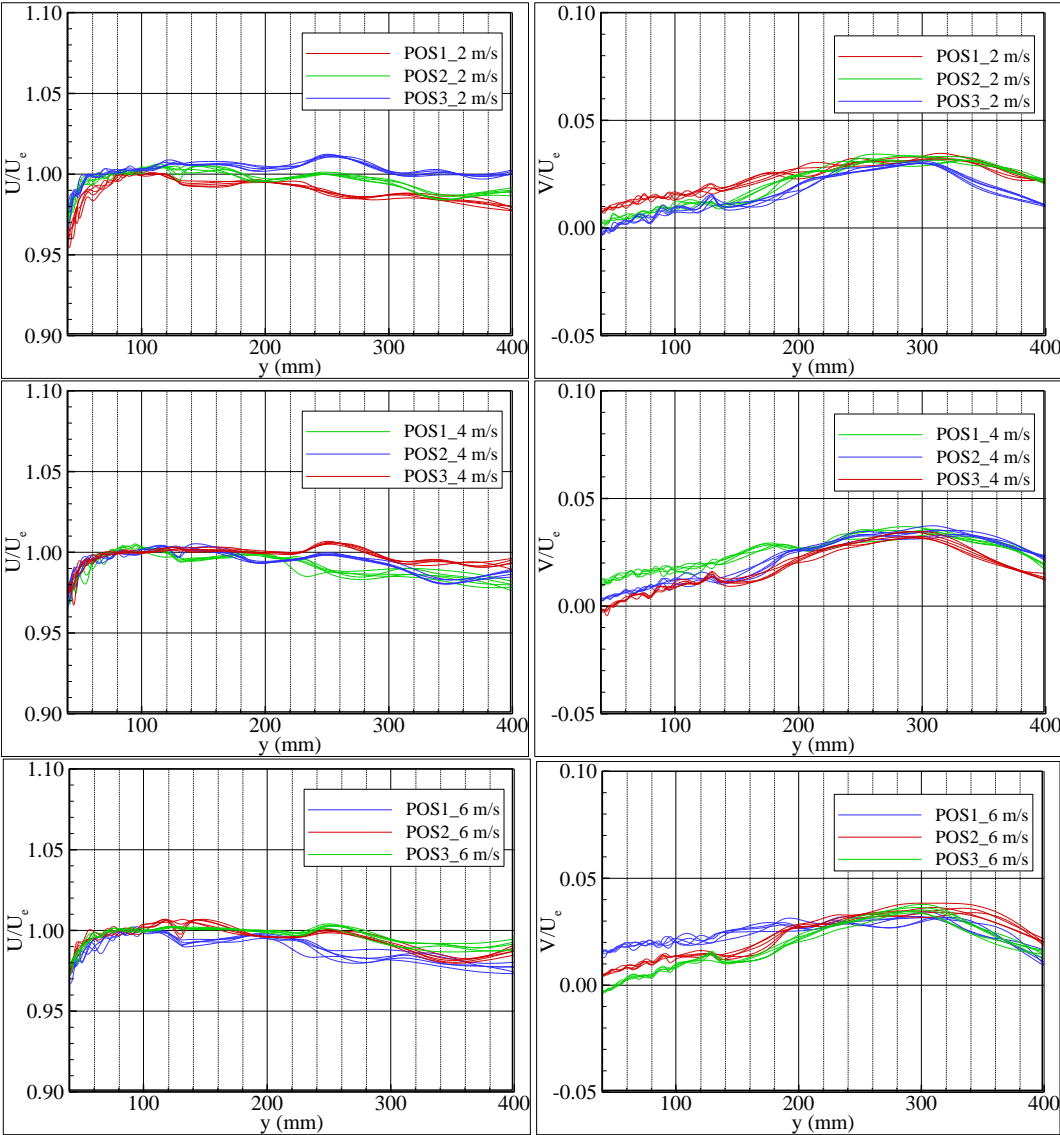


Figure 6.11 : Variation of nondimensional streamwise (left) and transverse velocities.

As can be observed from the figure, the boundary layer of the test bed extends approximately up to 50-55 mm from the wall for all positions and inflow velocities. The non-dimensional streamwise velocity distributions are very similar at the three streamwise test positions until about $y=200$ mm from the wall. After this point there exist slight fluctuations in the streamwise velocity profiles, however the difference in

the non-dimensional velocity between the streamwise positions is at most 3% and generally much lower than this value. The transverse velocity magnitudes are generally about 1 to 3% of the streamwise velocity up to $y=200$ mm and there are slight differences in the non-dimensional transverse velocities measured at different streamwise locations up to this wall-normal coordinate. For $200 < y < 300$ mm, it can be said that the transverse velocity settles down in a value around 4% of the streamwise velocity followed by a drop to 2-3% after $y=300$ mm. At 2 and 4 m/s freestream velocities, there is about 1% difference between the non-dimensional transverse velocity profiles measured at POS3 and the others however this difference totally vanishes at 6 m/s in flow velocity and the profiles form a thick bunch beginning from $y=200$ mm.

Presented in Figure 6.12 are the streamwise (left column) and transverse turbulence intensities at various test positions. It is observed that the streamwise turbulent intensities (TI_x) are higher than average values that were presented in Table 6.1 at the outer edge of the test bed boundary layer. The measurement grid that was used in determining the average values in Table 6.1 were beginning from 50 mm wall normal distance whilst the present inflow measurement grid starts from 40 mm normal distance to test bed wall. Moreover, it is seen from Figure 6.12 that the streamwise turbulence intensity quickly drops from 5% to 3% in average in this 10 mm distance which may explain the difference in the TI_x values compared to the average values. The streamwise turbulence intensity fluctuations settle down beginning from $y=80$ mm and vary around 1.4 to 1.7% for 2 m/s inflow velocity and 1.4 to 2.0% for 4 and 6 m/s inflow velocities at all streamwise positions. Since the present inflow measurements were carried out very close to the vertical midplane of the tunnel test section where the flow behaviour is much more uniform, it can be accepted as normal that the measured TI_x values are lower than the average values calculated from the large mesh measurements. The transverse turbulent intensity (TI_y) of the measured profiles is about 2.8% for 2 m/s inflow velocity and 2.6% for 4 m/s and 6 m/s freestream velocities at $y=40$ mm. After $y=100$ mm the TI_y values converge to average values of 0.95%, 0.99% and 1.02% for 2, 4 and 6 m/s inflow velocities respectively. Although, these values are almost constant until 400 mm for 2 and 4 m/s inflow velocities, at 6 m/s freestream velocity there exists an increasing trend followed by relatively large fluctuations around 1.4% average TI_y value. The

overall TI_y values measured are lower than the global average transverse turbulence intensities of the large measurement grid. This is again a highly expected situation due to the location and grid size of the present measurements.

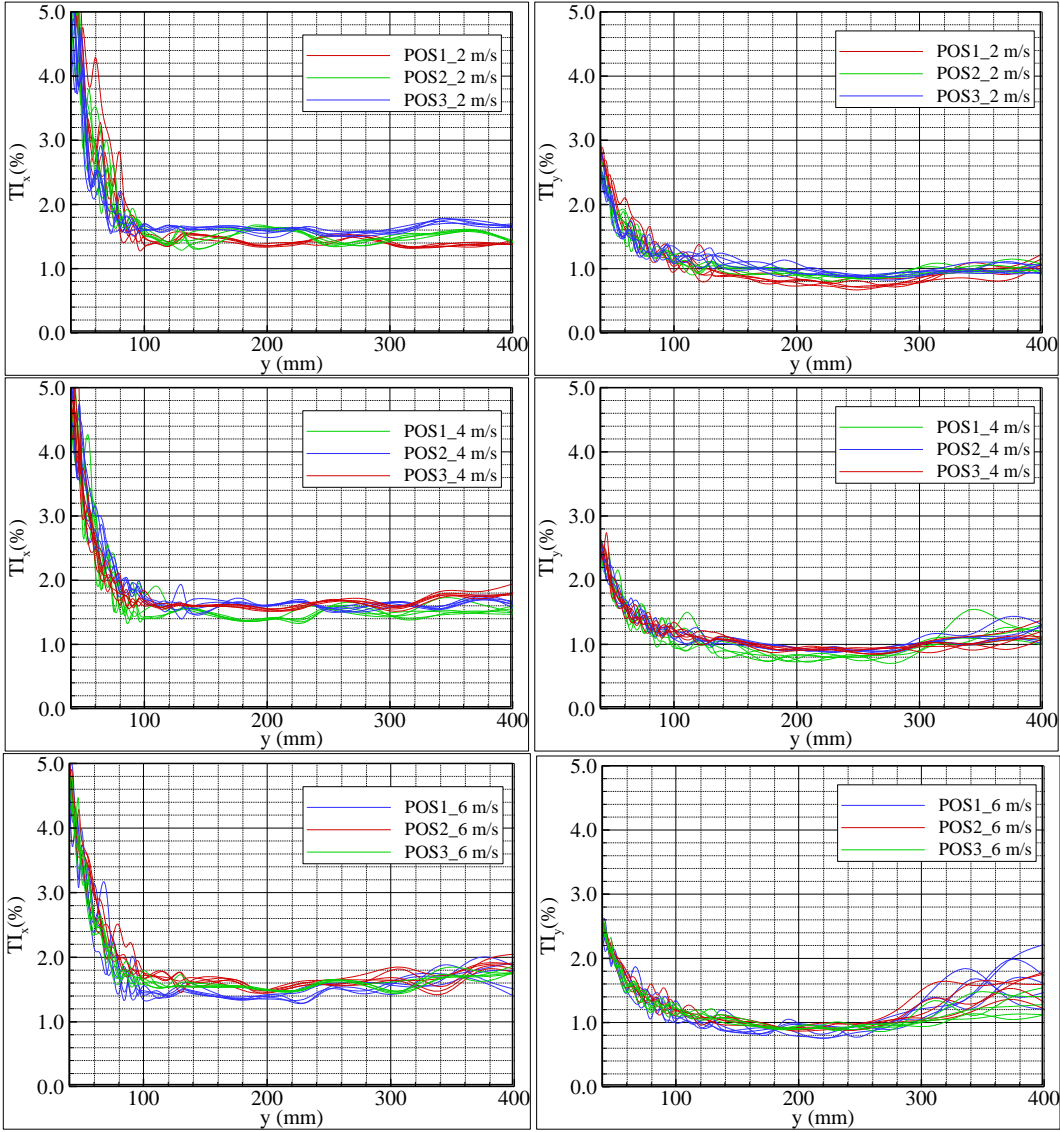


Figure 6.12 : Variation of streamwise (left) and transverse turbulence intensities.

6.3.2 Acceleration parameter measurements

It can be assumed that the flow developing on the present flat plate test bed which is perfectly aligned with the tunnel test section walls will be a zero-pressure gradient flow. However, it is important to check the level of the pressure gradient since corrections may be needed in the skin friction drag calculation methods in the presence of favourable or adverse pressure gradients (Dixit and Ramesh, 2009). Moreover, the existence of both may also change the turbulence characteristics up to a certain degree (Nagano and Houra, 2002; Stefes and Fernholz, 2005).

Accordingly, in order to control the zero (or near zero)-pressure gradient condition, 2D LDV measurements were performed at 80 different streamwise positions at $y=60$ mm distance from the test bed wall for inflow velocities of 2, 4, and 6 m/s. This led to a 400 mm distance parallel to the wall with 5 mm intervals. The level of the pressure gradient can be witnessed by the acceleration parameter (K) which is defined as:

$$K = \frac{\nu}{U_e^2} \frac{dU_e}{dx} \quad (6.1)$$

where ν is the kinematic viscosity and U_e is the streamwise velocity. The flow is considered to be zero-pressure gradient required that $K < 1 \times 10^{-8}$ (Schultz and Flack, 2007; Flack et al., 2007). The measured acceleration parameters are presented in Table 6.2. It is observed that the acceleration parameter stays below 1×10^{-8} for the entire test velocities and thus the zero-pressure gradient condition is assured during the measurements.

Table 6.2 : Acceleration parameters.

U_e (m/s)	K
2	9.36×10^{-9}
4	7.59×10^{-9}
6	6.05×10^{-9}

6.4 Roughness Characterization of the Test Plates

In order to calculate the roughness characteristics of the tested flat plates a series of roughness measurements were performed by using Uniscan OSP100 Laser Profilometer. It was possible to measure the roughness profiles of the actual test specimens that were tested in the boundary layer measurements by taking advantage of the modified traverse mechanism of the profilometer (Figure 6.13). The two legs located at the left hand side in the figure, which haul the traversing mechanism together with a third leg, were mounted about 6 cm outside with steel brackets. By this way it was possible to fit the test specimens on the tray of the profilometer for roughness measurements. 102 roughness profiles with a length of 91 mm were measured for every tested surface with 25 microns and 0.5 mm spatial resolution in the streamwise direction and transverse direction, respectively. The scan speed of the

profilometer was set to 12.7 mm/sec and two line averages were taken for each profile measurement.



Figure 6.13 : The OSP100 profilometer with the modified legs of the traverse mechanism.

An in-house developed MATLAB code was used in the analysis of the gathered roughness profiles. The analysis included the subtraction of the elevation and the meanline of the profiles followed by a noise removal according to the Chauvenet Criteria (Colemann and Steele, 2009). The roughness amplitude and texture parameters, autocorrelation (AC) and power spectral density (PSD) functions were calculated at the selected four cut-off lengths, 2.5 mm, 5 mm, 8 mm and 50 mm. A moving-average filter with 81, 161, 257 and 1601 points was used for the 2.5 mm, 5 mm, 8 mm and 50 mm cut-off lengths, respectively.

The roughness parameters, presented in Table 6.3, were calculated in the MATLAB code after the filtering procedure with various cut-off lengths. The detailed explanations and definitions of the roughness parameters presented in the table were given in Chapter 4. The roughness properties of the smooth reference ACRYLIC plate was not needed to be measured since it was a perfectly smooth surface with much lower roughness heights than the laser profilometer can measure. By evaluating the roughness amplitude parameters (R_t , R_a , R_q), it can be concluded that

the SAND40 surface is much more rougher than the others, as expected. The roughest coated surface is the FRR, which displays rather higher amplitude parameters compared to the other coated surfaces due to the application method of rolling. If Table 6.3 is considered for the roughness amplitude parameters of the FR, HC and SPC coated surfaces, it can be observed that the cut-off length has an important effect on the comparative properties of the surfaces. For instance, the HC coated surface appears to be smoother than the SPC and FR coated ones for 2.5 mm and 5 mm cut-offs, however it is rougher than the mentioned two surfaces if 8 mm and 50 mm cut-offs are considered. The roughness amplitude ranking between the SPC and FR test specimens also vary depending upon the cut-off length. The SPC specimen is rougher than FR for 2.5 mm cut-off whilst for 5 mm and 8 mm cut-offs it has only slightly higher R_t values and for 50 mm it appears to be smoother than FR. Generally, it can be said that the roughness amplitude parameters of the FR, HC and SPC are coherently in the same order of magnitude for all the considered cut-offs.

Observing the skewness parameters (Sk) of the test specimens reveals that the entire surfaces are positively skewed, except SPC and FR when analysed with 50 mm cut-off length. The SAND40 surface has a relatively high positive skewness parameter which is equal to or slightly larger than 0.5 at all cut-off lengths, similar to the results of Chapter 5. On the other hand, FRR test specimen is the one with the most positively skewed roughness height probability density function (PDF) with a Sk value around 1.0. FR, SPC and HC specimens have skewness values close to zero, implying that the roughness height PDFs are close to being evenly distributed around the mean.

The kurtosis parameters (Ku) of the test specimens are generally close to 3, except FRR, meaning that their peakednesses are similar to that of a Normal distribution. The FRR coated test specimen has rather higher Ku parameter, higher than 4.5 for the entire considered cut-offs, which implies that the roughness height PDF of this surface has a sharp peak with thinner tails. The kurtosis values slightly decrease as the cut-off length increases.

As indicator of openness of the surfaces, the Sm , De and S parameters are presented in the table. The definitions of these parameters were explained in detail in Chapter 5. SAND40 test specimen is the one with the most open texture. FRR also has higher

S_m parameter than the other coated test specimens do at all cut-off lengths. For the smallest two cut-off lengths, the FR surface has higher S_m parameters than the HC and SPC specimens; however, HC surface seems to be more open when the roughness analysis is performed at higher cut-off lengths. The correlation length parameter, $\tau_{0.5}$, is also an indicator about the openness of the surface texture. The FRR surface displays the highest correlation length except for the 50 mm cut-off. The correlation length highly depends on the long wave cut-off and increases as the cut-off length increases for the entire surfaces. However, the ranking of the specimens relying on the correlation length also changes between the selected cut-off lengths. By considering the results of the frictional drag properties of the test specimens which will be explained in Section 6.7, it can generally be said that it is neither a low roughness height parameter nor a large openness parameter that results in a low skin friction drag value but the complex balance of the surface height and texture properties.

The variance of the slope distribution (m_2) for the SAND40 specimen is almost 2 orders larger than those of the other specimens. This parameter does not show a big reaction to the variations in the cut-off length.

FR and SPC surface generally have very close m_2 values; FRR coated surface has larger values compared to these two at all cut-offs and the opposite applies for the HC specimen. The exactly same behaviour is also observed for the variances of the curvature distributions (m_4) of the surfaces. The zeroth moment is theoretically equal to the variance of the roughness height distribution, Rq^2 , and shows similar behaviour with the Rq . The FRR specimen has the highest bandwidth parameter (α) at all cut-off lengths.

Presented in Figure 6.14 and Figure 6.15 are the autocorrelation functions of the test specimens for 2.5 mm, 5 mm, 8 mm and 50 mm cut-off lengths. The plots in Figure 6.15 show a closer look of the part of the autocorrelation function (AC) that specifies the correlation length. Generally, it can be said that the spray applied coatings FR, SPC and HC have similar AC trends especially at the smaller two cut-off lengths whilst FRR and SAND40 surfaces display entirely different trends.

Table 6.3 : The roughness parameters at various cut-off lengths.

		$Rt(\mu\text{m})$	$Ra(\mu\text{m})$	$Rq(\mu\text{m})$	Sk	Ku	$Sm(\mu\text{m})$	De (#/mm)	S (μm)	$m_0(\mu\text{m}^2)$	m_2	$m_4(1/\mu\text{m}^2)$	α	$\tau_{0.5}(\mu\text{m})$
Cut-off = 2.5 mm	FR	15.0	1.7	2.2	0.2	3.5	237.2	1871.2	566.6	4.7	1.69E-04	3.58E-08	5.8	84.8
	HC	13.7	1.5	2.0	0.2	3.4	229.7	1906.8	538.8	3.9	1.22E-04	1.78E-08	4.7	45.3
	SPC	17.1	1.9	2.5	0.1	3.5	211.2	1851.0	552.1	6.1	1.83E-04	2.65E-08	4.8	47.1
	FRR	43.5	3.7	5.8	1.1	7.8	247.5	1821.4	694.1	40.7	3.22E-04	7.67E-08	30.1	343.9
	SAND40	686.3	81.3	103.8	0.5	3.5	995.5	2585.4	409.6	10884.1	2.94E-02	2.27E-06	28.6	182.3
Cut-off = 5 mm	FR	20.9	2.5	3.2	0.1	3.2	367.4	2190.0	510.1	10.4	1.72E-04	3.61E-08	12.8	435.7
	HC	19.1	2.3	2.9	0.1	3.1	343.5	2200.2	484.3	8.7	1.23E-04	1.79E-08	10.3	444.9
	SPC	22.0	2.5	3.2	0.1	3.5	276.8	1942.4	547.3	10.7	1.84E-04	2.66E-08	8.3	227.5
	FRR	78.4	7.8	11.9	1.2	7.0	478.8	2364.6	484.6	172.1	3.55E-04	8.09E-08	110.6	609.8
	SAND40	746.8	91.2	115.7	0.5	3.5	1138.9	2747.2	394.3	13504.1	2.99E-02	2.24E-06	33.8	218.5
Cut-off = 8 mm	FR	25.8	3.3	4.2	0.1	3.0	481.9	2611.0	432.4	17.8	1.73E-04	3.63E-08	21.6	672.4
	HC	26.1	3.5	4.3	0.1	2.9	505.0	2842.2	379.2	19.1	1.24E-04	1.80E-08	22.3	866.1
	SPC	27.4	3.3	4.2	0.0	3.3	368.8	2364.6	469.3	18.5	1.85E-04	2.67E-08	14.3	609.5
	FRR	106.5	12.0	17.5	1.1	6.2	844.6	2793.8	413.3	366.1	3.89E-04	8.54E-08	206.9	832.1
	SAND40	767.2	94.0	119.4	0.6	3.5	1153.8	2775.0	385.3	14347.8	3.01E-02	2.29E-06	36.3	230.8
Cut-off = 50 mm	FR	46.7	8.0	9.6	-0.1	2.4	1167.7	5244.4	251.9	94.2	1.82E-04	3.75E-08	107.0	2983.9
	HC	56.4	10.4	12.9	0.3	2.7	1570.2	7779.2	139.7	173.8	1.32E-04	1.92E-08	192.1	3675.5
	SPC	45.3	7.6	9.4	-0.2	2.9	816.5	6832.6	163.0	95.5	1.92E-04	2.77E-08	71.9	3036.2
	FRR	159.7	23.2	31.2	1.0	4.5	2367.6	4676.4	258.2	1075.0	4.79E-04	9.71E-08	453.9	1639.8
	SAND40	804.3	99.1	125.8	0.6	3.5	1248.6	2887.0	369.2	15931.6	3.05E-02	2.32E-06	39.6	252.9

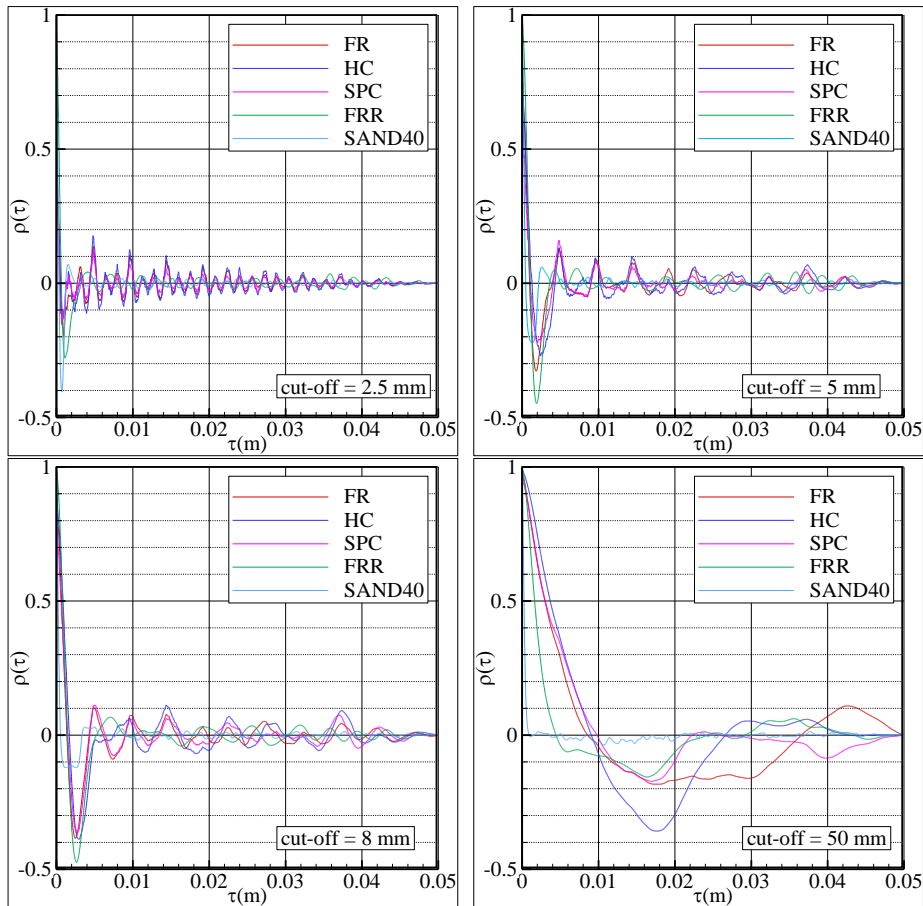


Figure 6.14 : Autocorrelation functions calculated for various cut-off lengths.

The FR and SPC test specimens exhibit AC with very similar characters up to $\tau=16$ mm at all cut-off lengths. Depending upon the AC of the test specimens, the correlation length parameters $\tau_{0.5}$ and τ_0 are expected to show different characteristics for each test surface. For instance, if $\tau_{0.5}$ is considered as the correlation length, SAND40 surface appears to have the larger correlation length compared to the FR, HC and SPC as a result of the 2.5 mm cut-off length analysis. However, if τ_0 is used instead of $\tau_{0.5}$, the vice versa is valid and the ranking of the surfaces in terms of the correlation length does not change substantially depending upon the cut-off length. For instance, SAND40 has the lowest correlation length (τ_0) at the entire cut-off lengths. SPC, FR and HC have very close values of τ_0 to each other at all cut-off lengths and FRR test specimen surface either display larger (cut-off 2.5 mm), very close (cut-off 5 and 8 mm) or smaller (cut-off 50 mm) τ_0 values to those of the SPC, FR and HC. On the other hand, it is notable that all of the test specimen surfaces except SAND40 coated one have an important contribution from the long wave-lengths.

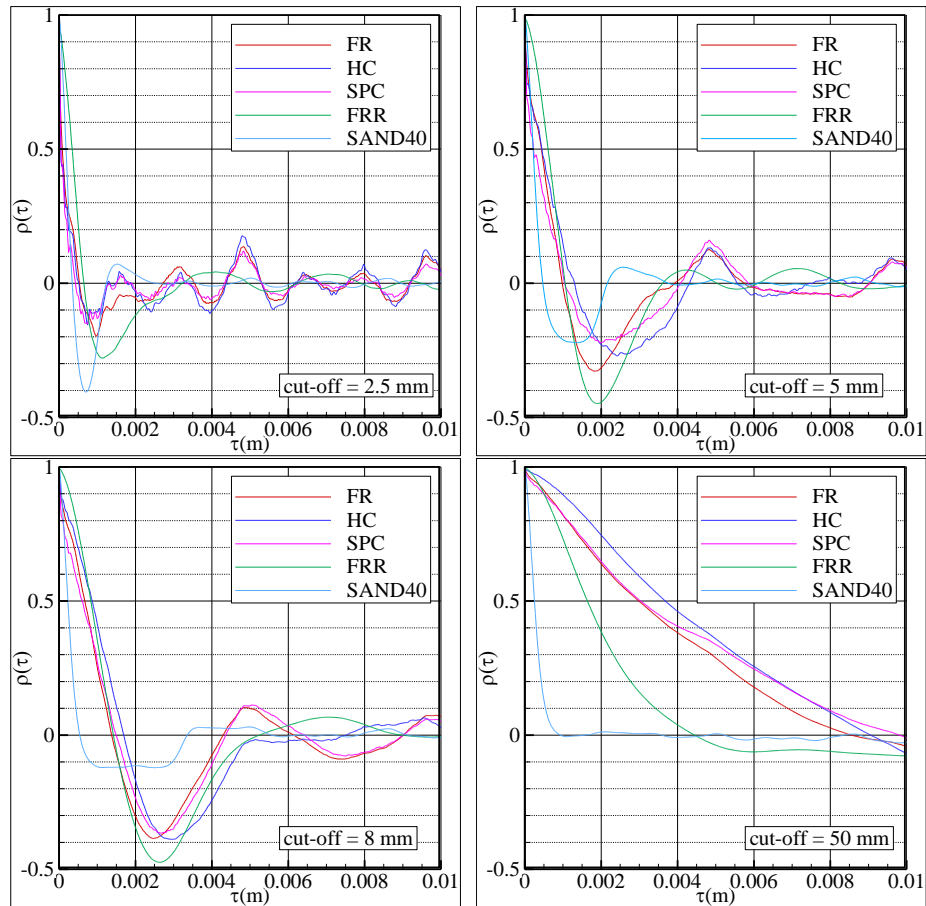


Figure 6.15 : Autocorrelation functions calculated for various cut-off lengths, closer look.

From Figure 6.1 to Figure 6.19 the power spectral density functions (PSD) of the surfaces are shown comparatively for 2.5 mm, 5 mm, 8 mm and 50 mm cut-off lengths respectively. The maximum wave number (k), which is 20000, in the plots were selected by taking the Nyquist theorem into account and given maximum wave number is the half of the sampling wave number ($1/25 \text{ } 1/\mu\text{m}$). The PSD and the AC of the measured roughness heights actually have the same information. However, investigation in the frequency domain presents a more pronounced graphic that may be easier to follow. The increasing long wavelength cut-off has an effect on the power of the long and middle range wavelength (or small and mid-range wave number $-k$ -) part of the spectrum. This effect completely loses its influence for $k > 400$ (or for wavelengths smaller than 2.5 mm). The cut-off length effect on the calculated spectrum is more clearly observed in Figure 6.20, at the top left figure. The plateaus of the spectrum located around $150 < k < 400$ elongate and move to the higher wavelength part (or to the left) of the spectra as the cut-off length increases

due to the changing balance of the spectra with the additional larger wavelengths counted in the calculation.

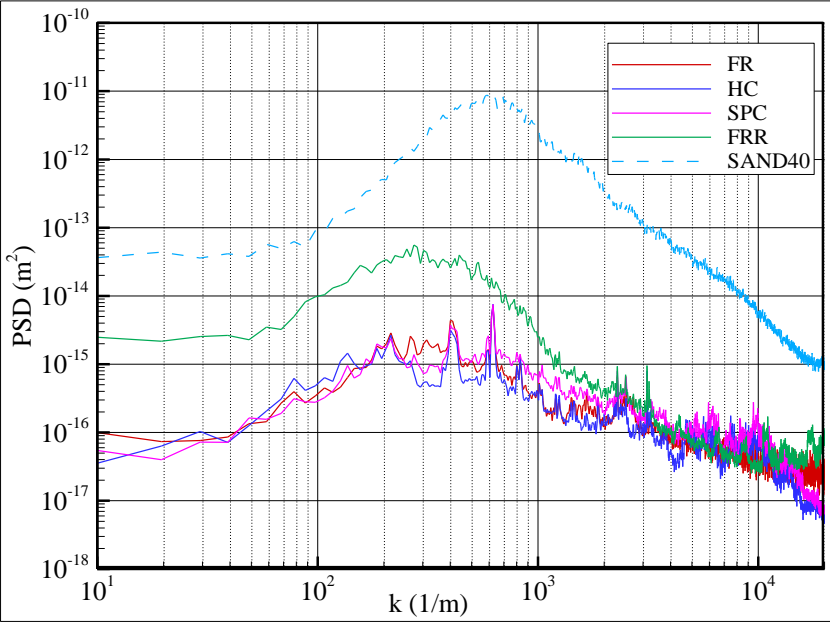


Figure 6.16 : Power spectral density functions calculated for cut-off length of 2.5 mm.

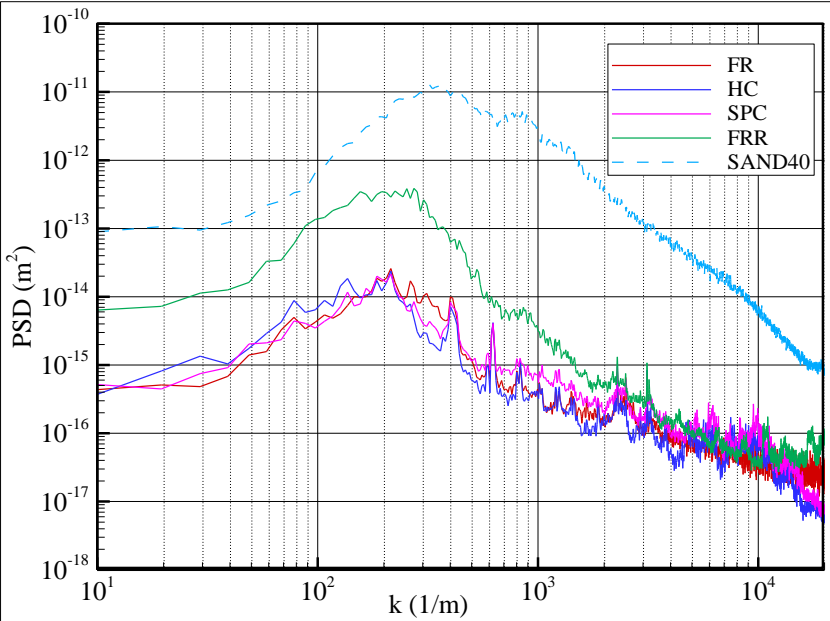


Figure 6.17 : Power spectral density functions calculated for cut-off length of 5 mm.

It is observed that the spectrum of the SAND40 test specimen displays a substantially different character compared to the others by containing much more power in almost all wavelength ranges due to its much larger roughness heights. FRR specimen also have rather higher power compared to the other coated surfaces up to approximately

$k=2000$, however the overall shape of its spectra is very similar to those of the other coated specimens.

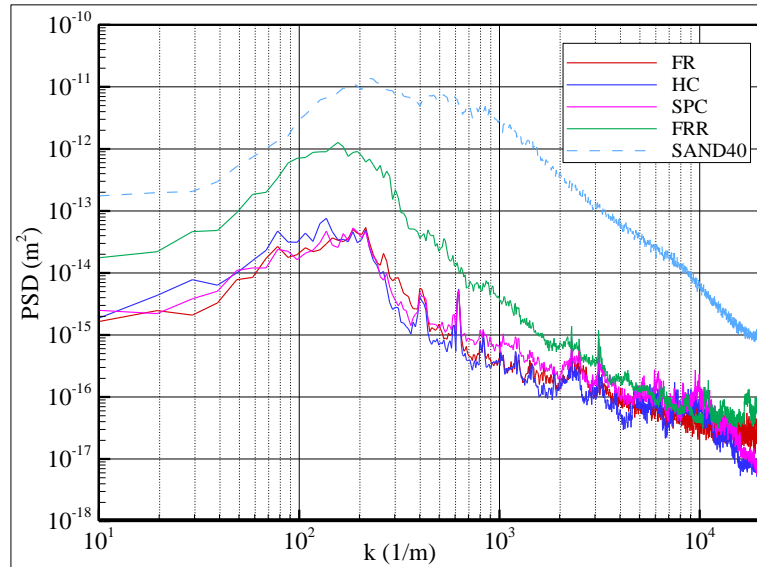


Figure 6.18 : Power spectral density functions calculated for cut-off length of 8 mm.

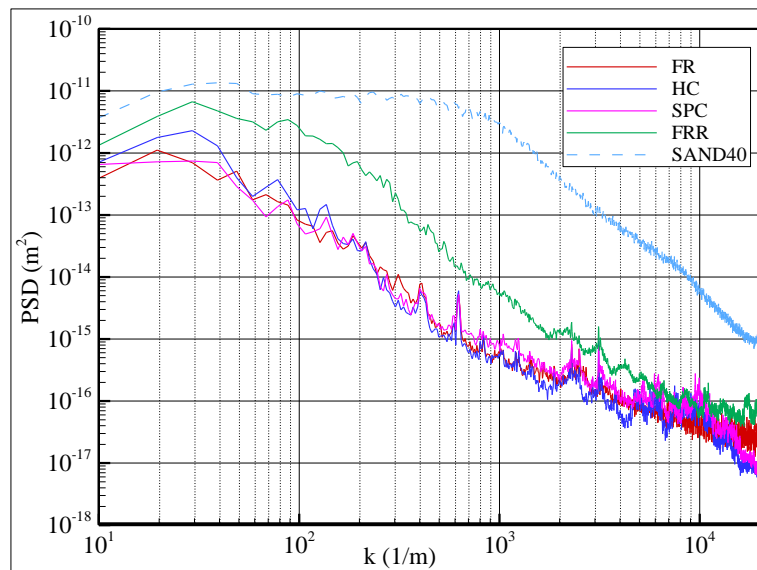


Figure 6.19 : Power spectral density functions calculated for cut-off length of 50 mm.

Shown in Figure 6.20 are the PSDs of tested surfaces presented in small groups in order to emphasize the similarities or dissimilarities in their trends. Only the top left plot offers the variation of the PSD due to the selection of the cut-off lengths and presents the spectra at various cut-offs. The other three plots include the PSDs only calculated at 50 mm cut-off. It is seen from the top right plot that the FR test specimen almost only have contribution from the long wave-lengths and does not show any peak after approx. $k=3200$. This is not inline with the results of the FR

coated test plate that was used in the experiments explained in Chapter 5. Since, the roughness measurements of this chapter were carried out with a smaller spatial resolution; it is not possible for this difference to arise from the lack of spatial resolution. This brings into mind that it may be due to the differences in the application, although both were prepared by spraying. On the other hand, this figure also emphasizes that the difference in the application of the FR anti-fouling coating significantly changes the spectral behaviour of the surface. The FR and FRR shares the peaks located at $k = 2500$ and 3200 whilst FRR also displays small peaks about $k = 11000$ and 17000 . The SPC specimen displays a very similar spectra to that of the FR up to $k = 5000$ with slightly higher power at each frequency; however it reserves peaks at higher wavenumber such as $k = 5200, 6200, 7400, 8250, 9500$ and 11200 . HC test specimen preserve peaks at $k = 2300, 2500$ and 3200 similar to the FR, with additional noisy peaks at around $k = 5000, 6000$ and 7500 .

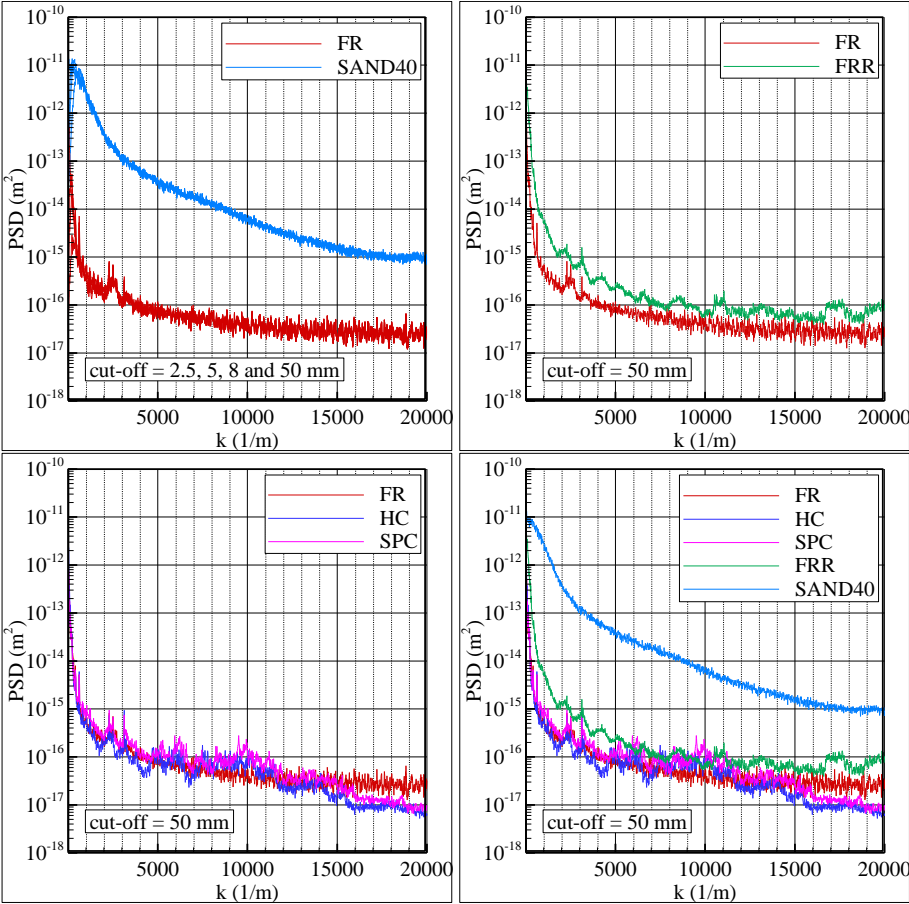


Figure 6.20 : Power spectral density functions observed in semi-log scale.

6.5 Data Collection and Analysis

The velocity-time data were gathered by using the two-dimensional DANTEC LDV system whose details were given in Section 5.4. The relatively old laser tube was replaced with a new one by Spectra-Physics in order to increase the attenuated laser power as well as increasing the stability of the beams. The adjustment of the laser beams were also done by DANTEC prior to the experiments.

In order to be able to gather data very near to the wall, it is inevitable to use a two-component laser probe, which has four laser beams that have 90° angles between each other in the xy plane, without a tilt angle. Although the use of a beam expander with the probe is rather necessary in order to decrease the probe volume for a more reliable measurement, it also increases the needed tilt angle for approaching to the vicinity of the wall. This essential tilt angle for the probe, which was 7° in the experiments given in Chapter 5, may also generate a slight effect on the measured wall normal velocity, v , whose amplitude is already small compared to the streamwise component, u , due to the third velocity component, w . Increasing the amplitude of the measured velocity components by rotating the probe 45° is a way of decreasing the above-mentioned unwanted effect of the tilt angle. Moreover, this configuration may also reduce the needed tilt angle. In the present experiments, a tilt angle of 5° was found to be suitable with a 45° rotated 60 mm four-beam probe that was used together with a 1.98 ratio beam expander and 500 mm focal length lens. The resulting probe volume dimensions were approx. 0.1229 mm and 0.1166 mm in both the streamwise (dx) and transverse (dy) directions for the U1 and U2 velocity channels respectively. The probe volume dimensions in the cross-flow direction (dz) were 1.633 mm and 1.549 mm for the two velocity channels. Due to the rotation of the laser probe the U1 and U2 channels were not directly associated with the streamwise and transverse velocity components and a transformation was needed in order to calculate each component. This transformation can be done in the BSA Flow software along with the correction needed for the tilt angle. However, in this study it was preferred to do the needed transformation while post-processing by using a MATLAB code in which the calculation of the velocity moments was also performed. The wavelength of the green beams (U1) and blue beams (U2) were 514.5 and 488 nm respectively, whilst the beam diameters and beam spacing for both were 1.35 mm and 38 mm respectively.

Velocity-time data were collected at 56 points, which were selected with logarithmically increasing intervals, throughout the boundary layer, and at one point at the outer flow (at 80 mm from the wall) for each test case. Data collection took place for 120 or 200 seconds at each point leading to large data populations of 30000 to 50000 at every point depending upon the sampling rate, which in turn aimed the minimization of the uncertainty of the results. Moreover, additional experiments were conducted for all of the test plates at one freestream velocity (6 m/s) for collection of data suitable for turbulence spectrum calculation. Five points were selected in the boundary layer for the collection of turbulence spectrum data which were $y/\delta = 0.005, 0.01, 0.05, 0.10, \text{ and } 0.4$. Data was collected at the specified points for 1250 seconds or 1000000 samples, whichever came first. Accordingly, the size of the data populations changed depending upon the data rate and under these circumstances data populations of at least 350000 samples were collected for the first two points very near the wall and at least 750000 samples at the other three points.

The entire data was collected at the coincidence mode by using overlapping. The boundary layer mesh was divided into two regions as the inner and outer during the data collection. The inner region contained the first 15 points in the mesh up to 0.457 mm distance from the wall. The sensitivity was slightly decreased in the inner region in order to be able reject the noise due to the reflections from the wall. Accordingly, sensitivity was set to 1100 V in the inner region whilst it was selected as 1150 V for the outer region. The level validation ratio and burst detector signal to noise ratio were selected as 8 and 3dB respectively for both regions. The minimum and maximum record lengths were 32 and 256 for the entire measurements. Very clean burst spectra were observed during the measurements with the mentioned set-ups.

The collected time dependant data for every measurement point in the boundary layer were saved as “.txt” files. The analysis of the data was carried out by using a couple of MATLAB programs and several EXCEL sheets. Subsequently, the moments of the time dependant data were calculated. Transit time averaging technique was used in the calculation of the moments in order to eliminate the bias errors. Noise elimination was done by using Chauvenet’s criterion (Coleman and Steele, 2009) prior to the further analysis of the data. This procedure did not affect the results at all, since the signals exhibited almost noise-free character. Mean

velocities, turbulent normal and shear stresses, triple correlations, boundary layer parameters, and uncertainties related to the moments are calculated at this stage. The calculated mean streamwise velocity profiles and the Reynolds shear stresses were used for the calculation of the friction velocities, local frictional drag coefficients and roughness functions.

6.6 Uncertainty

Two methods were used for the uncertainty analysis as in Chapter 5. The method of Benedict and Gould (1996) was used to account for the statistical uncertainty associated with the random sampling and limited sample population. On the other hand, repetitive tests were performed for the calculation of uncertainty according to Coleman and Steele (2009) for the calculation of uncertainty due to possible inconsistencies in the experimental setup. 95% confidence bounds were used in both uncertainty analysis procedures.

In Figure 6.21, the uncertainty percentages, which were calculated according to Benedict and Gould (1996), in the streamwise (U) and transverse (V) velocities are presented for the entire test cases. As a typical character of boundary layer LDV experiments, the uncertainty values are higher very near the wall due to the encountered lower data rate and thus smaller sample populations especially up to the log-law layer. The maximum uncertainty levels in the streamwise and transverse velocities are about 2% and 60% respectively for $y/\delta < 0.05$. The uncertainty percentages quickly decrease to average values of 0.18% and 7.82% at $y/\delta = 0.1$ and continue decreasing till the end of the boundary layer. The mean uncertainty in U and V for $y/\delta > 0.15$ can be given as 0.12% and 2.48% respectively.

Shown in Figure 6.22 are the variations of uncertainty percentages in the Reynolds stresses. The uncertainty percentages in these flow properties are rather lower compared to the ones given in Chapter 5, which is an accomplishment due to the improvements in the test set-up. Especially the use of the LDV probe with a 45° rotation angle considerably decreased the uncertainty in the transverse velocity component which is normally a very small value compared to the streamwise component. The uncertainty levels of the shear and wall-normal Reynolds stresses and triple correlations are closely related to that of the transverse component. On the other hand, the increased sample size collected at each point is also very effective in

decreasing the overall uncertainty. The maximum uncertainty in the Reynolds stresses is 10% which is only encountered in a very limited region in the vicinity of the wall. The average uncertainty percentages for \overline{uu} , \overline{vv} and \overline{uv} are 1.30%, 1.62% and 2.93% respectively between $0.02 < y/\delta < 0.5$. However, the uncertainty levels increase around $y/\delta \approx 1$ and increase the overall average. This behaviour is due to the high turbulence intensities and unsettled fluctuations that were observed at the outer edge of the boundary layer as a result of the inflow measurements. Accordingly, the average uncertainty in \overline{uu} , \overline{vv} and \overline{uv} are 2.01%, 1.97% and 3.72% respectively for $0.05 < y/\delta$.

The uncertainty variation for the triple correlations \overline{uuu} and \overline{vvv} can be investigated from Figure 6.23. The trends of the uncertainty variation throughout the boundary layer are very similar to those of the mean velocities. The uncertainties reach up to very high values of 78-80% for $y/\delta < 0.01$. The average uncertainty in \overline{uuu} and \overline{vvv} can be given as 7.25% and 9.83% for $0.05 < y/\delta$.

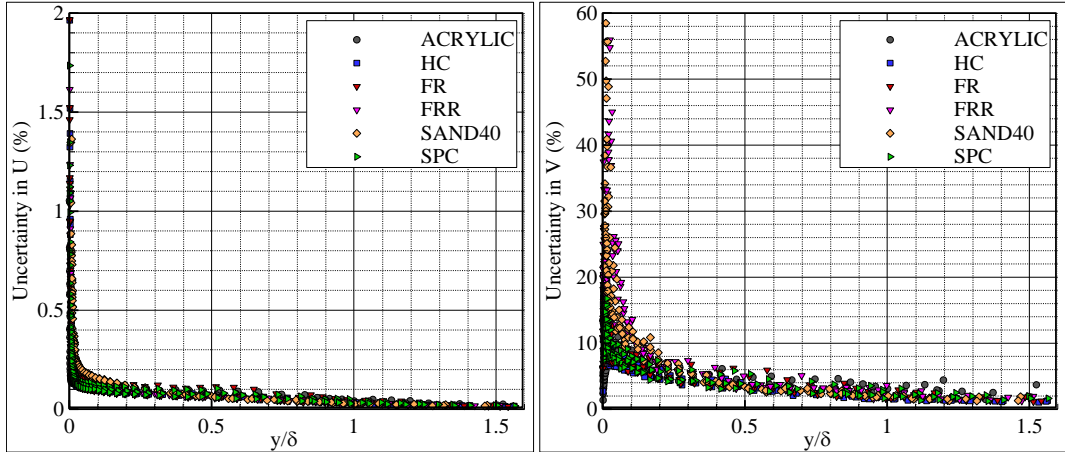


Figure 6.21 : Variation of uncertainty in streamwise (left) and transverse velocities throughout the boundary layer.

For the implementation of the uncertainty analysis method of Coleman and Steele (2009), 7 replicate tests were performed with the ACRYLIC test specimen and 5 replicate tests were carried out with the SAND40 specimen. The tests were performed at an inflow velocity of 2 m/s with both of the test specimens. The 95% confidence bounds of the statistics were determined via the multiplication of the standard deviation of the statistical variables by the related two-tailed t value of $t=2.447$ for 6 degrees of freedom and $t=2.776$ for 4 degrees of freedom for the ACRYLIC and SAND40 cases, respectively. According to this uncertainty analysis with repetitive tests, it was also possible to calculate the uncertainty percentages in

the calculated local skin friction drag coefficients, roughness functions and boundary layer parameters. As a result of the analysis the uncertainty in the boundary layer thickness was calculated as 8.1% and 5.2% for the SAND40 and ACRYLIC test specimens respectively. The uncertainty level for the integral boundary layer parameters were rather less compared to those of the boundary layer thicknesses. The uncertainty in displacement and momentum thicknesses for the SAND40 and ACRYLIC cases were approximately 2.7% and 1.6% respectively.

On the other hand, the uncertainty for the friction velocity and local skin friction coefficient which were calculated by using the Total Stress method were determined as 0.37% and 0.99% for the ACRYLIC test surface. The uncertainties of the same variables along with the roughness function were obtained as 0.95%, 2.29% and 2.58% for the SAND40 test specimen.

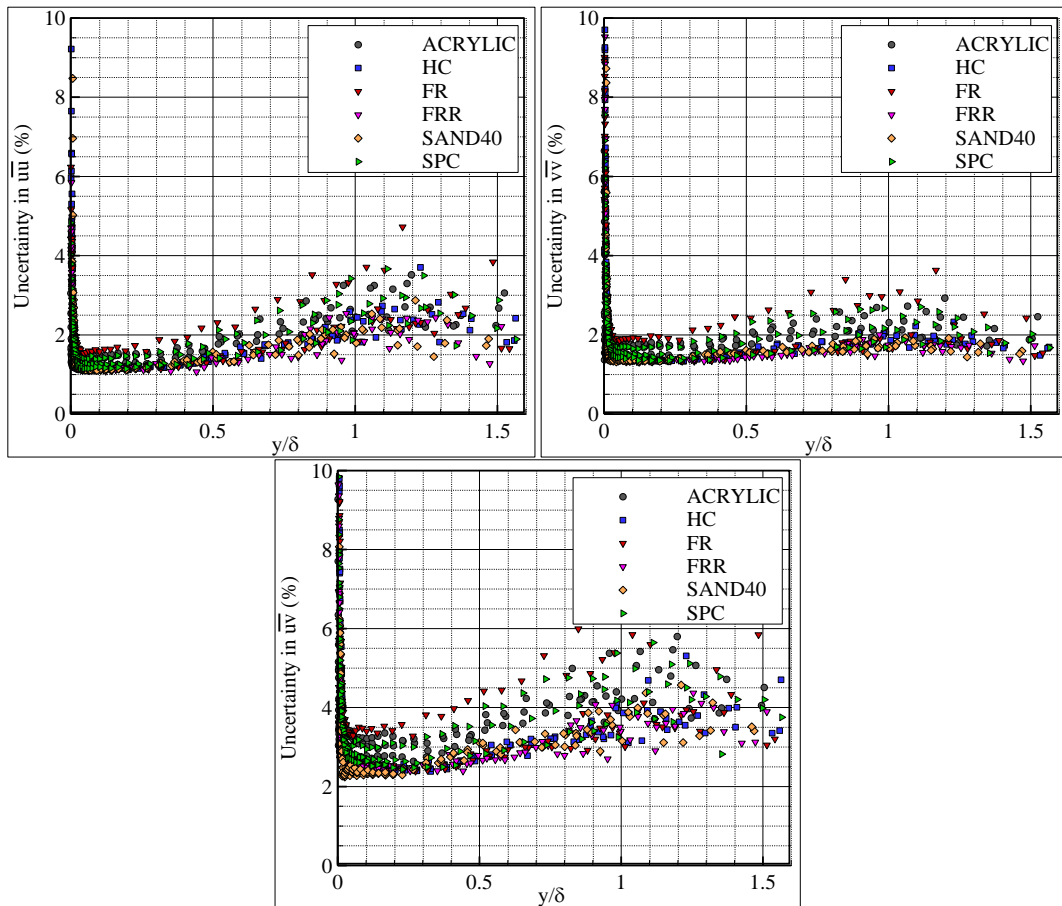


Figure 6.22 : Variation of uncertainty in the Reynolds stresses.

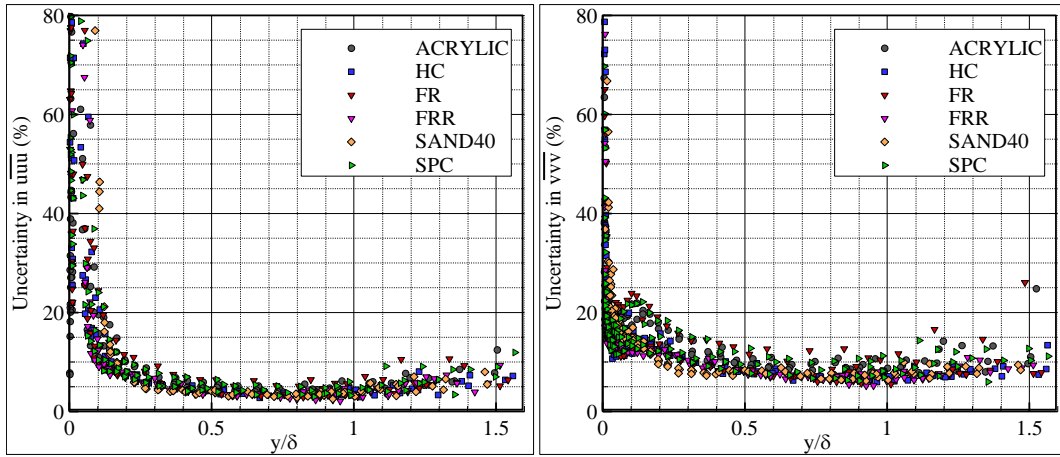


Figure 6.23 : Uncertainty percentages for the streamwise (left) and transverse triple correlations.

The variation of the uncertainty percentages for the streamwise and transverse velocity components through the boundary layer can be seen in Figure 6.24. The uncertainty levels are higher at the near vicinity of the wall with maximum values of 5.6% and 95.1% for the streamwise and transverse velocities respectively. The average uncertainty in U for $0.05 < y/\delta$ may be given as 1.7% and 1.9% for smooth and rough surfaces respectively. The mean uncertainties in V for the same region of the boundary layer for smooth and rough surfaces are rather close values to each other and were determined as 11.1% and 10.2% respectively.

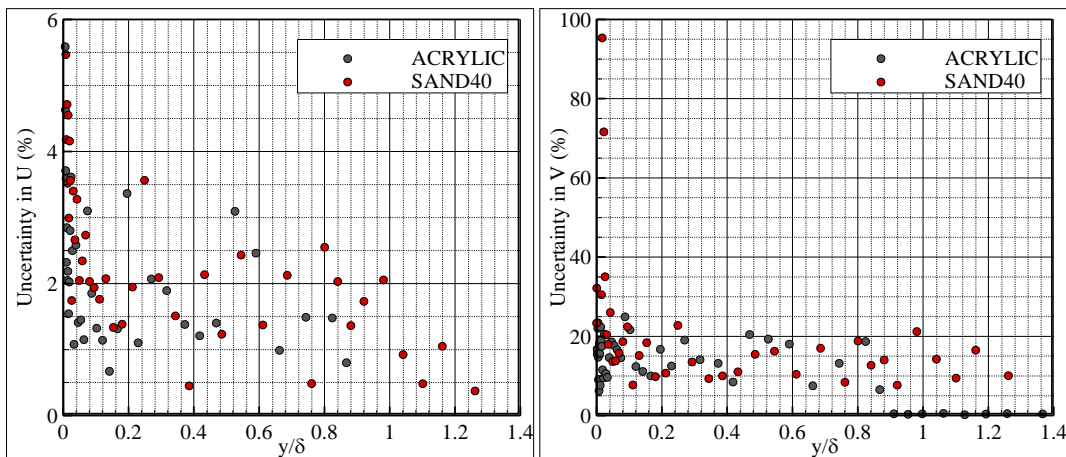


Figure 6.24 : Uncertainty percentages for the streamwise (left) and transverse velocities.

6.7 Results

The results of two-dimensional LDV boundary layer measurements, which were conducted over transitionally rough surfaces coated with marine anti-fouling along with smooth and fully rough reference surfaces, are presented in this section. The

basic findings about the boundary layer properties such as the boundary layer and integral thickness parameters, local skin friction drag coefficients, roughness functions, Reynolds normal and shear stresses, the higher order moments which include the triple correlations along with the skewness and flatness factors are discussed along with the comparisons relevant and published in the literature. The results of the autocorrelation and turbulence spectra of the measured velocity components are also presented and discussed together with the effects of surfaces on these quantities. Finally, transfer functions between the roughness spectra and the turbulence spectra are calculated and suitable analytical functions are proposed.

6.7.1 Boundary layer parameters

Presented in Table 6.4 are the basic boundary layer parameters of the entire test cases. In this table, δ represents the thickness of the boundary layer whilst δ_1 and θ are the displacement and momentum thicknesses, respectively. H is the shape factor defined as the ratio of displacement thickness to momentum thickness. Re_{δ_1} and Re_{θ} are the displacement and momentum thickness Reynolds numbers respectively. The mean freestream velocities (U_e) and the kinematic viscosity (ν) of the tunnel water are also included in the table. It is observed from the table that, the boundary layer thickness varied between 45 mm and 55 mm (SAND40_POS1_2), whereas the encountered minimum and maximum displacement thickness values were 4.7 mm and 7.3 mm. The momentum thickness, on the other hand, changed between 3.8 mm and 5.1 mm (SAND40). The shape factor varied between 1.23 and 1.43 (SAND40). The Reynolds number based on the displacement thickness changed between 8893 (HC) and 36541 (SAND40), whereas the one based on the momentum thickness varied between 6995 (HC) and 25924 (SAND40). Accordingly, it can be said that it was possible to cover a larger Reynolds number range compared to the experiments given in Chapter 5.

It can be said that the FRR test specimen has higher boundary layer, displacement and momentum thickness and shape factor values compared to the smooth and other coated surfaces which altogether point out the expectation of a higher skin friction drag. On the other hand, SAND40 specimen which is the fully rough reference surface has significantly higher boundary layer parameter values than the others, as expected.

Table 6.4 : Variation of the boundary layer parameters.

Surface	U_e	$v \times 10^6$	δ	δ_1	θ	H	Re_{δ_1}	Re_{θ}
ACRYLIC_POS1_2	2.04	1.12	46	5.5	4.3	1.28	10049	7826
ACRYLIC_POS1_4	4.06	1.13	47	4.9	3.9	1.24	17600	14173
ACRYLIC_POS1_6	6.08	1.11	47	4.7	3.8	1.23	25950	21134
HC_POS1_2	2.02	1.23	45	5.4	4.3	1.27	8893	6995
HC_POS1_4	4.05	1.22	45	4.9	4.0	1.24	16407	13204
HC_POS1_6	6.09	1.22	46	4.7	3.8	1.23	23565	19125
FR_POS1_2	2.04	1.13	47	5.4	4.2	1.27	9701	7652
FR_POS1_4	4.05	1.20	45	4.9	3.9	1.25	16569	13246
FR_POS1_6	6.10	1.12	46	4.7	3.8	1.23	25620	20776
FRR_POS1_2	2.03	1.09	49	5.8	4.5	1.29	10851	8442
FRR_POS1_4	4.07	1.15	48	5.3	4.2	1.27	18739	14790
FRR_POS1_6	6.07	1.13	46	5.1	4.1	1.25	27639	22068
SPC_POS1_2	2.03	1.17	47	5.5	4.3	1.28	9542	7445
SPC_POS1_4	4.08	1.16	45	4.9	3.9	1.26	17269	13732
SPC_POS1_6	6.08	1.17	47	4.7	3.8	1.23	24589	19964
SAND40_POS1_2	2.06	1.11	55	7.3	5.1	1.43	13499	9454
SAND40_POS1_4	4.06	1.13	48	6.9	4.8	1.43	24775	17360
SAND40_POS1_6	6.09	1.12	48	6.7	4.7	1.41	36541	25924

6.7.2 Mean velocity profiles in outer and inner scaling

Presented in Figure 6.25 are the mean streamwise velocity profiles of the tested surfaces which are plotted in outer variables including the entire test cases. The non-dimensionalization of the streamwise velocity component (U) and wall normal distance (y) are conventionally made using the outer flow velocity (U_e) and the boundary layer thickness (δ) in this figure. The velocity profiles of SAND40 test specimen are easily followed with the highest velocity defect whilst the others generally collapse within the uncertainty.

Figure 6.26 shows the mean velocity profiles of the tested surfaces at tested freestream velocities of 2 m/s, 4 m/s and 6 m/s, using inner scaling. The viscous velocity profile ($y^+ = U^+$) and the logarithmic law for a smooth surface (Equation 2.12) are also included in the figure for comparison. The friction velocities, which were calculated with the total stress method, were used for the non-dimensionalisation. It is observed that the smooth reference ACRYLIC surface closely follows the smooth logarithmic law (Log-law) line as expected. At 2 m/s freestream velocity, the velocity profiles of the FR, SPC and HC test specimens almost overlap with that of the ACRYLIC. A downwards shift is expected in the velocity profiles due to the increased skin friction drag as a result of the surface

roughness in general. Although a significant shift is not observed for the FR, SPC and HC test specimens, it is seen that their profiles dissociate as the inflow velocity increases which points at the increasing values of roughness functions for these surfaces as the Reynolds number increases. On the other hand, the velocity profile of the FRR and SAND40 surfaces display easily observed larger deviations from the smooth log-law. Especially, the shift in the velocity profiles of the SAND40 is enormous as can be expected in a fully rough flow regime.

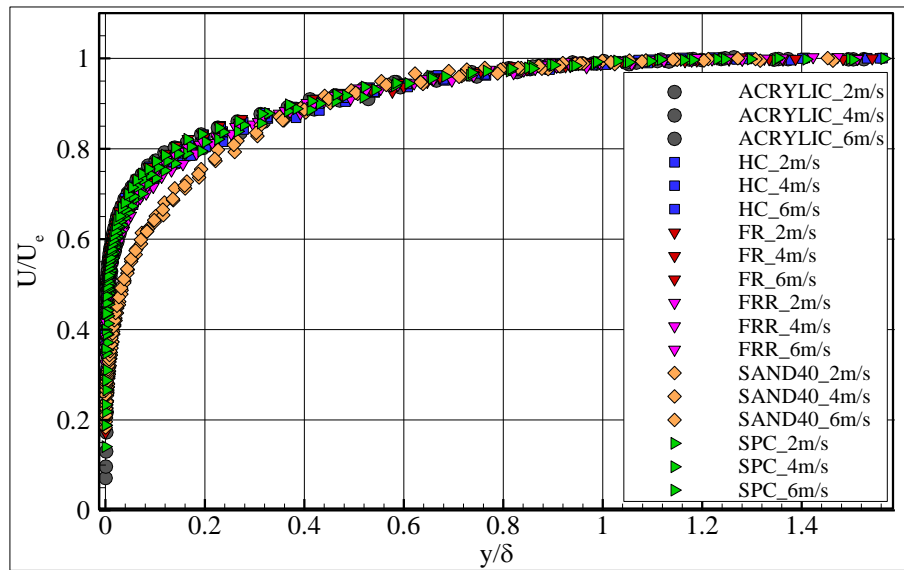


Figure 6.25 : Mean velocity profiles for the entire test cases, in outer scaling.

The mean velocity profiles of the tested surfaces for various inflow velocities are plotted in Figure 6.27 in velocity defect form using Rotta outer length scaling (Clauser, 1956) at the top plot. The velocity defect profiles are also given in conventional outer scaling at the plot located at the bottom of the figure. The displacement thickness, which is an integral length parameter, is used as the outer length scale in Rotta scaling rather than the boundary layer thickness which is difficult to be determined accurately and has a relatively arbitrary definition. In this kind of scaling, the non-dimensionalization includes both the outer and inner velocity scales which are the freestream and friction velocities respectively. As a result, a very good collapse of the velocity defect profiles is observed throughout the logarithmic and outer part of the boundary layer. Moreover, the velocity defect profiles of the entire test cases also collapse in the conventional outer scaling. The excellent collapse of the profiles supports Townsend's (1976) Reynolds number similarity similar to the works of e.g. Schultz and Flack (2007 and 2009).

Accordingly, an increase in the wake strength for rough surfaces is not expected since no lack of collapse was observed in the overlap region of the defect profiles.

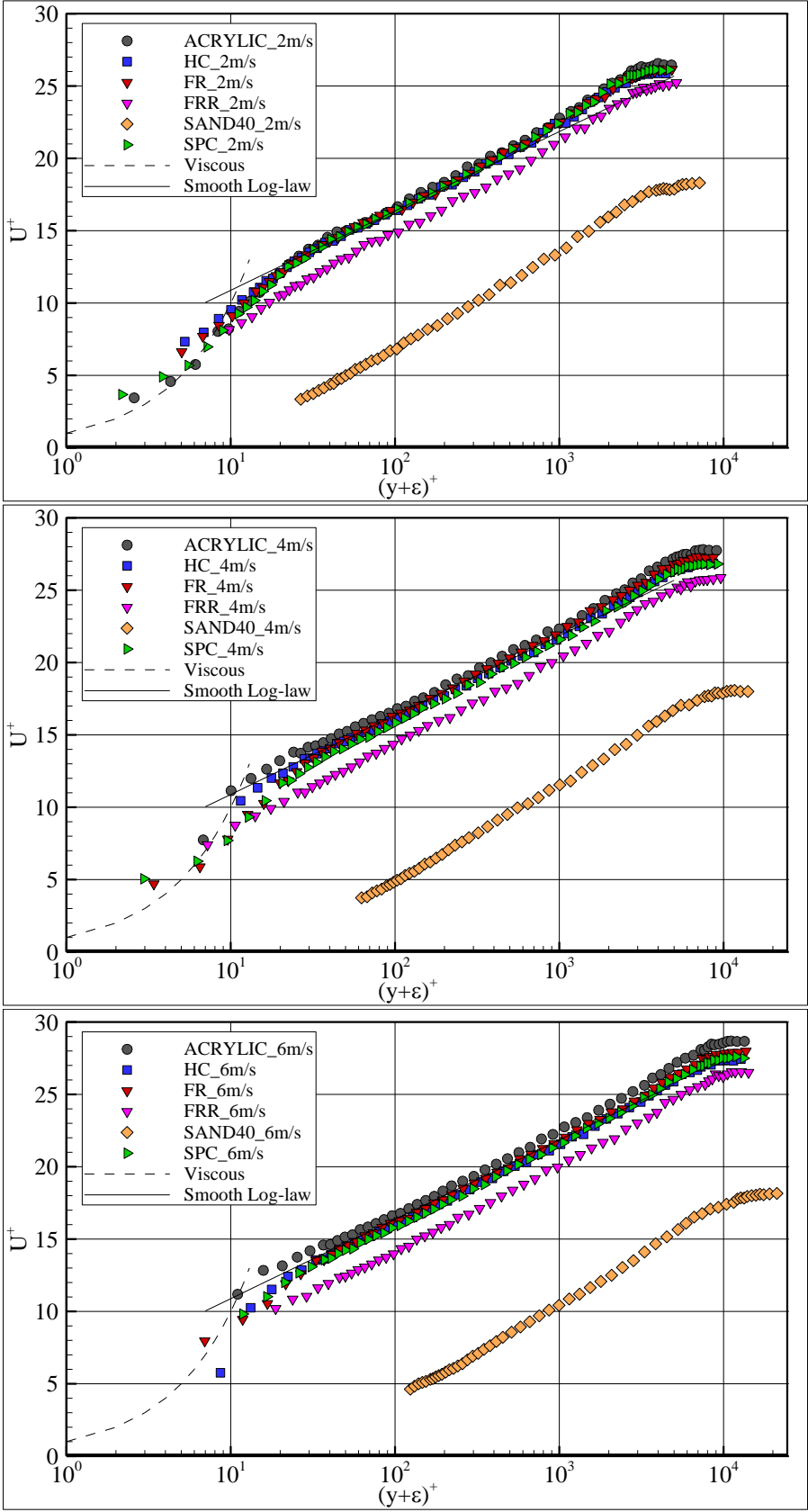


Figure 6.26 : Streamwise velocity profiles in inner scaling.

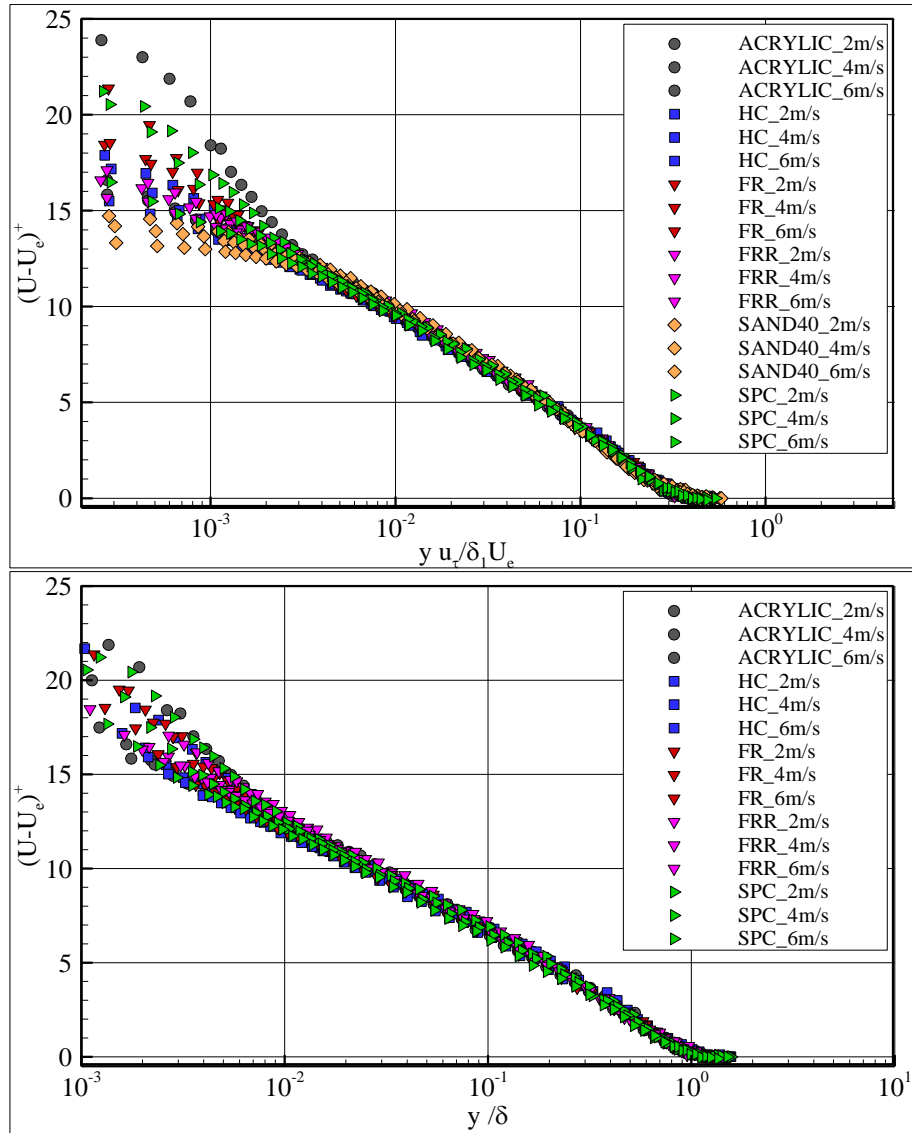


Figure 6.27 : Velocity profiles in defect form, in Rotta scaling (top) and conventional outer scaling (bottom).

6.7.3 Local frictional drag coefficients and roughness functions

The calculated friction velocities (u_τ) in m/s, local skin friction drag coefficients (c_f), wake strength (Π) and error in origin (ε) in mm are presented in Table 6.5 for the entire test cases. It should be noted here that the calculated ε values also include the positioning errors of the probe volume. The presented friction velocities and local skin friction drag coefficients are calculated with two different methods, being the velocity profile fitting method (VP) according to Krogstad et al. (1992) and the total stress method (TS) according to Brzek et al. (2009). The effect of the very slight pressure gradient was also used as a correction in the method. The two methods are explained in detail in Section 2.7. The two methods used for the calculation of the friction velocity for the ACRYLIC surface provided very close results within a

maximum difference of 1.44% (and 1.18% in average) whilst the maximum difference in the u_τ values of two methods were 2.26% (and 1.93% in average) for the SAND40 specimen. The difference in the calculated friction velocities of the coated test specimens generally did not exceed the average difference in the ACRYLIC cases. The differences in friction velocities due to calculation methods also have an effect on the local skin friction drag coefficients. Accordingly, the variation of the calculated c_f values by the two methods was 2.16% in average for the ACRYLIC and coated test specimens whilst it was 3.98% for the SAND40 cases. The wake strengths and error in origin given in the table were calculated as outcomes of the velocity profile fitting method. The error in origin values are at most 400 μm which is observed SAND40 test specimen for 6 m/s freestream velocity and change between 15 μm and 120 μm for the coated surfaces. On the other hand, the wake strength varies between 0.21 and 0.31 for the entire test cases and no significant difference is observed for the coated test specimens or the fully rough reference surface on the contrary of the increased wake strength for rough walls proposed by Tani (1988), Krogstad et al. (1992), Keirsbulck et al. (2002) and Akinlade et al. (2004). The change in the wake strength observed for rough surfaces was generally attributed to the higher growth rate and greater entrainment of irrotational fluid in the rough wall boundary layers, by these authors. Although almost no difference was observed in the encountered wake strength values of rough walls, the difference in the value of this parameter with those were given as 0.55 by Coles (1956) and as 0.52 by Bandhopadhyay (1987) for zero-pressure-gradient turbulent boundary layers are about 40%. However, this difference is related with the inflow properties and are certainly associated with the high (about 4%) streamwise turbulence intensity values that were observed just after the outer edge of the boundary layer approximately at $y/\delta = 1.6 - 1.8$. Brzek et al. (2009) observed Π values decreasing from 0.66 to 0.02 in the presence of 5.2% freestream turbulence intensity for rough walls. Moreover, Candries (2001) reports wake strength values ranging between 0.15 and 0.52, which generally accumulates around 0.3, for smooth, coated and rough test surfaces which were tested in the ECT with a rather similar test set-up with the present experiments.

Table 6.5 : The friction velocities and local skin friction drag coefficients.

Surface	Re_{δ_1}	u_τ (VP)	ε	Π	u_τ (TS)	$c_f \times 10^3$ (VP)	$c_f \times 10^3$ (TS)
ACRYLIC_POS1_2	10049	0.0764	-	0.31	0.0771	2.81	2.86
ACRYLIC_POS1_4	17600	0.1445	-	0.26	0.1462	2.54	2.60
ACRYLIC_POS1_6	25950	0.2090	-	0.25	0.2120	2.36	2.43
HC_POS1_2	8893	0.0776	0.070	0.28	0.0782	2.95	2.99
HC_POS1_4	16407	0.1487	0.080	0.24	0.1510	2.69	2.78
HC_POS1_6	23565	0.2180	0.035	0.21	0.2220	2.56	2.66
FR_POS1_2	9701	0.0771	0.060	0.28	0.0780	2.86	2.93
FR_POS1_4	16569	0.1470	0.015	0.26	0.1485	2.64	2.69
FR_POS1_6	25620	0.2150	0.023	0.23	0.2180	2.48	2.55
FRR_POS1_2	10851	0.0806	0.120	0.30	0.0805	3.15	3.14
FRR_POS1_4	18739	0.1560	0.040	0.25	0.1574	2.94	2.99
FRR_POS1_6	27639	0.2260	0.080	0.28	0.2289	2.77	2.85
SPC_POS1_2	9542	0.0771	0.020	0.30	0.0778	2.88	2.93
SPC_POS1_4	17269	0.1500	0.010	0.25	0.1520	2.71	2.78
SPC_POS1_6	24589	0.2190	0.050	0.22	0.2210	2.60	2.65
SAND40_POS1_2	13499	0.1150	0.250	0.30	0.1124	6.25	5.97
SAND40_POS1_4	24775	0.2300	0.300	0.27	0.2258	6.40	6.17
SAND40_POS1_6	36541	0.3410	0.400	0.25	0.3352	6.28	6.07

The local skin friction coefficient results for all test cases except the SAND40 surface are shown in Figure 6.28. The reason for not including the SAND40 case results was due to the effort to be able to observe discernable trends amongst the results of the other tested surfaces with better accuracy, since the comparatively very high c_f values of SAND40 obscures potential trendlines by changing the y-axis range considerably. The presented values were obtained by the total stress method for the entire test cases. Non-linear-least-squares-based trendlines shown in the figure were constructed based on the model equation given in Equation 5.2. The departures from the given trendlines are in the level of uncertainty for the presented results. The c_f trendlines of the given surfaces display roughly a downward shift with respect to that of the ACRYLIC; however the associated slopes are slightly different. This difference in the slopes reminds that the decrease in the skin friction drag expected by the increasing Reynolds number is slightly higher for the coated surfaces compared to the smooth reference. Similar behaviour was also observed in the results of Chapter 5. It is observed that the FR, HC and SPC coated plates display similar drag performance within the uncertainty, for the lowest Reynolds number values. Moreover, the difference in c_f between the smooth reference and the SPC and FR cases stay in the uncertainty at the lowest Re_{δ_1} . The difference between the c_f values

of the coated surfaces and the smooth reference is higher than 4.5%, which is clearly above the uncertainty level (2.3%), in the high Reynolds number range. On the other hand, the differences between SPC and HC cases are in the uncertainty level at the entire tested Reynolds number range whilst the differences between SPC and FR are 3.23% and 3.77% at the higher two Reynolds numbers respectively. FRR test specimen indicate rather higher local skin friction drag coefficients over the tested Reynolds number range between 8.92% and 14.74% increase in c_f compared to the smooth reference.

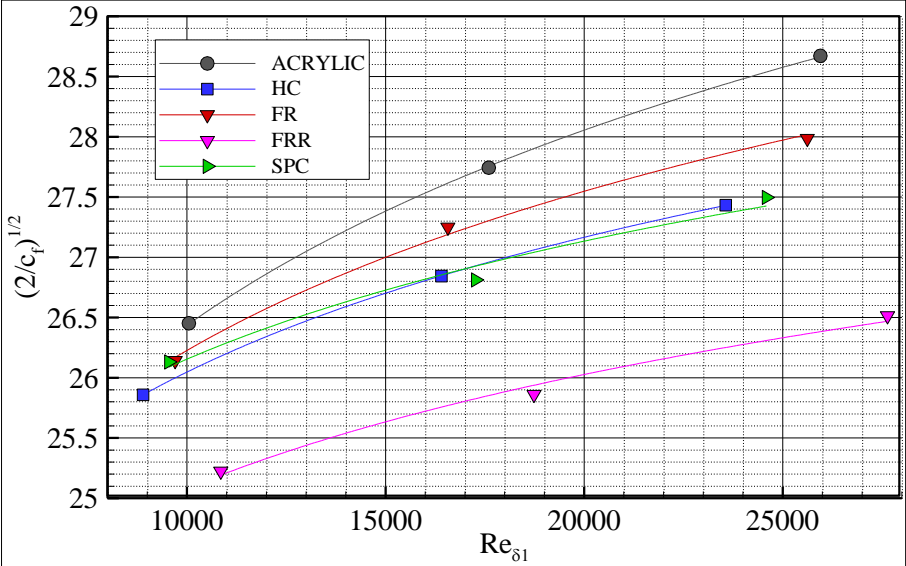


Figure 6.28 : Local skin friction drag coefficient of the tested surfaces.

The roughness functions (ΔU^+) calculated by using the mentioned two methods are given in Table 6.6 along with the roughness Reynolds number (k_s^+). The k_s^+ values that are presented in the table were calculated according to Flack and Schultz (2010) formula:

$$k_s = 4.43Rq(1 + Sk)^{1.37} \tag{6.2}$$

The two roughness parameters needed in the formula were used from the roughness analyses results gathered at a cut-off length of 50 mm. The formula of Flack and Schultz (2010) was derived by using surface statistics and roughness parameters measured with a sampling length of 50 mm and sampling interval of 25 μm, which are exactly the same values to those used in the present roughness measurements.

The difference of the results of VP and TS methods in the calculated roughness functions varies between 1.6% and 16%. It is observed from the table that the highest

roughness function values were obtained for the SAND40 test specimen, as expected whilst FRR surface has the highest roughness function values between the coated surfaces.

Table 6.6 : The roughness functions and roughness Reynolds numbers.

Surface	Re_{δ_1}	ΔU^+ (VP)	ΔU^+ (TS)	k_s^+
ACRYLIC_POS1_2	10049	-	-	-
ACRYLIC_POS1_4	17600	-	-	-
ACRYLIC_POS1_6	25950	-	-	-
HC_POS1_2	8893	0.37	0.30	5.4
HC_POS1_4	16407	0.66	0.75	10.6
HC_POS1_6	23565	0.87	1.01	15.6
FR_POS1_2	9701	0.19	0.22	2.4
FR_POS1_4	16569	0.42	0.37	4.2
FR_POS1_6	25620	0.63	0.65	6.7
FRR_POS1_2	10851	1.72	1.40	27.2
FRR_POS1_4	18739	2.15	2.04	50.6
FRR_POS1_6	27639	2.33	2.30	74.8
SPC_POS1_2	9542	0.23	0.19	2.1
SPC_POS1_4	17269	0.87	0.90	4.1
SPC_POS1_6	24589	1.16	1.04	5.9
SAND40_POS1_2	13499	9.55	8.83	104.3
SAND40_POS1_4	24775	11.25	10.55	205.3
SAND40_POS1_6	36541	12.02	11.31	308.4

The variation of the roughness functions with the displacement thickness Reynolds number can be more clearly observed in Figure 6.29. The figure shows that, all of the tested surfaces display an increasing trend as the Reynolds number increases. A better way of presenting the roughness function results is the use of roughness Reynolds number as the independent variable. Shown in Figure 6.30 are the ΔU^+ values of the surfaces for each test case against k_s^+ values. The correlations of Dey (1989) and Ligrani and Moffat (1986) are also included in the figure along with the Colebrook-White formula (Colebrook, 1939). The figure also embodies the transitionally rough regime data of Schultz and Flack (2007) for comparison. The data of Schultz and Flack (2007) obtained for a single regularly rough surface with varying flow velocities exhibit a well ordered curvy character and a slow departure from the smooth behaviour beginning from $k_s^+=2.5$. The results of the fully rough reference SAND40 surface cases fall on the fully rough asymptotic line of Colebrook (1939). The roughness function data of the FR test specimen almost follow the correlation of Ligrani and Moffat (1986) whilst those of SPC lie between the

correlation of Dey (1989) and Ligrani and Moffat (1986). The data from Candries (2001) for a roller applied fouling-release (FR) antifouling coating were also included in the figure for comparison. It should be mentioned here that the tested surface of Candries (2001) was a coated with a different fouling-release type coating scheme compared to the FR coating used in the present study and the k_s^+ values of his surfaces were calculated in the same manner, using Equation 6.1. Candries(2001) and Candries and Atlar (2005) did not propose any correlation with the Colebrook-White law for their data from boundary layer experiments on the surfaces coated with marine antifouling paints, either. As may be observed from Figure 6.30, the first three points of the data of Candries (2001) lie closer to the relation of Ligrani and Moffat (1986), although the subsequent two points form a group with the present data, one of them exactly collapsing with the data of FRR. The data of the FR, HC and FRR surfaces together imply a rather slowly increasing roughness function trend compared to the given reference correlations with lower than expected roughness functions for $10 < k_s^+ < 100$ range. The roughness function values of the mentioned surfaces present a well ordered form together with the two points from Candries (2001) and imply a new correlation for the surfaces coated with anti-fouling surfaces although the investigated k_s^+ range still obscures the global trend. The appearing notable tendency of the data gives motivation for the proposal of two new relations, which are already included in the figure, for the anti-fouling coated surfaces in the limitation of the present data. The associated relations can be given with a power function and a relation similar to Dey (1989)'s respectively:

$$\Delta U^+ = 0.1302(k_s^+)^{0.7008} \quad (6.3)$$

and

$$\Delta U^+ = 2.2 \ln(1 + 0.03k_s^+) \quad (6.4)$$

Obviously, the given relations can only be justified up to $k_s^+ \approx 100$ with the present data by ignoring a part of the data gathered for SPC and from Candries (2001). However, it is apparent that there is a great need to develop new correlations by considering a large amount of data for marine anti-fouling coatings, by substantially expanding the present data especially for larger roughness Reynolds numbers.

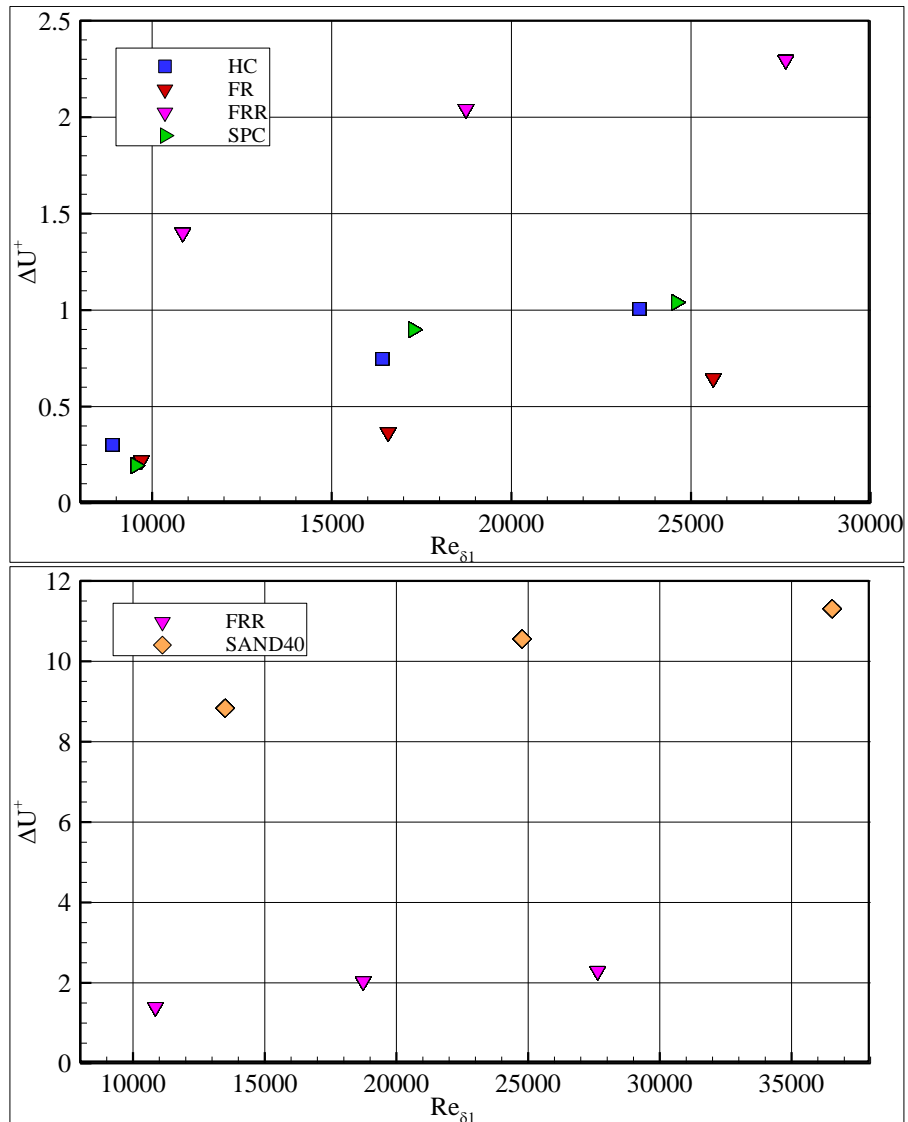


Figure 6.29 : Variation of the roughness functions for the test cases.

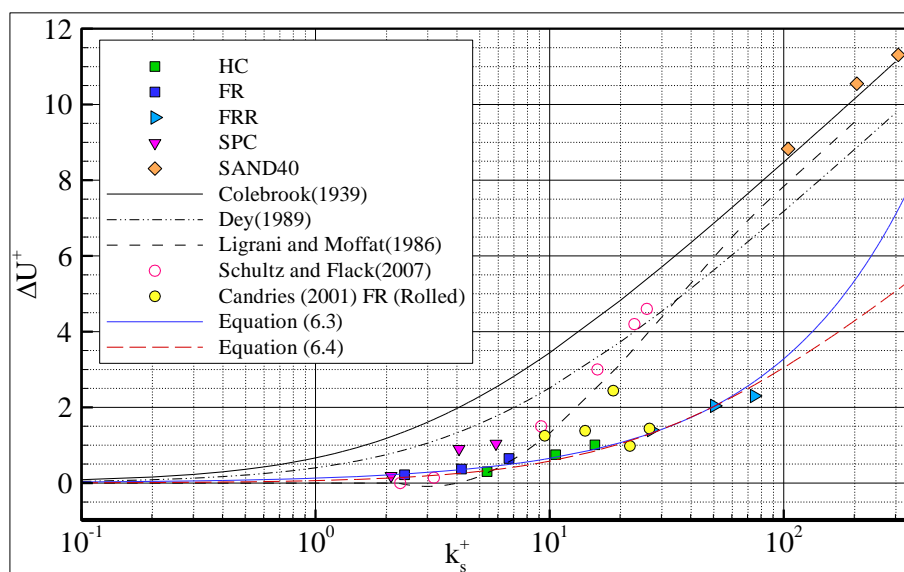


Figure 6.30 : Correlation of the roughness function and the roughness Reynolds number including the new relations.

6.7.4 Reynolds Stresses

Presented in Figure 6.31 are the streamwise Reynolds normal stresses, \overline{uu}/u_τ^2 or \overline{uu}^+ , in inner variables for all test cases. The results in inner variables imply that the surface roughness of the tested coated and fully rough surfaces alters the \overline{uu}^+ values being valid from $(y + \varepsilon)^+ \approx 20 - 40$, when compared to the smooth reference. This behaviour is less significant at lower inflow velocities, however the effect is more pronounced especially at 6 m/s test cases. The high peak values near the wall observed at $(y + \varepsilon)^+ \approx 10 - 20$, which are generally associated primarily with the viscous effects and streamwise vortices (Grass, 1971; Jimenez, 2004), decrease as the roughness Reynolds number increases and totally disappears for the SAND40 surface since the viscous region and some parts of the inner region is destroyed together with the breakup of the streamwise vortices due to the roughness elements extending further away the wall for this surface. However, the rise in \overline{uu}^+ which begins from $(y + \varepsilon)^+ \approx 100$ and continue up to $(y + \varepsilon)^+ \approx 15$ exist in all the test cases of coated surfaces along with the smooth reference. The rise come to a rest around 8.0 to 9.5 with a peak located at $(y + \varepsilon)^+ \approx 10 - 20$ for the entire coated surfaces and the smooth reference. This observation is consistent with the previous works of for example DeGraff and Eaton (2000), Brzek et al. (2008), and Ligrani and Moffat (1986). \overline{uu}^+ values of the entire cases are around 3.5-5.0 for $(y + \varepsilon)^+ \approx 1000$ which is also in good agreement with e.g. Brzek et al. (2008), Schultz and Flack (2007) and Raupach et al. (1991). A lower stress region is apparent for the SAND40 surface over the band $25 < (y + \varepsilon)^+ < 300$. This region consistently produced lower streamwise fluctuations for all testing positions and freestream velocities for the SAND40 surface compared to the rest of the surfaces. This is in accordance with the results documented in Chapter 5 and Schultz and Flack (2007) who reported lower \overline{uu}^+ values in a similar but narrower range for a surface with roughness geometry similar to honed pipe with roughness Reynolds number of 26 at 27080 momentum thickness Reynolds number. This may be attributed to the high streamwise turbulence energy production of fully rough surfaces in these regions (Ligrani and Moffat, 1986). In the outer region, Reynolds number dependence is noticed for the tested surfaces. Similar Reynolds number profiles perfectly collapse within the uncertainty beginning from $(y + \varepsilon)^+ \approx 400 - 700$ for the coated and

smooth surfaces depending upon the inflow velocity and $(y + \varepsilon)^+ \approx 1000$ for the SAND40.

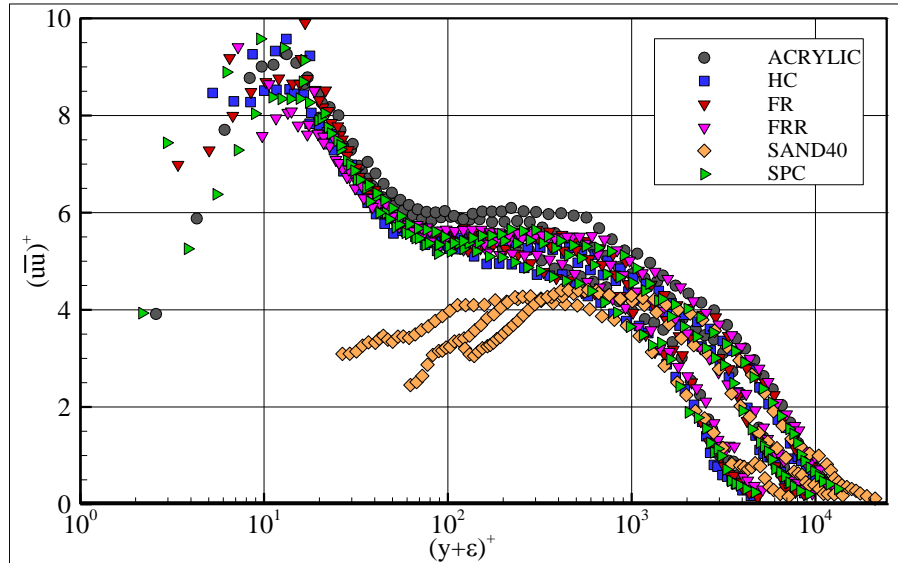


Figure 6.31 : Streamwise Reynolds normal stresses in inner scaling.

The profiles of wall-normal Reynolds stresses, $\overline{v'v'}/u_\tau^2$ or $\overline{v'v'}^+$, in inner scaling for the smooth and rough surfaces are presented in Figure 6.32 at the top graphic. It was only possible to capture the increasing trend of the profiles for some of the test cases which can be observed up to $(y + \varepsilon)^+ \approx 50 - 70$. The profiles altogether spread in a broad band of $\overline{v'v'}^+$ values due to the Reynolds number dependency. It is observed that the profiles of similar Reynolds numbers overlap for the smooth, coated and rough surfaces and the overall shape of the profiles are nearly identical for different surfaces. There exists a large plateau in the profiles beginning from $(y + \varepsilon)^+ \approx 50$ whose extension increases with the increasing Reynolds number. The plateau forms around $\overline{v'v'}^+$ values of 1.4 to 1.6 which is in agreement with the results of Brzek et al. (2008). The Reynolds number effect almost forms three groups of profiles in the outer layer. As seen from the figure, there exists no distinctive difference between the profiles due to the surface roughness in the overlap and outer region of the boundary layer when they are expressed in inner scaling which supports the wall similarity hypothesis as for e.g. Krogstad et al. (2005), Raupach et al. (1991), Schultz and Flack (2007) and Flack et al. (2005).

The plot located at the bottom of Figure 6.32 presents the wall-normal Reynolds stresses for each test case against normalized wall distance. The profiles of the smooth and coated surfaces collapse within the uncertainty and provide support to

the wall similarity concept. However, the lower profiles of the SAND40 surface for the range $(y + \varepsilon)/\delta > 0.15$ produce a discrepancy with this concept. This may be attributed to the effect of step change in the surface roughness in the present experimental set-up. According to Antonia and Luxton (1971), a distance of almost 20δ from smooth to rough junction is required to obtain self-preserving nature of turbulence properties for rough boundary layer. On the other hand, Bandyopadhyay (1987) showed that the sand roughness requires a distance of nearly 35δ in order to reach the self-preserving state following the step change from smooth to rough. Accordingly, the unexpected low values of the wall-normal fluctuations obtained for SAND40 may be attributed to the effect of the sudden transition from smooth to rough surface since the measurements were carried out at about 10δ distance to the beginning of the sand grit.

The Reynolds shear stress ($-\overline{uv}$) profiles for the entire test cases are given in inner (top plot) and outer scaling in Figure 6.33. The friction velocities calculated with the total stress method were used for the non-dimensionalization of the shear stresses in both plots. If the Reynolds shear stress profiles in inner scaling are considered, it is observed that the profiles form plateaus at the constant stress region with a peak value between 0.95 and 1.04 at approx. $30 < (y + \varepsilon)^+ < 500$. This peak values also validate the calculated friction velocities. There is a Reynolds number dependence monitored at the outer layer which also causes the profiles spread over a comparatively wide band. For similar Reynolds numbers, the $-\overline{uv}$ profiles associated with the smooth, coated or rough surfaces form groups by collapsing on each other in the level of uncertainty and no significant difference was observed between the tested surfaces in the outer layer. This is in agreement with Ligrani and Moffat (1986) and Schultz and Flack (2007) who did not find any influence of roughness on the Reynolds shear stresses. The Reynolds shear stress profiles can alternatively be examined in outer scaling given in the plot located at the bottom of Figure 6.33. Similar to the wall-normal fluctuations, no difference is observed between the coated and smooth surface Reynolds shear stress profiles although those of SAND40 surface follow a lower trend for $(y + \varepsilon)/\delta > 0.15$. Krogstad et al. (1992) and Krogstad and Antonia (1999) found that the difference in the $\overline{v'v'}$ profiles of various rough surfaces were considerably and even more pronouncedly reflected to the Reynolds shear stresses. In the present experiments, the behaviour of the $-\overline{uv}$

profiles of SAND40 surface is observed in a very similar manner to that of the $\overline{v}v^+$ profiles. This discrepancy again can be attributed to the effect of step change in the surface roughness in the present experimental set-up.

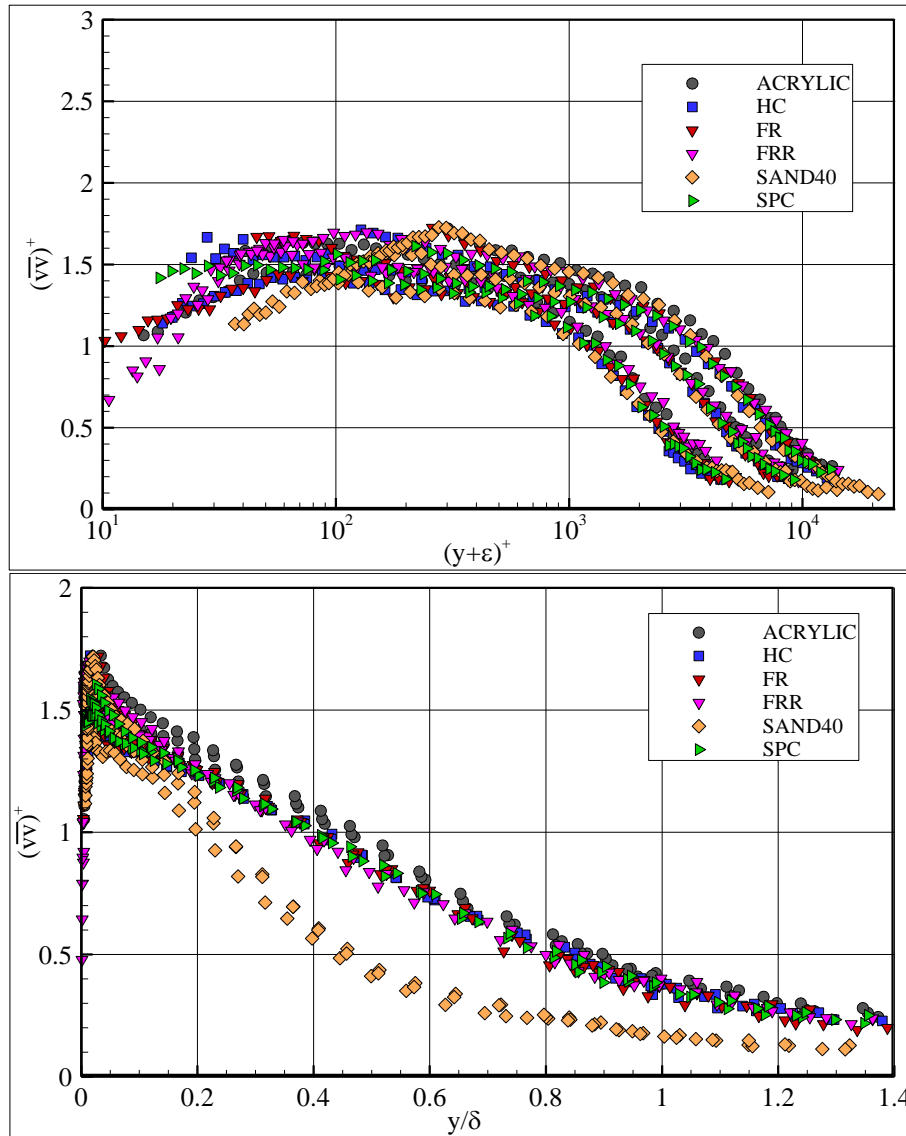


Figure 6.32 : Wall-normal Reynolds stresses in inner (top) and outer scaling.

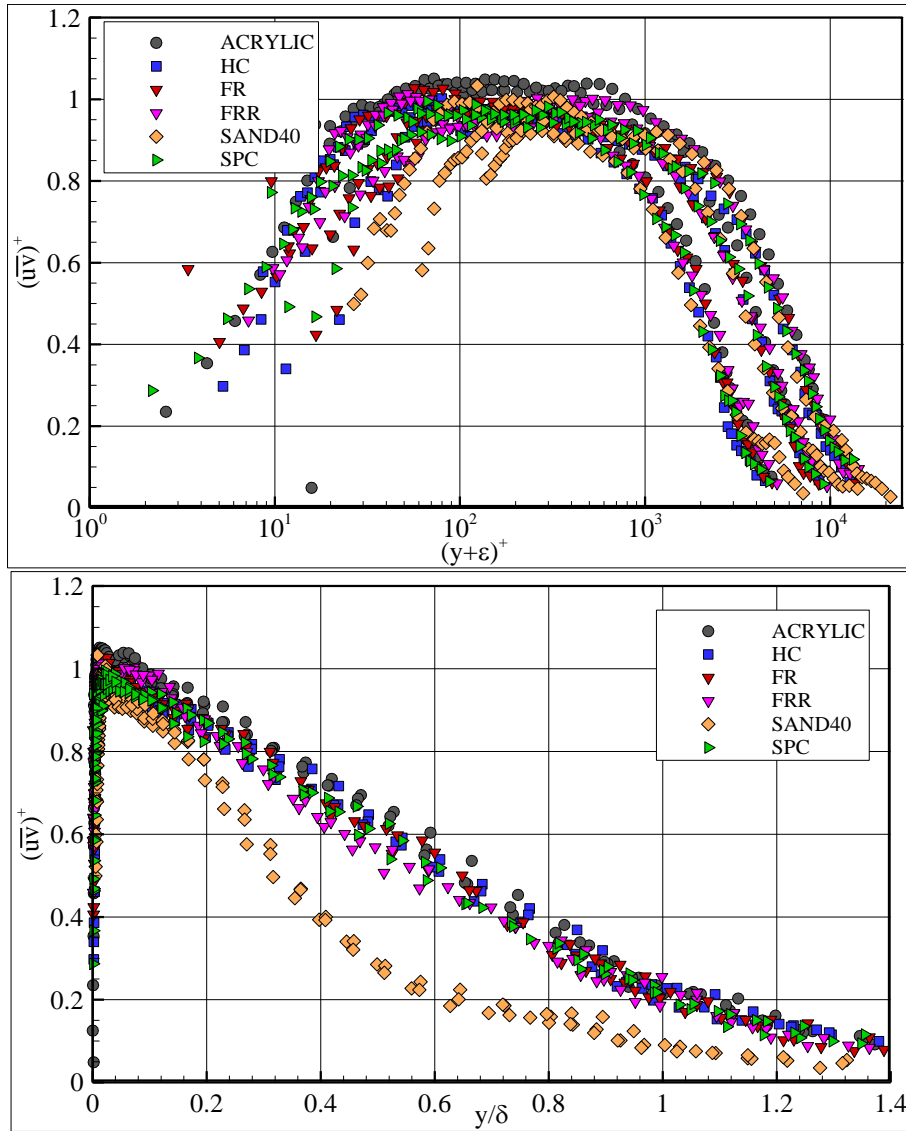


Figure 6.33 : Reynolds shear stresses in inner (top) and outer scaling.

6.7.5 Higher-order statistics

The examination of the mean flow properties along with the normal and shear Reynolds stresses indicated that the roughness effects were confined to the inner region of the boundary layer for the transitionally rough surfaces. Antonia and Krogstad (2001) emphasize that the third-order moments (or triple correlations) may be a more sensitive indicator of the wall roughness effect. Andreopoulos and Bradshaw (1981), Raupach et al. (1991) and Schultz and Flack (2007) also investigated the mentioned quantities as indicators of roughness effect. Accordingly, based on the encouragement coming from the lower uncertainty levels encountered with the velocity component fluctuations, the analyses of the higher-order moments including the triple fluctuating velocity correlations, flatness and skewness factors

were decided to be presented in this section for the investigation of the roughness effects in these quantities. To the Author's knowledge this is the first time that the higher order turbulence statistics are investigated for surfaces coated with marine anti-fouling.

The third-order moments of the streamwise (top) and transverse fluctuating velocity components are presented in Figure 6.34 for the entire test cases in outer scaling. The values for $(y + \varepsilon)/\delta < 0.01$ are not included in the figures due to the localised high uncertainty values very near to the wall. The triple correlation of the streamwise fluctuating velocity component represents the average transport of turbulent kinetic energy due to streamwise fluctuations by the turbulent motion in the streamwise direction. The triple moments display very weak Reynolds number dependence similar to that was noted by Murlis, Tsai and Bradshaw (1982). The general form of the \overline{uuu}^+ profiles associated with the smooth and coated surfaces present great similarity to those observed in Raupach (1981), Raupach et al. (1991) and Akinlade (2005) whilst the trend of the SAND40 profiles is similar to that given in Schultz and Flack (2007) for a fully rough surface. The \overline{uuu}^+ values of the SAND40 surface appear to be higher up to $(y + \varepsilon)/\delta \cong 0.2$, present a collapse within the uncertainty between $(y + \varepsilon)/\delta \cong 0.2$ and 0.3 , followed by a rather rapid approach to value of zero compared to the other cases. The \overline{uuu}^+ profiles of this surface has a minimum value of approximately -2.15 at $(y + \varepsilon)/\delta = 0.3$. The difference between the rough and smooth walls similar to that observed up to $(y + \varepsilon)/\delta \cong 0.2$ was also noted by Flack et al. (2005 and 2007). The difference between the smooth and rough surfaces observed until $(y + \varepsilon)/\delta = 0.2$ are attributed to the reduced frequency of sweep events (occurrence of high-speed fluid from regions distant from the wall) for the smooth walls compared to the rough surfaces, resulting in an increase in the turbulent flux of Reynolds stresses in the streamwise direction for rough surfaces (Akinlade, 2005). The lack of collapse in the profiles of SAND40 with those of the other tested surfaces in the outer region may be related with the strong step effect that the flow over such a highly rough surface encounters in the present experimental set-up. On the other hand, the \overline{uuu}^+ profiles of the other tested surfaces collapse within the uncertainty in the inner layer whilst some differences are observed in the outer layer where the coated and smooth surface profiles present their minimum points between

2.95 and 4.45 at about $0.5 < (y + \varepsilon)/\delta < 0.7$. The profiles achieve reasonable collapse beyond this region.

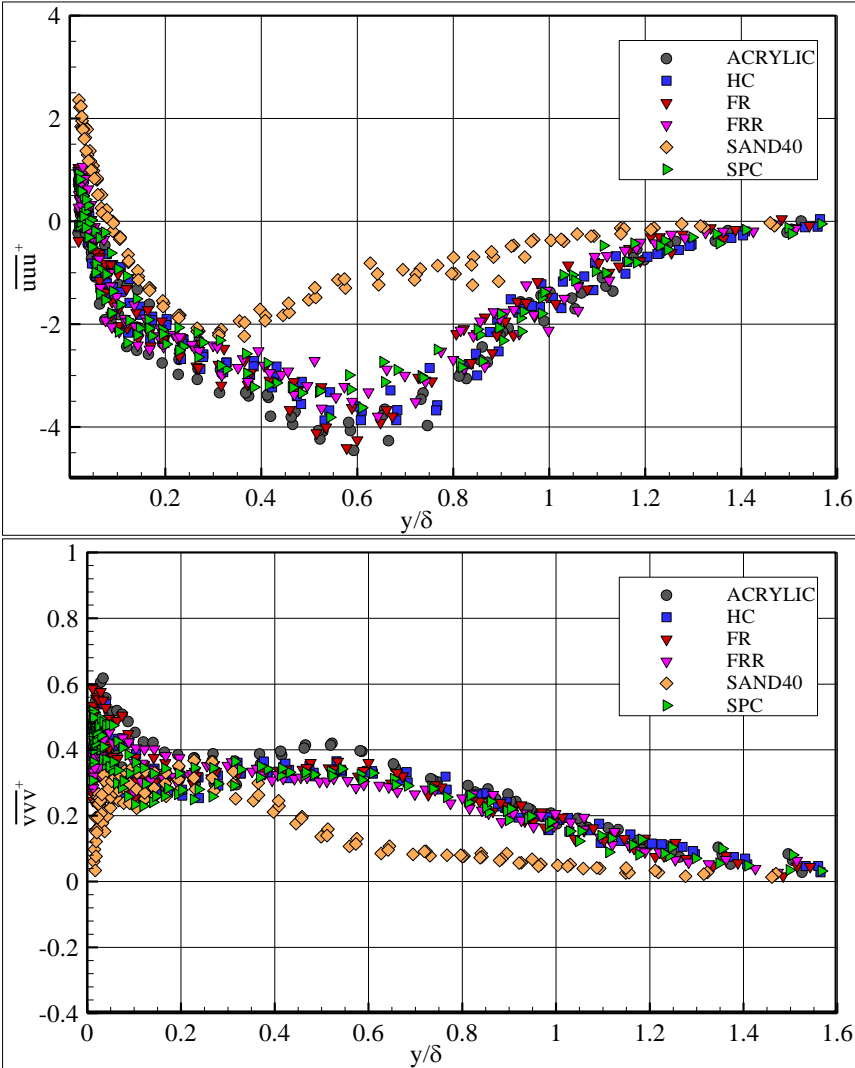


Figure 6.34 : Streamwise (top) and transverse fluctuating velocity components triple correlations.

The variation of the third order moments of the transverse fluctuating velocity component (\overline{vvv}^+) for the tested surfaces at various inflow velocities are given in the plot located at the bottom in Figure 6.34, in outer scaling. This quantity represents the average transport of turbulent kinetic energy due to wall-normal fluctuations by the turbulent motion in the transverse direction. The values of this triple product are positive throughout the boundary layer for the entire test cases which imply that the transport of the turbulent kinetic energy occurs away from the wall, as expected from a smooth wall and was observed in most of the rough wall studies (e.g. Flack et al., 2005; Raupach et al., 1991; Akinlade, 2005; Schultz and Flack, 2007). However, this is in contrast with the findings of Antonia and Krogstad (2001), who presented

negative $\overline{v'v'}$ values over a surface, composed of two-dimensional rods for a significant portion of the boundary layer. This suggests that the orientation of the turbulent kinetic energy transport may depend on the geometrical structure or texture of the surface roughness. No such behaviour was observed in the present study. The $\overline{v'v'}$ profiles of the coated surfaces show agreement between each other and with the smooth reference ACRYLIC, within their experimental uncertainty at the outer layer for $(y + \varepsilon)/\delta > 0.6$. The triple product values of the coated surfaces and SAND40 are slightly lower than those of the smooth surface near the wall up to $(y + \varepsilon)/\delta \cong 0.2$ which is inline with the findings of Raupach (1980 and 1981) and Flack et al. (2007). The profiles of the SAND40 surface overlap with those of the coated surfaces near the wall for $(y + \varepsilon)/\delta < 0.3$ and follow a distinctive trend until they reach to zero outside the boundary layer. This behaviour of the fully rough reference may also be attributed to the step effect.

The distributions of $\overline{u^2v^+}$ (top plot) and $\overline{uv^2}$ quantities, which represent the normalized streamwise and wall-normal turbulent flux of the Reynolds shear stresses respectively, are presented in Figure 6.35 for the entire test cases. The difference in the trends of the SAND40 are also observed in these quantities due to the effect coming from the individual wall-normal turbulent fluctuations. For the fully rough reference, a drop in the $\overline{u^2v^+}$ values are encountered near the wall until $(y + \varepsilon)/\delta \cong 0.2$, compared to the smooth and coated surfaces. A similar trend was also reported by Krogstad and Antonia (1999) for wire mesh and by Akinlade (2005) for wire mesh, perforated sheet and sand grain roughness. The gradient $\partial \overline{u^2v^+} / \partial y$ represents the turbulent diffusion of $\overline{u^2}$ in the Reynolds stress transport equation of $\overline{u^2}$. Therefore, the reduction of $\overline{u^2v^+}$ values near the wall for the rough surface will lead to a gain in the streamwise Reynolds stresses $\overline{u^2}$ by turbulent diffusion whilst a loss is expected for the smooth and coated surfaces. The $\overline{u^2v^+}$ profiles of the coated surfaces display a collapse with those of the smooth wall through the outer layer and support outer layer similarity. The general shape of the distribution of this quantity is in agreement with the literature (e.g. Flack et al., 2005) whilst the location and magnitude of the peak at $(y + \varepsilon)/\delta \cong 0.6$ with varying values of 0.75 to 0.90 according to surfaces are in line with those reported by Raupach et al. (1991).

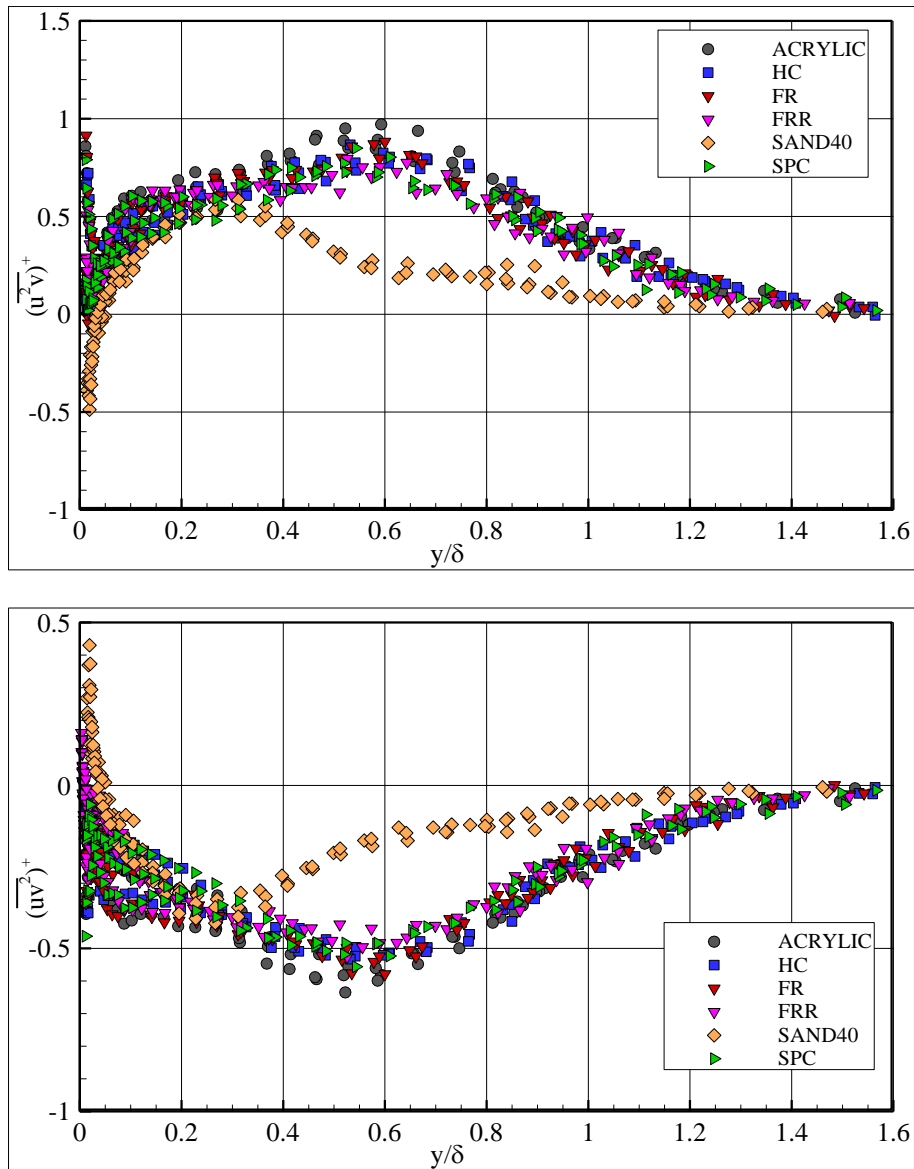


Figure 6.35 : The normalized streamwise (top) and wall-normal turbulent transport of Reynolds stresses in outer scaling.

The plot located at the bottom of Figure 6.35 show the distribution of the non-dimensional velocity triple product $\overline{uv^2}^+$ for the tested surfaces at various freestream velocities. This quantity represents the wall-normal turbulent transport of the Reynolds shear stresses. The general trends in the distribution of $\overline{uv^2}^+$ quantity for smooth and coated surfaces are very similar and demonstrate outer layer similarity. On the other hand, for the SAND40 and FRR surfaces the $\overline{uv^2}^+$ values near the wall are greater than those of the smooth and other coated surfaces with a change of sign for both of them. Andreopoulos and Bradshaw (1981) and Flack et al. (2007) noted similar near-wall differences for rough surfaces including a change of sign within 10k from the wall and concluded that such differences are associated with strong

sweeps near the surface of a rough wall. On the other hand, the profiles of the smooth and coated surfaces other than FRR stay in the negative zone throughout the boundary layer and present minimum values around -0.5 at approximately $(y + \varepsilon)/\delta \cong 0.5$. The present findings are in accordance with those of for e.g. Flack et al. (2007) and Raupach (1981).

The skewness and flatness factors may provide useful information about the ejection and sweep events occurring in the boundary layer. The third and fourth moments of the velocity fluctuations are non-dimensionalized with the third or fourth powers of the associated root-mean-square values of the velocity fluctuations respectively in order to determine the skewness (S) and flatness (F) parameters.

Presented in Figure 6.36 are the distributions of the skewness factors associated with the streamwise (located at the top, S_u) and wall-normal (S_v) turbulent velocity fluctuations, for the entire test cases in semi-log scales. The S_u values of the smooth and coated surfaces almost perfectly collapse throughout the boundary layer whereas those of the SAND40 surface present positive values for $(y + \varepsilon)/\delta < 0.07$. Very small positive values were also observed in a more restricted part of the near wall region for the higher two Reynolds number cases of the coated surfaces. The positive skewness values near the rough walls may occur due to the less strict wall-normal boundary condition which in turn results in the strong sweep events in which more high momentum fluid is swept into the near wall region (Grass, 1971; Flack et al., 2007; Akinlade, 2005). It is observed that the entire test cases display non-zero skewness factors in the overlap and outer regions which indicate the degree of temporal asymmetry of the turbulent fluctuations such as sweep versus ejection or acceleration versus deceleration. Relatively large negative skewness values occurring in the outer layer imply the existence of deceleration-dominated ejection events due to arriving low-speed fluid from the wall. The overall observations related with the S_u distribution are in agreement with e.g. Flack et al. (2005).

If the skewness factors of the wall-normal turbulent fluctuations (S_v), which are shown in Figure 6.36 at the bottom, are considered, it is observed that these values are positive along the boundary layer and does not change sign for any of the tested surfaces. However, lower values are encountered for the SAND40 surface very near the wall when compared to the smooth and coated test surfaces.

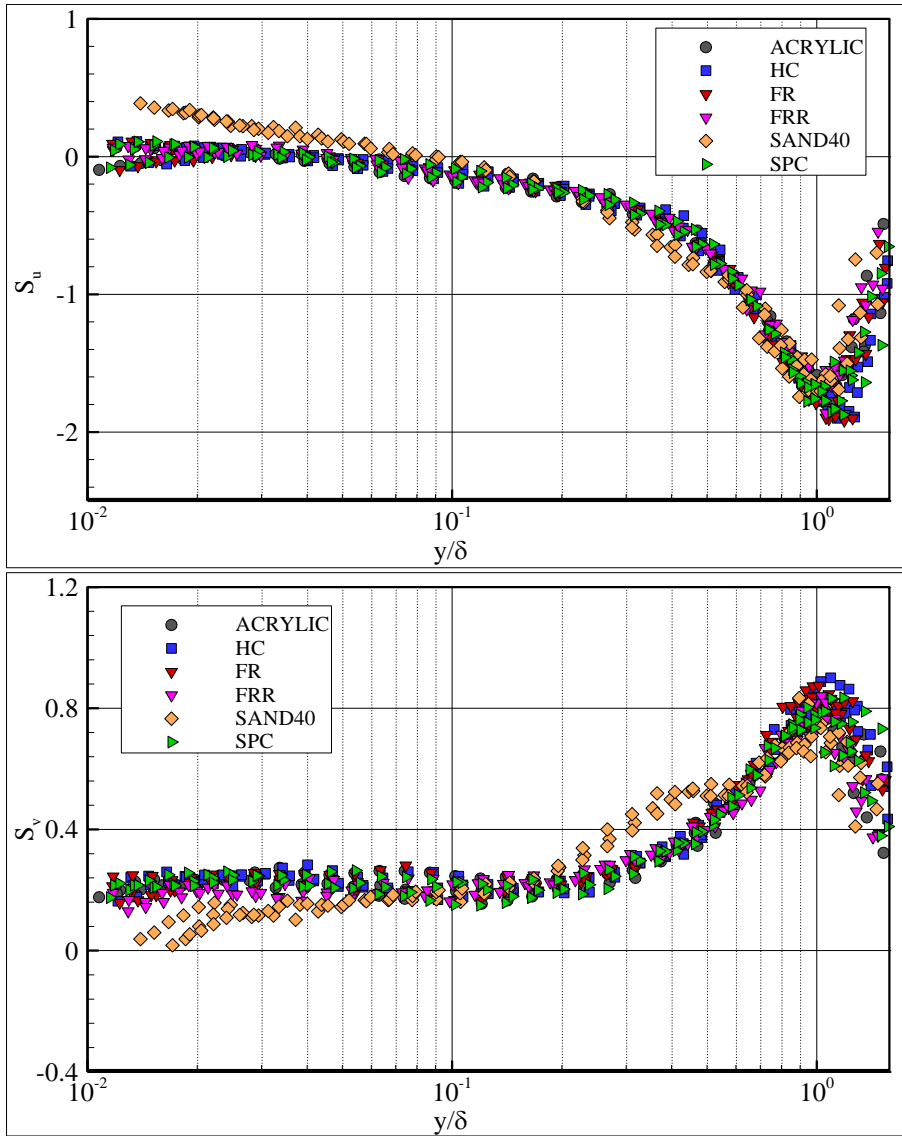


Figure 6.36 : Skewness distributions for the streamwise (top) and transverse velocity fluctuations.

This behaviour is associated with the lower triple products of wall-normal fluctuations that was observed for this fully rough surface in the same region of the inner layer and reflects the lower rate of transport of $\overline{v^2}$ by wall-normal fluctuations due to the less strict wall boundary and energy being sucked by the larger cavities between the roughness elements. The SAND40 surface S_v distribution displays higher values at the outer layer which indicates higher asymmetry in the wall-normal fluctuations and the higher occurrence of sudden large values of wall-normal turbulent velocity. Bandhopadhyay and Watson (1988) and Keirsbulck et al. (2002) observed significant differences in the wall-normal skewness factors between smooth and rough surfaces which extended into the outer layer. Bandhopadhyay and Watson (1988) related the observed differences to the shape of the hairpin vortices which can

induce different wall-normal motions and thus different wall-normal diffusion of turbulence in the rough walls.

The variations of the flatness factors for the streamwise (located at the top plot, F_u) and transverse (F_v) turbulent fluctuations are given in Figure 6.37.

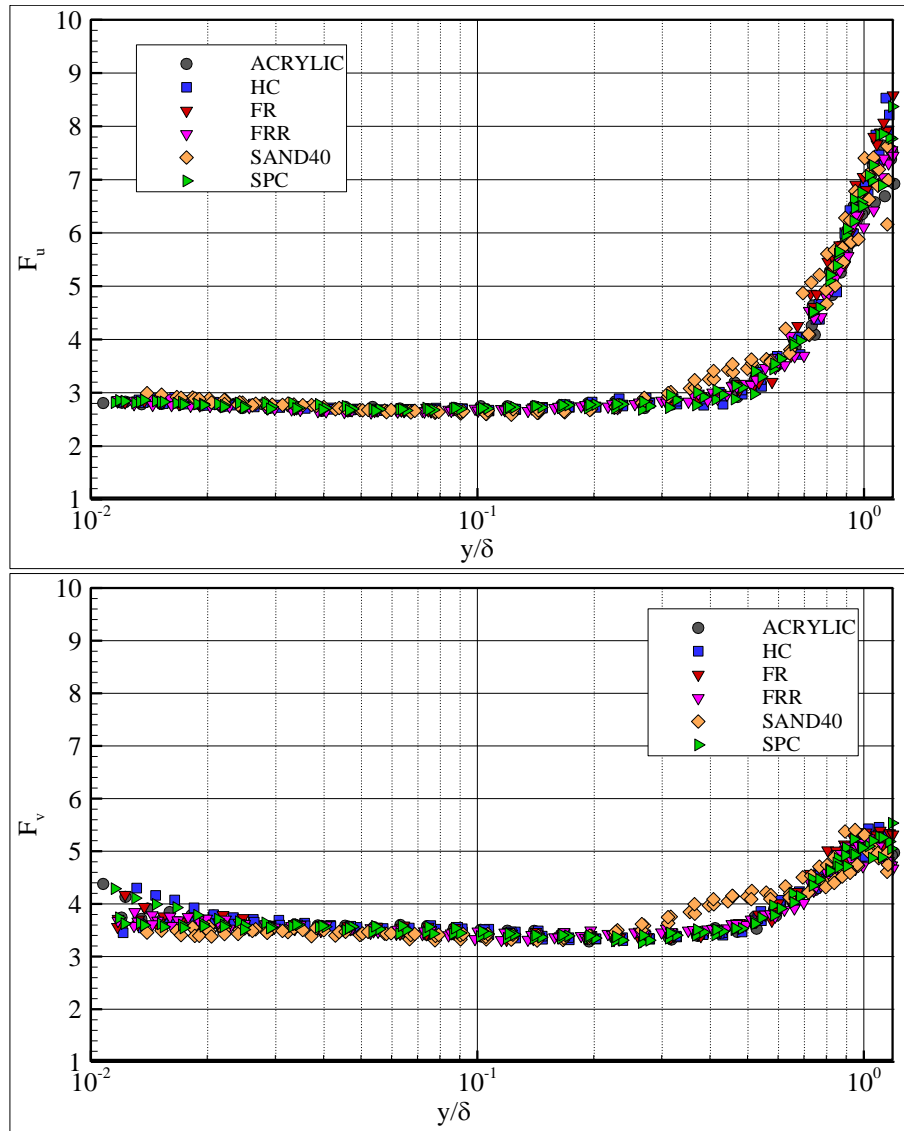


Figure 6.37 : Variation of flatness factors for the streamwise (top) and transverse velocity fluctuations.

The F_u values associated with the smooth, coated and rough walls collapse well in most part of the boundary layer and are slightly lower than the Gaussian value of 3, until $(y + \varepsilon)/\delta \cong 0.6$. Similar observations were reported by Flack et al. (2005) and Bergstrom and Akinlade (2005). The F_v values profiles also overlap for smooth, coated and rough surfaces in most parts of the boundary layer with a value of about 3.5 in average. However, slightly higher values are observed for the SAND40 surface

both for F_u and F_v around $(y + \varepsilon)/\delta \cong 0.35$ to 0.55 . This behaviour may be associated with the occurrence of the low-speed fluid that is driven from the low-velocity region by large vortical structures. The large values of F_u that are encountered in the outer region points out the occurrence of intermittent large-scale negative fluctuations as a result of the large eddies that transport low-speed fluid from the near wall region. This property is less emphasized for the F_v values and the smaller values of F_v compared to F_u close to the end of the boundary layer imply that wall-normal fluctuations are less intermittent than the streamwise ones.

6.7.6 Autocorrelation and spatial correlation functions

The correlation between the same measured quantity (e.g. the streamwise fluctuating velocity component) measured at two different times at the same spatial location is defined as the autocorrelation function (AC) of that quantity, also called as the Eulerian autocorrelation in some references (Bradshaw, 1971; Benedict and Gould, 1998). The autocorrelation function is given by:

$$R_{u_i u_i}(t_s) = \overline{u_i(t)u_i(t + t_s)} \quad (6.5)$$

where t is time, t_s is the time lag between samples, u_i is the i^{th} fluctuating velocity component and $i=1,2$ and 3 . In this thesis, u_1 and u_2 , are conventionally symbolised with u and v . The correlation coefficient, which is also usually referred as the autocorrelation function itself since it is also a function of the time delay, can be defined as:

$$r_{u_i u_i}(t_s) = \frac{\overline{u_i(t)u_i(t + t_s)}}{\overline{u_i(t)^2}} \quad (6.6)$$

The autocorrelation function is often employed in the estimation of characteristic time scales of the flow. It is also possible to obtain the characteristic length scales and spatial correlation functions from the autocorrelation function, only in the streamwise direction, by using the Taylor's hypothesis. For the application of Taylor's idea, it is assumed that the vortical structures (or eddies) will not change in shape noticeably as they pass from a fixed point in space if the turbulent velocity fluctuations are small compared to the mean velocity (Bradshaw, 1971). Taylor's hypothesis implies that the autocorrelation function of a velocity component with

time lag t_s is the same with the spatial correlation of that component with space separation Ut_s , where U is the mean streamwise velocity at the point of interest.

The calculation of the autocorrelations functions are carried out with a MATLAB code, in which also the power spectral density functions are calculated, by using the refined reconstruction method of Nobach (2000) which is explained in detail in Section 3.5 of Chapter 3. The duration of the blocks of sample data were selected as 2 seconds in order to have more than one correlation lengths in one block. The sample populations were divided into at least 100 blocks after the reconstruction. The time lag was selected as 0.001 s in producing the functions and the reconstruction was carried out accordingly.

In Figure 6.8, the variation of the autocorrelation functions calculated for the smooth reference surface at 5 different points in the boundary layer is presented. The dimensions of $R_{uu}(t_s)$ and t_s are m^2/s^2 and s respectively. It is observed that, although the AC are similar at $y/\delta = 0.005$ and 0.01, in general the correlation lengths (the time for the AC to get a value of zero) increases as the measurement point moves from the vicinity of the wall towards the outer layer. This behaviour is similar for all of the tested surfaces and is a result of the larger eddy sizes encountered at the outer layer.

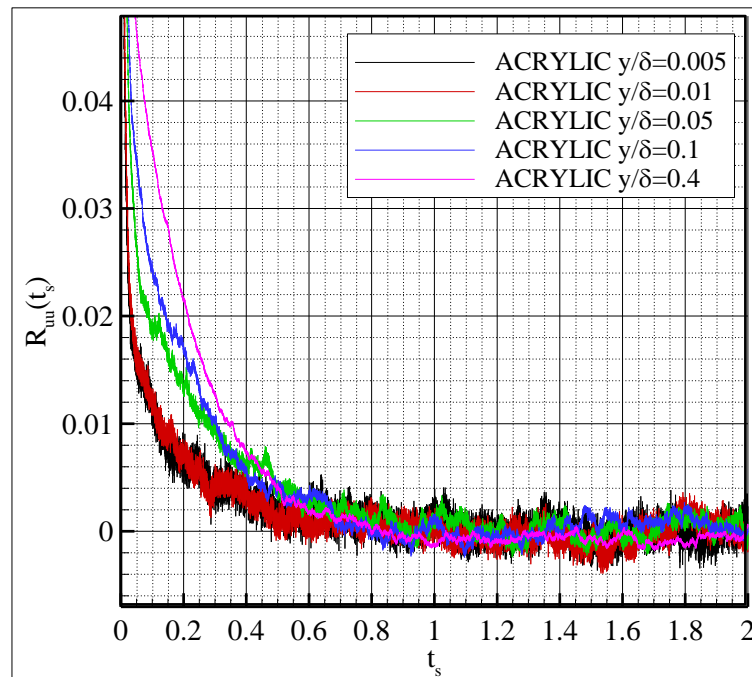


Figure 6.38 : The variation of autocorrelation function through the boundary layer.

Presented in Figure 6.39 are the comparisons of the calculated autocorrelation functions related with each test surface for $y/\delta = 0.05, 0.1, \text{ and } 0.4$. The observation of the presented ACs of the tested surfaces by eye does not display appreciable differences between surfaces at the given wall-normal positions. It is partially due to the noise encountered in the profiles of the ACs which may shelter the differences. The noise comes from the relatively high reconstruction rate, which is necessary for the resolution of the power spectral density functions. However, it can be said that the ACs of the SAND40 surface tend to approach to a value of zero faster than the other tested surfaces at $y/\delta = 0.05$ and 0.1 whilst the area under its curve may be larger than those of other tested surfaces at $y/\delta = 0.4$. Nevertheless, the comparison of the characteristic integral scales that can be calculated from the AC may be a more convenient way to observe the possible differences between the tested surfaces. The integral time scale (TI) can be calculated as follows:

$$TI = \int_0^{\infty} r_{uu}(t_s) dt_s \quad (6.7)$$

The variation of the integral time scales in the boundary layer is comparatively presented for the tested surfaces in Figure 6.40. It is observed that, the TI values increase towards the outer edge of the boundary layer. The integral time scale is a measure of the time scale of the energy containing largest eddies (Hinze, 1975). Moreover, it is observed that the test surfaces have effect on the time scale. The SAND40 surface display shorter TI values compared to the other surfaces in the inner layer whilst at $y/\delta = 0.4$ it has slightly larger TI value than those of the ACRYLIC and HC surfaces, but lower than those of FR and SPC. On the other hand, the FR surface presents a rather higher value at $y/\delta = 0.005$. However, this high value is most probably associated with the very low data rate that was encountered for this surface at the mentioned wall-normal location. On the other hand, SPC, FRR, FR and HC test specimens also show variation from the smooth wall behaviour at different wall-normal locations whilst the FRR surface indicate a 1.6 times lower TI value at $y/\delta = 0.1$. It should be noted here that, the given integral time scales may generally be slightly higher than they normally are, due to the effect of block averaging on the autocorrelation functions. The block averaging technique is a very useful method in decreasing the estimator variances; however it may smooth the resulting AC and thus slightly increase the correlation length. Nevertheless, it is

important to emphasize that all of the test cases were analysed with exactly the same way and the analysis does not have an effect on the comparative trends observed in Figure 6.40.

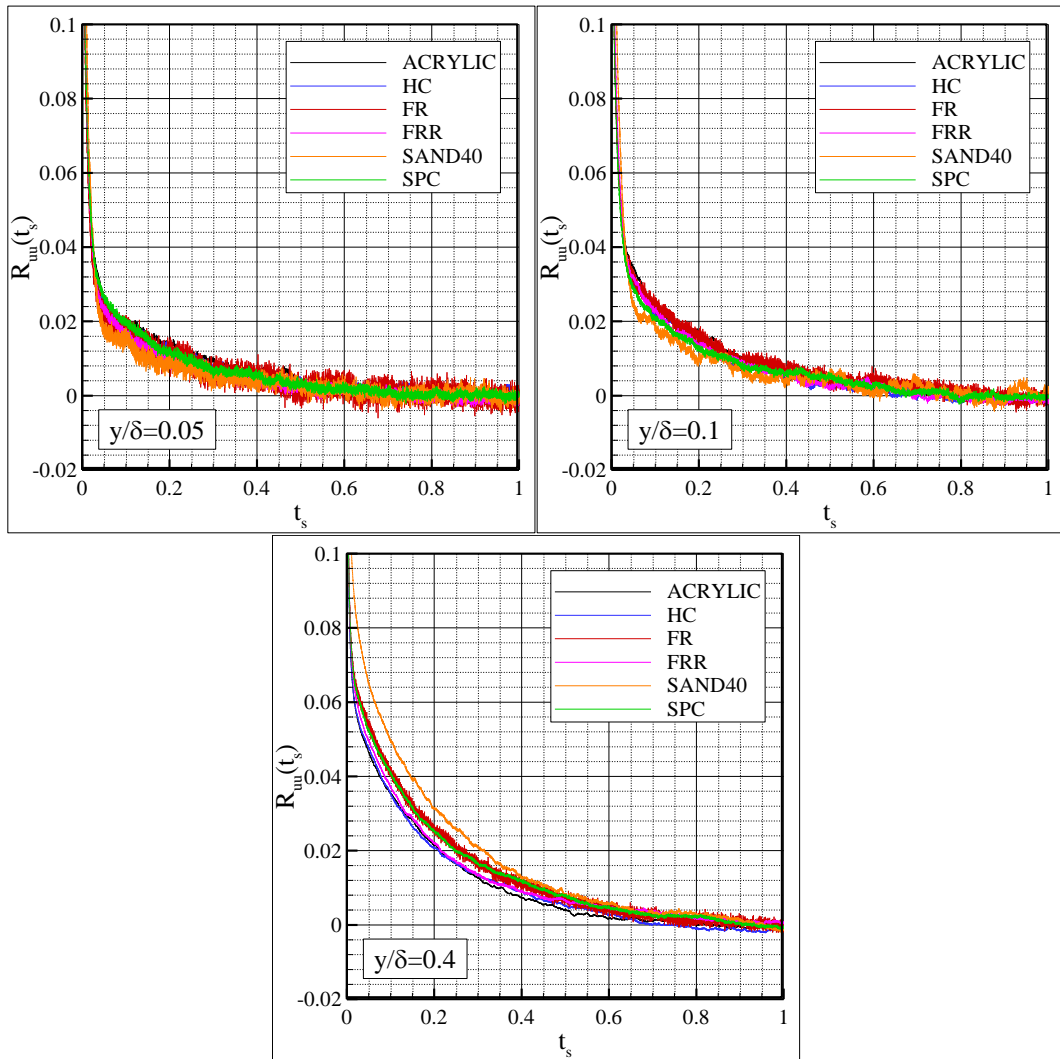


Figure 6.39 : Comparison of the autocorrelation functions for various surfaces.

The observed trend in Figure 6.40 is also expected in the same manner for the integral length scales, by considering the relation between the integral time and longitudinal length scale due to the Taylor's hypothesis. This finding is inline with the physics of channel flow boundary layer investigated by Jimenez (1999) who notes that energy-containing scales are small near the wall while those at the core are large.

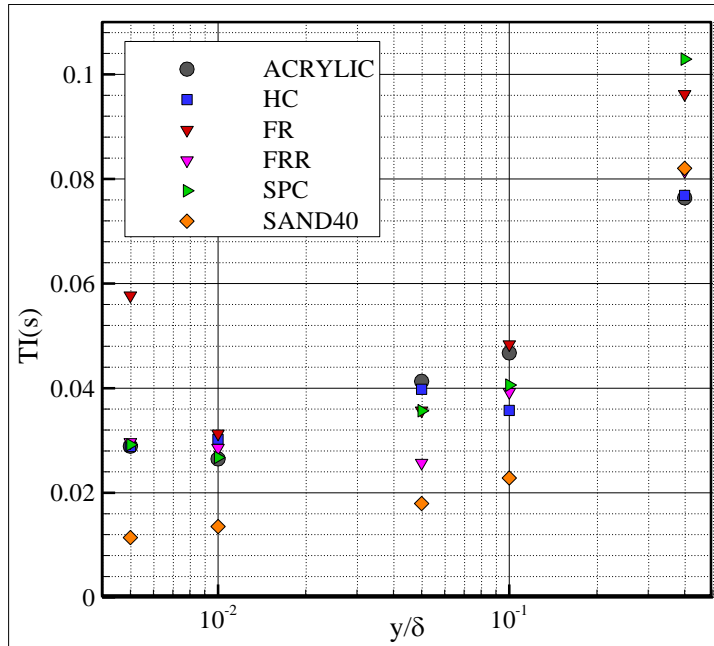


Figure 6.40 : Variation of the integral time scales.

The effect of surface roughness on the time and length scales is still being discussed in the literature (Jimenez, 2004). Krogstad et al. (1992) and Krogstad and Antonia (1994) proposed that the correlation times for all the velocity components were approximately two times shorter for rough surfaces compared to the smooth one, both in the roughness sublayer and outer layer, up to $y/\delta = 0.5$. Their rough surface was a mesh roughness with $\delta/k \approx 50$ and it has been difficult to reproduce the similar effect in other studies (e.g. Flack et al., 2007). It is found in the present study that very similar behaviour is observed for the SAND40 ($\delta/k \approx 60$, with Rt parameter calculated for 50 mm cut-off length as k) surface in a narrower region, for the roughness sublayer and overlap region. The calculated integral time scales of the SAND40 test specimen are 2 to 2.5 times shorter compared to the ACRYLIC specimen up to $y/\delta = 0.1$. On the other hand, Sabot et al. (1977) and Nakagawa and Hanratty (2001) found little or no change in the correlation lengths in the outer layer for a rough pipe with spanwise fences and two-dimensional sinusoidal roughness respectively. In this study, outer layer similarity was observed for the fully rough reference SAND40 specimen. However, SPC and FR specimens appeared to have about 1.3 times larger TI values compared to the smooth reference at $y/\delta = 0.4$, whilst almost no difference was observed for FR and about 1.15 times smaller values were observed for SPC at the lower two y/δ values. This behaviour warrants further

investigation whilst presenting an invasive example against the outer layer similarity at the same time.

The variation of the spatial correlation functions can be investigated for seeking further proof for the above mentioned behaviour. Accordingly, the streamwise spatial correlation functions (SCF) are presented against space lag normalised with the boundary layer thickness in Figure 6.41 for the tested surfaces at various boundary layer locations. The mean streamwise velocities calculated at the associated wall-normal locations were used as the convection velocity in the preparation of the given plots. At $y/\delta = 0.005$, it is observed that the coated surfaces do not show appreciable differences between each other although they follow a distinct trend compared to the smooth reference ACRYLIC. The SCFs of the coated surfaces are enhanced at the moderate $\Delta x/\delta$ but diminished considerably for that of SAND40 at this wall-normal position. The noise due to encountered relatively lower data rate in the close vicinity of the wall may be masking the differences between the coated surfaces, especially those of FRR compared to the others, in the first two locations very near the wall. There exists a noticeable difference in the spatial correlation function of FRR compared to the smooth and coated surfaces at $y/\delta = 0.05$ which is reflected to its integral time/length scale. On the other hand, a consistent significant difference is observed in the spatial correlation function of SAND40 surface at $y/\delta = 0.005, 0.01, 0.05$ and 0.1 . However, this behaviour vanishes at the outer layer and generally rather small differences are observed between the tested surfaces although the SCFs of the SPC and FR follow a slightly higher trend at this location which explains the 1.3 times larger integral scales.

These differences in the SCFs observed in the inner and overlap regions may be associated with the modification of the hairpin vortex regeneration mechanism related with the formation and sustainment of coherent vortex packets (Zhou et al., 1996; Wu and Christensen, 2007). As a result of the investigation of SCFs, it is seen that a slightly different trace was observed in the SCFs of the FR and SPC test specimens regarding the difference observed at the outer layer in the TI values of them. However, there is a high possibility that the difference may be in the combined experimental uncertainty. Accordingly, it can be said that outer layer similarity was generally observed for the entire test cases as a result of the investigation of the streamwise spatial correlation functions.

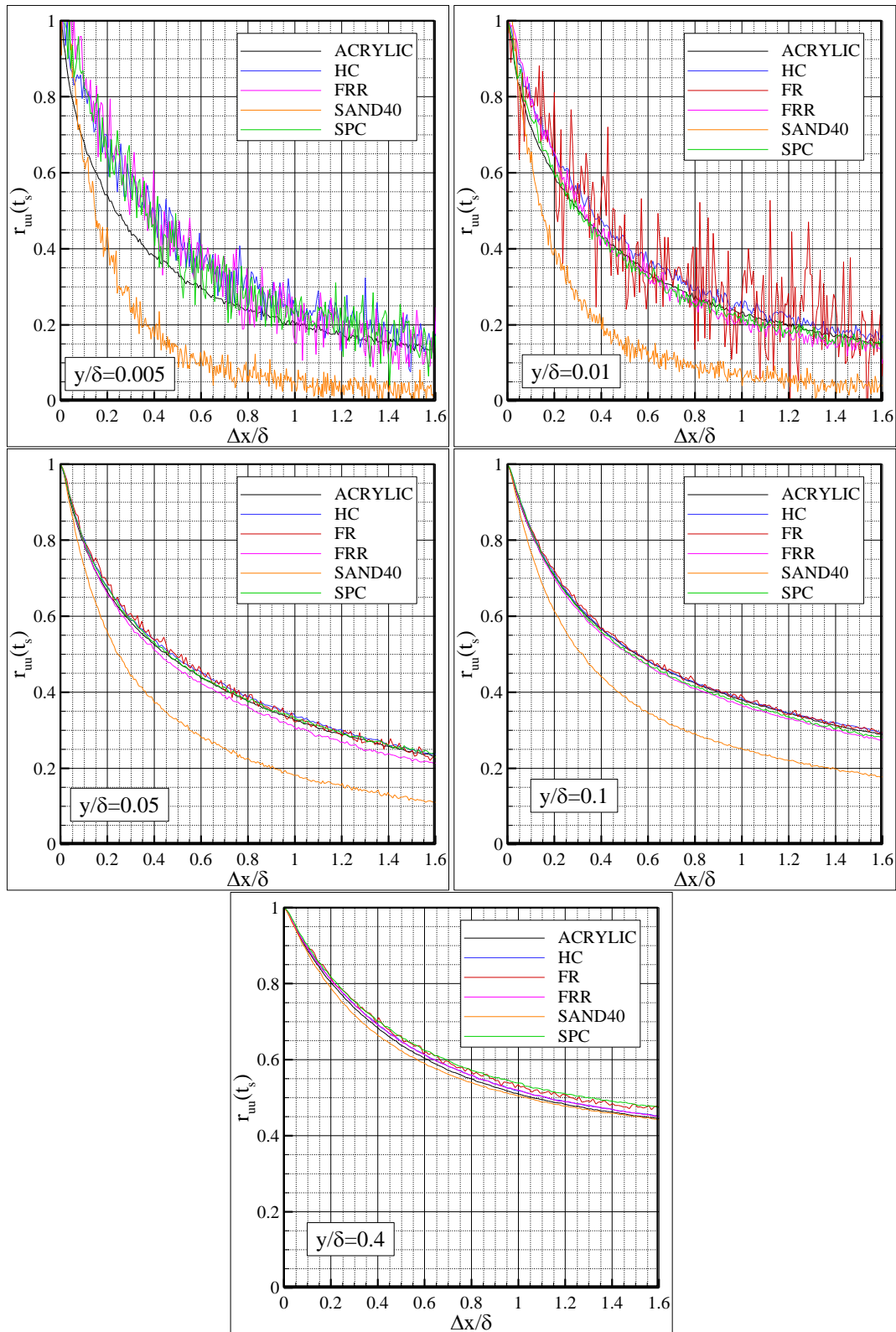


Figure 6.41 : The variation of spatial correlation coefficient.

6.7.7 Turbulence spectra

The turbulent flow consists of unsteady vortical structures (or eddies) which appear on a wide range of time/length scales and interact with each other. The eddies in each

scale have a contribution to the energy and generally the energy flows from the larger eddies to the smaller ones until being dissipated by the viscosity. The distribution of the energy across various frequency or length scales can be investigated by the power spectral density functions of the turbulent velocity fluctuations. In this section, the turbulence spectra calculated for the tested surfaces are presented in dimensional and non-dimensional forms and the results are discussed in detail along with the literature.

The calculations of the one-dimensional time spectra are carried out for the streamwise and wall-normal fluctuating velocity components by using two reconstruction techniques. The major method used in the present study for the calculation of power spectral density functions from the measured randomly sampled LDV boundary layer velocity data was the refined sample and hold reconstruction technique (S&H) of Nobach (2000) which is explained in detail in Section 3.5 of the thesis. A second method was additionally employed in order to have a comparison between the two methods; however the bulk of the results are presented according to Nobach (2000). The second method is namely the linear interpolation method (LIN). The LIN scheme is explained in Moreau et al. (2011) along with a refinement algorithm. The purpose of the scheme is to reconstruct the randomly sampled LDV data so that a set of data with equal intervals are acquired. The sample data population gathered via LDV measurements is given with $r(l)$. Assume that the sample at the wanted interval is $x(l)$ and the given nearest samples are $r(l-m_1)$ and $r(l+n_1)$ where $m_1 \in [1, l]$ and $n_1 \in [l, N - l]$ N being the total number of samples. Accordingly, the value of $x(l)$ can be estimated via linear interpolation as:

$$x(l)_{est} = \frac{n_1}{m_1 + n_1} r(l - m_1) + \frac{m_1}{m_1 + n_1} r(l + n_1) \quad (6.8)$$

The autocorrelation function can be calculated with the estimated values along with the measured ones at constant intervals and via discrete Fourier transform of the autocorrelation the power spectral density function is acquired.

The discrete Fourier transform can also be numerically carried out in a couple of ways such as by using the Fast Fourier Transform algorithm (FFT) or Continuous Cosine Transform (CFT) algorithm. Both of the mentioned algorithms were used in the present study and the results will be compared in the following figures. The FFT

algorithm will not be explained here since it can be found in many textbooks of numerical analysis and it is not in the scope of this study. Such algorithm is also readily available in MATLAB as used in this study. On the other hand, the CFT algorithm was used with the addition of variable windowing technique following Tummers and Passchier (1996) which is known to give very good results with the LDV data (Nobach et al., 1998). The cosine transform with variable windowing can be applied to the autocorrelation function as below:

$$S_j = 2\Delta\tau \left[R_0 + 2 \sum_{k=0}^{2K-1} d_k(f) R_k \cos(2\pi f k \Delta\tau) \right] \quad (6.9)$$

where R_0 and R_k are the 0th and k^{th} autocorrelation function values, $\Delta\tau$ is the sampling interval, f is the discrete sampling frequency, $2K-1$ is the number of values obtained as the autocorrelation function estimation after the refinement process and $j=0, \dots, 2K-1$. $d_k(f)$ is the variable window of Tummers and Passchier (1996) which is given as:

$$d_k(f) = \begin{cases} 0.5 \left(1 + \cos\left(\frac{\pi f k \Delta\tau}{\epsilon}\right) \right) & \text{for } f k \Delta\tau < \epsilon \\ 0 & \text{otherwise} \end{cases} \quad (6.10)$$

where ϵ is an arbitrarily chose parameter, a value of 6 was used in this study as proposed by Nobach et al. (1998).

Moreover, the original executable Pascal code of Holger Nobach, which can be downloaded from Nambis website, is also used as a benchmark, in order to compare and justify the results of the inhouse built MATLAB code for spectral analysis.

Presented in Figure 6.42 and 6.43 are the streamwise turbulence spectra calculated with the code of Nobach (denoted with PSD), the refined sample and hold algorithm together with variable windowing continuous cosine transform (S&H_CFT) and linear reconstruction algorithm with variable windowing continuous cosine transform (LIN_CFT) or FFT (LIN) carried out with the specially prepared MATLAB code for two different LDV data set with a high and low data rate, respectively. The high data rate set of data belongs to the boundary layer flow over SAND40 surface at $y/\delta = 0.4$ whilst the one with the low data rate is from those of SPC surface at $y/\delta = 0.005$. Numbers 1 and 4 in the labels of the plots denote the wall-normal location

whilst C stands for the data being collected with the coincidence mode (with overlapping). The code of the plot legends can be given as “surface_data collection mode_wall-normal location_resampling frequency_number of blocks_block size_reconstruction algorithm_Fourier transform method”.

From Figure 6.42, for the high data rate data set, it is observed that all of the presented results of the different algorithms carried out with the MATLAB code are in very good agreement with that of the benchmark code. It is also noticed that the power spectral density function calculated by LIN does not show any difference between the CFT or FFT. On the other hand, it is seen that increasing the resampling frequency from 20 kHz to 40 kHz slightly reduces the flattening of the tail of the spectrum at the high frequencies, i.e. above 1 kHz, with the S&H methods. The slight difference in the tails of the S&H CFT results and the benchmark is probably due to the noise suppression technique additionally used in the benchmark. The selection of the resampling frequency should be carried out with care, by taking into account the maximum data rate that can be recorded safely with the LDV due to the processor delay. The processor delay can be roughly estimated by dividing the streamwise probe volume dimension with the average streamwise velocity since the processor waits for such a time period until a particle moves into the measurement volume, scatters light back and moves out of the volume for recording one velocity data. In the present measurements, the maximum data rate that can be recorded is calculated as 25 kHz in average. The improvement observed at the flattening of the tail for 40 kHz resampling rate may be a specific example for this case. Accordingly, at most 20 kHz resampling frequency was used in the calculations of the turbulence spectra and 40 kHz is only used in the preliminary calculations for comparison.

However, if Figure 6.43 is examined, in which the turbulence spectra results with the mentioned various algorithms are compared for a data set collected with a relatively lower data rate, it is seen that the LIN results form a unnatural hump at the midfrequency range and lose their agreement with the benchmark and the S&H methods. On the other hand, the results of the S&H algorithm with CFT are in very good agreement at all resampling frequencies with 20 kHz being better than 10 kHz. Accordingly, it can be concluded that LIN algorithm for the reconstruction of the data can be reliably used for the LDV data sets with a high data rate, i.e. more than 1 kHz; however a much more complex algorithm with a refinement procedure is

absolutely needed for the power spectral density function calculation of the data sets with lower data rates.

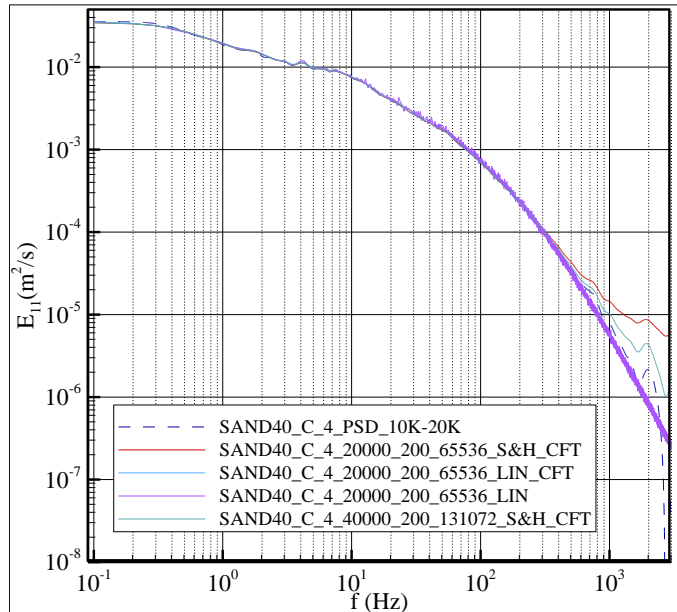


Figure 6.42 : Comparison of the used algorithms in MATLAB code and benchmark test, average sampling rate of the data set is 1470 Hz.

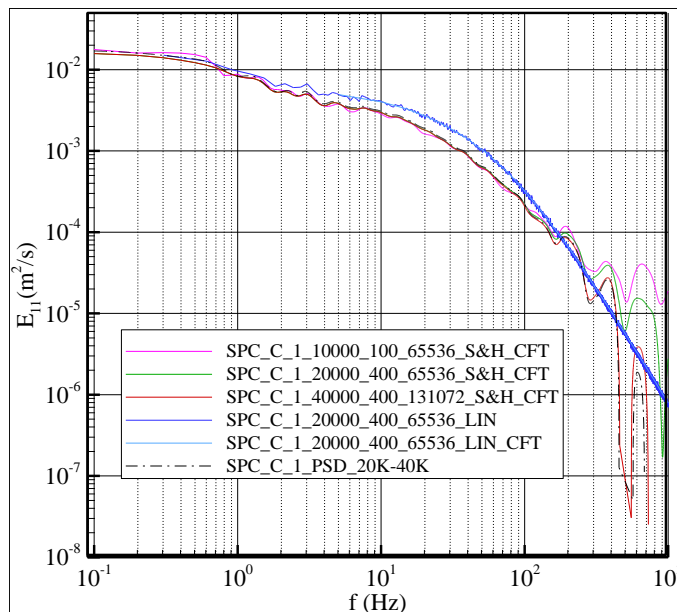


Figure 6.43 : Comparison of the used algorithms in MATLAB code and benchmark test, average sampling rate of the data set is 300 Hz.

In Figure 6.44, the comparison of the S&H algorithm with FFT and CFT are given along with the benchmark results for the ACRYLIC surface data at $y/\delta = 0.005$ with 20 kHz resampling frequencies. It is easily observed that the large variance encountered at the tail of the turbulence spectra with FFT is totally smoothed with variable windowing and CFT. The S&H algorithm result with CFT is in very good

agreement with the benchmark. Accordingly, it was decided that the prepared MATLAB code may be reliably used in the calculations of the turbulence spectra with refined S&H algorithm together with the variable windowed CFT and 20 kHz resampling frequency.

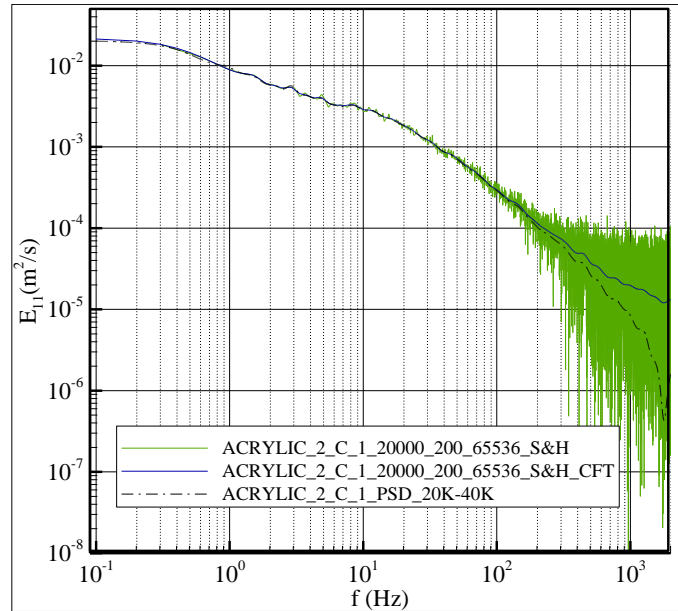


Figure 6.44 : Comparison of the S&H algorithms in MATLAB code with and without CFT and benchmark test, average sampling rate of the data set is 1250 Hz.

The calculated one-dimensional turbulence time spectra are converted to the wavenumber spectra by using the Taylor's hypothesis. Therefore, the $E_{11}(f)$ are multiplied with the mean streamwise velocity (U_{mean}) at the point of interest and divided by 2π so that the wavenumber spectrum $E_{uu}(k)$ is obtained. The wavenumbers are calculated by multiplying the frequency with 2π and dividing it by U_{mean} .

The streamwise wavenumber turbulence spectra are presented in Figure 6.45 comparatively for the test specimens at five different locations in the boundary layer. The wavenumber spectra of the FR test specimen is not included in the plots for the two points nearest to the wall since the data rates over this surface acquired at $y/\delta = 0.005$ and 0.01 were rather low which led to noisy and unreliable spectrum results. It is seen that the $E_{uu}(k)$ of the SAND40 surface show a great difference from those of smooth and coated surfaces distinguished with a remarkable variation in the magnitude and the slopes, at the entire wall-normal positions, including the outer layer. The spectra of SPC and HC surfaces almost overlap with those of

ACRYLIC until $k=100$; however display a distinctive trend at higher wavenumbers for $y/\delta = 0.005$. The related spectra of the FR, SPC, HC and ACRYLIC surfaces perfectly collapse beginning from $y/\delta = 0.05$. On the other hand, the $E_{uu}(k)$ profiles of the FRR surface do not present noticeable difference from that of the smooth reference at $y/\delta = 0.005$ and 0.01 ; however it maintains a moderate difference in magnitude from those of the smooth and other coated surfaces at $y/\delta = 0.05$ and 0.1 . There is a possibility that relatively lower data rates very near the wall, i.e. 300-500 Hz, for the entire surfaces except the ACRYLIC may be masking the differences in the spectra at these two locations closest to the wall. FRR streamwise spectrum presents outer layer similarity although it is investigated in dimensional form.

Perry and Abell (1977) and Perry et al. (1986) proposed scaling arguments and spectral ranges which scale on outer, inner or Kolmogorov parameters for the wave number spectra associated with the three turbulent velocity components. They defined three spectral ranges which consist of inactive, active and fine-scale eddies with an order of increasing wavenumber. The range of inactive eddies, which is composed of the largest eddies and thus located at the small wavenumber part of the spectrum, scales with the boundary layer thickness and friction velocity (outer layer scaling).

The active range comprises the midrange wavenumbers and eddy scales (on the order of Taylor microscale) and obeys inner-layer scaling with wall-normal distance and friction velocity. The fine-scale eddy range represents the part of the spectrum at the highest wavenumbers in which the dissipation is important and this range scales with the Kolmogorov scales (Kolmogorov, 1941; Ligrani and Moffat, 1986) or in other words the dissipation rate (ε) and kinematic viscosity (ν) from which the Kolmogorov scales can be derived. The three ranges of the spectrum overlap in two wavenumber intervals. One of them being the overlap of the inactive and active eddies ranges, overlap 1, in which the spectra of the streamwise (x) and lateral (z) fluctuating velocity components are proportional to k^{-1} . This overlap region and inactive eddy range do not exist in the wall-normal spectrum since the inactive eddies have negligible transverse motion (Raupach et al., 1991). Perry et al. (1987) explains this lack of overlap 1 region according to the attached eddy hypothesis and note that the contributions to wall-normal fluctuations are from the attached eddies of

scale on the order of wall-normal distance (y) only, and hence outer-flow scaling can not be expected.

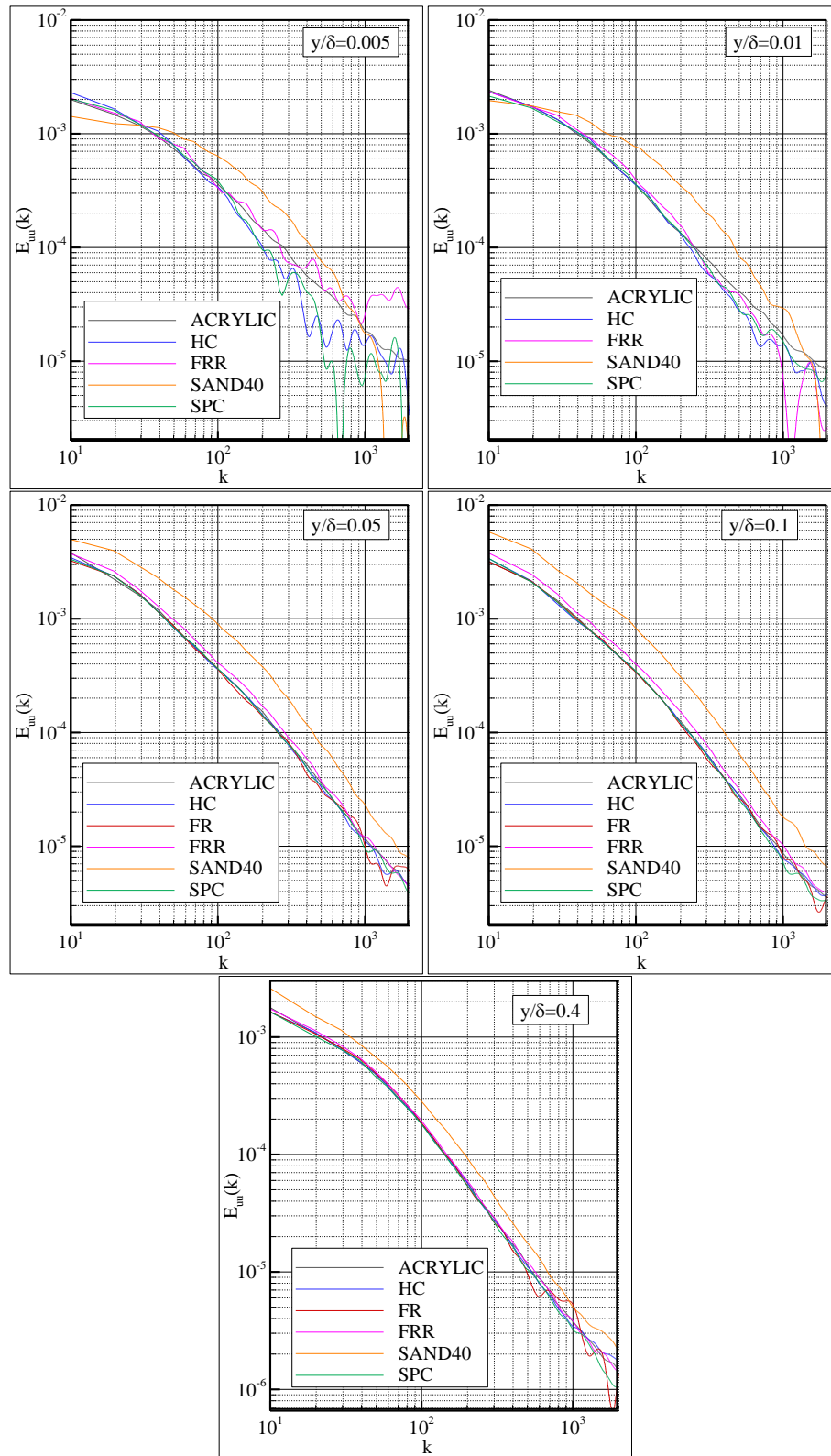


Figure 6.45 : The dimensional streamwise turbulence spectra variation on the surfaces, at five different locations in the boundary layer.

The second overlap region, overlap 2, is the overlap of the active and fine-scale eddy ranges. Overlap 2 is also called as the inertial subrange which exists in the spectra of all fluctuating velocity components. The spectrum follows the Kolmogorov (1941) $-5/3$ power law and proportional to $k^{-5/3}$ in this region.

Following the spectral scaling of Perry et al. (1986), the streamwise spectra are presented for the entire test cases in inner-layer scaling in Figure 6.46 along with the k^{-1} and $k^{-5/3}$ slopes. Rather similar behaviour to that were presented in Raupach et al. (1991) and Perry et al. (1987) is observed in overall with collapse in the outer and inner spectral ranges. Only the spectra of the SAND40 surface are distinguished with a variation in the inactive eddy range. The magnitude of the spectra reach to higher values defined at lower ky values as y/δ decreases. On the other hand, the spectra of the entire surfaces follow the k^{-1} slope at the lower wavenumber range around $ky \approx 0.1$ and obey the $-5/3$ power law almost beginning from $ky \approx 1$. This finding is inline with the expected general behaviour of the streamwise spectra.

In Figure 6.47, the streamwise turbulence spectra calculated for the entire test cases are shown in outer scaling. Coherence with the k^{-1} slope is observed for the entire test cases whilst the inertial subrange (after $k\delta \cong 100$) forms a wider bunch due to the variation of y/δ values included in the figure. This behaviour is a result of the finer-scale eddies not scaling with the outer-flow. These observations are also in agreement with Perry et al. (1987).

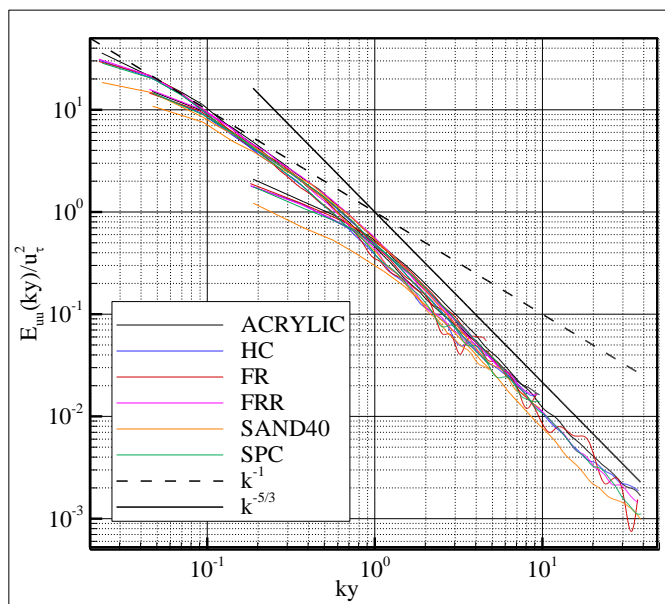


Figure 6.46 : Streamwise turbulence spectra at various positions for all tested surfaces in inner scaling.

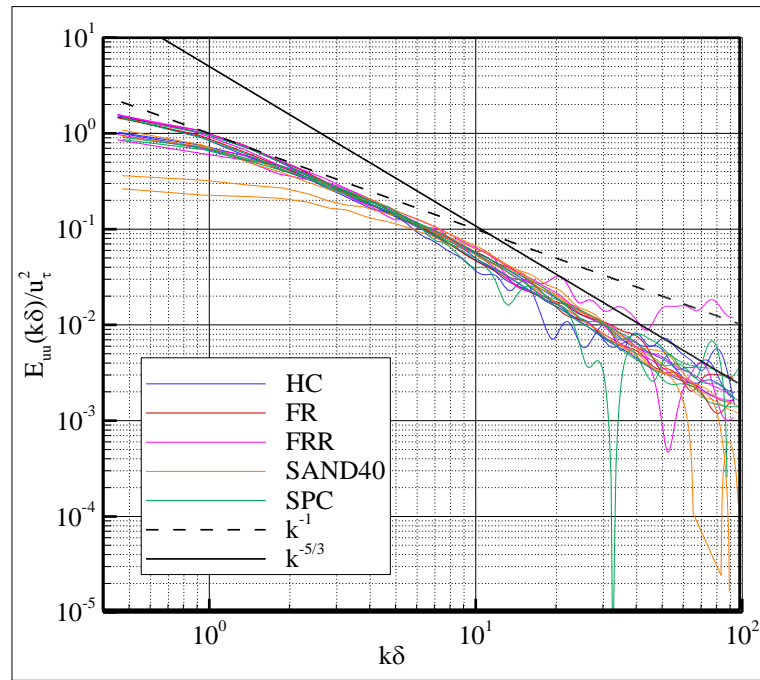


Figure 6.47 : Streamwise turbulence spectra at various positions for all tested surfaces in outer scaling.

The comparative plots of the streamwise turbulence spectra of the tested surfaces at various positions in inner scaling are presented in Figure 6.48 with a separate plot for each wall-normal location. The presented spectra seem to be rather disordered at the higher ky values for $y/\delta=0.005$ due to the resolution problem as a result of lower data rates very near the wall. Except the mentioned lack of order, both the -1 and $-5/3$ power law ranges can be observed for the presented spectra of the entire tested surfaces. At wavenumbers below the inertial subrange, SAND40 surface spectra consistently show variation from the others because of the differences in the energy contained in the large scale structures which also imply non-universal inactive motions for the fully rough reference. This difference is as high as 68% and 60% at the nearest two locations to the wall and gradually decreases until 27% away from the wall at $y/\delta=0.1$. The difference between the spectra of the coated surfaces and smooth reference is at most 18% ($y/\delta=0.05$) and 5% ($y/\delta=0.4$) in minimum at the inactive range. On the other hand, the collapse and similarity of the SAND40 spectra with those of the smooth and coated surfaces for $ky > 0.06 - 0.2$ is a consequence of the active motions and universal wall structure occurring in the inner layer which was also observed as a similarity (but not a total collapse) between the fully rough and smooth wall spectra in Ligrani and Moffat (1986). At $y/\delta=0.4$, the streamwise spectrum of the SAND40 specimen displays lower energy throughout the measured

wavenumbers and the overall difference between the SAND40 and smooth cases is about 25% to 43%. These percentages are large enough to indicate possible differences between the cases. The \overline{uu}^+ values of the SAND40 values were also found to be lower at this location of the boundary layer and the behaviour of the streamwise spectra is a consequence of the lower \overline{uu}^+ values. On the other hand, the flatness factor associated with the streamwise fluctuations was reported to be higher at $y/\delta=0.4$ and it was related with the occurrence of the low-speed fluid that is driven from the low-velocity region by large vortical structures. The entire picture about the presented flow characteristics of the SAND40 surface shows indications of the step change of roughness. Antonia and Luxton (1971) report significantly lower normal and shear Reynolds stresses (in their non-dimensional forms in inner scaling) in the outer region of a rough boundary layer flow up to $x/\delta=16$ distance from the beginning of the step change. Efros and Krogstad (2011) also showed that after approximately $x/\delta=7$ distance from the step change from smooth to rough wall the turbulent normal and shear stresses appeared to be rather lower whilst after approximately $x/\delta=10$ the same quantities were only slightly lower in the outer region compared to those of the smooth wall and fully-developed rough wall boundary layer. The roughness used in both of the mentioned studies were two-dimensional one of them composed of rectangular slats with $\delta/k \approx 23$ and the latter composed of spanwise arranged square bars with $\delta/k \approx 100 - 140$. A faster adaptation to roughness may be expected in our case with $\delta/k \approx 70$ compared to Antonia and Luxton (1971); however the adaptation may be slower than the one observed in Efros and Krogstad (2011). It should be noted here that the present measurements were carried out at approximately $x/\delta=10$ and there exists a high possibility for the flow adaptation not being completed according to the given examples from the literature. On the other hand, it is unfortunate that the change in the spectral behaviour was not investigated in either of the mentioned studies.

Given in Figure 6.49 are the spectra associated with the streamwise velocity fluctuations presented comparatively for the tested surfaces in outer scaling at various positions in the boundary layer. The bunch formed by the spectra of the smooth and coated surfaces at the inactive eddy region for low wavenumbers is observed to shrink when expressed in outer scaling.

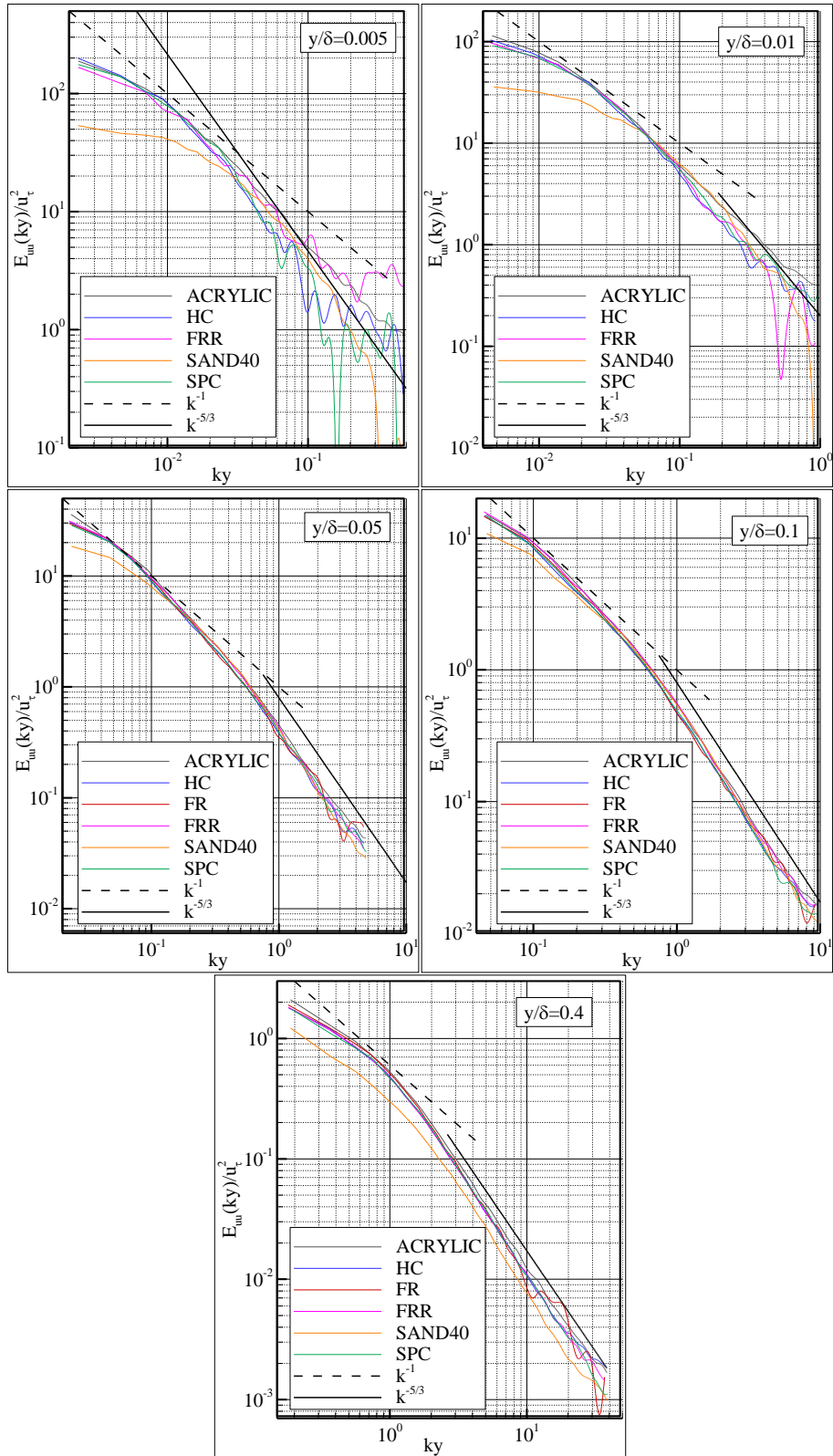


Figure 6.48 : Comparative plots of the streamwise turbulence spectra for the tested surfaces at various positions in inner scaling.

The difference between the smooth and coated spectra in this region varies between 10% and 4.5%, decreasing away from the wall. On the other hand, the differences in the magnitude of the inactive range spectra between the SAND40 and smooth

surfaces are in the same order with the ones observed in inner scaling and takes values of 66%, 59%, 60 and 25% for $y/\delta=0.005, 0.01, 0.05$ and 0.1 , respectively. Moreover, at $y/\delta=0.4$, the distinguished behaviour of the fully rough surface continues in the same way with the one observed in inner-flow scaling. However, outer layer similarity is obviously observed for the smooth and coated cases. The scale of the fine-scale eddy hierarchy on a rough surface is thought to scale with the roughness height (Perry et al., 1987). Therefore, it is expected that the surfaces with different roughness properties may have different hierarchies in the inertial subrange depending upon their ratio of δ/k . Although these parts of the spectra are polluted due to the lower data rates very near the wall, the difference in the trends of the smooth, rough and coated surfaces can still be clearly examined at $y/\delta=0.005$ and 0.01 , at the higher $k\delta$ range. Moreover, at a fixed y/δ location, the y^+ values are much higher for rough walls compared to the smooth surfaces and thus a longer inertial subrange is expected for rough walls. This can also be observed from the given plots at $y/\delta=0.005$ and 0.01 for the SAND40 and coated surfaces whilst the ACRYLIC surface almost does not show $-5/3$ power law region at $y/\delta=0.005$ and is attuned for a rather limited region at $y/\delta=0.01$.

The wavenumber turbulence spectra associated with the wall-normal turbulent velocity component are presented in dimensional form in Figure 6.50 for the tested surfaces, comparatively at different locations in the boundary layer. It is observed that the energy contents of the coated and rough cases are rather larger than that of the smooth surface at the inactive region. SAND40 surface also displays higher energy through the captured higher wavenumbers. The spectra of the coated surfaces display 72% higher values in average compared to the smooth case at $y/\delta=0.005$. The differences in the spectra of the coated surfaces compared to those of the smooth one decrease away from the wall until 15% and vanish at $y/\delta=0.4$. However; SAND40 spectra retain their higher magnitudes compared to the smooth reference through the boundary layer with 81% difference at the two locations nearest to the wall, although the difference between two diminishes away from the wall with values of 65%, 55% and 22% respectively.

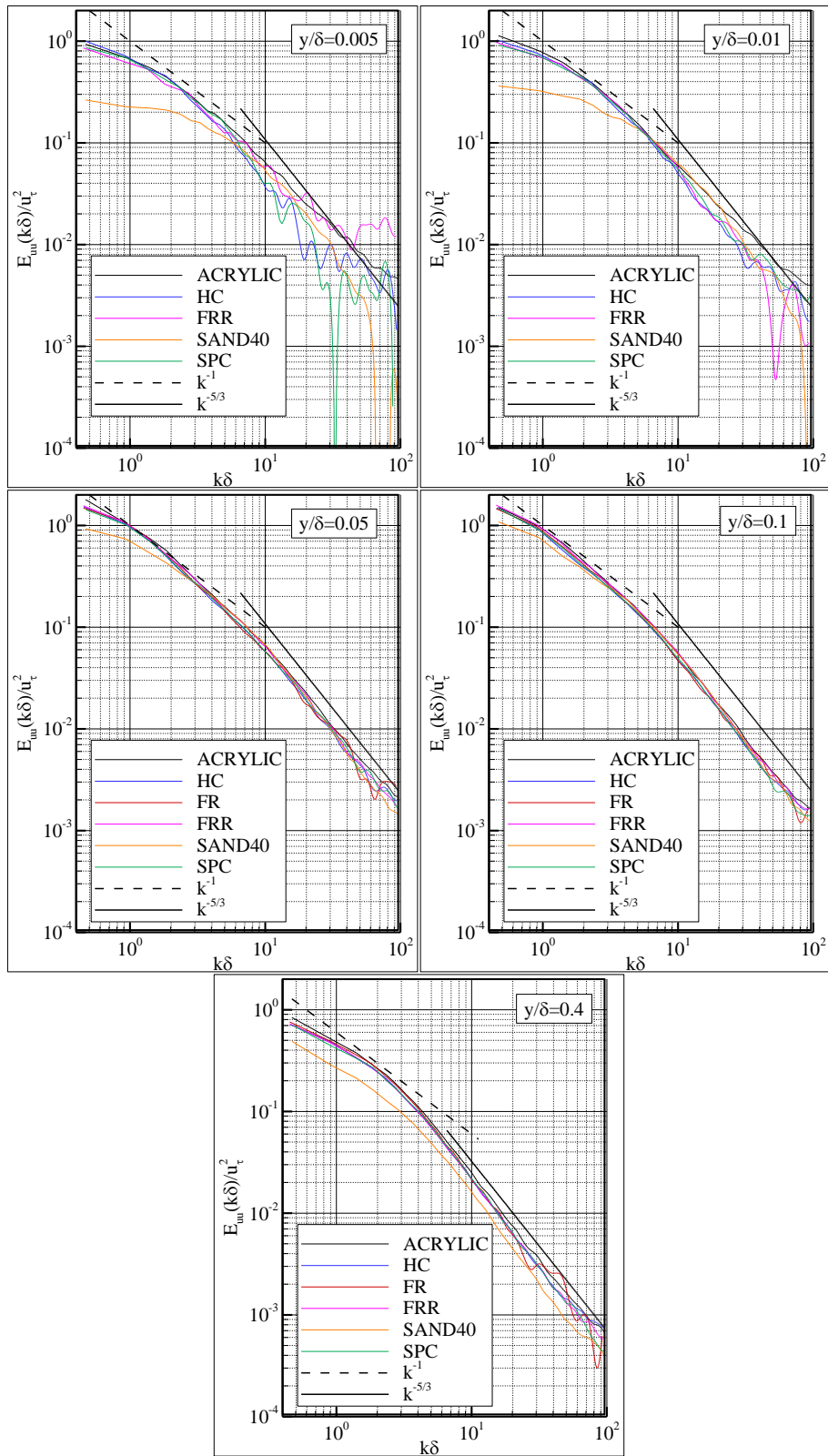


Figure 6.49 : Comparative plots of the streamwise turbulence spectra for the tested surfaces at various positions in outer scaling.

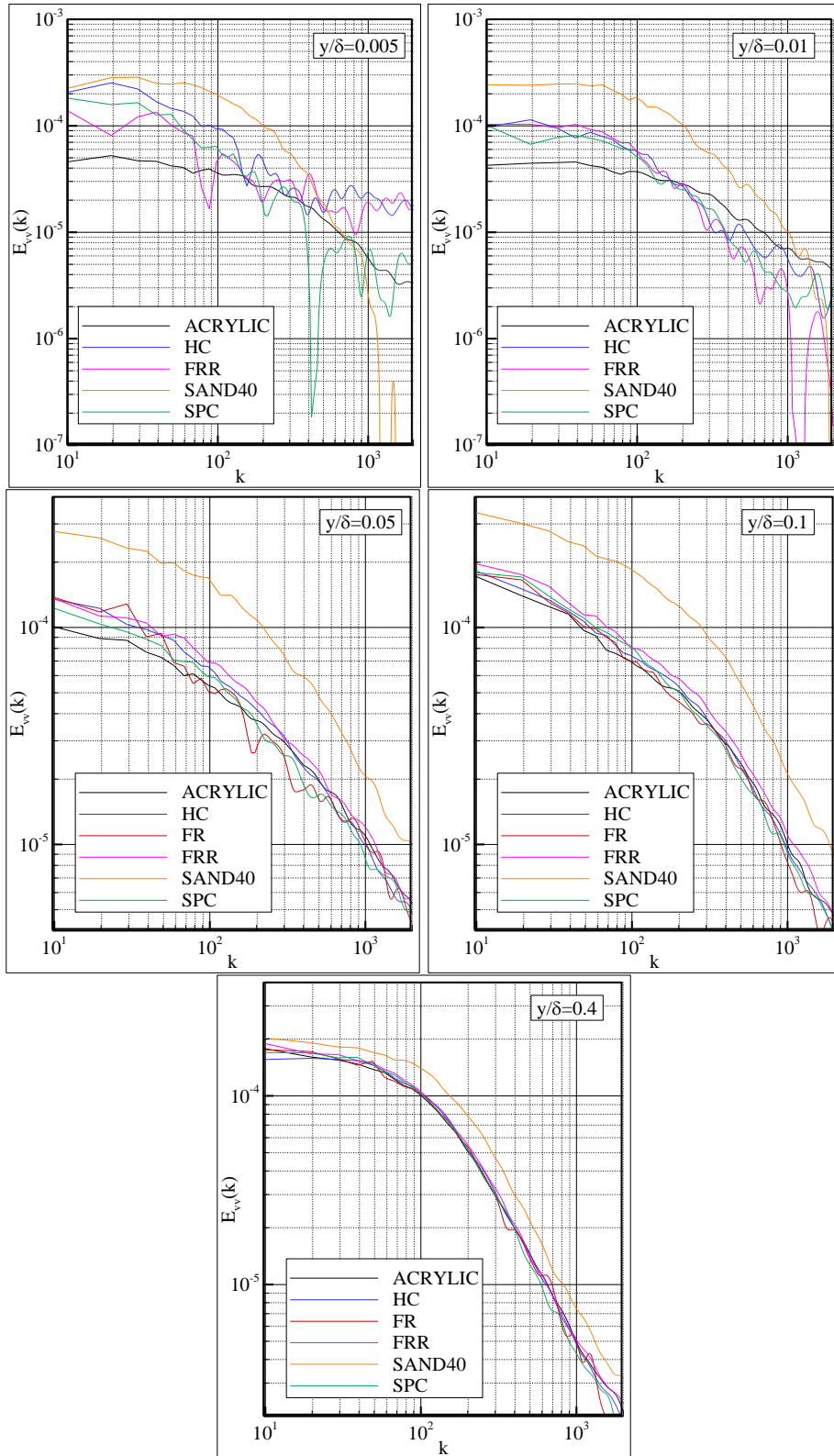


Figure 6.50 : The dimensional wall-normal turbulence spectra variation on the surfaces, at five different locations in the boundary layer.

The v spectra are shown for the smooth reference at various locations in the boundary layer in Figure 6.51. The presented spectra do not collapse as expected in the low non-dimensional wavenumber range. A lack of collapse was also observed in

Perry and Li (1987) and it was related to the possible misalignment of the hot-wire filaments. However, it was reported that the low-wavenumber peel-offs did not depend on varying y/δ . In the present study, the peel-offs are organised depending upon the measurement location in the boundary layer whilst it is observed that there is a collapse for the spectra measured at $y/\delta=0.05$ and 0.1 . Poggi et al. (2003) observed a similar behaviour in u spectra in the buffer region and mesolayer and associated this behaviour with the lack of isotropic conditions due to shear effects. Accordingly, it can be proposed that the collapse in the inactive region in inner scaling may only be achieved in some parts of the log-law region, namely the inertial sublayer where a constant stress region exists. Moreover, the dimensional energy levels and energy distribution along the wavenumbers do not change considerably through the inertial sublayer. Indeed, the u spectra measured at $y/\delta=0.05$ and 0.1 almost collapse for the entire surfaces whilst the v spectra slightly increase towards the outer layer. It is also interesting to note that; the largest variation of the energy levels in the dimensional v spectra are observed in the inactive range of the smooth surface whilst for the fully rough SAND40 surface there is almost no variation in the v spectra through the constant stress region. There is no inverse power law region as expected (Raupach et al., 1991) whilst the scaling region with $-5/3$ power law seems to move towards the lower wave-numbers as the wall is approached.

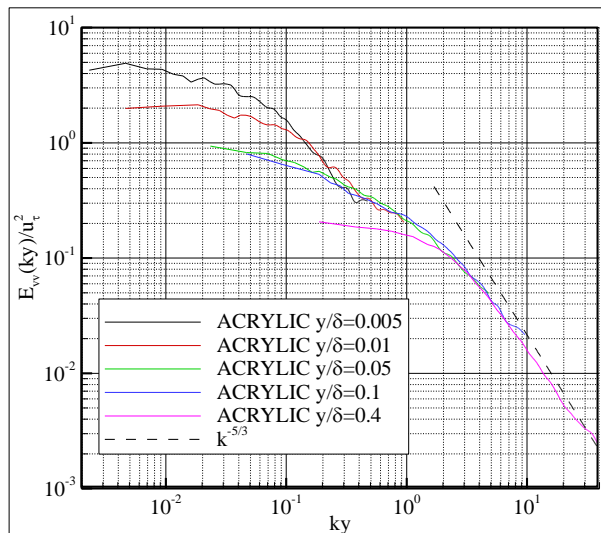


Figure 6.51 : Wall-normal turbulence spectra at various positions for the smooth surface in inner scaling.

In Figure 6.52, comparative plots of the wall-normal turbulence spectra for the tested surfaces at various positions are presented in inner scaling. Inverse power law region do not exist in any of the given spectra, as expected. The $-5/3$ power law region gets

shorter closer to the wall. There is contamination in the given plots of $y/\delta=0.005$ and 0.01 due to lower data rate encountered in the vicinity of the wall. Wall-normal velocity spectra seem to be effected from this contamination more than the streamwise spectra. This is related with the smaller time and length scale composition of wall-normal velocity component compared to the streamwise one.

It is observed from Figure 6.52 that, the energy contained in the inactive region (low wavenumber) is significantly high for the coated and fully rough surfaces compared to that of the smooth surface at the two points nearest to the wall. The mentioned differences are 77% for HC ($\delta/k=3408$), 65% for SPC ($\delta/k=2836$), 58% for FRR ($\delta/k=1064$) and 55% for SAND40 ($\delta/k=70$) measured at their peak values between $k_y=0.005$ and 0.01 compared to ACRYLIC. The variation of the given percentages between the coated surfaces may be in the combined experimental uncertainty; however it is interesting to note that the spectra values at this region increases as δ/k increases for the coated and rough surfaces. At $y/\delta=0.01$ the higher energy contents, compared to smooth reference, of the coated surfaces change between 40% to 48% whilst it is 53% for the SAND40 specimen, all measured at $k_y=0.02$.

The differences between the spectra of the tested coated and smooth surfaces diminish as the outer region of the boundary layer is approached. Volino et al. (2007) reported almost no difference in the pre-multiplied v spectra of their rough surface with $\delta/k \approx 70$ at $y/\delta=0.1$ and 0.4 which is inline for the present results for coated surfaces. On the other hand, Krogstad et al. (1992) and Krogstad and Antonia (1999) showed significant differences in the v spectra almost over the entire wavenumber range for the mesh roughness and rods even at $y/\delta=0.5$. Moreover, their mesh surface displayed lower energy at $y/\delta=0.5$ for the $k\delta$ range of 1 to 30. This is a similar behaviour with the one observed for the present SAND40 case, however a lower energy region exists over the entire measured wavenumber range.

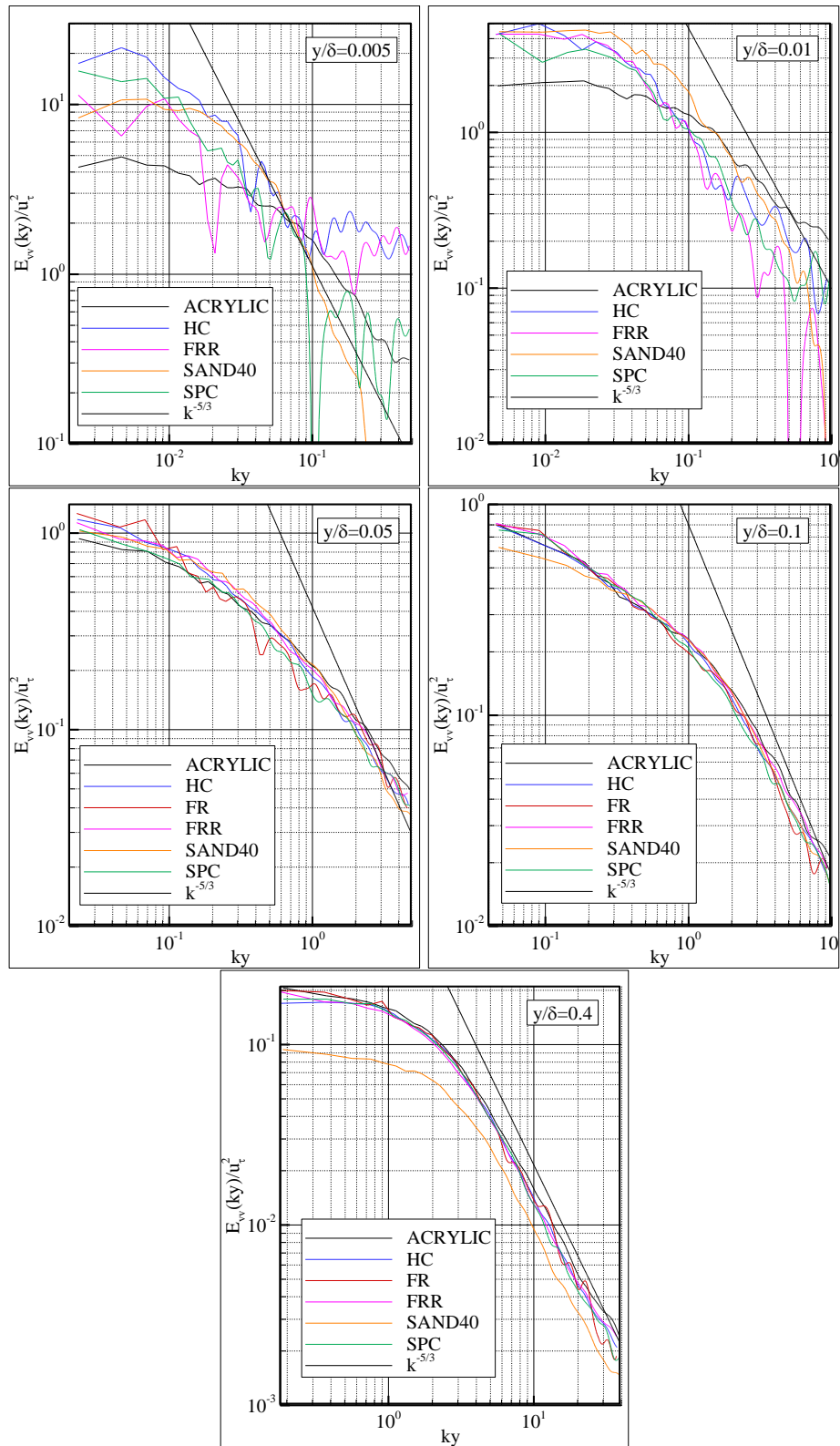


Figure 6.52 : Comparative plots of the wall-normal turbulence spectra for the tested surfaces at various positions in inner scaling.

6.7.8 Transfer functions

The calculation of transfer functions between the roughness spectra and turbulence spectra can be a meaningful attempt since noticeable differences were observed in the streamwise and wall-normal velocity spectra between the coated and rough surfaces. The differences were even more pronounced in the wall-normal turbulence spectra. Therefore, the transfer functions may reveal these differences between the turbulence spectra of the surfaces also in a more powerful way along with defining the relation between the roughness and turbulence in the spectral domain. To the best of the Author's knowledge, this is the first time in the literature that transfer functions were proposed between the roughness and turbulence spectra.

Accordingly, the transfer functions between the roughness spectra of the test specimens and streamwise and transverse turbulence spectra were calculated as was explained in Section 3.6, considering the roughness spectra as the input and turbulence spectra as the output of a linear system.

The question was the roughness spectra calculated at which cut-off length would be more convenient to use in the calculation of the transfer functions. To the Author's belief, it is better to include as many scales as possible in the roughness spectra since the flow over the rough surface interacts with all the longitudinal and wall-normal scales of roughness and thus the resulting variations in the turbulence spectra may be associated with different wavelengths encountered in the surface roughness. However, before reaching at a decision, the transfer functions for the entire surfaces were calculated for each calculated roughness spectra varying with the cut-off lengths. In Figure 6.53, the calculated transfer functions at various cut-off lengths of the roughness spectra are presented for the SPC test specimen. It may be recalled from Section 6.4 that the increasing long wavelength cut-off length has an effect on the power of the small and mid-range wave number part of the roughness spectra and this effect completely loses its influence for $k > 400$. The same behaviour is observed in the calculated transfer functions in Figure 6.53 which is also in the same fashion for the entire tested surfaces. Therefore, it is apparent that the shape of the roughness function dominates that of the transfer function at the low wavenumbers and it may be a better choice to use the roughness spectra whose general shape resembles the turbulence spectra. This may also be helpful in determining analytical functions for the calculated transfer functions. As a result, putting the explained three main

reasons together, it was decided to use the roughness spectra with 50 mm cut-off length for the transfer function calculations.

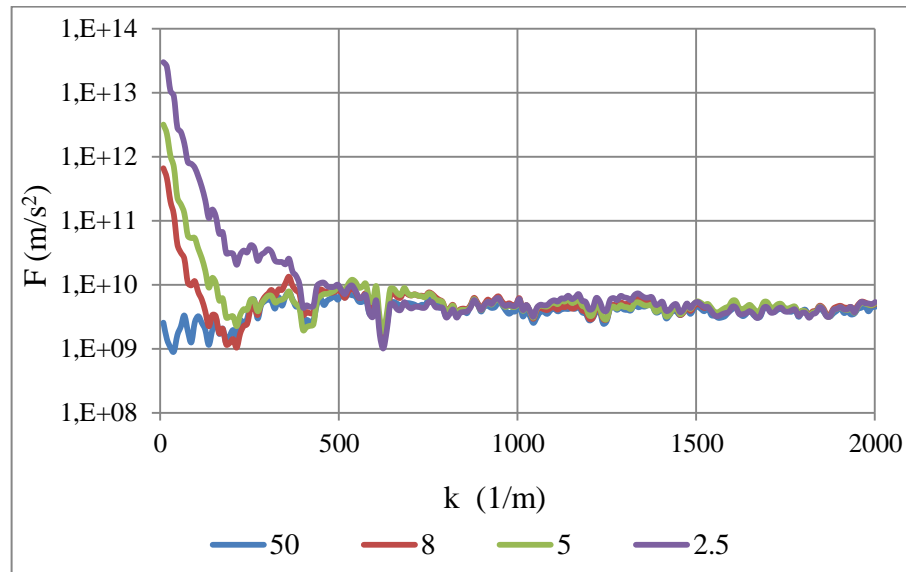


Figure 6.53 : The effect of cut-off lengths used in the roughness analysis on the transfer function, SPC surface.

Presented in Figure 6.54 are the transfer functions between the roughness and streamwise turbulence spectra for the coated surfaces and fully rough reference. The numbers given next to the surface name in the figure legend shows the location in the boundary layer as 1, 2, 3, 4 and 5 being $y/\delta=0.005$, 0.01, 0.05, 0.1 and 0.4 respectively. The F_{uu} calculated for $y/\delta=0.005$ are not included in this figure due to the encountered unrealistic fluctuations in F_{uu} at high wavenumbers arising from the resolution problem of turbulence spectra because of the low data rate at this location of the boundary layer. It is observed from the figure that the transfer functions form groups of three according to the roughness type at the given wall-normal locations. The test specimens coated with anti-fouling by spraying form the group with the highest magnitude, all of them almost collapsing at the low and midrange wavenumbers and with slight differences at the higher wavenumbers for $k>1000$. This behaviour is highly expected since the roughness spectra of the spray-applied antifouling also formed a group of their own. The transfer functions of the FRR surface, which is a surface coated with a foul-release antifouling by rolling, show a similar general trend to those of the spray-applied surfaces; however with a much lower magnitude forming a group by itself. On the other hand, the F_{uu} of the SAND40 specimen display a totally different trend with an even less magnitude, which decreases as the wavenumber increases on the contrary to the other groups. It

should also be emphasized that the transfer functions collapse at the logarithmic region of the boundary layer. The F_{uu} at $y/\delta=0.4$ also display a very similar trend to that observed in the figure with only slightly different magnitudes, but were not included in the plot in order to keep the trends clearly visible.

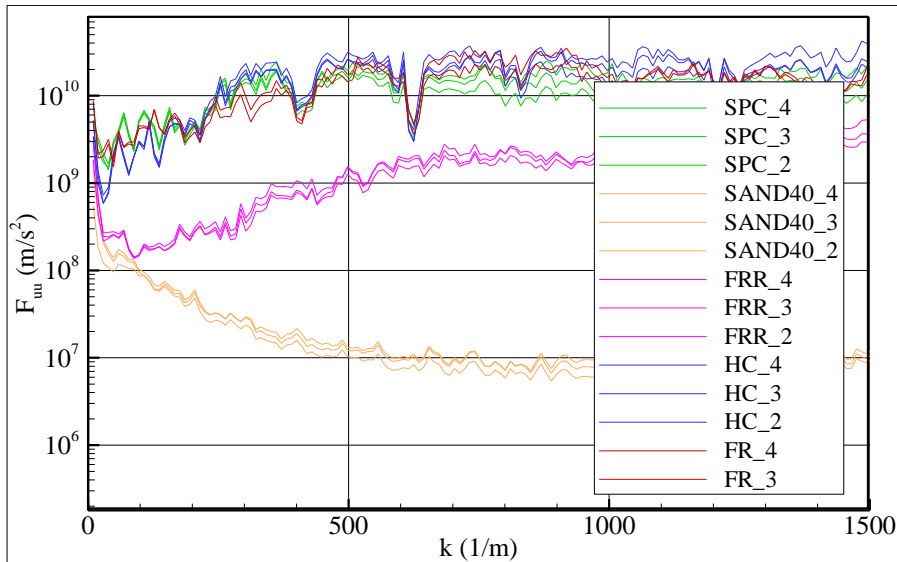


Figure 6.54 : The transfer functions between the roughness and streamwise turbulence spectra, F_{uu} .

The transfer functions for the wall-normal turbulence spectra are shown in Figure 6.55 for the tested surfaces. The three groups observed for the F_{uu} are also present for the F_{vv} . The streamwise and wall-normal transfer functions are very similar to each other both in shape and magnitude. However, the slopes observed along the increasing part of the F_{vv} seen up to $k \approx 500$ are slightly steeper compared to those of the F_{uu} . This behaviour arises due to the lower magnitudes at $k=0$ which are quickly compensated up to $k \approx 500$. The lower magnitudes encountered in F_{vv} are due to the lower energy content of the v spectra at low wavenumbers compared to the u spectra. This is a consequence of the large scale motion which exerts its influence in planes parallel to the wall and thus contributes to the streamwise and vertical normal stresses but not to the wall-normal stresses (Townsend, 1976; Krogstad and Antonia, 1999). The F_{vv} of the surfaces also collapse at the points in the constant stress region which is related with the almost constant energy levels and energy distribution along the wavenumbers through the inertial sublayer.

By considering the three groups of transfer functions formed for the spray-applied antifouling, roller-applied foul-release antifouling and the sand grain surfaces, three sets of analytical functions were determined by using a MATLAB code, separately

for the wall-normal locations in the inertial sublayer and outer layer. Analytical functions were not determined for the nearest point to the wall $y/\delta=0.005$ because of the discrepancies associated with the low data rate at this point. Fourth order Fourier series perfectly define all groups of the transfer functions with varying constants for the investigated wavenumber range. The general form of the transfer functions are given with the below formulation for both F_{uu} and F_{vv} :

$$\begin{aligned}
 F(k) = & a_0 + a_1\cos(kw) + b_1\sin(kw) + a_2\cos(2kw) \\
 & + b_2\sin(2kw) + a_3\cos(3kw) + b_3\sin(3kw) \\
 & + a_4\cos(4kw) + b_4\sin(4kw)
 \end{aligned}
 \tag{6.11}$$

where k is the wavenumber and $k \in [0,2000]$. The constants in the formula are tabulated in Table 6.7 for the determined functions along with the goodness of fit R^2 values. The goodness of fit varies between minimum and maximum values of 0.72 and 0.98, respectively.

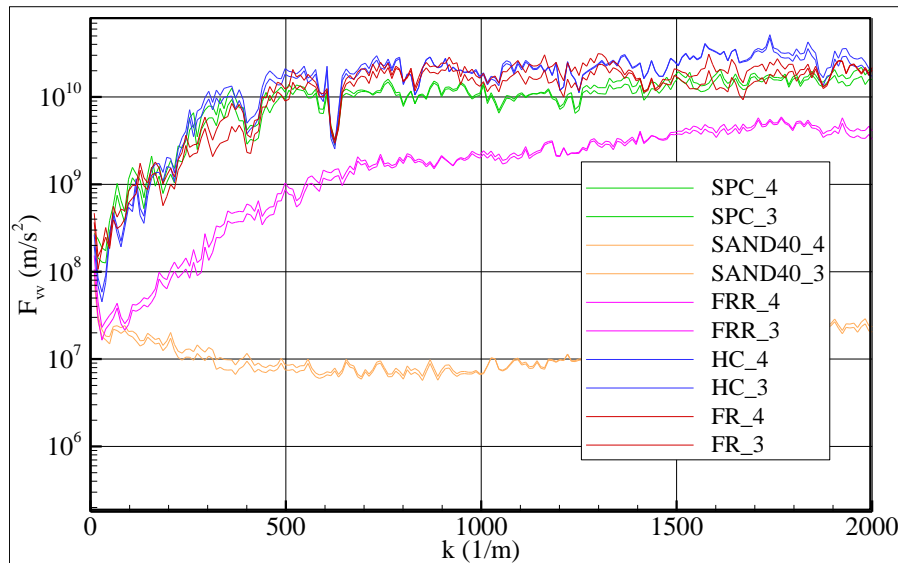


Figure 6.55 : The transfer functions between the roughness and wall-normal turbulence spectra, F_{vv} .

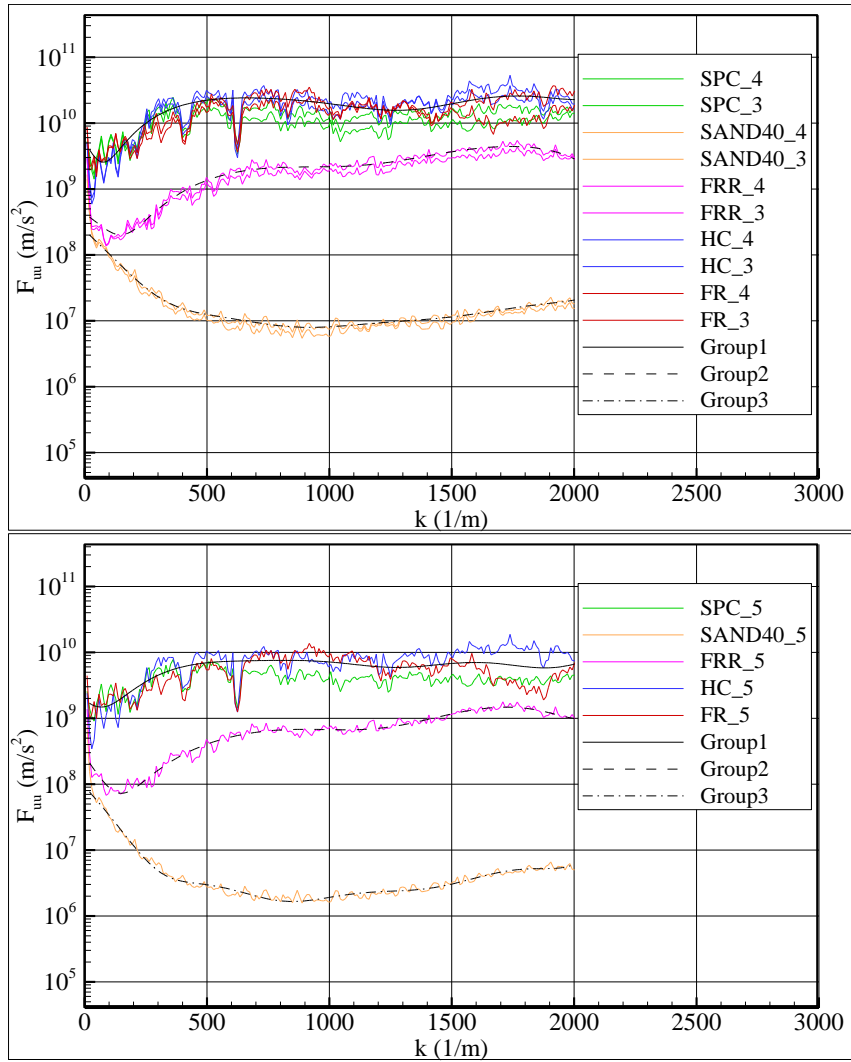


Figure 6.56 : The agreement of the proposed functions for F_{uu} .

In Figure 6.56, the streamwise transfer functions are plotted along with the fitted analytical functions. Group1 and Group2 refer to the spray-applied and roller-applied antifoulings respectively whilst Group3 is the name for the SAND40 surface. The upper plot contains the transfer functions of the inertial subrange wall-normal coordinates and the plot at the bottom presents those in the outer layer of the boundary layer. There exists a very good agreement between the calculated transfer functions and the analytically defined ones. The agreement of the wall-normal transfer functions and the given analytical functions can be observed in Figure 6.57. It is seen that the agreement is at high level between the two as expected from the calculated goodness of fit values.

Table 6.7 : The parameters of the fourth order Fourier function for the transfer functions along with the goodness of fit.

		$a0$	$a1$	$b1$	$a2$	$b2$	$a3$	$b3$	$a4$	$b4$	w	R^2	
F_{uu}	Inertial Sublayer	Group1	1.15E+05	1.39E+04	-1.67E+05	-1.11E+05	-2.43E+04	-2.28E+04	4.95E+04	1.10E+04	5.19E+03	1.60E-03	0.80
		Group2	-2.76E+13	4.39E+13	-5.49E+12	-2.15E+13	5.46E+12	5.93E+12	-2.32E+12	-7.04E+11	3.82E+11	-9.20E-05	0.95
		Group3	1.54E+12	-2.44E+12	-2.80E+11	1.20E+12	2.79E+11	-3.32E+11	-1.18E+11	3.96E+10	1.94E+10	9.45E-05	0.88
	Outer Layer	Group1	6.77E+03	-4.40E+02	-1.25E+03	-1.90E+03	-1.72E+03	-1.72E+03	-8.64E+02	-8.19E+02	4.43E+02	2.26E-03	0.72
		Group2	2.08E+13	-3.32E+13	2.99E+12	1.64E+13	-2.98E+12	-4.61E+12	1.27E+12	5.61E+11	-2.10E+11	-1.01E-04	0.96
		Group3	2.47E+11	-3.92E+11	5.22E+10	1.91E+11	-5.18E+10	-5.23E+10	2.19E+10	6.13E+09	-3.59E+09	-1.16E-04	0.85
F_{vv}	Inertial Sublayer	Group1	-6.50E+06	6.72E+06	8.42E+06	1.34E+06	-5.81E+06	-1.85E+06	8.51E+05	2.88E+05	1.64E+05	9.22E-04	0.88
		Group2	2.07E+03	-9.14E+02	1.58E+03	-8.35E+02	-2.87E+02	-1.25E+02	1.21E+02	-4.33E+01	1.49E+02	2.72E-03	0.98
		Group3	1.93E+11	-3.06E+11	4.61E+10	1.49E+11	-4.58E+10	-4.07E+10	1.95E+10	4.76E+09	-3.20E+09	-8.26E-05	0.89
	Outer Layer	Group1	-1.56E+12	2.48E+12	3.22E+11	-1.22E+12	-3.22E+11	3.37E+11	1.38E+11	-4.01E+10	-2.30E+10	1.45E-04	0.79
		Group2	9.95E+02	-3.92E+02	-7.31E+02	-4.38E+02	-1.36E+02	-7.92E+01	7.22E+01	4.27E+00	7.48E+01	2.71E-03	0.98
		Group3	1.55E+01	1.21E+01	1.50E+01	1.66E-01	1.03E+01	-2.79E+00	3.52E+00	-1.25E+00	8.94E-02	-1.89E-03	0.92

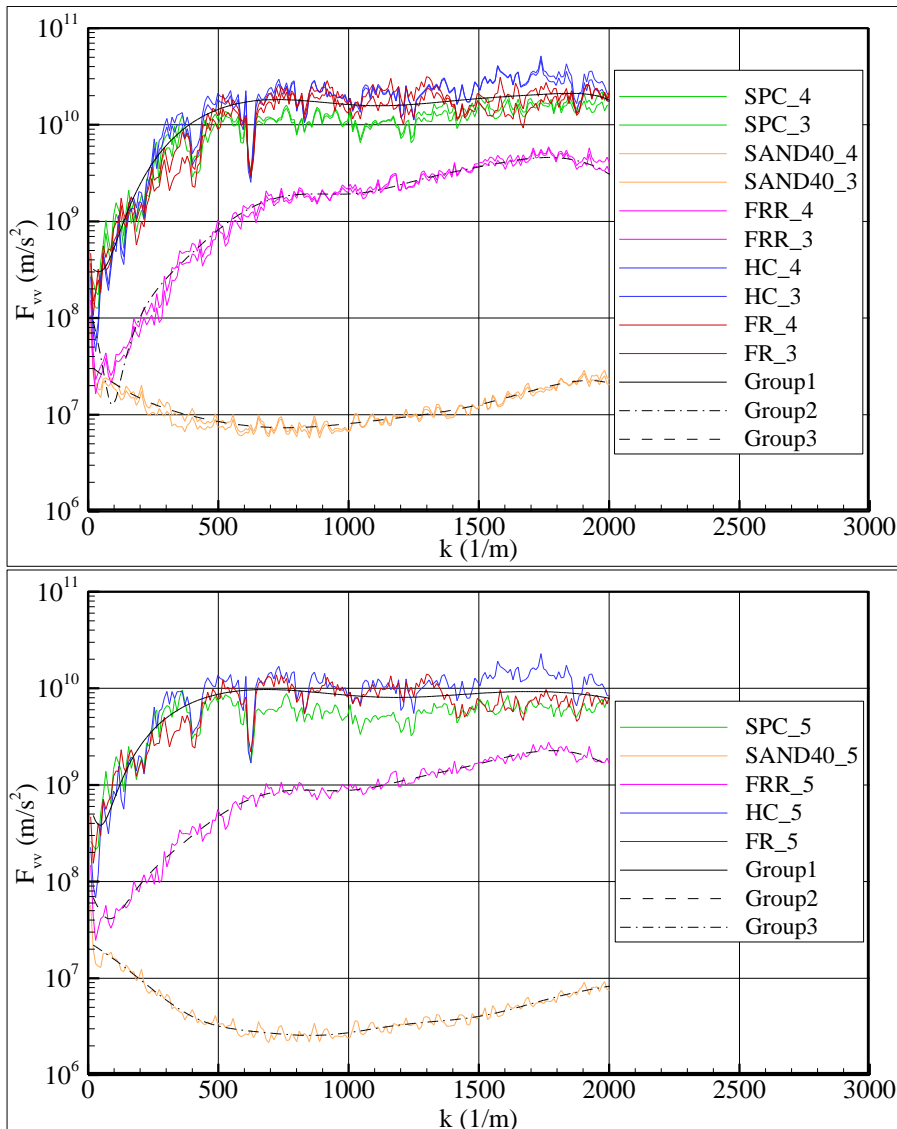


Figure 6.57 : The agreement of the proposed functions for F_{vv} .

According to the results, it may be concluded that the streamwise and wall-normal turbulence spectra related with the flow over a rough surface can be determined by measuring the roughness spectrum and multiplying it with the derived transfer functions. The importance of estimating the turbulence spectra for a flow over a rough surface is related to its bonds with the numerical prediction of the drag characteristics along with the entire flow field parameters. As it is well-known, today there exist two main ways for the numerical solution of flow over a rough surface and thus drag prediction: Resolving the surface texture with a very fine mesh or using a correction of roughness in the turbulence models for RANS calculations. The first choice is almost equivalent to DNS modelling if one thinks about the needed mesh resolution over a transitionally rough surface, whilst the modelling of

roughness in the latter is only based on the equivalent sand grain roughness concept and Nikuradse's roughness functions (Wilcox, 2006). Patel (1998) and Ikeda and Durbin (2007) note the limitations of RANS simulations of rough wall flows. Within the limitations of today's high performance computing capacity seeking a numerical solution with a 3-dimensional mesh that is capable of resolving the roughness scales at high Reynolds numbers is far from being practical. On the other hand, this study along with the others in the literature (e.g. Dey, 1989; Candries and Atlar, 2005, Ünal et al., 2012) showed that the roughness functions of the surfaces coated with marine antifouling do not obey the Colebrook-White law or Nikuradse's in the transitional regime and it will be a false attempt to try modelling the flow over such a surface by a correction with equivalent sand roughness or roughness height value in the turbulence model. The transfer functions may be a solution for filling this gap since turbulence spectra consist of valuable information about the flow physics. For example, the kinetic energy, the dissipation rate, and several length scales can be directly calculated from the turbulence spectra which all can constitute boundary conditions as an input for numerical simulation.

The derived transfer functions are limited to 2-dimensional characteristics of the flow with the investigated surface types and boundary layer locations in this study. Therefore; further work is required for extending the limits of this study by 3-dimensional turbulence spectra measurements over several different surfaces and confirming the behaviour throughout the boundary layer with additional measurement points in the buffer layer, overlap and outer layer. However, it is thought that this study forms a fundamental step in investigating the roughness effects on the turbulent boundary layer by spectral analysis and modelling the effect via transfer functions.

6.8 Conclusions

The results of two-dimensional LDV boundary layer measurements, which were conducted over transitionally rough surfaces coated with marine anti-fouling along with hydraulically smooth and fully rough reference surfaces, were presented in this chapter. The surface roughness measurements of the tested surfaces carried out with a laser profilometer and associated characteristics were also presented. The boundary layer flow measurements were specifically designed for data collection suitable for

the turbulence spectra investigation of this flow. As part of this investigation, the basic findings about the boundary layer properties such as the integral parameters, local skin friction drag coefficients, roughness functions, turbulent normal and shear stresses are examined in detail in the chapter beside the turbulence spectra investigation. Following these, the higher order moments which include the triple correlations along with the skewness and flatness factors are discussed that are usually not included in the rough wall studies due to the lack of needed accuracy in the statistics. The results of the autocorrelation and turbulence spectra of the measured velocity components that were calculated with the refined sample and hold reconstruction method were presented and the effects of surface topographies on these quantities were discussed. Finally, transfer functions between the roughness spectra and the turbulence spectra were calculated and suitable analytical functions representing the mutual relationship between the two spectra were proposed. This was an extremely important milestone, as being one of the important objectives of the thesis, to be able to make an original contribution to the state-of-the-art rough wall turbulent boundary layer flows caused by marine antifouling.

Within the above framework, by considering the findings with the analysed boundary layer parameters, the FRR test specimen appeared to have the higher values of boundary layer, displacement and momentum thicknesses and shape factor compared to the hydraulically smooth reference and other coated surfaces whilst the sprayed antifouling coated surfaces did not show any significant difference in these quantities. The fully rough reference surface (SAND40) also had significantly higher boundary layer parameters than the others, as expected.

A very good collapse of the velocity defect profiles was observed throughout the logarithmic and outer region of the boundary layer both in the conventional outer scaling and Rotta scaling and no significant difference was observed in the wake strength values for the smooth reference surface, coated surfaces or the fully rough surfaces which supported Townsend's (1976) Reynolds number similarity.

It was observed that the FR, HC and SPC coated plates displayed similar drag performances within the uncertainty, for the lowest Reynolds number values whilst the difference between the c_f values of the coated surfaces and the smooth reference was higher than 4.5% in the high Reynolds number range. On the other hand, the differences between the SPC and HC cases were in the uncertainty level at the entire

tested Reynolds number range whilst the differences between the SPC and FR coated surfaces were found to be 3.23% and 3.77% at the two higher Reynolds numbers tested, respectively. FRR test specimen displayed rather high local skin friction drag coefficients over the tested Reynolds number range and this indicated an increase in c_f compared to the smooth reference between 8.92% and 14.74%. The fully rough test specimen also displayed noticeably higher skin friction drag than the other tested surfaces. The trends in the variation of skin friction drag were reflected to the calculated roughness functions as such the entire tested surfaces displayed increasing roughness function values as the Reynolds number increased. Whilst the roughness functions of the coated surfaces did not show any correlation with the relations of Colebrook (1939), Dey (1989) or Ligriani and Moffat (1986) the two new relations were proposed to represent the correlation of the roughness properties and roughness functions within the investigated Reynolds number range. As far as the Author's knowledge is concerned this is believed to be another original contribution of the thesis for some of the modern antifouling coatings in the market.

As far as the results of Reynolds stresses are concerned, it was observed that there exists a consistent variation in the streamwise turbulent normal stresses in the buffer region due to the effect of the surface roughness. The peak values of streamwise turbulent normal stresses near the wall decrease as the roughness Reynolds number increases and totally disappears for the fully rough surface since the viscous region and some parts of the inner region is destroyed together with the breakup of the streamwise vortices due to the roughness elements extending further away from the wall at this surface. In the outer region, Reynolds number dependence is noticed for the tested surfaces. Similar Reynolds number profiles perfectly collapse within the uncertainty beginning from $(y + \varepsilon)^+ \approx 400 - 700$ for the coated and smooth surfaces and $(y + \varepsilon)^+ \approx 1000$ for the SAND40 surface, respectively. For the transverse turbulent normal stresses there exists no distinctive difference between the profiles due to the surface roughness in the overlap and outer region of the boundary layer when they are expressed in inner scaling. The profiles of the same quantity for the smooth and coated surfaces also collapsed within the uncertainty in outer scaling providing support to the wall similarity concept. However, those of the SAND40 presented a discrepancy with lower values over the range $(y + \varepsilon)/\delta > 0.15$ which was attributed to the effect of step change in the surface roughness in the present

experimental set-up. Similar behaviour was also observed for the Reynolds shear stresses.

To the Author's knowledge, the higher order statistics of turbulence were for the first time investigated in the literature for turbulent boundary layer flow developing over surfaces coated with marine antifouling. The triple moments of the turbulent velocity components displayed weaker Reynolds number dependence. The \overline{uuu}^+ values displayed differences between the rough and smooth walls up to $(y + \varepsilon)/\delta \cong 0.2$ which were attributed to the reduced frequency of sweep events for the smooth walls compared to the rough surfaces resulting in an increase in the turbulent flux of Reynolds stresses in the streamwise direction for rough surfaces. The \overline{vvv}^+ values were positive throughout the boundary layer for the entire test cases which imply that the transport of the turbulent kinetic energy occurs away from the wall. The $\overline{u^2v}^+$ and $\overline{uv^2}^+$ profiles of the coated surfaces displayed a collapse with those of the smooth wall through the outer layer and supported outer layer similarity. For the SAND40 and FRR surfaces, the $\overline{uv^2}^+$ values near the wall were greater than those of the smooth and other coated surfaces with a change of sign for both of them which are associated with strong sweeps near the surface of a rough wall. The different trends of the SAND40, which contradict with the outer layer similarity, were also observed in these quantities due to the reflection of the behaviour of the wall-normal turbulent fluctuations. The streamwise skewness values of the smooth and coated surfaces almost perfectly collapsed throughout the boundary layer whereas those of the SAND40 surface presented positive values for $(y + \varepsilon)/\delta < 0.07$ which may occur due to the less strict wall-normal boundary condition and result in strong sweep events. The skewness factors of the wall-normal turbulent fluctuations were positive along the boundary layer and did not change sign for any of the tested surfaces. However, lower values were encountered for the SAND40 surface very near the wall and higher values at the outer layer. These suggest higher asymmetry in the wall-normal fluctuations and the frequent appearance of sudden large values of the wall-normal turbulent velocity. The streamwise flatness factors associated with the smooth, coated and rough walls collapse well in most part of the boundary layer and their values are slightly lower than the Gaussian value of 3, until $(y + \varepsilon)/\delta \cong 0.6$. The wall-normal flatness factors also overlap for smooth, coated and rough surfaces in most parts of the boundary layer with a value of about 3.5 in average.

However, slightly higher values were observed for the SAND40 surface both for F_u and F_v around $(y + \varepsilon)/\delta \cong 0.35$ to 0.55 . This behaviour may be associated with the occurrence of the low-speed fluid that is driven from the low-velocity region by large vortical structures.

It was observed that, the integral time scale values increased towards the outer edge of the boundary layer since the energy-containing scales are small near the wall while those at the outer part are large. Moreover, the test surfaces had an effect on the time scale. The calculated integral time scales of the SAND40 test specimen were 2 to 2.5 times shorter compared to the ACRYLIC specimen up to $y/\delta = 0.1$ whilst the FRR surface indicated a 1.6 times lower TI value at $y/\delta = 0.1$. Therefore, outer layer similarity was observed in the integral time scales of the tested surfaces.

By considering the spatial correlation functions calculated according to the Taylor's hypothesis, it was observed that at $y/\delta = 0.005$, spatial correlation functions of the coated surfaces were enhanced at the moderate $\Delta x/\delta$ but diminished considerably for SAND40 compared to the smooth surface. There existed a noticeable difference in the spatial correlation function of FRR compared to the smooth reference and coated surfaces at $y/\delta = 0.05$ which was also reflected to its integral time/length scale. On the other hand, a consistent significant difference is observed in the spatial correlation function of SAND40 surface at $y/\delta = 0.005, 0.01, 0.05$ and 0.1 which vanished at the outer layer. The differences in the SCFs observed in the inner and overlap regions may be associated with the modification of the hairpin vortex regeneration mechanism related with the formation and sustainment of coherent vortex packets.

As far as the suitability of the power spectral density function calculation methods for LDV data is concerned, it was observed that linear reconstruction algorithm for the reconstruction of the data can be reliably used for the LDV data sets obtained with high data rates, i.e. more than 1 kHz; however a much more complex algorithm with a refinement procedure such as refined sample and hold algorithm is absolutely essential for the data sets obtained with lower data rates. The best results were acquired with the refined sample and hold algorithm used together with the variable windowed continuous Fourier transform.

The turbulence spectra for surfaces coated with new generation marine antifouling and thus irregular engineering surfaces were for the first time investigated in this study with detailed comparative analyses between various surfaces and emphasis on the transitional roughness effects on the turbulence spectra. The streamwise turbulence spectra of the tested surfaces in inner and outer scaling generally showed similar behaviour with the classification done by Perry et al. (1987) and the inverse and $-5/3$ power law ranges were observed in a similar manner. In the inner scaling, at wavenumbers below the inertial subrange, SAND40 surface spectra consistently show variation from the others which imply non-universal inactive motions for the fully rough reference. This difference was at most 68% and gradually decreased until 27% away from the wall. The difference between the spectra of the coated surfaces and smooth reference was at most 18% ($y/\delta=0.05$) and 5% ($y/\delta=0.4$) in minimum at the inactive range. On the other hand, collapse or at least similarity was observed for the fully rough surface at the active and fine-scale eddy ranges. Outer layer similarity was observed for the smooth and coated cases streamwise spectra but not for the fully rough surface. In outer scaling, in the mesolayer, surfaces with different roughness properties had different hierarchies in the inertial subrange depending upon their ratio of δ/k along with a longer inertial subrange region for the coated and fully rough surfaces.

The wall-normal turbulence spectra appeared to show more powerful indications of the roughness effect. The collapse of the wall-normal spectra in the inactive region in inner scaling was only achieved in some parts of the log-law region, namely the inertial sublayer where a constant stress region exists. There was no inverse power law region whilst the scaling region with $-5/3$ power law seemed to move towards the lower wave-numbers as the wall is approached. Noticeable differences were observed in the mesolayer at inactive region of the wall-normal spectra such as 77% for HC ($\delta/k=3408$), 65% for SPC ($\delta/k=2836$), 58% for FRR ($\delta/k=1064$) and 55% for SAND40 ($\delta/k=70$) compared to smooth. The differences in the v spectra values at this region increased as δ/k increased.

To the best of the Author's knowledge, it is the first time in the literature that transfer functions were proposed between the roughness and turbulence spectra and it is thought that this study forms a fundamental step in investigating the roughness effects on the turbulent boundary layer by modelling the effect via transfer functions.

As a result of the calculated transfer functions, three distinct groups were observed for the spray-applied antifoulings, roller-applied foul-release antifoulings and sand roughened surfaces. The streamwise and wall-normal transfer functions of each surface collapsed at the points in the constant stress region which is related with the almost constant energy levels and energy distribution along the wavenumbers through the inertial sublayer. Fourth order Fourier functions were the best to define the calculated transfer functions with goodness of fit values of minimum 0.72 and maximum 0.98. The transfer functions can be used to predict the turbulence spectra which encapsulate valuable information such as the kinetic energy, the dissipation rate, and several length scales that can be used as boundary conditions as an input for numerical simulations. It is believed that the transfer functions can constitute a strong alternative to the classical modelling of rough wall flow in numerical simulations by overcoming the present deficiencies.

7. CONCLUSIONS AND RECOMMENDATIONS FOR FUTURE WORK

7.1 Introduction

Research on rough wall turbulent boundary layer has gone a long way since the first surface roughness effect studies. However, there still exist unresolved major problems associated with the unsatisfying correlation of roughness and friction drag for irregularly rough surfaces in the transitional regime and the signs about the lack of outer layer similarity as well as lack of data for irregular surfaces. The lack of wall similarity brings forward the impossibility of universal numerical modelling for rough walls. The combination of the lack of correlation and wall-similarity imply that separate experimental or numerical-experimental (DNS) work may be needed for the evaluation of the effect of different types of wall roughness except for the sandgrain and some other regular roughness types. Accordingly, there is a need to define universal links between the roughness and turbulence characteristics. Transfer functions may constitute such a link by considering the wide spectral information both for roughness and turbulence. On the other hand, marine antifouling coatings and their performance are also extremely important practical engineering applications of the rough-wall turbulent boundary layer phenomenon requiring further research. Understanding the effect of roughness perturbation on the turbulent boundary layer flow over surfaces coated with new generation marine antifoulings may also shed light to the modelling and estimation of transitional roughness effects.

Accordingly, this study aims to make a contribution to the further understanding and advancement of the state-of-the-art rough-wall turbulent boundary layer flows developed over marine antifouling coatings. The relation and effect of surface roughness on the turbulent boundary layer characteristics were investigated by many aspects in this study with dedicated boundary layer experiments. Particular attention was paid to the irregular transitional roughness and marine antifouling coatings within the objectives of the thesis. The existence of outer layer similarity was investigated amongst several flow parameters. The validity of Colebrook-White law for the surfaces coated with several marine antifoulings was investigated. To the best

of the Author's knowledge, the higher order turbulence statistics and turbulence spectra were investigated in detail for the first time in the literature for the antifouling coated surfaces. The transfer functions between surface roughness and turbulence spectra were also proposed for the first time in the literature.

Two groups of zero-pressure-gradient turbulent boundary layer experiments were performed over surfaces coated with different types of marine antifouling together with hydraulically smooth and fully rough references by using two-dimensional Laser Doppler Velocimetry (LDV). The experiments were conducted in the Emerson Cavitation Tunnel of Newcastle University by using flat plate test beds. The first set of experiments included novel nanostructured antifouling as well as commercially-in-use foul-release type ones. The mean velocity, boundary layer parameters, local skin friction drag, roughness functions and Reynolds stresses were evaluated for the first set of data. The second set of boundary layer experiments were performed for a variety of commercially-in-use marine antifouling including the self-polishing-copolymer (SPC) with copper and spray and roller application of foul-release (FR) type. Smooth and fully rough reference surfaces were also used as references. The mean velocity, boundary layer parameters, local skin friction drag, roughness functions, Reynolds stresses, third and fourth order turbulence statistics, autocorrelation and spatial correlation functions, turbulence spectra and transfer functions were calculated and discussed in detail for the tested surfaces. In order to complement the boundary layer tests, detailed surface roughness measurements were also performed by using a laser profilometer and the BMT hull roughness analyser that is traditionally used in marine industry. Several roughness parameters, autocorrelation and power spectral density functions at various cut-off lengths were presented.

This chapter summarizes the conclusions drawn from the entire experimental investigations and results of the associated detailed analysis. The conclusions on specific areas are grouped together for the ease of the reader. Following the conclusions recommendations are given for future studies.

7.2 Main Conclusions

7.2.1 Roughness characterization

As a result of the roughness measurements and analysis of the tested surfaces coated with newly formulated nanostructured and commercially-in-use antifoulings the following conclusions can be given as:

- It was observed that the entire tested antifoulings, which appeared to present low skin friction drag properties, had an important contribution from the long wave-lengths in their roughness distributions.
- One of the most successful nanostructured antifoulings, in terms of the skin friction drag, had a similar power spectral density function with the one of the commercial foul-release coating in the long and middle wavelength part of the spectra; however the commercially-in-use one appeared to reserve shorter wavelength components in addition to the long and middle wavelengths.
- The difference in the application (i.e. spray or rollering) of the foul-release antifouling coatings significantly changed the spectral behaviour and the roughness parameters of the surface.
- The resulting surface spectral properties of the spray-applied foul-release coating also differed from application to application. One of the specimens contained shorter wavelength components whilst the other did not.

7.2.2 Skin friction drag characteristics

The main conclusions about the skin friction drag properties of the tested marine antifoulings follow:

- Two of the nanostructured amphiphilic coatings with fluorinated copolymer showed about 2% drag reduction with respect to the smooth reference at the higher edge of the tested Reynold number range.
- The general trend in the frictional characteristics of these two superior coatings over the tested Reynolds number range were found to be relatively different than the other surfaces tested with decreasing roughness functions as the Reynolds number increases.

- The spray-applied foul-release type antifouling coated test specimens displayed about 4.0-4.5% lower skin friction drag compared to the other spray-applied antifouling coatings.
- When applied with rollering, the same foul-release type antifouling displayed 5.2% higher frictional drag compared to the other spray-applied antifouling coated specimens.

7.2.3 Correlation of roughness and skin friction drag

As a result of the investigation of the validity of the well-known roughness and friction drag relations for the surfaces coated with marine antifouling the below conclusions were achieved:

- No correlation was observed between the roughness function variations of the present data and the Colebrook-White law.
- Two new relations were proposed for the correlation of the roughness properties and roughness functions within the investigated Reynolds number range. However; further work is needed in order to ensure the validity of the proposed relations at the higher Reynold number range.
- The roughness parameter measured with the conventional BMT hull roughness analyser, Rt_{50} , appeared not to show any correlation with the frictional drag properties for most of the tested antifouling coated surfaces.

7.2.4 Outer layer similarity

The conclusions on the outer layer similarity, which is one of the most contentious subjects in rough wall research, can be given as:

- The collapse of the velocity defect profiles were observed in both conventional outer layer scaling and Rotta scaling through the logarithmic and outer layer; providing support for the universality of the velocity defect law.
- No significant difference was observed in the wake strength values for the smooth, coated or the fully rough surfaces which supported Townsend's (1976) Reynolds number similarity.

- Outer layer similarity was observed in the Reynolds stresses and higher order turbulence statistics for the tested coated surfaces.
- The fully rough reference sand grit surface showed discrepancies in both sets of the experiments, obliterating the validity of outer layer similarity in the Reynolds stresses and higher order moments of turbulent fluctuations. However; this behaviour of the fully rough reference was attributed to the step change effect due to the relatively limited distance from the beginning of the sand grit.
- Outer layer similarity was observed in the spatial correlation functions and integral time scales of the entire tested surfaces.

7.2.5 Turbulence spectra

To the Author's knowledge, the relation between the transitionally rough surface roughness and the turbulence properties was investigated in the present study in the spectral domain for the first time. The main conclusions about the roughness effects on turbulence spectra are:

- The streamwise and wall-normal turbulence spectra of the tested surfaces in inner and outer scaling generally showed similar behaviour with the classification proposed by Perry et al. (1987).
- In the inner scaling, at wavenumbers below the inertial subrange, fully rough sand grit test specimen spectra consistently showed variation from the others which implied non-universal inactive motions. This difference was at most 68% and gradually decreased until 27% away from the wall.
- The difference between the spectra of the coated surfaces and smooth reference was at most 18% in the inner layer and 5% in the outer layer at the inactive range.
- Outer layer similarity was observed for the smooth and coated cases streamwise spectra but not for the fully rough surface.
- In outer scaling, in the mesolayer, surfaces with different roughness properties had different hierarchies in the inertial subrange of the streamwise

turbulence spectra depending upon their ratio of δ/k along with a longer inertial subrange region for the coated and fully rough surfaces.

- The wall-normal turbulence spectra appeared to show more powerful indications of the roughness effect. The collapse of the wall-normal spectra in the inactive region in inner scaling was only achieved in the constant stress region.
- There was no inverse power law region in the wall-normal turbulence spectra whilst the scaling region with $-5/3$ power law seemed to move towards the lower wave-numbers as the wall is approached.
- Noticeable differences were observed in the mesolayer at inactive region of the wall-normal spectra for the coated and fully rough surfaces with a maximum increment of 77% for the surface with the highest δ/k and a minimum 55% for the fully rough reference compared to smooth. The differences in the wall-normal spectra values at this region increased as δ/k increased.

7.2.6 Transfer functions

To the best of the Author's knowledge, it is also the first time that transfer functions were proposed between the surface roughness spectra and turbulence spectra in the literature. The conclusions on the transfer functions can be summarized as below:

- The calculated transfer functions formed three distinct groups for the spray-applied antifouling, roller-applied foul-release antifouling and sand roughness.
- The streamwise and wall-normal transfer functions of each surface collapsed at the points in the constant stress region which is related with the almost constant energy levels and energy distribution along the wavenumbers through the inertial sublayer.
- Fourth order Fourier functions were the proposed to define the calculated transfer functions with high goodness of fit values.

It is thought that this study forms a fundamental step in investigating the roughness effects on the turbulent boundary layer by spectral analysis and especially modelling

its effect via transfer functions. The turbulence spectra over a marine antifouling and sand roughness can be estimated by using the proposed transfer functions and thus several flow parameters (e.g. kinetic energy, dissipation rate, length scales) that can be deduced from the turbulence spectra can constitute boundary conditions as inputs for numerical simulations.

7.3 Recommendations for Future Work

As a consequence of the difficulties encountered in the accomplishment of the present study the following recommendations can be made for the future studies:

- The proposed transfer functions are limited to two-dimensional characteristics of the flow with the investigated surface types and boundary layer locations in this study. Therefore; further work is required for extending the limits of this study by 3-dimensional turbulence spectra measurements over several different surfaces and confirming the behaviour throughout the boundary layer with additional measurement points in the buffer layer, overlap and outer layer.
- The turbulence wavenumber spectra and spatial correlation function calculations were carried out by using the Taylor's hypothesis in this study. Accordingly, the mean streamwise velocities were used as the convection velocities. However, to the Author's knowledge, there has not been any study in the literature that focuses on the convection velocities in the flow over transitionally rough surfaces and the validity of this hypothesis is not certain although it is widely used in the literature. Such a research requires spatial investigation of the flow statistics which may be possible by using high-speed PIV instrument with very fine scaled interrogation areas. Therefore, such a study will shed light on the validity of the Taylor's hypothesis for the flow over transitionally rough walls as well as giving information on the underrecognized flow structure.
- Although tremendous effort was put forward in order to have as high data rate as possible for better resolving the turbulence spectra, the encountered particle rates were not high enough, especially very near the wall, masking the behaviour of the turbulence spectra at the fine-scale eddy range. The

reflections of the laser very near the wall is one of the biggest problems that decreases the validation and thus average rate of data. It was observed that dark red opaque surfaces slightly reduced the laser reflections. Moreover, there exist special seeding particles which are to be used with a special filter on the probe that eliminate/reduce such reflection problems. However, these special particles can only be used in much more small water tunnels due to the associated very high cost. On the other hand, several optical improvements can be made to the LDV system. As an example, a beam displacer can be an effective suggestion which shifts one of the beams resulting in co-planar beams. Such an optical modification will eliminate the need of a tilt angle for the probe which is highly effective on the data rate. The use of hot-films for spectra data collection may also be a solution; however it may bring the major problem of disturbing the flow with the presence of the probe. Nonetheless, a higher particle rate is needed in order to better resolve the roughness effect in the fine-scale eddy range.

- The present work includes the investigation of the flow characteristics in two-dimensions being in the streamwise and wall-normal directions. Unfortunately, three-dimensional LDV measurements with the aid of two probes are rather problematic in a water tunnel due to the difference in the reflection properties of the water and air. Nevertheless, the variation of the third velocity component and associated statistics may be indicative of important clues about the flow over irregularly rough transitional surfaces and three-dimensional investigations are recommended for future study. The transfer functions related with the third turbulent velocity component spectra can also be determined by this way.
- According to the results obtained in this study, it is obvious that the surfaces coated with the marine antifouling do not obey the Colebrook-White law. Although two new correlations were proposed, their validity may be limited with the present data in a limited Reynolds number range. Several combinations of various roughness parameters may be determined for seeking a correlation between the roughness parameters and the skin friction drag. There is no doubt that, a systematical analysis is also needed in order to seek such a correlation considering a wide range of roughness parameters along

with extending the present data. This has an extreme practical importance in predicting the contribution of the coatings in overall drag (e.g. ship resistance).

REFERENCES

- Adrian, R.J., Christensen, K.T., and Liu, Z.C.** (2000). Analysis and Interpretation of Instantaneous Turbulent Velocity Fields. *Experiments in Fluids*, **29**, 275-290.
- Adrian, R.J., Yao, C.S.** (1987). Power Spectra of Fluid Velocities Measured by Laser Doppler Velocimetry, *Experiments in Fluids*, **5**, 17-28.
- Afzal, N.** (2008) Alternate Scales for Turbulent Boundary Layer on Transitional Rough Walls: Universal Log Laws. *Journal of Fluids Engineering Transactions of ASME* 130:041202
- Akinlade, O.G.** (2005). *Effects of Surface roughness on the Flow Characteristics in a Turbulent Boundary Layer*, PhD Thesis, University of Saskatchewan, Saskatoon.
- Akinlade, O.G., Bergstrom, D.J., Tachie, M.F., and Castillo, L.** (2004). Outer Flow Scaling Of Smooth And Rough Wall Turbulent Boundary Layers. *Experiments in Fluids*, **37**, 604–612.
- Allen, J.J., Shockling, M.A., and Smits, A.J.** (2005). Evaluation of a Universal Transitional Resistance Diagram for Pipes with Honed Surfaces. *Physics of Fluids*, **17**, p.121702.
- Andreopoulos, J., and Bradshaw, P.** (1981). Measurements of Trubulence Structure in the Boundary Layer on a Rough Surface. *Boundary Layer Meteorology*, **20**, 201-213.
- Antonia, R.A., and Krogstad, P.A.** (2001). Turbulence Structure in Boundary Layers over Different Types of Surface Roughness. *Fluid Dynamics Research*, **28**, 139.
- Antonia, R.A., and Luxton, R.E.** (1971). The Response of a Turbulent Boundary Layer to a Step Change in Surface Roughness. Part 1. Smooth to Rough. *Journal of Fluid Mechanics*, **48**, 721-761.
- Antonia, R.A., and Shafi, H.S.** (1999). Small Scale Intermittency in a Rough Wall Turbulent Boundary Layer. *Experiments in Fluids*, **26**, 145.
- Atlar, M., Politis, G., and Ellis, J.** (2010 and 2012). Personal Communication.

- Atlar, M.** (2011). *Recent Upgrading Of Marine Testing Facilities At Newcastle University*. In: AMT'11, the second intl conference on advanced model measurement technology for the EU maritime industry, 4–6 Apr 2011. Newcastle University, UK.
- Atlar, M., Ünal, B., Ünal, U.O., Politis, G., Martinelli, E., Galli, G., Davies, C., Williams, D.** (2012). An Experimental Investigation on the Frictional Drag Characteristics of Nanostructured and Fluorinated Fouling Release Coatings, *Biofouling (under review)*.
- Bakken, O.M., Krogstad, P.A., Ashrafian, A., and Andersson, H.I.** (2005). Reynolds Number Effects in the Outer Layer of the Turbulent Flow in a Channel with Rough Walls, *Journal of Fluid Mechanics*, **530**, 327-352.
- Bandyopadhyay, P.R.** (1987). Rough-Wall turbulent Boundary Layers in the Transition Regime. *Journal of Fluid Mechanics*, **180**, 231-266.
- Bandyopadhyay, P.R., and Watson, R.D.** (1988). Structure of Rough Wall turbulent Boundary Layers. *Physics of Fluids*, **31**, 1877-1883.
- Barenblatt, G.I.** (1993). Scaling Laws for Fully Developed Shear Flow. Part 1. Basic Hypothesis and Analysis. *Journal of Fluid Mechanics*, **248**, 513-520.
- Barenblatt, G.I., and Chorin, A.J.** (1998). Scaling of the Intermediate Region in Wall-Bounded Turbulence: The Power Law. *Physics of Fluids*, **10**, 1043.
- Barenblatt, G.I., Chorin, A.J., and Protokiskin, V.M.** (2000). A Note on the Overlap Region in Turbulent Boundary Layer. *Physics of Fluids*, **12**, 2159-2161.
- Barenblatt, G.I., and Protokiskin, V.M.** (1993). Scaling Laws for Fully Developed Turbulent Shear Flows. Part 2. Processing of Experimental Data. *Journal of Fluid Mechanics*, **248**, 521-529.
- Batchelor, G.K.** (1953). *The Theory of Homogeneous Turbulence*. Cambridge University Press, London.
- Beigbeder, A., Linares, M., Devalckenaere, M., Degee, P., Claes, M., Beljonne, D., Lazzaroni, R., Dubois, P.** (2008a). CH-Pi Interactions As The Driving Force For Silicone-Based Nanocomposites With Exceptional Properties. *Advanced Materials*, **20**, 1003.
- Beigbeder, A., Degee, P., Conlan, S.L., Mutton, R., Clare, A.S., Pettitt, M.E., Callow, M.E., Callow, J.A., Dubois, P.** (2008b). Preparation and Characterization Of Silicone-Based Coatings Filled With Carbon Nanotubes and Natural Sepiolite And Their Application As Marine Fouling-Release Coatings. *Biofouling*, **24**, 291.

- Beigbeder, A., Jeusette, M., Mincheva, R., Degee, P., Claes, M., Brocorens, P., Lazzaroni, R., Dubois, P.** (2009). On the Effect of Carbon Nanotubes on the Wettability and Surface Morphology of Hydrosilylation-Curing Silicone Coatings. *Journal of Nanostructured Polymers and Nanocomposites*, **5**, 37-43.
- Beigbeder, A., Mincheva, R., Pettitt, M.E., Callow, M.E., Callow, J.A., Claes, M., Dubois, P.** (2010). Marine Fouling Release Silicone/Carbon Nanotube Nanocomposite Coatings: On the Importance of the Nanotube Dispersion State. *Journal of Nanoscience and Nanotechnology*, **10**, 2972-2978.
- Bendat, J.S., and Piersol, A.G.** (1986). *Random Data: Analysis and Measurement Procedures*. John Wiley, New York.
- Bendat, J.S., and Piersol, A.G.** (1998). *Random Data: Analysis and Measurement Procedures*. 2nd Edition, John Wiley, New York.
- Benedict, L.H., and Gould, R.D.** (1996). Towards Better Uncertainty Estimates for Turbulence Statistics. *Experiments in Fluids*, **22**, 129–136.
- Benedict, L.H., Gould, R.D.** (1995). *Experiences Using Kalman Reconstruction for Enhanced Spectrum Estimates*, Proceeding of ASME/JSME Fluids Engineering and Laser Anemometry Conference, South Caroline, 1-7.
- Benedict, L.H., Nobach, H., Tropea, C.** (2000). Estimation of Turbulent Velocity Spectra from Laser Doppler Data, *Measurement Science & Technology*, **11**, 1089-1104.
- Bergstrom, D.J., and Akinlade, O.G.** (2005). *Effect of Surface Roughness on the Triple Products in turbulent Boundary Layers*. 58th Annual Meeting of American Physical Society, division of Fluid Dynamics, November 20-22, Chicago.
- Bettermann, D.** (1965). Contribution a L'etude de la Couche Limite Turbulent le Long de Plagues Regueuses. Center National de la Recherche Scientifique, **Report No 65-6**.
- Bons, J.P.** (2002). St and CF Augmentation for Real Turbine Roughness with elevated Freestream Turbulence. *ASME, Paper No.GT-2002-30198*.
- Bons, J.P.** (2010). A Review of Surface Roughness Effects in Gas Turbines. *Journal of Turbomachinery Transactions of ASME*, **132**, 021004.
- Bowden, B.S., and Davison, N.J.** (1974). Resistance Increments Due to Hull roughness Associated with Form Factor Extrapolation Methods. National Physical Laboratory, Ship Technical Manual 3800.
- Bradshaw, P.** (1971). *An Introduction to Turbulence and Its Measurement*. Pergamon Press, Germany.

- Bradshaw, P.** (2000). A Note on Critical Roughness Height and Transitional Roughness. *Physics of Fluids*, **12** (6), 1611-1614.
- Bryne, D.** (1980). *The Hull Roughness of Ships in Service*, MSc Thesis, Department of Marine Technology, University of Newcastle Upon Tyne, Newcastle Upon Tyne.
- Brzek, B., Cal, R.B., Johansson, G., Castillo, L.** (2007). Inner and Outer Scalings in Rough Surface Zero Pressure Gradient Turbulent Boundary Layers. *Experiments in Fluids*, **44**, 115-124.
- Brzek, B., Cal, R.B., Johansson, G., Castillo, L.** (2008). Transitionally Rough Zero-Pressure-Gradient Turbulent Boundary Layers. *Experiments in Fluids*, **44**, 115-124.
- Brzek, B., Chao, B., Turan, Ö., and Castillo, L.** (2010). Characterizing Developing Adverse Pressure Gradient Flows Subject to Surface Roughness. *Experiments in Fluids*, **48**, 663-677.
- Brzek, B., Torres-Nieves, S., Lebron, J, Cal, R., Meneveau, C., and Castillo, L.** (2009). Effects of Freestream Turbulence on Rough Surface Turbulent Boundary Layers. *Journal of Fluid Mechanics*, **635**, 207-243.
- Britz, D., Antonia, R.A.** (1996). A Comparison of Methods of Computing Power Spectra of LDA Signals, *Measurement Science & Technology*, **7**, 1042-1053.
- Burattini, P., Leonardi, S., Orlandi, P., and Antonia, R.A.** (2008). Comparison Between Experiments and Direct Numerical Simulations in a Channel Flow with Roughness on One Wall. *Journal of Fluid Mechanics*, **600**, 403-426.
- Buschmann, M.H., and Gad-el-Hak, M.** (2003). Debate Concerning the Mean Velocity Profile of a Turbulent Boundary Layer. *AIAA Journal*, **41**, 565-572.
- Buschmann, M.H., and Meniert, J.** (1999). Power Law or Logarithmic Law for Turbulent Boundary Layers with Low Reynolds Number. Colloquium Fluid Mechanics, Prague, Germany.
- Cal, R.B., Brzek, B., Johansson, T.G., and Castillo, L.** (2009). The Rough Favourable Pressure Gradient turbulent Boundary Layer. *Journal of Fluid Mechanics*, **641**, 129-155.
- Candries, M.** (2001). *Drag, Boundary-Layer and Roughness Characteristics of Marine Surfaces Coated with Antifoulings*. PhD Thesis, Department of Marine Technology, University of Newcastle upon Tyne, Newcastle upon Tyne.

- Candries, M., and Atlar, M.** (2005). Experimental Investigation of The Turbulent Boundary Layer Of Surfaces Coated With Marine Antifoulings. *Journal of Fluids Engineering Transactions of ASME*, **127**, 219-232.
- Candries, M., Atlar, M., Mesbahi, E., and Pazouki, K.** (2003) The Measurement of the Drag Characteristics of Tin-Free Self-Polishing Co-Polymers and Fouling Release Coatings Using a Rotor Apparatus. *Biofouling*, **19**, 27-36.
- Canham, H.J.S.** (1975). Resistance, Propulsion and Wake Tests with HMS Penelope. *Transactions of the Royal Institution of Naval Architects*, **117**, 61-94.
- Castillo, L., and Walker, D.J.** (2002). Effect of Upstream Conditions on the Outer Flow of Turbulent Boundary Layers. *AIAA Journal*, **40**, 1292-1299.
- Castro, I.P.** (2007). Rough-Wall Boundary Layers: Mean Flow Universality. *Journal of Fluid Mechanics*, **585**, 469-485.
- Cebeci, T., and Smith, A.M.O.** (1974). *Analysis of Turbulent Boundary Layers*. Academic Press, London.
- Chao, Y.C., Leu, J.H.** (1992). A Fractal Reconstruction Method for LDV Spectral Analysis, *Experiments in Fluids*, **13**, 91-97.
- Clauser, F.H.** (1954). Turbulent Boundary Layer in Adverse Pressure Gradients. *Journal of the Aeronautical Sciences*, **21**, 91-108.
- Clauser, F.H.** (1956). The Turbulent Boundary Layer. *Advances in Applied Mechanics*, **4**, 1-51.
- Choi, K.-S., Yang, X., Clayton, B., Glover, E.J., Atlar, M., Semenov, B.N., Kulik, M.** (1997). Turbulent Drag Reduction Using Compliant Surfaces. *Proceedings of the Royal Society of London A*, **453**, 2229-2240.
- Colebrook, C.F.** (1939). Turbulent Flows in Pipes with Particular Reference to the Transition Region between the Smooth and Rough Pipe Flows. *Journal of the Institution of Civil Engineers*, **11**, 133-155.
- Colebrook, C.F., and White, C.M.** (1937). Experiments with fluid Friction in Roughened Pipes. *Proceedings of the Royal Society London Series A*, **161**, 367-381.
- Coleman, H.W., and Steele, W.G.** (2009). *Experimentation and Uncertainty Analysis for Engineers*. New York: John Wiley & Sons.
- Coles, D.E.** (1956). The Law of the Wake in the Turbulent Boundary Layer. *Journal of Fluid Mechanics*, **1**, 191-226.

- Connelly, J.S., Schultz, M.P., and Flack, K.A.** (2006). Velocity-Defect Scaling for Turbulent Boundary Layers with a Range of Relative Roughness. *Experiments in Fluids*, **40**, 188-195.
- Darcy, H.** (1857). *Recherches Experimentales Relatives au Mouvement de L'eau Dans Les Tuyaux*, Paris: Mallet-Bachelier.
- Davidson, P.A.** (2005). *Turbulence: An Introduction for Scientists and Engineers*, Oxford University Press, New York.
- Degraaff, D.B., and Eaton, J.K.** (2000). Reynolds Number Scaling of the Flat-Plate Turbulent Boundary Layer. *Journal of Fluid Mechanics*, **422**, 319-346.
- Del Alamo, J.C., and Jimenez, J.** (2009). Estimation of Turbulent Convection Velocities and Corrections to Taylor's Approximation. *Journal of Fluid Mechanics*, **640**, 27-54.
- Dey, S.K.** (1989). *Parametric Representation of Hull Painted Surfaces and the Correlation with Fluid Drag*. PhD Thesis, Department of Marine Technology, University of Newcastle upon Tyne, Newcastle upon Tyne.
- DIN 4777.** (1990). Profile Filters for Electric Stylus Instruments- Phase Corrected Filters, Deutches Institut für Normung, Berlin.
- Dirling, R.B.** (1973). A Method for Computing Rough Wall Heat Transfer Rates on Re-Entry Nosedips. *AIAA Paper*, **No.73-763**.
- Dixit, S.A., and Ramesh, O.N.** (2009). Determination of Skin Friction in Strong Pressure-Gradient Equilibrium and Near-Equilibrium Turbulent Boundary Layers. *Experiments in Fluids*, **47**, 1045-1058.
- Djenidi, L., Antonia, R.A., Amielh, M., and Anselmet, F.** (2008). A Turbulent Boundary Layer Over a Two-Dimensional Rough Wall. *Experiments in Fluids*, **44**, 37-47.
- Djenidi, L., Elavarasan, E., and Antonia, R.A.** (1999) Turbulent Boundary Layer over Transverse Square Cavities. *Journal of Fluid Mechanics*, **395**, 271-294.
- Dvorak, F.A.** (1969). Calculation of Turbulent Boundary Layers on Rough Surfaces in Pressure Gradients. *AIAA Journal*, **7**, 1752-1759.
- Efros, V., and Krogstad, P.A.** (2011). Development of a Turbulent Boundary Layer After a Step From Smooth to Rough Surface. *Experiments in Fluids*, **51**, 1563- 1575.
- Fahl, D.** (1982). Motif Combination. *Wear*, **83**, 165-179.
- Flack, K.A., and Schultz, M.P.** (2010). Review of Hydraulic Roughness Scales in the Fully Rough Regime. *Journal of Fluids Engineering*, **132**, 041203.

- Flack, K.A., Schultz, M.P., Connelly, J.S.** (2007). Examination of Critical Roughness Height for Outer Layer Similarity. *Physics of Fluids*, **19**, 095104.
- Flack, K.A., Schultz, M.P., and Shapiro, T.A.** (2005). Experimental Support for Townsend's Reynolds Number Similarity Hypothesis on Rough Walls. *Physics of Fluids* **17(3)**, 035102.
- Flores, O., and Jimenez, J.** (2006). Effect of Wall Boundary Disturbances on Turbulent Channel Flows. *Journal of Fluid Mechanics*, **566**, 357-376.
- Finnie, A.A., and Williams, D.N.** (2010). Paint and Coatings Technology for the Control of Marine Fouling. In: Durr, S., and Thomason, J.C., Editors. *Biofouling*, Oxford, UK: Wiley-Blackwell. p.185-206.
- Finley, P.J., Chong Phoe, K., and Jeck Pohn, C.** (1996). Velocity Measurements in a Thin Turbulent Wake Layer. *La Houille Blanche*, **21**, 713-721.
- Fuchs, W., Nobach, H., Tropea, C.** (1994). Laser Doppler Anemometry Data Simulation: Application to Investigate the Accuracy of Statistical Estimators, *AIAA Journal*, **32**, 1883-1889.
- Furuya, Y., and Fujita, H.** (1967). Turbulent Boundary Layers on a Wire-Screen Roughness. *Bulletin of JSME*, **10**, 77-86.
- Gad-el-Hak, M., and Buschmann, M.H.** (2011). Turbulent Boundary Layers: Is the Wall Falling or Merely Wobbling? *Acta Mechanica*, **218**, 309-318.
- Ganapathisubramani, B., Longmire, E.K., and Marusic, I.** (2003). Characteristics of Vortex Packets in Turbulent Boundary Layers, *Journal of Fluid Mechanics*, **478**, 35-46.
- Gaster, M., Roberts, J.B.** (1977). The spectral Analysis of Randomly Sampled Records by a Direct Transform, *Proceedings of the Royal Society of London A*, **354**, 27-58.
- George, W.K., and Castillo, L.** (1997). Zero Pressure Gradient turbulent Boundary Layer. *Applied Mechanics Review*, **50**, 689-729.
- Granville, P.S.** (1987). Three Indirect Methods for the Drag Characterization of Arbitrarily Rough Surfaces on Flat Plates. *Journal of Ship Research*, **31**, 70-77.
- Grass, A.J.** (1971). Structural Features of Turbulent Flow over Smooth and Rough Boundaries. *Journal of Fluid Mechanics*, **50**, 233-255.
- Grigson, C.W.B.** (1992). Drag Losses of New Ships Caused by Hull Finish. *Journal of Ship Research*, **36**, 182-196.

- Hagen, G.** (1854). Über den Einfluss der Temperatur auf die Bewegung des Wassers in Röhren, *Math. Abh. Akad. Wiss. Berlin*, pp.17-98.
- Hama, F.R.** (1954). Boundary-Layer Characteristics for Smooth and Rough Surfaces. *Transactions of the Society of Naval Architects and Marine Engineers*, **62**, 333-358.
- Haslbeck, E.G., and Bohlander, G.** (1992). Drag Losses of New Ships Caused by Hull Finish. *Journal of Ship Research*, **31**, 70-77.
- Head, M.R., and Bandhopadhyay, P.** (1981). New Aspects of Turbulent Boundary Layer Structure. *Journal of Fluid Mechanics*, **107**, 297-337.
- Herpin, S., Stanislas, M., and Soria, J.** (2010). The Organization of Near-Wall Turbulence: A Comparison Between Boundary Layer SPIV Data and Channel Flow DNS Data. *Journal of Turbulence*, **11 (47)**, 1-30.
- Hinze, J.O.** (1959; 1975). *Turbulence*. McGraw-Hill, New York.
- Holm, E., Schultz, M.P., Haslbeck, E., and Tallbott, W.** (2004). Evaluation of Hydrodynamic Drag on Experimental Fouling-Release Surfaces, Using Rotating Disks. *Biofouling*, **20**, 219-226.
- Howell, D., and Behrends, B.** (2006). A Review of Surface Roughness in Antifouling coatings Illustrating the Importance of Cutoff Length. *Biofouling*, **22**, 401-410.
- Hösel, W., Rodi, W.** (1977). New Biasing Elimination Method for Laser Doppler Velocimeter Counter Processing, *Review of Scientific Instruments*, **48**, 910-919.
- Host-Madsen, A.** (1994). *A New Method for Estimation of Turbulence Spectra for Laser Doppler Anemometry*, Proceeding of 7th International Symposium on Applications of Laser Technology to Fluid Mechanics, Lisbon, paper 11.1.
- Hunt, J.C.R., and Carloti, P.** (2001). Statistical Structure at the Wall of the High Reynolds Number Turbulent Boundary Layer. *Flow Turbulence and Combustion*, **66**, 453-475.
- Ikeda, T., and Durbin, P.A.** (2007). Direct Simulations of a Rough Wall Channel Flow. *Journal of Fluid Mechanics*, **571**, 235-263.
- Ioselevich, V.A., and Pilipenko, V.I.** (1974). Logarithmic Velocity Profile for Flow of a Weak Polymer Solution near a Rough Surface. *Sov.Phys.Dokl.*, **18**, 790.
- International Towing Tank Conference (ITTC).** (1978). Report of the Powering Performance Committee. 15th ITTC, Hague.

- International Towing Tank Conference (ITTC).** (1990). Proceedings of the 19th ITTC Conference, Report of the Powering Performance Committee, Madrid.
- International Towing Tank Conference (ITTC).** (2005). Report of the Powering Performance Committee. 24th ITTC, Edinburgh.
- ISO 12085** (1996). Geometric Product Specification-Surface Texture: Profile Method-Motif Parameters, Geneva.
- ISO** (1998). ISO 4288:1996/Cor 1:1998. Geometrical Product Specifications – Surface Texture: Profile Method – Rules and procedures for The Assessment of Surface Texture. International Standards Organization. Report No BS 3900-K2:2001, London.
- Jenkins, G.M., and Watts, D.G.** (1968). *Spectral Analysis and Its Applications*, Holden-Day.
- Jimenez, J.** (1999). The Physics of Wall Turbulence, *Physica A*, **263**, 252-262.
- Jimenez, J.** (2004). Turbulent Flow over Rough Walls. *Annual Review of Fluid Mechanics*, **36**, 173-196.
- Jimenez, J., and Moin, P.** (1991). The Minimal Flow Unit Near Wall Turbulence. *Journal of Fluid Mechanics*, **225**, 221-240.
- Johansson, L.E.** (1985). The Local Effect of Hull Roughness on Skin Friction Calculation Based on Floating Element Data and Three-Dimensional Boundary Layer Theory. *Transactions of the Royal Institution of Naval Architects*, **127**, 187-201.
- Karlssoon, R.I.** (1978). The Effect of Irregular Surface Roughness on the Frictional Resistance of Ships. International symposium on Ship Viscous Resistance, Paper 9, Göteborg.
- Keirsbulck, L., Labraga, L., Mazouz, A., and Tournier, C.** (2002). Surface Roughness Effects on turbulent Boundary Layer Structures. *Journal of Fluids Engineering Transactions of ASME*, **124**, 127-135.
- Kim, H.T., Kline, S.J., and Reynolds, W.C.** (1971). The Production of Turbulence Near a Smooth Wall in a Turbulent Boundary Layer. *Journal of Fluid Mechanics*, **50**, 133-160.
- Kolmogorov, A.N.** (1941). Local Structure of Turbulence in an Incompressible Fluid for Very Large Reynolds numbers. Comptes Rendus (Doklady) de l'Academie des Sciences de l'U.R.S.S., 31, 301-305. (Reprinted in: *Turbulence: Classic Papers on Statistical Theory*, Editors: S.K. Friedlander and L. Topper, Interscience Publishers, New York, 1961.)

- Kotey, N.A., Bergstrom, D.J., and Tachie, M.F.** (2003). Power Laws for Rough Wall Turbulent Boundary Layers. *Physics of Fluids*, **15**, 1396-1404.
- Krogstad, P.A., Andersson, H.I., Bakken, O.M., and Ashrafiyan A.** (2005). An Experimental and Numerical Study of Channel Flow with Rough Walls. *Journal of Fluid Mechanics*, **530**, 327-352.
- Krogstad, P.A., and Antonia, R.A.** (1994). Structure of Turbulent Boundary Layers on Smooth and Rough Walls. *Journal of Fluid Mechanics*, **277**, 1-21.
- Krogstad, P.A., and Antonia, R.A.** (1999). Surface Roughness Effects in Turbulent Boundary Layers. *Experiments in Fluids*, **27**, 450-460.
- Krogstad, P.A., Antonia, R.A., Browne, L.W.B.** (1992). Comparison between Rough And Smooth Wall Turbulent Boundary Layers. *Journal of Fluid Mechanics*, **245**, 599-617.
- Krogstad, P.A., Kaspersen, J.H., and Rimestad, S.** (1998). Convection Velocities in a Turbulent Boundary Layer, *Physics of Fluids*, **10 (4)**, 949-957.
- Kunkel, G.J., and Marusic, I.** (2006). Study of the Near-Wall-Turbulent Region of the High Reynolds Number Boundary Layer Using an Atmospheric Flow, *Journal of Fluid Mechanics*, **548**, 375-402.
- Lackenby, H.** (1962). Resistance of Ships, with Special Reference to Skin Friction and Hull Surface Condition. *Proceedings of Institute of Mechanical Engineers*, **176**, 981-1014.
- Langelandsvik, L.I., Kunkel, G.J., and Smits, A.J.** (2008). Flow in a Commercial Steel Pipe. *Journal of Fluid Mechanics*, **595**, 323-339.
- Le-Boeuf, R.L., and Mehta, R.D.** (1995). On Using Taylor's Hypothesis for Three-Dimensional Mixing Layers. *Physics of Fluids*, **7**, 1516.
- Lee, S.H., and Sung, H.J.** (2007). Direct Numerical Simulation of the Turbulent Boundary Layer Over a Rod Roughened Wall. *Journal of Fluids Mechanics*, **584**, 125-146.
- Leer-Andersen, M., and Larsson, L.** (2003). An Experimental/Numerical Approach for Evaluating Skin Friction on Full-Scale Ships with Surface Roughness. *Journal of Marine Science and Technology*, **8**, 26-36.
- Leonardi, S., Orlandi, P., and Antonia, R.A.** (2007). Properties of d and k-type Roughness in Turbulent Channel Flow. *Physics of Fluids*, **19**, 125101.
- Leonardi, S., Orlandi, P., Djenidi, L., and Antonia, R.A.** (2004). Structure of Turbulent Channel Flow with Square Bars on One Wall. *International Journal of Heat and Fluid Flow*, **25**, 384-392.

- Leonardi, S., Orlandi, P., Smalley, R.J., Djenidi, L., and Antonia, R.A.** (2003). Direct Numerical Simulations of Turbulent Channel Flow with Transverse Square Bars on One Wall. *Journal of Fluid Mechanics*, **491**, 229-238.
- Lewthwaite, J.C., Molland, A.F., and Thomas, K.W.** (1985). An Investigation into the Variation of Ship Skin Frictional Resistance with Fouling. *Transactions of Royal Institute of Naval Architects*, **127**, 269-284.
- Ligrani, P.M., and Moffat, R.J.** (1986). Structure of Transitionally Rough and Fully Rough Turbulent Boundary Layers. *Journal of Fluid Mechanics*, **162**, 69-98.
- Loeb, G.I., Laster, D., and Gracik, T.** (1984). *The Influence of Microbial Fouling Films on Hydrodynamic Drag*. In: Marine Biodeterioration, An Interdisciplinary Study, Editors: J D Costlow, R Tipper, Naval Institute Press, Annapolis.
- Marquardt, D.W., Acuff, S.K.** (1983). *Direct Quadratic Spectrum Estimation with Irregularly Spaced Data*, In: Time Series Analysis of Irregularly Observed Data, Ed. E Parzen, Springer, Berlin, 211-223.
- Marabotti, I., Morelli, A., Orsini, L.M., Martinelli, E., Galli, G., Chiellini, E., Lien, E.M., Pettitt, M.E., Callow, M.E., Callow, J.A., Conlan, S.L., Mutton, R.J., Clare, A.S., Kocijan, A., Donik, C., and Jenko, M.** (2009). Fluorinated/Siloxane Copolymer Blends For Fouling Release: Chemical Characterisation And Biological Evaluation with Algae and Barnacles. *Biofouling*, **25**, 481-493.
- Martinelli, E., Agostini, S., Galli, G., Chiellini, E., Glisenti, A., Pettitt, M.E., Callow, M.E., Callow, J.A., Graf, K., and Bartels, F.W.** (2008). Nanostructured Films Of Amphiphilic Fluorinated Block Copolymers For Fouling Release Application. *Langmuir*, **24**, 13138-13147.
- Martinelli, E., Fantoni, C., Galli, G., Gallot, B., and Glisenti, A.** (2009a). Low Surface Energy Properties of Smectic Fluorinated Block Copolymers/SEBS Blends. *Molecular Crystals and Liquid Crystals*, **500**, 51-62.
- Martinelli, E., Glisenti, A., Gallot, B., and Galli, G.** (2009b). Surface Properties of Mesophase-Forming Fluorinated Bicycloacrylate/Polysiloxane Methacrylate Copolymers. *Macromol. Chem. Phys.*, **210**, 1746-1753.
- Mason, R.L., Gunst, R.F., and Hess, J.L.** (1989). *Statistical Design and Analysis of Experiments with Applications to Engineering and Science*. New York: Wiley.

- Mayo, W.T. Jr., Shay, M.T., Ritter, S.** (1974). *Digital Estimation of Turbulence Power Spectra from Burst Counter LDV Data*, Proceedings of 2nd International Workshop on Laser Velocimetry, Purdue University, 16-26.
- McKeon, B.J., Li, J., Jiang, W., Morrison, J.F., and Smits, A.J.** (2004). Further Observations on the Mean Velocity Distribution in Fully Developed Pipe Flow. *Journal of Fluid Mechanics*, **501**, 135-147
- Medhurst, J.S.** (1989). *The Systematic Measurement and Correlation of the Frictional Resistance and Topography of Ship Hull coatings, with Particular Reference to Ablative Antifouling*. PhD Thesis, University of Newcastle upon Tyne, Newcastle.
- Mehta, R.D., Bell, J.H., Reda, D.C., Wilder, M.C., Zilliac, G.G. and Driver, D.M.** (2000). *Pressure and Sensitive Coatings*. In: Flow Visualization: Techniques and Examples, Editors: A.J. Smits and T.T. Lim, Imperial College Press, London.
- Mejia-Alvarez, R., and Christensen, K.T.** (2010). Low-Order Representations of Irregular Surface Roughness and Their Impact on a Turbulent Boundary Layer. *Physics of Fluids*, **22**, 015106.
- Moffat R.J.** (1988). Describing The Uncertainties In Experimental Results. *Exp Ther Fluid Sci.*, **1(1)**: 3-17.
- Moin, P.** (2009). Revisiting Taylor's Hypothesis. *Journal of Fluid Mechanics*, **640**, 1-4.
- Moody, L.F.** (1944). Friction Factors for Pipe Flow, *Transactions of ASME*, **66**, 671-684.
- Moreau, S., Plantier, G., Valiere, J.-C., Bailliet, H., and Simon, L.** (2011). Estimation of Power Spectral Density from Laser Doppler Data via Linear Interpolation and Deconvolution. *Experiments in Fluids*, **50**, 179-188.
- Mummery, L.** (1990). *Surface Texture Analysis: The Handbook*, Hommelwerke, Muhlhausen.
- Müller, E., Nobach, H., Tropea, C.** (1994). *LDA Signal Reconstruction: Application to the Moment and Spectral Estimation*, Proceeding of 7th International Symposium on Applications of Laser Technology to Fluid Mechanics, Lisbon, paper 23.2.
- Müller, E., Nobach, H., Tropea, C.** (1998). Model Parameter Estimation from Non-Equidistant Sampled Data Sets at Low Data Rates, *Measurements Science and Technology*, **9**, 435-441.

- Murlis, J., Tsai, H.M., and Bradshaw, P.** (1982). The Structure of Turbulent Boundary Layers at Low Reynolds Numbers. *Journal of Fluid Mechanics*, **122**, 13-56.
- Musker, A.J.** (1981). Universal Roughness Functions for Naturally-Occurring Surfaces. *Transactions of Canadian Society of Mechanical Engineers*, **1**, 1-6.
- Musker, A.J.** (1990). *Turbulence Measurements in a Shear Layer Associated with a Ship Hull Roughness*. International Workshop on Marine Roughness and Drag, Paper 10, London.
- Na, Y., Hanratty, T.J., and Liu, Z.** (2001). The Use of DNS to Define Stress Producing Events for Turbulent Flow over a Smooth Wall. *Flow Turbulence and Combustion*, **66**, 495-512.
- Nagano, Y., and Houra, T.** (2002). Higher-order Moments and Spectra of Velocity Fluctuations in Adverse-Pressure-Gradient Turbulent boundary Layer. *Experiments in Fluids*, **33**, 22-30.
- Nakagawa, S. and Hanratty, T.J.** (2001). Particle Image Velocimetry Measurements of Flow over a Wavy Wall. *Physics of Fluids*, **13**, 3504-3507.
- Naughton, J.W., and Sheplak, M.** (2000). *Modern Skin Friction Measurement Techniques-Description, Use and What to Do with the Data*. 21st AIAA Aerodynamic Measurement Technology and Ground Testing Conference, Denver, USA, 19-21 June.
- Nikuradse, J.** (1933). Laws of Flow in Rough Pipes, NACA Technical Memorandum 1292.
- Nobach, H.** (1999). *Processing of Stochastic Sampled Data in Laser Doppler Anemometry*, Proceeding of the 3rd International Workshop on Sampling Theory and Applications, Norwegian University of Science and Technology, Trondheim, 149-154.
- Nobach, H.** (2000). *A Global Concept of Autocorrelation and Power Spectral Density Estimation from LDA Data Sets*, Dantec Measurement Technology Report, Denmark.
- Nobach, H.** (2002). Local Time Estimation for the Slotted Correlation Function of Randomly Sampled LDA Data, *Experiments in Fluids*, **32**, 337-345.
- Nobach, H., Müller, E., Tropea, C.** (1998a). *Correlation Estimator for Two-Channel, Non-Coincidence Laser-Doppler-Anemometer*, Proceedings of the 9th International Symposium of Applications of laser Techniques to fluid Mechanics, Instituto Superior Technico, Lisbon, paper 32.1.

- Nobach, H., Müller, E., Tropea, C.** (1998b). Efficient Estimation of Power Spectral Density from Laser Doppler Anemometer Data, *Experiments in Fluids*, **24**, 499-509.
- Orlandi, P., Leonardi, S., and Antonia, R.A.** (2006). Turbulent Channel Flow with either Transverse or Longitudinal Roughness Elements on One Wall. *Journal of Fluid Mechanics*, **561**, 279-305.
- Österlund, J.M.** (1999). *Experimental Studies on Zero Pressure Gradient Turbulent Boundary Layer Flow*. PhD Thesis, Royal Institute of Technology, Stockholm.
- Österlund, J.M., Johansson, A.V., Nagib, H.M., and Hites, M.H.** (2000). A Note on the Overlap Region in Turbulent Boundary Layers. *Physics of Fluids*, **12**, 1-4.
- Pailhas, G., Touvet, Y., and Aupoix, B.** (2008). Effects of Reynolds Number and Adverse Pressure Gradient on a Turbulent Boundary Layer Developing on a Rough Surface. *Journal of Turbulence*, **9(43)**, 1-24.
- Panton, R.L.** (2000). Power Law or Log Law; That is Not the Question. *Bulletin of American Physical Society*, **45**, 160, 53rd Annual Meeting of the Division of Fluid Dynamics November 19 - 21, 2000 Washington.
- Patel, V.C.** (1998). Perspective: Flow at High Reynolds Number and Over Rough Surfaces-Achilles Heel of CFD. *Journal of Fluids Engineering*, **120**, 434.
- Peklenik, J.** (1967). Investigation of Surface Topography. *Ann. C.I.R.P.*, **15**, 381-385.
- Perry, A.E., and Abell, C.J.** (1977). Asymptotic Similarity of Turbulence Structures in Smooth and Rough Walled Pipes. *Journal of Fluid Mechanics*, **79**, 785-799.
- Perry, A.E., and Chong, M.S.** (1982). On the Mechanism of Wall Turbulence. *Journal of Fluid Mechanics*, **119**, 173-217.
- Perry, A.E., and Li, J.D.** (1990). Experimental Support for the Attached-Eddy Hypothesis in Zero-Pressure-Gradient Turbulent Boundary Layers. *Journal of Fluid Mechanics*, **218**, 405-438.
- Perry, A.E., Henbest, S.M., and Chong, M.S.** (1986). A Theoretical and Experimental Study of Wall Turbulence. *Journal of Fluid Mechanics*, **165**, 163-199.
- Perry, A.E., Schofield, W.H., and Joubert, P.N.** (1969). Rough-Wall Turbulent Boundary Layer. *Journal of Fluid Mechanics*, **37**, 383-413.

- Perry, A.E., Lim, K.L., Henbest, S.M.** (1987). An Experimental Study of the Turbulence Structure in Smooth and Rough Wall Boundary Layers, *Journal of Fluid Mechanics*, **177**, 437-466.
- Perry, A.E., and Marusic, I.** (1995). A Wall-Wake Model for the Turbulence Structure of Boundary Layers. Part 1. Extension of Attached Eddy Hypothesis. *Journal of Fluid Mechanics*, **298**, 361-388.
- Poggi, D., Polpatto, A., and Ridolfi, L.** (2003). Analysis of the Small Scale Structure of Turbulence on Smooth and Rough Walls. *Physics of Fluids*, **15 (1)**, 1070-6631.
- Politis, G.** (2010). *Flow Mapping Report on the New Testing Section of ECT with and without High Speed Insert*. Emerson Cavitation Tunnel, School of Marine Science and Technology, Newcastle University.
- Politis, G., Ünal, B., Ünal, U.O., and Atlar, M.** (2011). *An Experimental Investigation into the Boundary Layer, Friction and Roughness Characteristics of 10 Different Coatings*. Emerson Cavitation Tunnel, School of Marine Science and Technology Report, Report no: MT-2011-001, Newcastle University.
- Porporato, A., and Sordo, S.** (2001). On the Incomplete Similarity for Turbulent Velocity Profiles in Rough Pipes. *Physics of Fluids*, **13**, 2596-2601.
- Raupach, M.R.** (1981). Conditional Statistics of Reynolds Stress in Rough Wall and Smooth Wall Turbulent Boundary Layers. *Journal of Fluid Mechanics*, **108**, 107-120.
- Raupach, M.R., Antonia, R.A., Rajagopalan, S.** (1991). Rough-Wall Turbulent Boundary Layers, *Applied Mechanics Review*, **44**, 1-25.
- Reynolds, A.J.** (1974). *Turbulent Flows in Engineering*, John Wiley & Sons, London.
- Rij, J.A., Belnap, B.J., and Ligrani, P.M.** (2002). Analysis and Experiments on three-Dimensional, Irregular Surface Roughness. *ASME Journal of Fluids Engineering*, **124**, 671-677.
- Robinson, S.K.** (1991). Coherent Motions in the Turbulent Boundary Layer. *Annual Review of Fluid Mechanics*, **23**, 601-639.
- Sabot, J., Saleh, I., and Comte-Bellot, G.** (1977). Effects of Roughness on the Intermittent Maintenance of Reynolds Shear Stress in Pipe Flow. *Physics of Fluids*, **20**, 150-155.
- Scargle, J.D.** (1982). Studies in Astronomical Time Series Analysis II: Sattistical Aspects of Spectral Analysis of Unevenly Spaced Data, *Astrophysics Journal*, **263**, 835-853.

- Seo, J.** (2003). *Investigation of the Upstream Conditions and Surface Roughness in Turbulent Boundary Layer*. PhD Thesis, Department of Mechanical and Aeronautical Engineering, Rensselaer Polytechnic Institute.
- Schlichting, H.** (1979). *Boundary Layer Theory*. McGraw-Hill, New York.
- Schultz, M.P.** (1998). *The Effect of Biofilms on Turbulent Boundary Layers*. DPhil Thesis, Florida Institute of Technology, Melbourne, Florida.
- Schultz, M.P.** (2000). Turbulent Boundary Layers On Surfaces Coated With Filamentous Algae. *Journal of Fluids Engineering Transactions of ASME*, **122**, 357-362.
- Schultz, M.P.** (2004). Frictional Resistance of Antifouling Coating Systems. *ASME Journal of Fluids Engineering*, **126**, 1039-1047.
- Schultz, M.P.** (2007). Effects of Coating Roughness and Biofouling on Ship Resistance and Powering. *Biofouling*, **23**(5), 331-341.
- Schultz, M.P., Bendick, J.A., Holm, E.R., and Hertel, W.M.** (2011). Economic Impact of Biofouling on a Naval Surface Ship. *Biofouling*, **27**, 87-98.
- Schultz, M.P., and Flack, K.A.** (2003). Turbulent Boundary Layers over Surfaces Smoothed by Sanding, *ASME Journal of Fluids Engineering*, **125**, 863-870.
- Schultz, M.P., and Flack, K.A.** (2005). Outer Layer Similarity in Fully Rough Turbulent Boundary Layers. *Experiments in Fluids*, **38**, 328-340.
- Schultz, M.P., and Flack, K.A.** (2007) The Rough-Wall Turbulent Boundary Layer from the Hydraulically Smooth to the Fully Rough Regime. *Journal of Fluid Mechanics*, **580**, 381-405.
- Schultz, M.P., and Flack, K.A.** (2009). Turbulent Boundary Layers on a Systematically Varied Rough Wall. *Physics of Fluids*, **21**, 015104.
- Schultz, M.P, and Myers, A.** (2003). Comparison of Three Roughness Function Determination Methods. *Experiments in Fluids*, **35**, 372-379.
- Schultz, M.P., and Swain, G.W.** (1999). The Effect of Biofilms on Turbulent Boundary Layers. *Journal of Fluids Engineering Transactions of ASME*, **121**, 44-51.
- Shockling, M.A., Allen, J.J., and Smits, A.J.** (2006). Roughness Effects in turbulent Pipe Flow, *Journal of Fluid Mechanics*, **564**, 267285.
- Sigal, A., and Danberg, J.E.** (1990). New Correlation of Roughness Density Effects on the Turbulent Boundary Layer. *AIAA Journal*, **28**, 554-556.

- Smith, S.V.** (2003). *Digital Signal Processing: A Practical Guide for Engineers and Scientist*, Amsterdam, Newnes.
- Sree, D., Kjelgaard, S.O., Seller, W.L.III.** (1994). *Spectral Enhancement of Randomly Sampled Signals by Pre- Filtering Techniques*, *Laser Anemometry: Advances and Applications*, 680-685.
- Shafi, H.S., and Antonia, R.A.** (1997). Small-Scale Characteristics of a Turbulent Boundary Layer over a Rough Wall. *Journal of Fluid Mechanics*, **342**, 263-293.
- Stefes, B., and Fernholz, H.-H.** (2005). The Influence of High Free-Stream Turbulence and a Favourable Pressure Gradient on an Incompressible Axisymmetric turbulent Boundary Layer. *European Journal of Mechanics B/Fluids*, **24**, 167-187.
- Tachie, M.F., Bergstrom, D.J., and Balachandar, R.** (2000). Rough Wall Turbulent Boundary Layers in Shallow Open channel Flow. *Journal of Fluids Engineering*, **122**, 533-541.
- Tachie, M.F.** (2000). *Open Channel Turbulent Boundary Layers and Wall Jets on Rough Surfaces*. PhD Thesis, Department of Mechanical Engineering, University of Saskatchewan, Saskatoon.
- Tani, I.** (1987). Equilibrium, Or None-Equilibrium, of Turbulent Boundary Layer Flows. *Proceedings of the Japan Academy Series B-Physical and Biological Sciences*, **63(3)**, 96-100.
- Tani, I.** (1988). Drag Reduction by Riblet Viewed As Roughness Problem. *Proceedings of the Japan Academy Series B-Physical and Biological Sciences*, **64(2)**, 21-24.
- Taylor, G.I.** (1938). The Spectrum of Turbulence. *Proceedings of the Royal Society of London*, **164 (919)**, 476-490.
- Tennekes, H., and Lumley, J.L.** (1972). *A First Course in Turbulence*, MIT Press, London.
- Townsend, A.A.** (1961). Equilibrium Layers and Wall turbulence. *Journal of Fluid Mechanics*, **11**, 97- 120.
- Townsend, A.A.** (1976). *The Structure of Turbulent Shear Flow*, Cambridge University Press, Cambridge.
- Townsin, R.L.** (2003). The Ship Hull Fouling Penalty. *Biofouling*, **10**, 187-197.
- Townsin, R.L., Bryne, D., Svensen, T.E., and Milne, A.** (1981). Estimating the Technical and Economic Penalties of Hull and Propeller Roughness. *Transactions of SNAME*, **89**, 295-318.

- Theodorson, T.** (1952). *Mechanism of Turbulence*. Proceeding of 2nd Midwestern Conference on Fluid Mechanics, Ohio State University, Columbus, Ohio.
- Thomas, T.R.** (1982). *Rough Surfaces*. Longman, London.
- Thomas, T.R.** (1999). *Rough Surfaces*. 2nd Edition, Imperial College Press, London.
- Tummers, M.J., and Passchier, D.M.** (1996). Spectral Estimation Using a Variable Window and the Slotting Technique with Local Normalization. *Measurement Science and Technology*, **7**, 1541-1546.
- Ünal, U.O., Ünal, B., Atlar, M.** (2012). Turbulent Boundary Layer Measurements over Flat Surfaces Coated by Nanostructured Marine Antifouling. *Experiments in Fluids*, **52(6)**, 1431-1448.
- Ünal, B., Ünal, U.O., Sampson, R., Politis, G., Atlar, M.** (2010). WP5.2 *Hydrodynamic Testing*. AMBIO Project Report, Deliverable 5.2b, March.
- Van Maanen, H.R.E., Nobach, H., Benedict, L.H.** (1999). Improved Estimator for the Slotted Autocorrelation Function of Randomly Sampled LDA Data, *Measurement Science & Technology*, **10**, L4-L7.
- Van Maanen, H.R.E., Tulleken, H.J.A.F.** (1994). *Application of Kalman Reconstruction to Laser Doppler Anemometry Data for Estimation of Turbulent Velocity Fluctuations*, Proceeding of 7th International Symposium on Applications of Laser Technology to Fluid Mechanics, Lisbon, paper 23.1.
- Van Maanen, H.R.E., Tummers, M.J.** (1996). *Estimation of the Autocorrelation Function of Turbulent Velocity Fluctuations Using the Slotting Technique with Local Normalization*, Proceedings of 8th International Symposium on Applications of Laser Technology to Fluid Mechanics, Lisbon, paper 36.4.
- Veynante, D., Candel, D.S.M.** (1988). A Promising Approach in Laser Doppler Velocimetry Data Processing: Signal Reconstruction and Nonlinear Spectral Analysis, *Signal Processing*, **14**, 295-300.
- Volino, R.J., Schultz, M.P., and Flack, K.A.** (2007). Turbulence Structure in Rough and Smooth Wall Boundary Layers. *Journal of Fluid Mechanics*, **592**, 263-293.
- Volino, R.J., Schultz, M.P., and Flack, K.A.** (2009). Turbulence Structure in a Boundary Layer with Two-Dimensional Roughness. *Journal of Fluid Mechanics*, **635**, 75-101.

- Volino, R.J., and Simon, T.W.** (2000). Spectral Measurements in transitional Boundary Layers on a Concave Wall under High and Low Free-Stream Turbulence Conditions. *Journal of Tubomachinery*, **122**, 450-457.
- Waigh, D.R., and Kind, R.J.** (1998). Improved Aerodynamic Characterization of Regular Three- dimensional Roughness, *AIAA Journal*, **36**, 1117-1119.
- Weinell, C.E., Olsen, K.N., Christoffersen, M.W., and Kiil, S.** (2003). Experimental Study of Drag Resistance Using a Laboratory Scale Rotary Set-up. *Biofouling*, **19**, 45-51.
- Wilcox, D.C.** (2006). *Turbulence Modelling for CFD*. 3rd Edition, DCW Industries Inc., California.
- White, F.M.** (1974). *Viscous Fluid flow*. McGraw-Hill, New York.
- Whitehouse, D.J.** (1994). Handbook of Surface Metrology. Institute of Physics Publishing, Bristol.
- Whitehouse, D.J.** (2002). Surfaces and Their Measurement. HPS, London.
- Whitehouse, D.J.** (2011). Handbook of Surface and Nanometrology. Taylor and Francis, 2nd Edition, London.
- Womersley, J.R., and Hopkins, M.R.** (1945). Suggestions Concerning the Use of The Correlogram for the Interpretation of Measurements of Surface Finish. *Journées des États de Surface*, 135-139.
- Wu, Y., and Christensen, K.T.** (2007). Outer-Layer Similarity in the Presence of a Practical Rough-Wall Topography. *Physics of Fluids*, **19**, 085108.
- Wu, Y., and Christensen, K.T.** (2010). Spatial Structure of a Turbulent Boundary Layer with Irregular Surface Roughness. *Journal of Fluid Mechanics*, **655**, 380-418.
- Zagarola, M.V., and Smits, A.J.** (1998). A New Mean Velocity Scale for Turbulent Boundary Layers. ASME Paper **FEDSM98-4950**.
- Zagarola, M.V., Perry, A.E., and Smits, A.J.** (1998). Log Laws or Power Law: The Scaling in the Overlap Region. *Physics of Fluids*, **9**, 2094-2100.
- Zhou, J., Adrian, R.J., and Balachandar, S.** (1996). Autogeneration of Near Wall Vortical Structures in Channel Flow, *Physics in Fluids*, **8**, 288.

CURRICULUM VITAE

Name Surname: Burcu Ünal
Place and Date of Birth: İzmir - 03/02/1979
Address: Istanbul Technical University Ayazaga Campus Naval Architecture and Ocean Engineering Faculty Maslak / İstanbul
E-Mail: erbasburc@itu.edu.tr
B.Sc.: Istanbul Technical University Naval Architecture and Marine Engineering
M.Sc.: Istanbul Technical University Naval Architecture and Marine Engineering (Thesis: *Analysis of Ship Motions*)

Professional Experience:

2001-2012 Research Associate, Istanbul Technical University, Naval Architecture and Ocean Engineering Faculty
2011-2012 Visiting Fellow, Newcastle University, School of Marine Science and Technology (15 October 2011- 16 March 2012)
2009 Visiting Research Associate, Newcastle University, School of Marine Science and Technology (6 November - 23 December 2009)
2008-2009 Visiting Research Associate, Newcastle University, School of Marine Science and Technology (31 October 2008 - 11 August 2009)
2005 Visiting Research Associate, Newcastle University, School of Marine Science and Technology (1 August - 14 December 2005)

List of Publications:

- Atlar, M., Ünal, B., Ünal, U.O., Politis, G., Martinelli, E., Galli, G., Davies, C., Williams, D., (2013). An Experimental Investigation on the Frictional Drag Characteristics of Nanostructured and Fluorinated Fouling Release Coatings. *Biofouling*, **29(1)**, 39-52.

- Ünal, U.O., **Ünal, B.**, Politis, G., Atlar, M. (2010). *Boundary Layer, Drag And Surface Roughness Characteristics Of Nanostructured Coatings On An Axy-Symmetrical Slender Body Tested In A Cavitation Tunnel*. 15th ICMCF (International Congress on Marine Corrosion and Fouling), Abstract Book.
- Politis, G., **Ünal, B.**, Ünal, U.O., Atlar, M. (2011). An Experimental Investigation into the Boundary Layer, Friction and Roughness Characteristics of 10 Different Coatings. MT-2011-001, School of Marine Science and Technology, Newcastle University.
- **Ünal, B.**, Ünal, U.O, Sampson, R., Politis, G., Atlar, M. (2010). WP5.2 Hydrodynamic Testing. EU FP6 AMBIO Project Report, Deliverable 5.2b. March.
- **Ünal, B.**, and Atlar, M. (2009). Comment on the ship performance data of ‘Spirit of Tasmania 1 & 2. MT-2009-001, School of Marine Science and Technology, Newcastle University.
- **Ünal, B.**, and Atlar, M. (2010). Comment on the ship performance data of Hjaltlans and Hrossey. MT-2010-003, School of Marine Science and Technology, Newcastle University.

PUBLICATIONS/PRESENTATIONS ON THE THESIS

- Ünal, U.O., **Ünal, B.**, Atlar, M. (2012). Turbulent Boundary Layer Measurements over Flat Surfaces Coated by Nanostructured Antifouling. *Experiments in Fluids*, **52(6)**, 1431-1448.
- **Ünal, B.**, Ünal, U.O., Politis, G., Sampson, R., Atlar M. (2010). *Boundary Layer and Surface Roughness Measurements on Nanostructured Anti-Fouling Coatings*. Proceedings of International Conference on Ship Drag Reduction, 73-80.
- **Ünal, B.**, Ünal, U.O., Atlar, M. (2009). *Flat Plate Turbulent Boundary Layer Experiments*. International Workshop on “Concepts & Strategies for Surface Engineering to Control Biofouling”, December 8-10, St. Petersburg, Florida, USA (Presentation in *Fouling Hydrodynamics Session*).